Ultracold bosonic atoms in optical lattices

by

Ana Maria Rey

Dissertation submitted to the Faculty of the Graduate School of the
University of Maryland at College Park in partial fulfillment
of the requirements for the degree of
Doctor of Philosophy
2004

Advisory Committee:

Prof. Theodore R. Kirkpatrick, Chairman/Advisor
Dr. Charles W. Clark, Advisor
Prof. Bei-Lok Hu,
Prof. Steve Rolston,
Prof. J. Robert Dorfman

There are men who fight one day and are good.
There are men who fight one year and are better.
There are some who fight many years and they are better still.
But there are some that fight their whole lives,
these are the ones that are indispensable.
Berthold Brecht

Abstract

Title of Dissertation: Ultracold bosonic atoms
in optical lattices

Ana Maria Rey, Doctor of Philosophy, 2004

Dissertation directed by: Prof. Theodore R. Kirkpatrick
Physics
Dr. Charles W. Clark
National Institute of Standards and Technology

This thesis covers most of my work in the field of ultracold atoms loaded in optical lattices. It makes a route through the physics of cold atoms in periodic potentials starting from the simple noninteracting system and going into the many-body physics that describes the strongly correlated Mott insulator regime. Even though this thesis is a theoretical work all the chapters are linked either with experiments already done or with ongoing experimental efforts.

This thesis can be divided into four different parts. The first part comprises chapters 1 to 3. In these chapters, after a brief introduction to the field of optical lattices I review the fundamental aspects pertaining to the physics of systems in periodic potentials.

The second part deals with the superfluid weakly interacting regime where standard mean field techniques can be applied. This is covered in chapters 4 and 5. Specifically, chapter 4 introduces the discrete nonlinear Schrödinger equation (DNLSE) and uses it to model some experiments. In chapter 5 I go one step further and include the small quantum fluctuations neglected in the DNLSE by studying quadratic approximations of the Bose-Hubbard Hamiltonian.

Chapters 6 to 8 can be grouped as the third part of the thesis. In them I adopt an effective action formalism, the so called two particle irreducible effective action (2PI) together with the closed time path (CTP) formalism to study far-from-equilibrium dynamics. The many-body techniques discussed in these chapters systematically include higher order quantum corrections, not included in the quadratic approximations of the Hamiltonian, which we show are crucial for a

correct description of the quantum dynamics outside the very weakly interacting regime.

Finally, chapter 9 to 11 are devoted to study the Mott insulator phase. In these chapters using perturbation theory I study the Mott insulator ground state and its excitation spectrum, the response of the system to Bragg spectroscopy, and propose a mechanism to correct for the residual quantum coherences inherent to the Mott insulator ground state. Even though small these are not ideal for the use of neutral atoms in optical lattice as a tool for quantum computation.

Acknowledgements

I want to use this lines to thank and acknowledge all the people that made this thesis possible.

First and foremost I would like to thank Charles Clark for giving me the invaluable opportunity to join the NIST group. Through his intelligent ideas, love for physics and dedication he gave me not only very good advice and guidance but also all the encouragement I needed to feel the work I was doing was worthwhile and important. It has been a pleasure to work with and learn from such an extraordinary person.

I also want to thank Prof. Ted Kirkpatrick for serving as my University of Maryland supervisor. He has always made himself available for help and advice. His ideas and suggestions were really valuable for the development of this thesis.

I am also grateful to Prof. Bei Lok Hu. He was an invaluable source of knowledge and assistance, especially with regard to the 2PI-CTP formalism discussed in chapters 6 to 8. There has never been an occasion when I've knocked on his door and he hasn't given me time. I cannot leave out Esteban Calzetta and Albert Roura. Discussions with Bei Lok, Esteban and Albert regarding the application of the 2PI-CTP formalism to the patterned loaded system made possible the publication of the paper.

I would also like to acknowledge help and support from Carl Williams. He was my other advisor at NIST, willing to help me all the time and providing me with very useful ideas.

I also owe special gratitude to everybody in the Physics Laboratory at NIST and colleagues in the Radiation Physics Building, in particular Blair Blakie, Zach Dutton, Nicolai Nygaard, Marianna Safranova, Jamie Williams and Mark Edwards. Besides colleagues they have been wonderful friends and helped me any time I needed help or advice. Especially I am greatly indebted with Blair who was not only my office mate when he was at NIST and helped me to sort out all the problems but also for his support and great ideas even now that he is in New Zealand. I also want to thank Nicolai not only for providing me all the LaTex style files for writing this thesis but also for all his time reviewing the manuscript. Guido Pupillo and Gavin Brennen also deserve a special mention. Because of their great ideas and critical thinking the work described in chapters 9 to 11 was possible. I can not forget to thank Prof. Keith Burnett. I worked with him during the summer of 2002 when he came to NIST. Besides an incredible person, he is also a bright physicist. He was the one who gave me the idea of using the superfluid

properties to study the approach to the Mott insulator phase.

I owe my deepest thanks to my family - my mother, my father, my sister and my brother. They have always stood by me in good and bad times. I really owe all my achievements to them.

Finally, I have no words to express the gratitude I have to my husband Juan Gabriel. He is the most important person in my life. We came together to pursue the PhD. program and without his love and support the completion of this work would not have been possible.

Table of Contents

List of Figures **xii**

1 Introduction **1**

2 Optical lattices **9**
2.1 Basic theory of optical lattices 9
2.1.1 AC Stark Shift 10
2.1.2 Dissipative interaction 11
2.1.3 Lattice geometry 12
2.2 Single particle physics 13
2.2.1 Bloch functions 13
2.2.2 Wannier orbitals 16
2.2.3 Tight-binding approximation 17
2.2.4 Semiclassical dynamics 19

3 The Bose-Hubbard Hamiltonian and the superfluid to Mott insulator transition **25**
3.1 Bose-Hubbard Hamiltonian 25
3.2 Superfluid-Mott insulator transition 27

4 Mean field theory **31**
4.1 Discrete nonlinear Schrödinger equation (DNLSE) 31
4.2 Dragging experiment 33
4.2.1 Experiment 34
4.2.2 Linear free particle model 35
4.2.3 Effect of the magnetic confinement 36
4.2.4 Interaction effects 38
4.3 Dynamics of a period-three pattern-loaded Bose-Einstein condensate in an optical lattice 40
4.3.1 Experiment 42
4.3.2 Case of no external potential 43
4.3.3 Dynamics with a constant external force 51

5 Quadratic approximations **61**
5.1 The characteristic Hamiltonian 62
5.2 Bogoliubov-de Gennes (BdG) equations 62
5.3 Higher order terms 65
5.3.1 Hartree-Fock-Bogoliubov equations 66
5.3.2 HFB-Popov approximation 67
5.4 The Bose-Hubbard model and superfluidity 67
5.5 Expectation values 70
5.6 Applications 71
5.6.1 Translationally invariant lattice 71
5.6.2 One-dimensional harmonic trap plus lattice 78
5.7 Improved HFB-Popov approximation 91
5.7.1 The two-body and many-body scattering matrices 92
5.7.2 The anomalous average and the many-body scattering matrix 93
5.7.3 Improved Popov approximation 95
5.8 Conclusions 99

6 The two particle irreducible effective action (2PI) and the closed time path (CTP) formalism **101**
6.1 2PI effective action $\Gamma(z, G)$ 102
6.2 Perturbative expansion of $\Gamma_2(z, G)$ and approximation schemes . . 107
6.2.1 The standard approaches 107
6.2.2 Higher order expansions 108
6.2.3 Zero mode fluctuactions 109
6.3 CTP formalism 110
6.4 HFB approximation 113
6.4.1 Equations of motion 113
6.4.2 Mode expansion of the HFB equations 114
6.5 Second-order expansion 116
6.5.1 Equations of motion 116
6.5.2 Conservation laws 123
6.6 Conclusions 124

7 Nonequilibrium dynamics of a patterned loaded optical lattice: Beyond the mean field approximation **127**
7.1 Mean field dynamics 127
7.1.1 Dynamical evolution 128
7.1.2 Comparisons with the exact solution 128
7.2 2PI-CTP approximations 131
7.2.1 Initial conditions and parameters 131
7.2.2 Numerical algorithm for the approximate solution 132
7.2.3 Results and discussions 133
7.3 Conclusions 136

8 From the 2PI-CTP approximations to kinetic theories and local equilibrium solutions 143
8.1 Rewriting the 2PI-CTP second-order equations 144
8.2 Boltzmann equations 147
8.3 Equilibrium properties for a homogeneous system 152
8.3.1 Quasiparticle formalism 153
8.3.2 HFB approximation 155
8.3.3 Second-order and Beliaev approximations 156
8.4 Conclusions 158

9 Characterizing the Mott Insulator Phase 159
9.1 Commensurate translationally invariant case 159
9.1.1 Perturbation theory 159
9.2 Harmonic confinement plus lattice 167
9.3 Conclusions 171

10 Bragg Spectroscopy 173
10.1 Formalism 174
10.2 Observables 176
10.3 Linear response 177
10.4 Zero-temperature regime 179
10.4.1 Bogoliubov approach 179
10.4.2 Inhomogeneous system 181
10.5 Mott insulator regime 183
10.5.1 Commensurate homogeneous system 184
10.5.2 Inhomogeneous system 186
10.6 Finite temperature 188
10.7 Conclusions 190

11 Scalable register initialization for quantum computing in an optical lattice 193
11.1 Homogeneous dynamics 194
11.2 Dynamics in presence of the external trap 197
11.3 Measurement 201
11.4 Conclusions 205

12 Conlusions 207

List of Figures

2.1 AC Stark shift induced by atom-light interaction. The laser frequency is $\omega = 2\pi\nu$ which is detuned from the atomic resonance by Λ 10

2.2 Optical lattice potential.(a)-(e) potentials for different configurations of 3 beams, (f) potential for the 4 counter-propagating laser beam configuration (The two pair of light fields are made independent by detuning the common frequency of one pair of beams from the other. E_R is the atomic recoil energy, $E_R = \hbar^2 k^2/2m$. This figure is a courtesy of P. Blair Blakie [34]) 14

2.3 Band structure of an optical lattice 16

2.4 Probability density of the Bloch wave function $\phi_{q=0}^{(n=1)}$ for different lattice depths. It can be observed the localization of the wave function increases with the lattice increases. 17

2.5 Wannier state log-density distribution corresponding to the lattice configurations shown in Fig. 2.2. Dotted white lines indicate the potential energy contours. The numbers labels the near neighbor sites: 1 the nearest neighbors, and so on. This figure is a courtesy of P. Blair Blakie [34]) 18

2.6 Ground state amplitudes $f_i^{(0)}$ as a function of the lattice site i for different values of ξ 20

2.7 Diffusion of a square wave packet in the presence of a linear potential.The parameters for the plot are $\xi = 0.1$. 21

2.8 Harmonic confinement plus lattice spectrum: The index n labels the eigenvalues in increasing energy order. 24

3.1 Zero-temperature phase diagram. The vertical lines indicate critical values for different filling factors 30

4.1 Condensate density in the x-direction at the observation time t_f. Light colors areas indicate regions of high condensate density. The dashed line indicates the final location of a co-moving point with the optical lattice. 34

4.2 Atom's average velocity in the lab frame vs. lattice velocity. Line: results from the Bloch dispersion relation, dots: tight-binding approximation results. $v_B = \hbar\pi/am$. 36

4.3 Atom's average velocity in the lab frame vs. lattice velocity in the presence of a magnetic trap. $v_B = \hbar\pi/am$. 37

4.4 Velocity of the atoms predicted by the variational model in the case when interactions are taken into account (dotted line). The single particle case is shown in red. The parameters used were $\gamma(0) = 10, \delta(0) = 0$ and $NU = 2E_R$. 39

4.5 Phase diagram UN vs v_{latt} for $V_o = 3E_r$ and $\gamma_o = 10$. 40

4.6 Localization of the wave packet in the self-focusing regime $v_{latt} = -0.7v_B$. Notice the change in the vertical scale in the last row . . 41

4.7 Evolution of the wave packet in the diffusive regime $v_{latt} = -0.15v_B$. 41

4.8 Patterned loading experiment. 42

4.9 Oscillation period (in units of $\hbar/J$) as a function of the interaction strength γ. 45

4.10 Minimum value of f^2 during an oscillation period as a function of γ. As γ increases the population imbalance between wells increases (see text). 46

4.11 Maximum contrast of the Fourier components as a function of γ. The maximum contrast is defined as $\Delta_{\max} \equiv (|c_1|^2 - |c_0|^2)_{\max}$ with the maximum value occurring when f^2 is at its minima. 48

4.12 Comparison between the population evolution of the central three wells for the inhomogeneous condensate and the homogeneous model. Inhomogeneous condensate: stars for the initially populated well and boxes for the initially empty wells. Homogeneous model: dashed line represents the initially populated wells, and the solid line represented the initially unpopulated wells. We used γ_{eff} as the local mean field energy (see text). The parameters used for the simulation were $J = 0.075E_{\text{R}}$ and $\gamma_{\text{eff}} = 2.64$. 49

4.13 Momentum distribution of the inhomogeneous condensate evaluated at various times for the same parameters as used in Fig.4.12. . . . 50

4.14 Evolution of momentum peak populations. Upper curves: population of the $q = \pm 2\pi/3$ momentum states. Lower curves: population of the $q = 0$ momentum state. Inhomogeneous condensate (dotted), homogeneous result (solid line), where the comparison is made by replacing γ by an average mean field energy $\gamma_{\text{ave}} \equiv \Lambda \sum_n |z_n|^4 = 1.85$. Parameters are the same as in Fig. 4.12. 51

4.15 Evolution of the normalized population for different values of ξ. One Bloch period is shown in the plots except $\xi = 0$ where the period is infinite. Solid line: $|\tilde{\Psi}_{3n}|^2$, dotted line: $|\tilde{\Psi}_{3n+1}|^2$, dash-dot line: $|\tilde{\Psi}_{3n+2}|^2$. The "nonclassical" motion can be seen where the $3n+1$-well populations initially increase more rapidly that the populations of the $3n+2$-wells. It can also be seen in the plots that $\xi = \xi^{\rm res}_{\rm max}/2$ and $\xi = \xi^{\rm res}_{\rm max}$ are resonant values. 55

4.16 The spectrum of values of external force, ordered in decreasing magnitude, for which a population resonance occurs i.e. the values of ξ for which $\tilde{\Psi}_0$ periodically disappears. 56

4.17 Effects of interactions on generalized Bloch oscillations for the pattern loaded system. Evolution of $|\tilde{\Psi}_n|^2$ for various interaction strengths. Upper plot: $\xi = 2\xi^{\rm res}_{\rm max}$. Lower plot: $\xi = 2\xi^{\rm res}_{\rm max}/7$. 57

4.18 Comparison between the evolution of a inhomogeneous condensate with the homogeneous result. Inhomogeneous condensate: $|\tilde{\Psi}_0|^2$ (boxes), $|\tilde{\Psi}_1|^2$ (stars), and $|\tilde{\Psi}_2|^2$ (diamonds). Homogeneous case: $|\tilde{\Psi}_{3n}|^2$ (dash-dot line), $|\tilde{\Psi}_{3n+1}|^2$ (solid line), and $|\tilde{\Psi}_{3n+2}|^2$ (dotted line), where we have taken γ as the local mean field energy. The parameters used were $J = 0.075E_{\rm R}$, $\xi = 2$ and $\gamma_{\rm eff} = 1.59$ 59

4.19 Evolution of the momentum peak populations. $q = 0$ (dashed line, squares), $q = -2\pi/3$ (dash-dot line, stars), $q = 2\pi/3$ (solid line, diamonds). Inhomogeneous condensate (dotted curves), homogeneous model (lines) using the same parameters as those in Fig. 4.18, but replacing γ by an average value $\gamma_{\rm ave} = 1.11$ for the homogeneous model. 59

5.1 Scattering processes included in the quadratic hamiltonian: a) Direct and exchange excitations, b) Pair excitations 63

5.2 Comparisons of the exact solution and BdG (and HFB-Popov) solutions as a function of $V_{eff} = U/J$, for a system with $M = 3$ and filling factors $n = 5$ and 5.33. Left: number fluctuations (Exact: solid line, BdG(and HFB-Popov): dotted line), middle: condensate fraction (Exact: solid line, BdG(and HFB-Popov): dotted line,analytic (5.79:red line), right: superfluid fraction $f_{\rm s}$ (Exact: solid line, BdG(and HFB-Popov): dotted line). The exact second order term (dashed line) of the superfluid fraction, $f_{\rm s}^{(2)}$ is also shown in these plots. The vertical line shown in the plots is an estimation of V_{eff}^{crit} when the system is commensurate 75

5.3 Comparisons of the exact solution and BdG(and HFB-Popov) solutions as a function of $V_{eff} = U/J$, for a system with $M = 3$ and filling factors $n = 50$ and 50.33. Left: number fluctuations (Exact: solid line, BdG(and HFB-Popov): dotted line), middle: condensate fraction (Exact: solid line, BdG(and HFB-Popov): dotted line, analytic Eq.(5.79): red line), right: superfluid fraction $f_{\rm s}$ (Exact: solid line, BdG(and HFB-Popov): dotted line). The exact second order term (dashed line) of the superfluid fraction, $f_{\rm s}^{(2)}$ is also shown in these plots. In this case the agreement is much better. 76

5.4 Comparisons of the condensate fraction given by the BdG solutions and the HFB equations as a function of $V_{eff} = U/J$, for a system with $M = 3$ and filling factor $n = 10$. 78

5.5 Comparisons of the condensate wave function found by numerically solving the BdG equations with the Thomas-Fermi solution. The parameters used were $U/J = 0.2$, $\Omega/J = 9.5 \times 10^{-4}$ and $N = 100$. The depletion is also shown in the plot. 82

5.6 Comparisons of the quasiparticle spectrum found by numerically solving the BdG equations(BdG) with the Thomas-Fermi solution (TF) and the noninteracting energies (Free). The parameters used were $U/J = 0.2$, $\Omega/J = 9.5 \times 10^{-4}$ and $N = 100$. 83

5.7 Low-lying quasiparticle amplitudes found by numerically solving the BdG equations. The parameters used were $U/J = 0.2$, $\Omega/J = 9.5 \times 10^{-4}$ and $N = 100$. 84

5.8 Comparisons between the product $F_n^s G_n^s$ calculated from the Thomas-Fermi approximation and the exact numerical solution of the BdG equations. The parameters used were $U/J = 0.2$, $\Omega/J = 9.5 \times 10^{-4}$ and $N = 100$. 85

5.9 Condensate density (triangles), total density (filled boxes) and local depletion (empty diamonds) as a function of the lattice site i for different values of $V_{eff.}$.The site indices i are chosen such that $i = 0$ corresponds to the center of the trap. Although these quantities are defined only at the discrete lattice sites we join them to help visualization. The empty boxes represent the exact solution for the case J=0. 86

5.10 Quasiparticle spectrum predicted by the HFB-Popov theory for different values of V_{eff}: Empty diamonds ($V_{eff} = 0.01$), stars ($V_{eff} = 0.09$), crosses ($V_{eff} = 3$), filled diamonds ($V_{eff} = 11$), empty boxes ($V_{eff} = 100$) and pentagons ($V_{eff} = 312$). The letter q labels the quasiparticle energies in increasing order. The quasiparticle energies are in recoil units. 87

5.11 Number fluctuations in the self consistent HFB-Popov approach as a function of lattice site for $V_{eff} = 0.01$ (boxes), $V_{eff} = 0.09$ (crosses), $V_{eff} = 3$ (circles),$V_{eff} = 11$ (triangles), $V_{eff} = 100$ (stars) and $V_{eff} = 312$ (diamonds). The maximum value reached by the profile decreases as V_{eff} is increased. The empty boxes shown for each of the curves correspond to the number fluctuations predicted by the homogeneous HFB-Popov model using a local density approximation. 88

5.12 Quasimomentum distribution as a function of qa, a the lattice spacing, q the quasimomentum, for different values of V_{eff}. 89

5.13 First order on-site superfluid fraction as a function of the lattice site i for different values of $V_{eff.}$.The site indices i are chosen such that $i = 0$ corresponds to the center of the trap. Filled boxes: $V_{eff.}$ =0.01, empty boxes: $V_{eff.} = 0.09$, empty diamonds: $V_{eff.} = 3$, stars: $V_{eff.} = 11$, crosses: $V_{eff.} = 100$ and triangles: $V_{eff.} = 312$. . 90

5.14 Diagrammatic representation of the two-body T_{2b} scattering matrix. In this figure $|\mathbf{kl}\rangle$ designates the initial states, $|\mathbf{ij}\rangle$ the final states and $|\mathbf{np}\rangle$ a set of intermediate states 92

5.15 Comparisons of the condensate fraction predicted from the exact diagonalization of the BHH (red), the improved Popov approximation (yellow), the BdG (and HFB-Popov) equations (blue) and the test field approximation (green) as a function of $V_{eff} = U/J$, for a system with $M = 3$ and filling factors $n = 5$ and 5.33. 97

5.16 Comparisons of the condensate fraction predicted from the exact diagonalization of the BHH (red), the improved Popov approximation (yellow), the BdG (and HFB-Popov) equations (blue) and the test field approximation (green) as a function of $V_{eff} = U/J$, for a system with $M = 3$ and filling factors $n = 50$ and 50.33. 98

5.17 Comparisons between $n_o/n\mathcal{T}_{mb} = f_c\mathcal{T}_{mb}$ and U as a function of U for a system with $M = 3$ and filling factors $n = 5$ and 50. 98

6.1 Two-loop (upper row) and three-loop diagrams (lower row) contributing to the effective action. Explicitly, the diagram a) is what we call the *double-bubble* , b) the *setting-sun* and c) the *basketball*. 102

7.1 Comparisons between the exact and the DNLSE solutions for six atoms and three wells. The time is given in units of $\hbar/J$. Top panel, strongly correlated regime ($\gamma = 12$); middle panel, intermediate regime ($\gamma = 2$); bottom panel, weakly interacting regime ($\gamma = 0.2$). The solid line is the DNLSE prediction for the population per well: $|z_0(t)|^2$ and $|z_{1,2}(t)|^2$, the triangles are used to represent the exact solution for the population per well calculated using the Bose Hubbard Hamiltonian: $\langle \hat{a}_0^\dagger \hat{a}_0 \rangle$, $\langle \hat{a}_{1,2}^\dagger \hat{a}_{1,2} \rangle$. The pentagons show the condensate population per well calculated from the exact solution: $|\langle \hat{a}_0 \rangle|^2$ and $|\langle \hat{a}_{1,2} \rangle|^2$. Due to the symmetry of the initial periodic conditions the curves for the $i = 1$ and 2 wells are the same in all depicted curves 137

7.2 Comparisons between the exact solution(solid line), the HFB approximation (boxes), the second-order large $\mathcal{N}$ approximation (pentagons) and the full 2PI second-order approximation(crosses) for the very weak interacting regime. The parameters used were $M = 3, N = 6, J = 1$ and $U/J = 1/30$. The time is given in units of $\hbar/J$. In the plots where the population, condensate and depletion per well are depicted the top curves correspond to the initially populated well solutions and the lower to the initially empty wells. Notice the different scale used in the depletion plot. In the momentum distribution plot the upper curve corresponds to the $k = \pm 2\pi/3$ intensities and the lower one to the $k = 0$ quasi-momentum intensity. 138

7.3 Comparisons for the case $M = 3, N = 8, J = 1$ and $U/J = 1/3$. The time is given in units of $\hbar/J$. In the plots the abbreviation 1st is used for the initially occupied well and 2nd for the initially empty wells. In the quasimomentum plots $k = 2\pi/a$ is the reciprocal lattice vector with a the lattice spacing. 139

7.4 Comparison between the evolution of the atomic population per well for $M = 2, J = 1/2$, $NU/J = 4$ and $N = 20, 40$ and 80. Time is in units of $\hbar/J$. In the plots P1 stands for the fractional atomic population in the initially populated wells and P2 for the population in the initially empty wells. The number of atoms N is explicitly shown in each panel. 140

7.5 Time evolution of the condensate population per well and the total condensate population,for the same parameters as Fig. 7.4. Time is in units of $\hbar/J$. In the plots C1 stands for the fractional condensate population in the initially populated well, C2 for the fractional condensate population in the initially empty one and CT for the total condensate fraction. 141

7.6 Dynamical evolution of the quasi-momentum intensities. The parameters used were $M = 2, J = 1/2$, $NU/J = 4$ and $N = 20, 40$ and 80. Time is in units of $\hbar/J$. In the plots ko denotes the $k = 0$ quasi-momentum component and k1 the $k = \pi/a$ one (a the lattice spacing). The plots are scaled to set the integrated quasi-momentum density to one for all N 142

9.1 Contour plot of the two dimensional band of the 1-ph excitations to fist order in perturbation theory. In the plot the brighter the color the higher the energy. The labels are $ky = 2\pi/MR$ and $kx = 2\pi/MR$. 163

9.2 Comparisons between the first order corrections to the 1-ph excitations calculated by diagonalizing the Bose-Hubbard Hamiltonian inside the 1-ph subspace and the analytic solution Eq. (9.22). The number of sites used for the plot was $M = 11$. Energies are in units of J. 164

9.3 Comparisons between the energy eigenvalues calculated by the exact diagonalization of the Hamiltonian (red dots), the diagonalization of the Hamiltonian in the restricted 1-ph subspace (green triangles) and the analytic solution (blue crosses), Eq. (9.22). The index n labels the eigenvalues in increasing order of energy. The filling factor g, the number of wells M and the ratio U/J is indicated in each plot. Energies are in units of J. 165

9.4 Quasimomentum distribution as a function of U/J for a unit filled lattice with six wells ($M = 6$). The exact solutions are displayed with solid lines and the first order perturbative results with dotted lines. Due to the lattice symmetry $n_{4\pi/3} = n_{2\pi/3}$ and $n_{5\pi/3} = n_{\pi/3}$. 166

9.5 Comparisons between the exact (red) and the perturbative (blue) spectra for a trapped system with $N = 9$, $M = 11$ and $\Omega/J = 1.875$ deep in the Mott regime. The lines indicate the energies of the states that are coupled directly to the ground state. 170

10.1 Bragg spectroscopic scheme considered in this paper. The lattice potential with atoms loaded into the ground band is perturbed by a shallow running wave perturbation (the Bragg potential). 174

10.2 Imparted energy: Comparisons between the the exact and Bogoliubov approximation for $N = M = 9$. The horizontal axis is in units of $\hbar$. For the plot we used $J\tau/\hbar = 10$. See text Eq. (10.23). 181

10.3 Comparisons of the imparted energy vs. Bragg frequency curves calculated from the exact diagonalization of the manybody Hamiltonian (red) and the from the HFB-Popov approximation(blue) for a trapped system with $N = 9$, $M = 11$ and $\Omega/J = 1.875$. The horizontal axis is in units of $\hbar$. The lines depicted in the plot are located at the different quasiparticle energies excited by the Bragg perturbation. 183

10.4 Density profile calculated from the exact diagonalization of the many-body Hamiltonian (red) and from the HFB-Popov approximation (blue) for a trapped system with $N = 9$, $M = 11$ and $\Omega/J = 1.875$. n labels the lattice site. 184

10.5 Dynamical structure factor vs. $\hbar\omega/J$ in the Thomas-Fermi (blue) and HFB-Popov (red) approximations. The horizontal axis is in units of $\hbar$. The system parameters are $U/J = 0.2$, $\Omega/J = 9.5\times10^{-4}$ and $N = 100$. 185

10.6 Eigenvalues of the quasiparticle spectrum plotted in increasing energy order. The vertical scale is in units of $\hbar$ 186

10.7 Transfer energy vs. Bragg frequency for a zero temperature homogeneous system with $M = N = 9$ and different transfer momenta q. The horizontal axis is in units of $\hbar$. The perturbation time was set to $J\tau/\hbar = 10$. Note the change of the vertical scale between the two panels. 186

10.8 Transfer energy vs. Bragg frequency for a zero temperature trapped system with parameters U/J=45, $\Omega/J = 1.857$, $M = 11$ and $N = 9$ and different transfer momenta q. The horizontal axis is in units of $\hbar$. The perturbation time was set to $J\tau/\hbar = 10$. Note the change of the vertical scale between the two panels. 187

10.9 Transfer energy as a function of the temperature for different U/J parameters. The plots are for a homogeneous system with $N = M = 9$. The horizontal axis in in units of $\hbar$. 191

10.10 Transfer energy as a function of the temperature for different U/J parameters. The plots are for an trapped system with $M = 11$, $N = 9$ and $\Omega/J = 1.875$. The horizontal axis in in units of $\hbar$. . . . 192

11.1 Comparisons between the time evolution of the percentage fidelity calculated by diagonalizing the Bose-Hubbard Hamiltonian (dots), the perturbative solution inside the one particle hole subspace (red) and the analytic solution Eq. 11.6 (blue). 196

11.2 Percentage fidelity as a function of time calculated using the perturbative solution 11.4 (red) and the analytic solution Eq. 11.6 (blue).The number of sites used for the plot is $M = 31$ 197

11.3 Schematic of an inhomogeneous lattice filled with N qubits with an onsite interaction energy U. An externally applied trapping potential of strength $V_j = \Omega j^2$, e.g. due to a magnetic field, acts to fill gaps in the central region of the trap. The center subspace $\mathcal{R}$ of the lattice defines the quantum computer register containing $K < N$ qubits. 198

11.4 Comparisons between the time evolution of the percentage fidelity $F_{com}(K = 5, t)$ calculated by evolving the initial target state using the Bose-Hubbard Hamiltonian (dots), the restricted one particle hole basis (red) and the analytic solution Eq. 11.16 (blue). In the plot we assumed a commensurate unit filled lattice with five sites and infinitely high boundaries. 200
11.5 Percentage fidelity as a function time calculated using the approximated solution 11.16 (blue) and the fidelity found numerically by restricting the dynamics to the one particle hole subspace. We assumed infinity high boundaries and $K = 31$. 201
11.6 Schematic of the relevant couplings in the problem. The unit filled state $|T\rangle$ describing a target quantum register and the states $|S_j^{\pm}\rangle$ having one doubly occupied lattice site and a neighboring hole are coupled to first order in J. A catalysis laser resonantly couples the ground states $|S_j^{\pm}\rangle$ to the excited states $|M_j^{\pm}\rangle$ describing a bound molecule at the doubly occupied site. The bound states quickly decay and give the possibility of monitoring population in the "faulty" register states $|S_j^{\pm}\rangle$. 202
11.7 Population in the unit filled register state $|T\rangle_{\mathcal{R}}$ during continuous measurement of the register beginning in the Bose-Hubbard ground state $|\Psi_g\rangle$. The plots show dynamics appropriate to tunneling in one dimension with $U/J = 500$. (a) Quantum trajectories corresponding to a null measurement result for three different register sizes K. The time scale to saturate the target state is independent of the number of qubits: $t_{sat} \approx \kappa^{-1}$. (b) Long time dynamics for $K = 501$, $N = 551$ and finite detector efficiencies η. The population in $|T\rangle_{\mathcal{R}}$ for $\eta = 1$ is indistinguishable from one. Also shown is the oscillatory dynamics at fundamental frequency U described by Eq. (11.16) if the measurement is turned off after the target state is reached. The arrow indicates $\rho_{T,T}(0)$. 203

Chapter 1

Introduction

Bose Einstein condensation (BEC) in bosonic gases was predicted by Einstein in 1925 [1] based on the quantum statistics ideas developed by Bose for photons [2]. The basic idea of BEC is that below a critical temperature a macroscopic number of particles occupy the lowest energy state: as the temperature, T, is decreased the de-Broglie wave length, which scales like $T^{-1/2}$, increases and at the critical point it becomes comparable to the inter-particle mean separation. At this point the wave functions of the particles are sufficiently smeared out so that there is always some overlap and a Bose Einstein condensate is formed. Although Einstein's prediction applied to a gas of noninteracting atoms, London suggested that, BEC could be the mechanism underlying the phenomenon of superfluidity in ^4He [3], despite the strong interactions in this system. Further evidence for this point of view came from neutron scattering experiments [4].

Experimental efforts to create a BEC in dilute gases date back to the 1980's [5]. The first experiments concentrated on using atomic Hydrogen but mainly the large rates of inelastic collision prevented these experiments from succeeding. It was not until 1995, using the advances made in laser cooling techniques[9], that BEC in dilute alkali atomic gases was achieved. The first series of experiments were done with Rubidium [6], sodium [7] and lithium [8] vapors. In these experiments atoms are typically collected in a magneto-optical trap (MOT) and compressed and cooled to micro-Kelvin temperatures using laser cooling techniques. They are then transferred to a magnetic trap where evaporative cooling allows the system to be cooled to nano-Kelvin temperatures. At a critical phase space density BEC takes place. In such a condensate a macroscopic number of atoms, generally up to 10^6, collectively occupy the lowest energy state.

The experimental realization of BEC in alkali gases opened unique opportunities for exploring quantum phenomena on a macroscopic scale. In contrast to experiments with liquid helium, where the strong interactions between particles wash out the effects due to the BEC, the relatively weak two-particle interaction in dilute alkali atoms allows these systems to be used as a theoretical and experimental arena to study coherent matter wave properties. Theoretically, the weakly interacting regime has the advantage that all the atoms can be described by a

single macroscopic wave function. This allows a very intuitive understanding of the system based on the so called Gross-Pitaevskii equation (GPE) [10]. Experimentally, the macroscopic wave packet can be probed by interference experiments, where by turning off the trapping fields the atoms are allowed to expand and the wave packets to interfere with each other.

The GPE assumes that all the atoms are in the condensate and neglects completely quantum correlations. In the weakly interacting regime, a description beyond the simplest mean field theory can be made by treating the small quantum fluctuations as perturbations. This treatment was proposed by Bogoliubov in 1947 [11]. The fluctuations lead to a small depletion of the condensate mode since other excited states different from the condensate get populated. Since in most of the experiments with dilute gases the condensate depletion is at most 3%, the GPE together with Bogoliubov analysis have been in general very successful describing these experiments. Much theoretical and experiment work has been done studying condensate properties such as condensate collective excitations, phonon modes, sound velocity and superfluid flow phenomena [12]-[19].

However, weakly interacting dilute gases described by a mean field picture are the simplest many body systems one can possible found. In order to be in the weakly interacting regime, the ratio between the interaction energy of uncorrelated atoms at a given density, E_{int}, and the quantum kinetic energy needed to correlate particles by localizing them within a distance of order of the mean inter-particle distance, E_{kin}, must be small. For three dimensional systems $E_{int} \sim n\frac{4\pi\hbar^2 a_s}{m}$ (a_s is the scattering length, which fully characterizes the low energy scattering processes, n is the mean particle density and m is the atomic mass) and $E_{kin} \sim \frac{\hbar^2}{2m}n^{2/3}$. Thus, the ratio between these two energies is proportional to $n^{1/3}a_s$. In dilute alkali vapors this ratio is generally of order 0.02. To enter the strongly correlated regime, an obvious way to proceed is either to raise the density or to raise the scattering length. It is indeed possible to tune the scattering length to large values by using a Feshbach resonance. This has recently been realized for example in ^{85} Rb where the scattering length was tuned over several orders of magnitude [20, 21]. The problem of this approach is, however, that the lifetime of the condensate strongly decreases due to three-body losses [22]. An entirely different way to reach the strongly correlated regime is by using optical lattices. By increasing the depth of the optical lattice the ratio between kinetic energy and potential energy can be changed without affecting the density or the scattering length. The beauty of this approach is that the lattice depth can be used as an experimental knob to change the kinetic to interaction energy ratio allowing us to reach different many-body regimes.

- Optical lattices

Optical lattices are periodic Stark shift potentials created by the interference of two or more laser beams. They have been widely used in atomic physics in the context of atom diffraction [23, 24] with applications to atom optics and atom interferometry [25]. They have also been used as a way to trap and cool atoms. The

first experiment where atoms were cooled to the micro-kelvin regime in a multi-dimensional optical lattice was carried out by Hemmerich *et al.* [26]-[28] followed by Grynberg *et al.* [29]. There have been various attempts to cool atoms directly in an optical lattice. Among them we can mention Raman cooling techniques, by which atoms have recently been partially cooled to the ground sate with filling factors of order one [30, 31, 32]. However, one of the most successful techniques to load ultracold atoms in the ground state, with almost no discernible thermal component, is by first forming a Bose Einsten condensate in a weak magnetic trap and then adiabatically turning on the lattice by slowly ramping up the intensity of the laser beams.

Atom dynamics in optical lattices is closely related to electron dynamics in solid state crystals, but optical lattice have favorable attributes such as the absence of defects and the high degree of experimental control [33, 34]. When ultracold bosonic atoms are loaded in shallow lattices, the system is in the weakly interacting regime and most of the atoms are Bose condensed. Combined with BEC, the ultimate source of coherent atom , optical lattices provide a way of exploring a quantum system analogous to electrons in crystals but with complete control over the lattice and the atoms. Beautiful experiments have been done in this regime and have provided an elegant demonstration of band structure [35, 36, 37], Bragg scattering and Bloch oscillations [38], as well as coherent matter wave interferometry [39, 40], superfluidity [41] and quantum chaos [42].

There has also been spectacular recent experimental progress in the strongly correlated regime. It was first realized by Jaksch *et al.* [43], that a BEC loaded in a lattice potential is a nearly perfect experimental realization of the Bose-Hubbard Hamiltonian, which describes bosons with local repulsive interactions in a periodic potential. M.P.A. Fisher *et al.* [44] predicted that a system modeled by the Bose-Hubbard Hamiltonian exhibits a quantum phase transition from a superfluid to an insulator state (superfluid-Mott insulator transition) as the interactions are increased. In fact, the Mott insulator transition in a 3D lattice starting from a BEC has experimentally observed by M. Greiner and coworkers [46]. Moreover, in recent years there have been many impressive experiments which have demonstrated the loss of quantum coherence as the system approaches the strongly correlated regime, for example by measuring number squeezing [45] or by studying the collapse and revival of coherence in a matter wave field [47].

One of the most important potential applications of the Mott insulator transition is to use it as a mean to initialize a quantum computer register. Deep in the Mott insulator regime the kinetic energy is very small with respect to the interaction energy and it is energetically favorable for the atoms to remain localized without tunneling. The negligible number fluctuations makes it possible to prepare the fiducial state with exactly one atom per site needed to initialize a quantum computer register [43, 48, 50]. Besides the possibility of high fidelity initialization, the easy scalability, low noise and high experimental control make ultracold neutral atoms loaded in an optical lattice one of the most attractive candidates for implementations of quantum computation.

The overall goal of this thesis is to study equilibrium and non equilibrium properties of cold bosons loaded in optical lattices starting from the superfluid regime, where mean field techniques can be applied, and going into the rich and complex strongly correlated regime where the standard GPE and Bogoliubov treatments fail to describe the system and a more general framework is required. Most of the work is done in the context of ongoing experimental efforts, especially the ones trying to achieve lattice based quantum information processing.

- Overview

In chapter 2, I start by reviewing the theory of optical potentials, the single particle band structure and the tight binding approximation. In chapter 3, I go one step further and consider the many-body properties of the system by introducing the Bose-Hubbard Hamiltonian. I give a review of the generic issues that characterize the superfluid to Mott insulator transition.

In chapter 4, I describe the equilibrium properties of lattice systems in the superfluid regime, where a mean field treatment is valid. I study the mean field Discrete Nonlinear Schrödinger equation (DNLSE), and use it to model two experiments done by the laser-cooling and trapping group at NIST. In the first one, an optical lattice was moved and the average displacement of the atoms was used as a means to probe the band structure of the system. In the second experiment,to which I refer as the patterned loading experiment [33],the atoms were loaded into every third site of an optical lattice, with the aim of having large enough spatial separation to address individual atoms. This patterned loading method may be a useful technique for the implementation of lattice based quantum computing proposals.

The DNLSE completely neglects quantum fluctuations. However, if the system is weakly interacting, the small quantum corrections can be included by using the Bogoliubov approximation. In the Bogoliubov approximation the complicated many-body quartic Hamiltonian is reduced to a quadratic one, which can be diagonalized exactly. Using the Bogoliubov approximation, in chapter 5 I study different standard quadratic approximations in two different lattice systems, a translationally invariant one with periodic boundary conditions which in general allows analytic solutions, and a system closer to real experimental situations where, besides the lattice potential, there is a superimposed harmonic confinement potential. I discuss the Bogoliubov de Genes equations (BdG), the Hartree-Fock-Bogoliubov (HFB) approximation and the HFB-Popov approximation. To test the validity of the different approximations and their departure from the exact solution as the interactions are increased I compare them with the exact numerical diagonalization of the Bose-Hubbard Hamiltonian. Because of the exponential scaling of the dimensionality of the Hilbert space with respect to system size, the exact solution (for a system with N atoms and M wells the number of states scales like $(N+M-1!)/(N!M!)$), the numerical comparisons are restricted to systems with a moderate number of atoms and wells.

In chapter 5, I also report on our idea of using the superfluid fraction to study

the approach to the Mott insulator transition. By deriving an expression for the superfluid density based on the rigidity of the system under phase variations we were able to explore the connection between the quantum depletion of the condensate and the quasi-momentum distribution on one hand and the superfluid fraction on the other.

At the end of the chapter, I present my attempt to approach the strongly correlated regime by using the improved Popov approximation [52, 53, 55]. The idea presented here is to upgrade the bare potential, which is the one that explicitly appears in the many-body Hamiltonian, to the many-body scattering matrix. By upgrading the bare potential, we are properly taking into account the effect of the surrounding atoms in the properties of binary collisions.

In chapter 6 and 7, motivated by the patterned loading experiment, we adopt a functional effective action approach capable of dealing with non equilibrium situations that require a treatment beyond mean field theory. Even though a description of the dynamics of the patterned loading system using the DNLSE was derived in chapter 4, it is shown by comparisons with the exact quantal solution calculated by time propagating the initial configuration with the Bose-Hubbard Hamiltonian that a mean field solution is valid only for short times and in the very weakly interacting regime. To deal with the dynamics far from equilibrium, we adopt a closed time path (CTP) [56] functional-integral formalism together with a two-particle irreducible (2PI) [57] effective action approach and derive equations of motion. We retain terms of up to second-order in the interaction strength when solving these equations. Under the 2PI-CTP scheme we consider three different approximations : a) the time dependent Hartree-Fock-Bogoliubov (HFB) approximation, b) the next-to-leading order $1/\mathcal{N}$ expansion and c) a full second-order perturbative expansion in the interaction strength. We derive mathematical expressions for the equations of motion in chapter 6 and apply them to the particular case of the patterned loaded lattice in chapter 7. We use this system to illustrate many basic issues in nonequilibrium quantum field theory, such as non-local and non-Markovian effects, pertaining to the dynamics of quantum correlation and fluctuations. We show that because the second-order 2PI approximations include multi-particle scattering in a systematic way, they are able to capture damping effects exhibited in the exact solution, which a collisionless approach fails to produce. While the second-order approximations show a clear improvement over the HFB approximation, they fail at late times, when interaction effects are significant.

The 2PI effective action formalism provides a useful framework where the mean field and the correlation functions are treated on the same self-consistent footing. However, it yields dynamical equation of motion that are non local in time and hard to estimate analytically. The idea in chapter 8 is to simplify the 2PI equations and to obtain near equilibrium solutions where, kinetic theories that describe excitations in systems close to thermal equilibrium are valid. In particular, we show in this chapter how the full second-order 2PI equations are in agreement with current kinetic theories [15],[58]-[62] and reproduce in equilibrium the higher order perturbative corrections well known in the literature since Beliaev's work [63].

In chapter 9, I jump into the Mott insulator phase and I study the physical properties of the system deep in the Mott insulator regime, which is the other regime where an analytic treatment based on perturbation theory is possible. A perturbative analysis should be applicable to study current experiments [64] that reach the strong Mott regime. I derive expressions for the excitation spectrum of the Mott state for both homogeneous and trapped systems and compare them with the solutions obtained by exact diagonalization of the Bose-Hubbard Hamiltonian. The main purpose of this chapter is to understand the many-body properties of the Mott insulator ground state and the nature of its many-body excitations which will be crucially important as more elaborate experiments with optical lattices in the strongly correlated regime are undertaken.

One key piece of evidence for the Mott insulator phase transition is the loss of global phase coherence of the matter wavefunction when the lattice depth increases beyond a critical value [46]. However, there are many possible sources of phase decoherence in these systems. It is known that substantial decoherence can be induced by quantum or thermal depletion of the condensate during the loading process, so loss of coherence is not a proof that the system resides in the Mott insulator ground state. Indeed, for this reason, in the experiments by Greiner et al. [46] a potential gradient was applied to the lattice to show the presence of a gap in the excitation spectrum. In chapter 10, we show that another common experimental technique, Bragg spectroscopy [65, 66], not only can identify the excitation gap that opens up in the Mott regime, but also can be used to map out the excitation spectrum and to determine the temperature of the system when it is deep in the Mott regime. Specifically, we study the total momentum and total energy deposited in the system by the Bragg perturbation calculated under a linear response analysis and obtain analytical solutions in the superfluid and deep Mott insulator regimes. We test the accuracy of the approximations and their deviation from the full quantal behavior as usual by comparing them with numerical solutions obtained by diagonalizing the Bose-Hubbard Hamiltonian for a moderate number of atoms and wells.

All of the proposals for quantum computation which utilize a lattice-type architecture have the Mott insulator transition as the initialization scheme to load exactly one atom per lattice site. Such architecture requires a lattice commensurately filled with atoms, which does not correspond exactly to the ground Mott insulator state. The ground state has a remaining coherence proportional to the tunneling matrix element. This degrades the initialization of the quantum computer register and can introduce errors during error correction. I finish this thesis with chapter 11, where I report on our proposal to solve this problem by using the spatial inhomogeneity created by a quadratic magnetic trapping potential together with a continuous measurement procedure which projects out the components of the wave function with more than one atom in any well.

Publications in the PhD work:

- Chapter 4

  Dynamics of a period-three pattern loaded Bose-Einstein condensate in an optical lattice, A. M. Rey, P. B. Blakie, Charles W. Clark, Phys. Rev. A **67**, 053610 (2003).

- Chapter 5

  Bogoliubov approach to superfluidity of atoms in an optical lattice, Rey AM, Burnett K, Roth R, Edwards M, Williams CJ, Clark CW, J. Phys. B: At. Mol. Opt. Phys, **36** , 825 (2003).

- Chapter 6 and 7

  Nonequilibrium Dynamics of Optical Lattice - Loaded BEC Atoms: Beyond HFB Approximation, A. M. Rey, B. L. Hu, E. Calzetta, A. Roura, Charles W. Clark, Phys. Rev A. **69**, 033610 (2004).

  BEC with fluctuations: beyond the HFB approximation, A. M. Rey, B. L. Hu, E. Calzetta, A. Roura, Charles W. Clark (Proceedings of the Laser Physics Workshop 2003), Las. Phys., **14**, 1, (2004).

- Chapter 10

  Bragg spectroscopy of ultracold atoms loaded in an optical lattice, Ana Maria Rey, P. Blair Blakie, Guido Pupillo, Carl J. Williams, Charles W. Clark, submitted to Phys. Rev. Lett. cond-mat/0406552.

- Chapter 11

  Scalable register initialization for quantum computing in an optical lattice, G. K. Brennen, G. Pupillo, A. M. Rey, C. W. Clark, C. J. Williams, submitted to Phys. Rev. Lett., cond-mat/0312069.

  Scalable quantum computation in systems with Bose-Hubbard dynamics, Guido Pupillo, Ana M. Rey, Gavin Brennen, Carl J. Williams, Charles W. Clark, to appear in J. Mod. Opt, quant-ph/0403052.

Chapter 2

Optical lattices

Optical lattices are periodic potentials created by light-matter interactions. When an atom interacts with an electromagnetic field, the energy of its internal states depends on the light intensity. Therefore, a spatially dependent intensity induces a spatially dependent potential energy. If such a modulation is obtained by the interference of several laser beams, the resultant optical potential felt by the atoms will have different potential wells separated by a distance of the order of the laser wavelength. The depths of the optical potential wells that can be obtained in an experiment are in the microKelvin range. Nevertheless, atoms can be trapped in this potentials when cooled at low temperatures, by laser and evaporative cooling techniques.

Cold atoms interacting with a spatially modulated optical potential resemble in many respects electrons in ion-lattice potential of a solid crystals . However, optical lattices have several advantages with respect to solid state systems. They can be made to be largely free from defects, such defects for example prevented the observation of Bloch oscillations in crystalline solids. Optical lattices also can be controlled very easily by changing the laser field properties. For example the lattice depth can be changed by modifying the laser intensity, the lattice can be moved by changing the polarization of the light or chirping the laser frequency and the lattice geometry can be modified by changing the laser configuration. Moreover, in contrast to solids, where the lattice spacings are generally of order of Angstrom units, the lattice constants in optical lattices are typically three order of magnitude larger.

The idea of this chapter is to introduce the basic theory of optical lattices and to review the single particle properties of atoms loaded in such periodic potentials.

2.1 Basic theory of optical lattices

Neutral atoms interact with light in both dissipative and conservative ways. The conservative interaction comes from the interaction of the light field with the induced dipole moment of the atom which causes a shift in the potential

energy called ac-Stark shift. On the other hand, the dissipation comes due to the absorption of photons followed by spontaneous emission. Because of conservation of momentum, the net effect is a dissipative force on the atoms caused by the momentum transfer to the atom by the absorbed and spontaneously emitted photons. Laser cooling techniques make use of this light forces.

For large detunings spontaneous emission processes can be neglected and the energy shift can be used to create a conservative trapping potential. This is the physics that describes optical lattices.

2.1.1 AC Stark Shift

Consider a two level atom, with internal ground state $|g\rangle$ and excited state $|e\rangle$ and energy difference $\hbar\omega_o$ in a lossless cavity of volume V, interacting with a monochromatic electromagnetic field with frequency $\omega = 2\pi\nu$ as schematically shown in Fig.2.1. Assume also that the experiment is performed within a time smaller than the spontaneous emission rate so that spontaneous emission can be neglected.

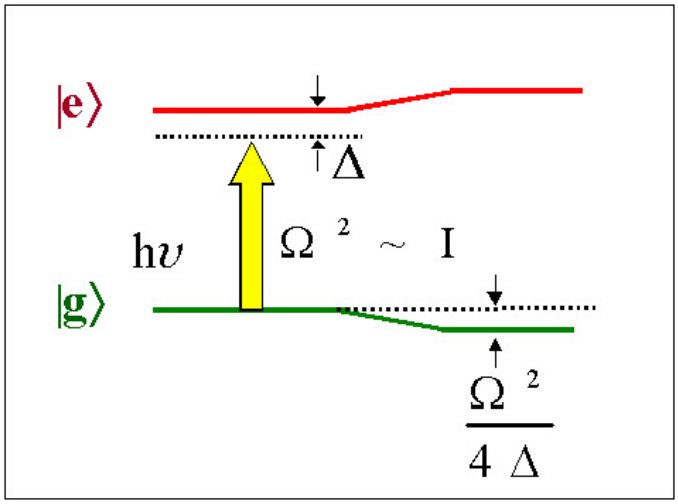

Figure 2.1: AC Stark shift induced by atom-light interaction. The laser frequency is $\omega = 2\pi\nu$ which is detuned from the atomic resonance by Λ

The uncoupled Hamiltonian describing the atoms and the electromagnetic field is given by

$$\hat{H}_o = \hbar\omega_o |e\rangle \langle e| + \hbar\omega(\hat{a}^\dagger\hat{a} + 1/2), \tag{2.1}$$

where $\hat{a}$ is the photon annihilation operator. If the detuning of the laser from the atomic transition, $\Delta = \omega - \omega_o$, is small $|\Delta| \ll \omega_o$, then the state with the atom in the ground state and N photons in the field, $|0\rangle \equiv |g, N\rangle$ has similar energy to the state with the atom in an excited state and $N-1$ photons $|1\rangle \equiv$

$|e, N-1\rangle, E_1 - E_0 = -\hbar\Delta$. The effect of the interactions is to couple these states. Under the dipole approximation which assumes that the spatial variation of the electromagnetic field is small compared with the atomic wave function, the coupling Hamiltonian denoted as $\hat{H}_I$ in the interaction picture is given by:

$$\begin{aligned} \hat{H}_I &= -\vec{d}\cdot\vec{E} \\ &= \left(|e\rangle\langle g| e^{i\omega_o t} + |g\rangle\langle e| e^{-i\omega_o t}\right)\left(\frac{\hbar\Omega^*(\vec{x})}{2}\hat{a}^\dagger e^{i\omega t} + \frac{\hbar\Omega(\vec{x})}{2}\hat{a}e^{-i\omega t}\right). \end{aligned} \tag{2.2}$$

Here $\Omega(x)$ is the Rabi frequency given by $\hbar\Omega(\vec{x}) = -2\sqrt{\frac{\hbar\omega\langle N\rangle}{2\in V}}u(\vec{x})\vec{\varepsilon}\cdot\vec{d}$, with $\vec{\varepsilon}$ the unit polarization vector of the field, $\vec{d}$ the dipole moment of the atom and $u(\vec{x})$ the field mode evaluated at the atomic position x,(for plane waves, for example $u(\vec{x}) = e^{-i\vec{k}\cdot\vec{x}}$). In the rotating wave approximation, valid in the limit $|\Delta| \ll \omega_o$, the type of processes with a rapidly oscillating phase, $\exp(\pm i(\omega_o + \omega)t)$, are neglected and only the near resonant frequency processes are considered. The interaction Hamiltonian is then reduced to

$$\hat{H}_I \approx \left(\frac{\hbar\Omega(\vec{x})}{2}|e\rangle\langle g|\hat{a}e^{i\Delta t} + \frac{\hbar\Omega^*(\vec{x})}{2}|e\rangle\langle g|\hat{a}^\dagger e^{-i\Delta t}\right). \tag{2.3}$$

Physically, the resonant process correspond to either the excitation of the atom along with the emission of a photon or the relaxation of the atom with the absorbtion of a photon. In the previous line we also assume a large number of photons and neglect the variation in the coupling constant due to ΔN, i.e $N \simeq N-1$.

If the detuning is large compared to the Rabi frequency, $|\Delta| \gg \Omega$, the effect of the interactions on the states, $|0\rangle$ and $|1\rangle$, can be determined with second order perturbation theory. In this case, the energy shift $E^{(2)}_{0,1}$ is given by

$$E^{(2)}_{0,1} = \pm\frac{|\langle 1|\hat{H}_{int}|0\rangle|^2}{\hbar\Delta} = \pm\hbar\frac{|\Omega(\vec{x})|^2}{4\Delta}, \tag{2.4}$$

with the plus and minus sign for the $|0\rangle$ and $|1\rangle$ states respectively. This energy shift is the so called ac-Stark shift. Since the atoms are practically always in the ground state, the energy of the atoms is changed according to the stark shift $\hbar\frac{|\Omega(\vec{x})|^2}{4\Delta}$, which defines the optical potential.

Furthermore, if instead of interacting with a monochromatic electromagnetic field, the atoms are illuminated with superimposed counter-propagating laser beams, the beams interfere and the interference pattern results in a periodic landscape potential or optical lattice.

2.1.2 Dissipative interaction

In the above discussion we implicitly assumed that the excited state has an infinite lifetime. However, in reality it will decay by spontaneous emission of photons. This

effect can be taken into account phenomenologically by attributing to the excited state an energy with both real an imaginary parts. If the excited state has a life time $1/\Gamma_e$ corresponding to a e-folding time for the occupation probability of the state, the corresponding life time for the amplitude will be twice this time. The energy of the perturbed ground state becomes a complex quantity which we can write as

$$E_0^{(2)} = \frac{\hbar}{4}\frac{|\Omega(\vec{x})|^2}{\Delta - i\Gamma_e/2} = V(\vec{x}) + i\gamma_{sc}(\vec{x}), \tag{2.5}$$

$$V(\vec{x}) = \hbar\frac{|\Omega(\vec{x})|^2\Delta}{4\Delta^2 - \Gamma_e^2} \approx \hbar\frac{|\Omega(\vec{x})|^2}{4\Delta}, \tag{2.6}$$

$$\gamma_{sc}(\vec{x}) = \frac{\hbar}{2}\frac{|\Omega(\vec{x})|^2\Gamma_e}{4\Delta^2 - \Gamma_e^2} \approx \hbar\frac{|\Omega(\vec{x})|^2\Gamma_e}{8\Delta^2}. \tag{2.7}$$

The real part of the energy corresponds to the optical potential whereas the imaginary part represents the the rate of loss of atoms from the ground state. The sign of the optical potential seen by the atoms depends on the sign of the detuning. For blue detuning , $\Delta > 0$, the sign is positive resulting in a repulsive potential, and the potential minima correspond to the points with zero light intensity. On the other hand, in a red detuned light field, $\Delta < 0$, the potential is attractive and the minima correspond to the places with maximum light intensity. Because the effective spontaneous emission rate of the atoms increases with the light intensity, the spontaneous emission in a red detuned optical lattice will always be more significant than in a blue detuned one.

The proper detuning for an optical lattice depends on the available laser power I ($|\Omega|^2 \propto I$) and the maximum dissipative scattering rate that can be tolerated. On one hand, with small detuning it is possible to create larger trap depths for a given laser intensity since the optical potential scales as $V \sim I/\Delta$. On the other, the inelastic scattering rate is inversely proportional to the detuning squared and scales like $\Gamma_e/\Delta\ V$. Therefore, the laser detuning should be chosen as large as possible within the available laser power in order to minimize inelastic scattering processes and create a conservative potential.

2.1.3 Lattice geometry

The simplest possible lattice is a one dimensional(1D) lattice lattice. It can be created by retroreflecting a laser beam, such that a standing wave interference pattern is created. This results in a Rabi frequency $\Omega(x) = 2\Omega_o \sin(kx)$ which yields a periodic trapping potential given by

$$V_{lat}(x) = V_o \sin^2(kx) = \frac{\hbar\Omega_o^2}{\Delta}\sin^2(kx), \tag{2.8}$$

where $k = 2\pi/\lambda$ is the absolute value of the wave vector of the laser light and V_o is four times times the depth of a single laser beam without retro-reflection, due to the constructive interference of the lasers.

Periodic potentials in higher dimensions can be created by superimposing more laser beams. To create a two dimensional lattice potential for example, two orthogonal sets of counter propagating laser beams can be used. In this case the lattice potential has the form

$$V_{lat}(x,y) = V_o\left(\cos^2(ky) + \cos^2(kx) + 2\varepsilon_1 \cdot \varepsilon_2 \cos\phi \cos(ky)\cos(kx)\right). \qquad (2.9)$$

Here k is the magnitude of the wave vector of the lattice light, ε_1 and ε_2 are polarization vectors of the counter propagating set and ϕ is relative phase between them. If the polarization vectors are not orthogonal and the laser frequencies are the same, they interfere and the potential is changed depending on the relative phase of the two beams. This leads to a variation of the geometry of the lattice in a chequerboard like pattern. A simple square lattice with one atomic basis can be created by choosing orthogonal polarizations between the standing waves. In this case the interference term vanishes and the resulting potential is just the sum of two superimposed 1D lattice potentials. Even if the polarization of the two pair of beams is the same, they can be made independent by detuning the common frequency of one pair of beams from that the other. Typically a negligible frequency difference compared with the optical frequency is required to achieve independence, thus even in this case to a good approximation the wave vectors can be considered equal.

A more general class of two 2D lattices can be created from the interference of three laser beams [34, 33] which in general yields non separable lattices. Such lattices can provide tighter on-site confinement, better control over the number of nearest neighbors and significantly reduced tunneling between sites compared with the counter propagating four beam square lattice. In Fig. 3 we show a variety of possible 2D optical lattice geometries that can be made by three and four interfering laser beams. Similarly a 3D lattice can be created by the interference of at least 6 orthogonal sets of counter propagating laser beams.

2.2 Single particle physics

In this section for simplicity we are going to restrict the analysis to a one dimensional lattice. Generalization to higher dimensions can be done straightforwardly, especially if the lattice geometry is separable. The main purpose of this section is to review the basic aspects that describe the behavior of noninteracting particle subject to a periodic potential.

2.2.1 Bloch functions

One of the most important characteristics of a periodic potential is the emergence of a band structure. Consider a one dimensional particle described by the Hamiltonian $H = \frac{\hat{p}^2}{2m} + V_{lat}(x)$, where $V_{lat}x) = V_{lat}(x+a)$. Bloch's theorem [67, 68]

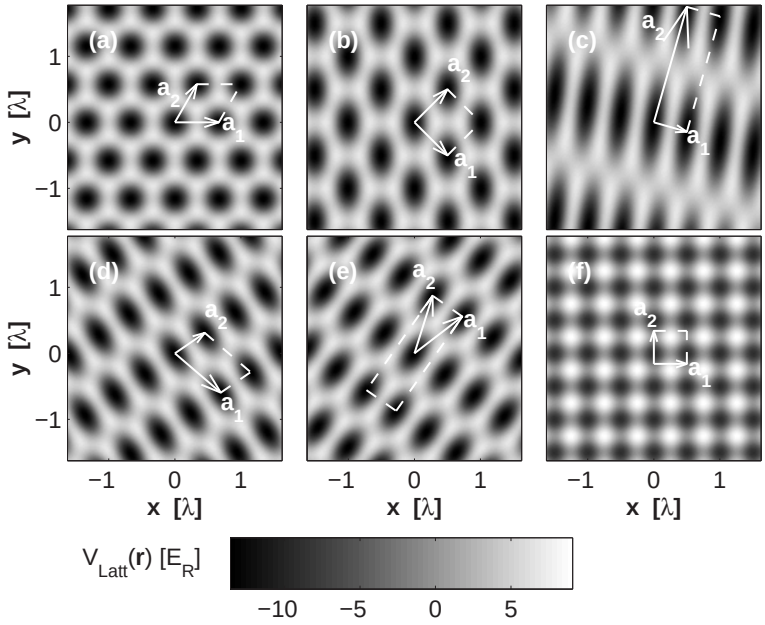

Figure 2.2: Optical lattice potential.(a)-(e) potentials for different configurations of 3 beams, (f) potential for the 4 counter-propagating laser beam configuration (The two pair of light fields are made independent by detuning the common frequency of one pair of beams from the other. E_R is the atomic recoil energy, $E_R = \hbar^2 k^2/2m$. This figure is a courtesy of P. Blair Blakie [34])

states that the eigenstates $\phi_q^{(n)}(x)$ can be chosen to have the form of a plane wave times a function with the periodicity of the potential:

$$\phi_q^{(n)}(x) = e^{iqx} u_q^{(n)}(x), \tag{2.10}$$

$$u_q^{(n)}(x+a) = u_q^{(n)}(x). \tag{2.11}$$

Using this ansatz into the Schrödinger equation, $H\phi_q^{(n)}(x) = E_q^{(n)}\phi_q^{(n)}(x)$, yields an equation for $u_q^{(n)}(x)$ given by:

$$\left[\frac{(\hat{p}+\hbar q)^2}{2m} + V_{lat}(x)\right] u_q^{(n)}(x) = E_q^{(n)} u_q^{(n)}(x) \tag{2.12}$$

Bloch's theorem introduces a wave vector q. The quantity q should be viewed as a quantum number characteristic of the translational symmetry of the periodic potential, just as the momentum is a quantum number characteristic of the full translational symmetry of the free space. Even though it is not the same, it turns out that $\hbar q$ plays the same fundamental role in the dynamics in a periodic potential as the momentum does in the absence of the lattice. To emphasize this similarity

$\hbar q$ is called the *quasimomentum* or *crystal momentum* . In general the wave vector q is confined to the first Brilloiun zone, i.e. $-\pi/a < q \leq \pi/a$.

The index n appears in Bloch's theorem because for a given q there are many solutions to the Schrödinger equation. Eq. (2.12) can be seen as a set of eigenvalue problems in a fixed interval, $0 < x < a$, one eigenvalue problem for each q. Therefore, each of them, on general grounds has an infinite family of solutions with a discretely spaced spectrum of modes labelled by the band index n. On the other hand, because the wave vector q appears only as a parameter in Eq. (2.12), for an infinite lattice, the energy levels for a fixed n has to vary continuously as q varies. The description of energy levels in a periodic potentials in terms of a family of continuous functions $E_q^{(n)}$ each with the periodicity of a reciprocal lattice vector, $2\pi/a$, is referred to as the band structure.

In the simple case of a sinusoidal potential, which is the one used in experiments, $V_{lat}(x) = V_0 \sin^2(kx)$, the band structure can be solved analytically. In this case the Schrödinger Equation is given by

$$-\frac{d^2}{dy^2}\phi_q^{(n)}(y) + \frac{V_0}{4E_R}\left(2 - 2\cos(2y)\right)\phi_q^{(n)}(y) = \frac{E_q^{(n)}}{E_R}\phi_q^{(n)}(y) \tag{2.13}$$

where $E_R = \hbar^2 k^2/2m$ is the atomic recoil energy and $y = kx$. For convenience, lattice depths are generally specified in recoil units. Equation (2.13) is just the Mathieu equation ([69])

$$\frac{d^2y}{dx^2} + (a + 2s\cos(2x))y = 0. \tag{2.14}$$

.

Solutions of the Mathieu equation are generally written in the Floquet form $e^{i\nu x}P(x)$ where ν is known as the characteristic exponent and $a = a(\nu, s)$ is the characteristic parameter which is a complicated function of s and ν. In the lattice language ν correspond to the quasimomentum , $s = V_0/4E_R$ and $a = E_q^{(n)}/E_R - V_0/2E_R$.

Fig. 2.3 shows the band structure of a sinusoidal potential for different potential depths. For $V_0 = 0$, the particles are free so the spectrum is quadratic in q. As the potential is increased the band structure appears. For small V_0 the discontinuity occurs only at the edge of the first Brillouin zone $qa \pm \pi$ and the gap is proportional to $V_0/2$. As the depth increases, the band gap increases and the band width decreases. For very deep lattices the spectrum is almost degenerate in q and exhibits a dependence on n similar to the one of a particle in a fixed finite interval(determined by the period of the potential).

In the absence of a lattice the eigenfunctions of the free system are plane waves. As the lattice depth is increased the barrier height between adjacent lattices sites increases and the eigenstates of the system tend to get localized at each lattice site (regions around the potential minima). In Fig. 2.4 the probability density of the Bloch wave function $\phi_{q=0}^{(n=0)}$ is plotted for different lattice depths. It can be observed how the amplitude of the wave function in between adjacent lattice sites decreases with increasinglattice depth.

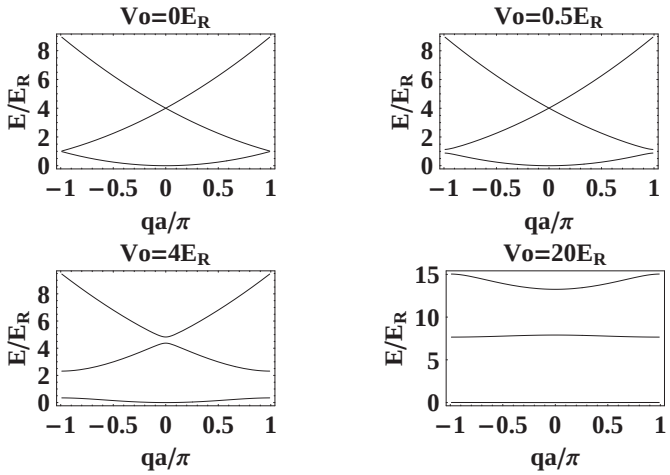

Figure 2.3: Band structure of an optical lattice

2.2.2 Wannier orbitals

Wannier orbitals are a set of orthonormal wave functions that fully describe particles in a band and are localized at the lattice sites. They are defined as:

$$w_n(x - x_i) = \frac{1}{\sqrt{M}} \sum_q e^{-iqx_i} \phi_q^{(n)}(x), \tag{2.15}$$

where the sum is over the first Brillouin zone, M is the total number of lattice sites and x_i is the position of the i^{th} lattice site. Wannier orbitals are thus a unitary transformation of the Bloch functions and are formally an equivalent representation to describe the periodic system. They constitute a more appropriate representation as the lattice depth is increased and particles get localized at individual lattices sites. The actual form of a Wannier function may be seen if we assume the periodic function $u_q^{(n)}(x)$ in equation 2.10 to be approximately the same for all Bloch states in a band. Under this approximation the Wannier function centered at the origin can be shown to be

$$w_n(x) \approx u^{(n)}(x) \frac{\sin(kx)}{kx}. \tag{2.16}$$

This looks like $u^{(n)}(x)$ at the site center, but spread out with oscillations of gradually decreasing amplitude. The oscillations are needed to ensure orhogonality between Wannier functions. In Fig. 2.5 we show the Wannier orbital centered at the origin site for each of the lattice configurations shown in Fig.2.2. The lattice depth in this pictures in deep enough that the Wannier orbitals are well localized. To observe the small oscillatory tails at the neighboring sites, the plots use a log-scale for the density color map.

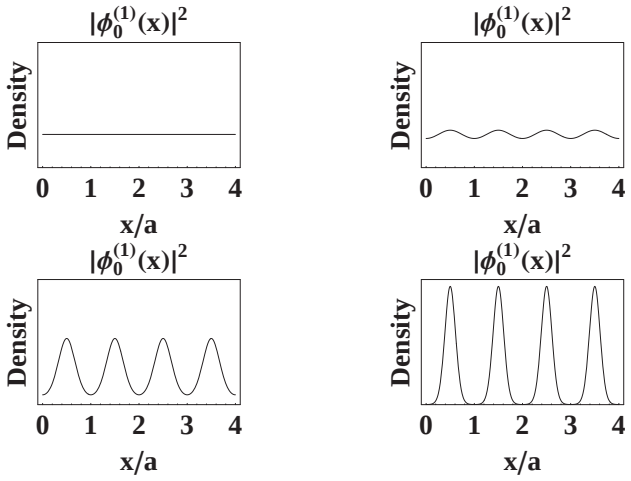

Figure 2.4: Probability density of the Bloch wave function $\phi_{q=0}^{(n=1)}$ for different lattice depths. It can be observed the localization of the wave function increases with the lattice increases.

2.2.3 Tight-binding approximation

The tight-binding approximation deals with the case in which the overlap between Wannier orbitals at different sites is enough to require corrections to the picture of isolated particles but not too much as to render the picture of localized wave functions completely irrelevant. Sometimes a very good approximation is only to take into account overlap between nearest neighbor orbitals. This tight-binding model is commonly used to solve the problem of a particle in a periodic potential when also an external potential is applied and it is going to be fundamental when considering particle interactions.

By expanding the wave function in Wannier orbitals,

$$\psi(x,t) = \sum_{n,i} z_i^{(n)}(t) w_n(x - x_i), \tag{2.17}$$

and using it in the Schrödinger equation that describes a particle moving in the potential of a 1D lattice plus a perturbative external potential $V(x)$, we get the following equations of motion

$$-i\hbar \frac{\partial}{\partial t} z_i^{(n)} = \sum_{jn'} -J_{ij}^{(n')} \delta_{nn'} z_j^{(n')}(t) + V_{ij}^{(n,n')} z_j^{(n')}(t), \tag{2.18}$$

with

$$J_{ij}^{(n)} = -\int dx w_n^*(x - x_i) H_o w_n(x - x_j) dx, \tag{2.19}$$

$$V_{ij}^{(n,n')} = -\int dx w_n^*(x - x_i) \mathcal{U}(x) w_{n'}(x - x_j) dx. \tag{2.20}$$

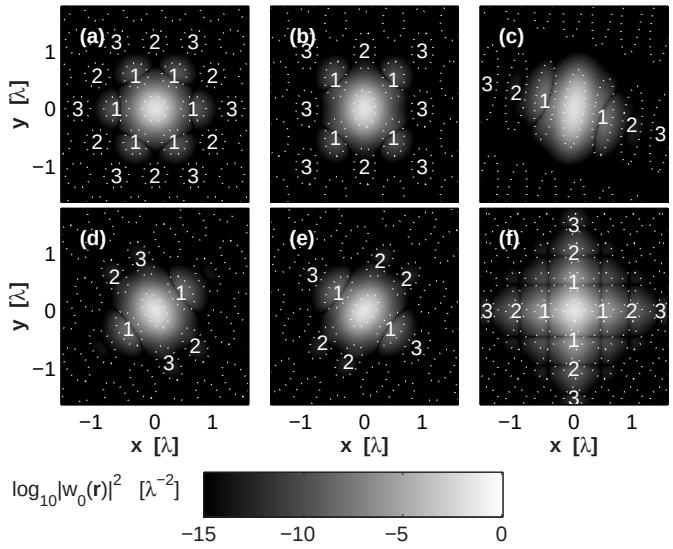

Figure 2.5: Wannier state log-density distribution corresponding to the lattice configurations shown in Fig. 2.2. Dotted white lines indicate the potential energy contours. The numbers labels the near neighbor sites: 1 the nearest neighbors, and so on. This figure is a courtesy of P. Blair Blakie [34])

If we assume that the external perturbation is not strong enough or sharp enough to induce interband transitions, we may represent the moving particle quite satisfactory by using Wannier functions of only the first band. Moreover, if the lattice is deep enough such that tunneling to next to nearest neighbors can be ignored, and the external perturbation is a slowly varying function such that it can be assumed constant inside each individual lattice site, i.e. $V_{ij}^{(n,n')} = V(x_i)\delta_{ji}\delta_{n,n'}$, the equations of motion reduce to

$$-i\hbar\frac{\partial}{\partial t}z_i(t) = -J\left(z_{i+1}(t) + z_{i-1}(t)\right) + V(x_i)z_i(t) + \varepsilon_o z_i(t), \tag{2.21}$$

with

$$J = -\int dx w_0^*(x_i) H_o w_0(x - x_{i+1}) dx, \tag{2.22}$$

$$\varepsilon_o = \int dx w_0^*(x) H_o w_0(x) dx \tag{2.23}$$

where J is the tunneling matrix element between nearest neighboring lattice sites, ε_o is the unperturbed on site energy shift and and z_i the first band coefficients $z_i(t) = z_i^{(0)}(t)$. Eq. (2.21) is known as the discrete Schrödinger equation (DSE) or tight-binding Schrödinger equation.

For deep lattices the localized Wannier orbitals can be approximated by a Gaussian function. However, because the Gaussian ansatz neglects the small

oscillations characteristic in the tail of the Wannier function, the tunneling matrix element J is then underestimated by almost an order of magnitude. For the special case of a sinusoidal potential $V_{lat}(x) = V_o \sin^2(kx)$ for which Mathieu functions are the exact solutions an analytic expression for J can be obtained by using tabulated Mathieu functions in Eq. (2.22) and fitting the data. The best fit we get is:

$$J/E_R = \alpha \left(\tilde{V}_o\right)^{\beta} e^{-\gamma\sqrt{\tilde{V}_o}} \tag{2.24}$$

with α =1.39666, β =1.051 and γ =2.12104 and $\tilde{V}_o = V_o/E_R$.

2.2.4 Semiclassical dynamics

Formalism

Solving Eq. (2.21) is presumably not possible for arbitrary $V(x_i)$. However, we get general insight to the nature of solutions by an application of the correspondence principle. It is well known that wave-packet solutions of the Schrödinger equation behave like classical particles obeying the equations of motion derived from the same classical Hamiltonian. The classical Hamilton equations are

$$\dot{x} = \frac{\partial H}{\partial p}, \qquad \dot{p} = -\frac{\partial H}{\partial x}. \tag{2.25}$$

Using the correspondence principle and the resemblance of the crystal momentum or quasimomentum to real momentum, the semiclassical equations of a wave packet in the first band of a lattice can be written as ([67], [68])

$$\dot{x} = v^{(0)}(q) = \frac{1}{\hbar}\frac{dE_q^{(0)}}{dq}, \qquad \hbar\dot{q} = -\frac{dV(x)}{dx}. \tag{2.26}$$

The semiclassical equations of motion describe how the position and wave vector of a particle evolve in the presence of an external potential entirely in terms of the band structure of the lattice. If we compare the acceleration predicted by the model with the conventional newtonian equation, $m\ddot{x} = -dV(x)/dx$, we can associate an effective mass induced by the presence of the lattice, m^*. This is given by

$$\frac{1}{m^*} = \frac{1}{\hbar^2}\frac{d^2}{dq^2}E_q^{(0)}. \tag{2.27}$$

Translationally invariant lattice

If no external potential is applied, $V(x) = 0$, plane waves are the solutions of DSE: $z_j(t) = f_j^{(q)} e^{-it(E_q+\varepsilon_o)/\hbar}$, $f_j^{(q)} = \frac{1}{\sqrt{M}} e^{iqaj}$ with M is the total number of lattice sites. If also periodic boundary conditions are assumed, the quasimomentum q is restricted to be an integer multiple of $\frac{2\pi}{Ma}$. The lowest energy band dispersion relation in this case is given by

$$E_q = -2J\cos(qa). \tag{2.28}$$

From the above equation it is possible to see the connection between J and the band width

$$J = \left(E_{q=\frac{\pi}{a}} - E_{q=0}\right)/4. \tag{2.29}$$

Linear external potential and Bloch oscillations

If $V(x)$ is assumed to be a linear potential, $V(x) = \frac{J\xi}{a}x$, it can be shown (see for example [70],[71],[72]), that in this case the energy spectrum of Eq. (2.21) is discrete and evenly spaced

$$(E_s - E_0) = J\xi s \quad s = 0, 1, 2, 3 \ldots. \tag{2.30}$$

The corresponding eigenfunctions are spatially localized and the amplitudes $z_j(t)$ given by :

$$z_j(t) = f_j^{(s)} e^{-iE_s t/\hbar}, \tag{2.31}$$

$$f_j^{(s)} = J_{s-j}(-2/\xi) \quad s = 0, 1, 2, 3, \ldots. \tag{2.32}$$

With J_s the s^{th} order Bessel function of the first kind. Because the quantities $f_j^{(s)}$ are just displaced Bessel functions, the s^{th} eigenstate of the system tends to be exponentially localized around the s^{th} site as ξ is increased. The localization is almost complete when $\xi = 4$, i.e. when the potential energy drop over a lattice period is equal to the zero field band width. The localization can be observed in Fig.2.6 where the ground state amplitudes $f_i^{(0)}$ are plotted for different values of ξ.

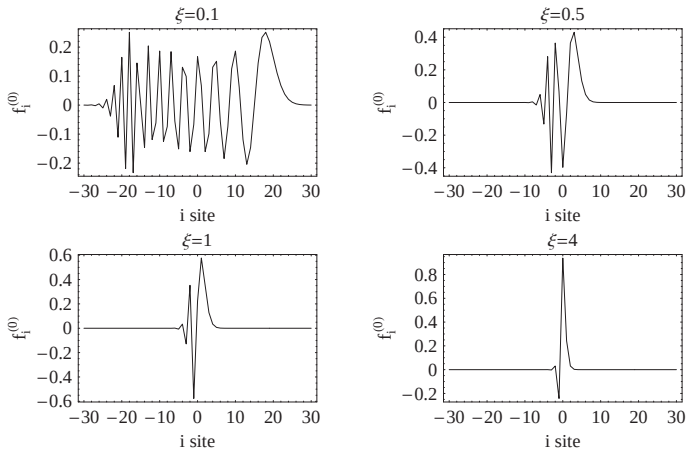

Figure 2.6: Ground state amplitudes $f_i^{(0)}$ as a function of the lattice site i for different values of ξ

An insight on the dynamics of a particle in this linear potential is obtained by calculating the time dependent probability of finding it at the site j at time t ,

$|z_j(t)|^2$, if it was in the state localized at the origin at time zero $z_j(0) = \delta_{0j}$. After some algebra it can be shown to be given by

$$P_j = |z_j(t)|^2 = J_j^2 \left(\frac{4 \sin(\xi\tau/2)}{\xi} \right), \tag{2.33}$$

with $\tau = tJ/\hbar$. The dynamical evolution of $P_{j\neq 0}$, for a given j consists of an initial period of growth until a maximum is reached followed by an oscillatory decay. The sequence is repeated again backwards until a time $\tau = 2\pi/\xi$ at which $P_{j\neq 0}$ vanishes and a new cycle starts.

In Fig. 2.7, the diffusion of a square wave packet occupying at $t = 0$ the central 20 sites is plotted. It can be seen that the center of mass of the wave function accelerates and then returns to its initial position after a period $\tau = 2\pi/\xi$.

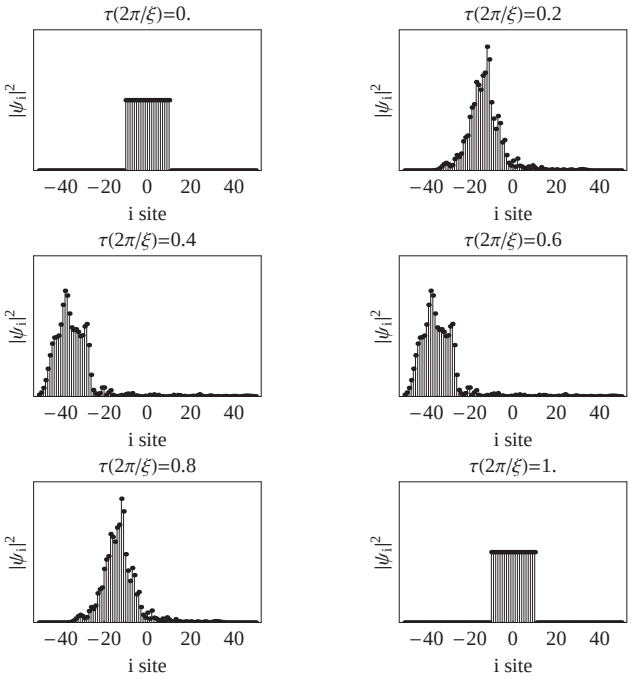

Figure 2.7: Diffusion of a square wave packet in the presence of a linear potential.The parameters for the plot are $\xi = 0.1$.

A simplified picture of the dynamics of a wave packet in this linear potential can also be obtained if we use the semiclassical model. If we assume a packet initially centered at $x(t = 0) = 0$, with average initial quasimomentum $q(t = 0) = q_o$, the semiclassical model predicts periodic oscillations of the center of mass with frequency ξ and amplitude $2/\xi$.

$$x(t) = \frac{2}{\xi}(1 - \cos(\xi\tau + q_o a)). \tag{2.34}$$

This periodic motion, known as Bloch oscillations, has been observed in systems of cold atoms [73] and Bose-Einstein condensates in optical lattices [38, 36]. On the other hand, if the external potential is strong enough to cause interband transitions, the tight-binding model does not apply anymore. In this case the atoms may gain enough energy from the external field to tunnel out through the energy gap into a second band when they reach the Brillioun zone boundary. This phenomenon is known as of Landau-Zener tunneling and it also has been observed in experiments [40].

Harmonic potential

A case of experimental interest is when, besides the periodic potential, the system is subject to a harmonic confinement, $V(x) = \frac{1}{2}m\omega_T^2 a^2 (x/a)^2 \equiv \Omega (x/a)^2$, with ω_T the trapping frequency (note that Ω is unrelated to the Rabi frequency discussed in section 2.1). The energy spectrum in this case is determined by the equation

$$E_s f_i^{(s)} = -J(f_{i+1}^{(s)} + f_{i-1}^{(s)}) + \Omega i^2 f_i^{(s)}. \tag{2.35}$$

It is possible to show that the solutions $f_i^{(s)}$ of Eq. 2.35 are the Fourier coefficients of the periodic Mathiue function with period π and the eigenvalues are the characteristic value of these periodic Mathiue functions [69]. The symmetric and antisymmetric solutions and eigenvalues are given respectively by

$$f_i^{(s=2r)} = \frac{1}{\pi}\int_0^{2\pi} ce_{2r}\left(x, \frac{4J}{\Omega}\right)\cos(2ix)dx \quad r = 0, 1, 2..., \tag{2.36}$$

$$f_i^{(s=2r+1)} = \frac{1}{\pi}\int_0^{2\pi} se_{2r}\left(x, \frac{4J}{\Omega}\right)\sin(2ix)dx,$$

$$E_{s=2r} = \frac{\Omega}{4}a_{2r}\left(\frac{4J}{\Omega}\right) \quad E_{s=2r+1} = \frac{\Omega}{4}b_{2r}\left(\frac{4J}{\Omega}\right), \tag{2.37}$$

with $ce_{2r}(x, 4J/\Omega)$ and $se_{2r}(x, 4J/\Omega)$ the even and odd periodic solution (with period π) of the Mathieu equation with characteristic parameter $a_{2r}(4J/\Omega)$ and $b_{2r}(4J/\Omega)$ respectively. The eigenvalues E_s are complicated functions of $\frac{4J}{\Omega}$ and therefore we are only going to consider expressions for certain limits:

- Case $J \gg \Omega$: This is the case where most experiments have been developed, for example for a 5 E_R lattice the parameter $q = \frac{4J}{\Omega}$ varies between 1.7x10^4 for a magnetic trap of 9 Hz to 35 for a trap of 200 Hz. In this regime the excitation spectrum is given by:

$$E_s = -2J + \sqrt{4\Omega J}(s + \frac{1}{2}) - \Omega\left(\frac{(2s+1)^2 + 1}{32}\right) \tag{2.38}$$
$$-\Omega\sqrt{\frac{\Omega}{J}}\left(\frac{(2s+1)^3 + 3(2s+1)}{2^{10}}\right) + \ldots$$

which to a first approximation is just the harmonic potential found if no lattice were present but with an effective frequency ω^* and effective mass m^* given by

$$\hbar\omega^* = \sqrt{4\Omega J} = \hbar\omega_t\sqrt{\frac{m}{m^*}}, \tag{2.39}$$

$$m^* = \frac{\hbar^2}{2Ja^2}, \tag{2.40}$$

It is worth it to emphasize that this result was derived under the tight-binding approximation and therefore it is not valid for very shallow lattices. The harmonic character of the spectrum can be easily checked if we take the continuous limit of Eq. (2.35). The differential equation obtained is just the harmonic oscillator equation,

$$(E_s + 2J)f^{(s)}(x) = -\frac{\hbar^2}{2m^*}\frac{\partial f^{(s)}(x)}{\partial x^2} + \frac{1}{2}m^*\omega^{*2}x^2 f^{(s)}(x). \tag{2.41}$$

The average width of the wave function is just $a_{ho}=\sqrt{\frac{\hbar}{m^*\omega^*}}$.

- Case $J \ll \Omega$: The single particle spectrum in this case is given by

$$\begin{aligned}
E_{s=2n} &\approx E_{s=2n-1} \\
&= \frac{\Omega}{4}\left((2n)^2 + \left(\frac{4J}{\Omega}\right)^2\frac{1}{((2n)^2-1)} + O\left(\frac{4J}{\Omega}\right)^4 + ..\right) \quad n \geq 3, \\
E_4 &\approx E_3 = \frac{\Omega}{4}\left(16 + \left(\frac{4J}{\Omega}\right)^2\frac{1}{30} + ..\right), \\
E_2 &= \frac{\Omega}{4}\left(4 + \left(\frac{4J}{\Omega}\right)^2\frac{5}{12} + ..\right), \\
E_1 &= \frac{\Omega}{4}\left(4 - \left(\frac{4J}{\Omega}\right)^2\frac{1}{12} + ..\right), \\
E_0 &= \frac{\Omega}{4}\left(-\left(\frac{4J}{\Omega}\right)^2\frac{1}{2} + ...\right).
\end{aligned} \tag{2.42}$$

It can be appreciated that the spectrum is nearly twofold degenerate and it goes like Ωn^2 to first order in (J/Ω) . In this regime then, the trapping potential is what mostly determines the energy spacing. In Fig. 2.8 the spectrum is shown for different values of $\frac{4J}{\Omega}$.

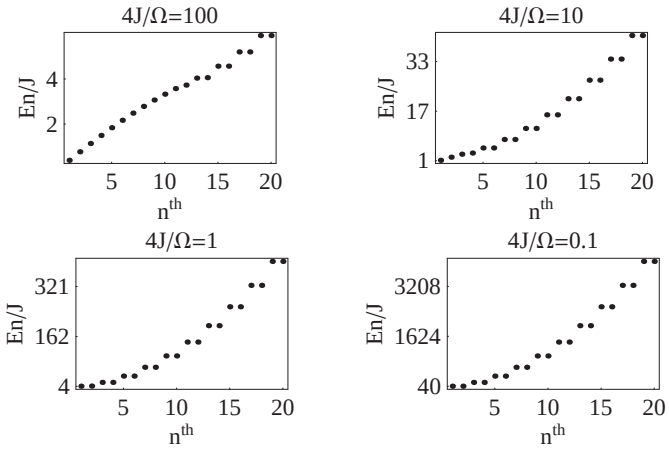

Figure 2.8: Harmonic confinement plus lattice spectrum: The index n labels the eigenvalues in increasing energy order.

Chapter 3

The Bose-Hubbard Hamiltonian and the superfluid to Mott insulator transition

In chapter 2 we studied the physics of non interacting particles in a periodic system. In this chapter we go one step ahead and describe the basic properties of a bosonic many body system with repulsive interactions in a periodic lattice potential.

The simplest non trivial model that describes interacting bosons in a periodic potential is the Bose Hubbard Hamiltonian. It includes the main physics that describe strongly interacting bosons, which is the competition between kinetic and interaction energy. This model has been used to describe many different systems in solid state physics, like short correlation length superconductors, Josephson arrays, critical behavior of ^{4} He and, recently, cold atoms in optical lattices [43]. It has been studied analytically with many different techniques such as mean field approximations [74, 75, 77], renormalization group theories [44] and strong coupling expansions [78]. Numerically most of the studies are based on quantum Monte Carlo methods and density matrix renormalization techniques [79]. The Bose Hubbard Hamiltonian predicts a quantum phase transition from a superfluid to a Mott insulator state. This transition has been observed experimentally in atoms confined in a 3D optical lattice [46]. In this chapter we start by reviewing the basic properties of the Bose Hubbard Hamiltonian and outline the most important aspects that characterize the superfluid to Mott insulator transition.

3.1 Bose-Hubbard Hamiltonian

We begin the analysis by considering the second quantized Hamiltonian that describes interacting bosonic atoms in an external trapping potential plus lattice. In the grand canonical ensemble it is given by:

$$\begin{aligned}\hat{H} &= \int d\mathbf{x}\hat{\Phi}^\dagger(\mathbf{x})\left(-\frac{\hbar^2}{2m}\nabla^2 + V_{lat}(\mathbf{x})\right)\hat{\Phi}(\mathbf{x}) + (V(\mathbf{x})-\mu)\hat{\Phi}^\dagger(\mathbf{x})\hat{\Phi}(\mathbf{x}) \quad (3.1)\\ &\quad + \frac{1}{2}\int d\mathbf{x}d\mathbf{x}'\hat{\Phi}^\dagger(\mathbf{x})\hat{\Phi}^\dagger(\mathbf{x}')V_{at}(\mathbf{x}-\mathbf{x}')\hat{\Phi}(\mathbf{x})\hat{\Phi}(\mathbf{x}'),\end{aligned}$$

where $\hat{\Phi}^\dagger(\mathbf{x})$ is the bosonic field operator which creates an atom at the position $\mathbf{x}$, $V_{lat}(\mathbf{x})$ is the periodic lattice potential, $V(\mathbf{x})$ denotes any additional slowly-varying external potential that might be present (such as a magnetic trap), μ is the chemical potential and acts as a lagrange multiplier to fix the mean number of atoms in the grand canonical ensemble and $V_{at}(\mathbf{x})$ is the interatomic scattering potential, which is in general a complicated function. However, since for cold gases the thermal de Broglie wavelength is much larger than the effective extension of the interaction potential, the only relevant scattering process is the s-wave scattering, and the actual inter-particle potential plays a minor role. Therefore, to a good approximation, the interatomic potential can be replaced by an effective contact interaction:

$$V_{at}(\mathbf{x}) \approx \frac{4\pi a_s \hbar^2}{m}\delta(\mathbf{x}), \quad (3.2)$$

with a_s is the scattering length and m the mass of an atom. In this thesis we are going to assume that the scattering length is positive so the interactions are repulsive.

Similar to the noninteracting situation, where we used Wannier orbitals to expand the single particle wave function, it is convenient to expand the field operator in a Wannier orbital basis. If the chemical potential of the system is less than the single particle excitation energy to the second band, only the first band has to be considered and the field operator can be written as:

$$\hat{\Phi}(\mathbf{x}) = \sum_n \hat{a}_n w_0(\mathbf{x}-\mathbf{x}_n), \quad (3.3)$$

where $w_0(\mathbf{x})$ is the Wannier orbital of the lowest vibrational band localized at the origin, and $\hat{a}_n$ is the annihilation operator at site n which obeys bosonic canonical commutation relations. The sum is taken over the total number of lattice sites. If Eq. (3.3) is inserted in $\hat{H}$ and only tunneling between nearest neighbors is considered, we obtain the Bose Hubbard Hamiltonian

$$\hat{H}_{BH} = -J\sum_{<n,m>}\hat{a}_n^\dagger\hat{a}_m + \frac{1}{2}U\sum_n \hat{a}_n^\dagger\hat{a}_n^\dagger a_n a_n + \sum_n (V_n-\mu)\hat{a}_n^\dagger\hat{a}_n, \quad (3.4)$$

with

$$J = -\int d\mathbf{x} w_0^*(\mathbf{x}-\mathbf{x}_n)\left(\frac{\hat{\mathbf{p}}^2}{2m}+V_{lat}(\mathbf{x})\right)w_0(\mathbf{x}+\mathbf{x}_{n+1}), \tag{3.5}$$

$$U = \frac{4\pi a_s \hbar^2}{m}\int d\mathbf{x}\,|w_0(\mathbf{x})|^4, \tag{3.6}$$

$$V_n = V(\mathbf{x}_n). \tag{3.7}$$

The first term in the Hamiltonian proportional to J is a measure of the kinetic energy of the system. J is the hopping matrix element between nearest neighbors (see also 2.24). Here the notation $< n, m >$ restricts the sum to nearest-neighbors sites. Next-to-nearest neighbor tunneling amplitudes are typically two orders of magnitude smaller than nearest-neighbor tunneling amplitudes, and to a good approximation they can be neglected.

The second term determines the interaction energy of the system. The parameter U measures the strength of the repulsion of two atoms at lattice site n.The integral (3.6) is not as sensitive as Eq. (3.5) to the oscillatory tails characteristic of the Wannier orbitals, and a Gaussian approximation can be used to estimate it [43]. Under the Gaussian approximation, the ground state wave function centered at the origin of a separable sinusoidal lattice, with lattice depth V_{j0} in the j^{th} direction, has the form $w_0(\mathbf{0}) \sim \prod_j \exp -\left(\frac{\mathbf{x}_j}{\sqrt{2}\mathbf{a}_{hoj}}\right)^2$, with $\mathbf{a}_{hoj} = \sqrt{\frac{\hbar}{m\omega_{hoj}}}$ and $\omega_{hoj} = \sqrt{\frac{4E_r V_{j0}}{\hbar^2}}$. Using this ansatz in the integral (3.6) yields an onsite interaction given by

$$U = \frac{\hbar a_s}{\sqrt{2\pi}}\frac{\overline{\omega}_{ho}}{\overline{a}_{ho}}, \tag{3.8}$$

with the bar indicating the geometric mean. To guarantee the validity of the one band approximation, the mean interaction energy per particle UN must be smaller than the energy gap to the first vibrational excitation, i.e. $UN < \hbar\overline{\omega}_{ho}$. N is the mean number of atoms. This inequality is readily satisfied in practice.

The third term in the Hamiltonian takes into account the energy offset at site n due to a slowly varying external potential $V(\mathbf{x})$.

The realization of the Bose-Hubbard Hamiltonian using optical lattices has the advantage that the interaction matrix element U and the tunneling matrix element J can be controlled by adjusting the intensity of the laser beams. As the intensity of the lattice is increased the tunneling rate decreases exponentially and the onside interaction increases as a power law, $V_0^{d/4}$, (d is the dimensionality of the lattice).

3.2 Superfluid-Mott insulator transition

At zero temperature the physics described by the Bose-Hubbard Hamiltonian can be divided into two different regimes. One is the interaction dominated regime

when J is much smaller than U, and the system is in the Mott insulator phase. The other is the kinetic energy dominated regime, where tunneling overwhelms the repulsion and the system exhibits superfluid properties. The onset of superfluidity is a consequence of the competition between the kinetic energy, which tries to delocalize the particles, and the interaction energy, which tries to localize them and make the number fluctuations small.

In the superfluid regime, the kinetic energy term dominates the Hamiltonian. In this regime, quantum correlations can be neglected and the system can be described by a macroscopic wave function since the many body state is almost a product over identical single particle wave functions. There is a macroscopic well-defined phase and the system is a superfluid. Because atoms are delocalized over the lattice with equal relative phases between adjacent sites, they exhibit an interference pattern when the lattice is turned off, as expected from an array of phase coherent matter wave sources. As interaction increases the average kinetic energy required for an atom to hop from one site to the next becomes insufficient to overcome the potential energy cost. Atoms tend to get localized at individual lattice sites and number fluctuations are reduced. In the Mott insulator phase the ground state of the system instead consists of localized atomic wave functions with a fixed number of atoms per site. The lowest lying excitations that conserve particle number are particle-hole excitations (adding plus removing a particle from the system). This phase is characterized by the existence of an energy gap. The gap is determined by the energy necessary to create one particle-hole pair.

The phase diagram [44],[74]-[76] that describes the Mott insulator transition of a translational invariant system with $V_n = 0$ exhibits lobe-like Mott insulating phases in the J-μ plane, see Fig. 3.1. Each Mott lobe is characterized by having a fixed integer density. Inside these lobes the compressibility, $\partial\rho/\partial\mu$ with ρ the average density of the system, vanishes. The physics behind this diagram can be understood as follows: If we start at some point in the Mott insulating phase and increase μ keeping J fixed, there is going to be a point at which the kinetic energy of adding an extra particle and letting it hop around will balance the interaction energy cost. With an extra particle free to move around the lattice phase coherence is recovered and the system enters the superfluid regime. Similarly, by decreasing μ from a point in the Mott phase, at some point eventually it will be energetically favorable to remove one particle from the system. The extra mobile hole will induce also phase coherence and the system will condense in a superfluid state. Since the kinetic energy of the system increases with J the width of the lobes decreases with J. The distance in the μ direction at fixed J between the upper and lower part of the lobe is the energy gap. At $J = 0$ the gap is just equal to U. Also at $J = 0$ the intersection points between the lobes with density $\rho = n$ and the ones with density $\rho = n + 1$ are degenerate. Because there is no energy barrier to the addition of an extra particle at these degenerated points the system remain superfluid. Mott insulator phases occur only at integer densities; non-integer density contours lie entirely in the superfluid phase because there is always an extra particle that can hop without energy cost.

The phase diagram includes two different types of phase transition. One type takes place at any generic point of the phase boundary, and it is driven by the energy cost to add or subtract small numbers of particles to the incompressible Mott state as explained above. On the other hand, the other type only occurs at fixed integer density and takes place at the tip of the lobes. This transition is driven at fixed density by decreasing U/J and enabling the bosons to overcome the on site repulsion. The two kinds of phase transition belong to different universality classes. In the generic one, the parameter equivalent to the reduced temperature $\delta = T - T_c$ for finite temperature transitions that measures the distance from the transition is $\delta \sim \mu - \mu_c$, with μ_c the chemical potential at the phase boundary. For the special fixed density on the other hand one must take $\delta \sim (J/U) - (J/U)_c$. As shown in ([44]) provided $\delta \sim \mu - \mu_c$, the compressibility has a singular part scaling near the transition as $\delta^{-\alpha}$, $\alpha > 0$. This scaling does not apply at the special fixed density Mott-Superfluid transition for which $\delta \sim (J/U) - (J/U)_c$ and differentiation with respect to delta becomes inequivalent to differentiation with respect to the chemical potential. Most of the features of the phase diagram discussed above can be verified by simple calculations done using a mean field approximation. The solution of the mean field model [74]- [76] predicts that the critical value at the tip of the Mott lobe depends on the density and dimensionality of the lattice as

$$(U/J)_c = t\left(2n + 1 + \sqrt{(2n+1)^2 - 1}\right), \tag{3.9}$$

where n is the integer density of the lobe, t the number of nearest neighbors, $t = 2d$, with d the dimensionality of the system. The parabolic phase boundary of the lobes in the plane μ vs (J/U) vs is given by

$$\mu/J = \frac{1}{2}\left((2n-1) - Jt/U \pm + \sqrt{(Jt/U)^2 - 2(Jt/U)(2n+1) + 1}\right). \tag{3.10}$$

Up to this point we have discussed the basic aspects of the superfluid-Mott insulator transition in a translationally invariant system. The situation is fundamentally different for a inhomogeneous system with a fixed total number of atoms and external confinement. This is the case realized in experiments, where besides the lattice there is a harmonic trap that collects the atoms at the center. In this case the density of atoms is not fixed since the atoms can redistribute over the lattice and change the local filling factor.

To deal with the inhomogeneous case, it is possible to define an effective local chemical potential, $\mu_n = \mu - V_n$, at each lattice site n [43]. If the change in the mean number of atoms between neighboring sites is small, the system can be treated locally as an homogeneous system. Because in the inhomogeneous case, the local chemical potential is fixed by the density, as the ratio U/J is changed the system can locally cross the boundary between the superfluid and Mott insulator phases. Therefore even for the situation when the local density was not commensurate at

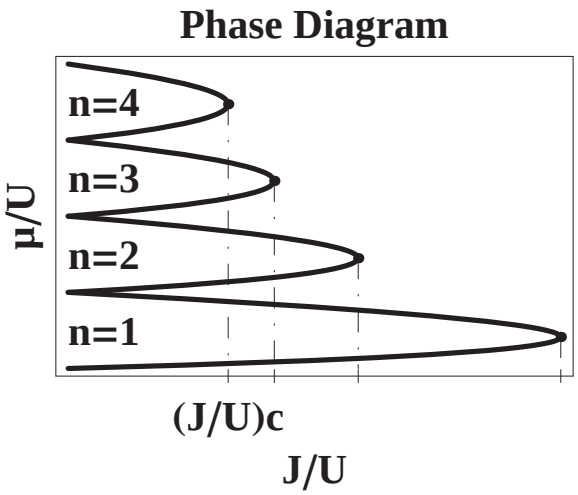

Figure 3.1: Zero-temperature phase diagram. The vertical lines indicate critical values for different filling factors

the beginning, as the ratio U/J is changed a local phase transition can take place. For the inhomogeneous case, the gradient in the local chemical potential leads to a shell structure with Mott insulator regions and superfluid regions in between. In [79], the authors used quantum Monte Carlo simulations to study the ground state of the one dimensional Bose Hubbard model in a trap. They found that Mott phases exist in extended domains above a threshold interaction strength, even without the commensurate filling required in the translationally invariant case.

Chapter 4

Mean field theory

In this chapter we introduce the mean field Discrete Nonlinear Schrödinger equations and use it first to investigate the behavior of a BEC adiabatically loaded into an optical lattice moving at constant velocity, and second to model the dynamical evolution of a BEC initially loaded into every third site of an optical lattice.

4.1 Discrete nonlinear Schrödinger equation (DNLSE)

In the weakly interacting regime, quantum fluctuations can be neglected to a good approximation. In this regime most of the atoms occupy the same condensate wave function. The macroscopic occupation of a single mode implies that the commutator of the annihilation and creation operators that create and destroy a particle in the condensate mode can be neglected with respect to the total number of atoms in the mode. Therefore, to a good approximation the field operator can be replaced by a c-number,

$$\hat{\Phi}(\mathbf{x}) \rightarrow \varphi(\mathbf{x}). \tag{4.1}$$

This procedure can be interpreted as giving to the field operator a non zero average, $\langle\hat{\Phi}(\mathbf{x})\rangle = \varphi(\mathbf{x})$, and thus a well defined phase to system. Because the original Hamiltonian is invariant under global phase transformation, this definition of BEC corresponds to an spontaneous symmetry breaking [11, 12, 80]. The function $\varphi(\mathbf{x})$ is a classical field having the meaning of an order parameter and is often called the "condensate wave function". It characterizes the off-diagonal long range order present in the one particle density matrix [81].

$$\lim_{|\mathbf{x}'-\mathbf{x}|\rightarrow\infty} \langle\hat{\Phi}^{\dagger}(\mathbf{x}')\hat{\Phi}(\mathbf{x})\rangle = \varphi^{*}(\mathbf{x}')\varphi(\mathbf{x}). \tag{4.2}$$

Strictly speaking, neither the concept of broken symmetry, nor the one of off-diagonal long range order can be applied to finite size systems with well defined number of particles. However the condensate wave function can still be determined by diagonalization of the one particle density matrix. The eigenstate with larger eigenvalue corresponds to $\varphi(\mathbf{x})$.

If we use the approximation (4.1) in the many-body Hamiltonian (3.1) we get a classical Hamiltonian given by:

$$\begin{aligned} H &= \int d\mathbf{x}\varphi^{\dagger}(\mathbf{x})\left(-\frac{\hbar^2}{2m}\nabla^2 + V_{lat}(\mathbf{x})\right)\varphi(\mathbf{x}) + (V(\mathbf{x})-\mu)\varphi^{\dagger}(\mathbf{x})\varphi(\mathbf{x}) \quad (4.3)\\ &+\frac{1}{2}\frac{4\pi a_s\hbar^2}{m}\int dx\varphi^{\dagger}(\mathbf{x})\varphi^{\dagger}(\mathbf{x})\varphi(\mathbf{x})\varphi(\mathbf{x}), \end{aligned}$$

The time dependent equations of motion for the condensate wave function can be obtained from the variational principle by minimizing the quantity $i\hbar\frac{\partial}{\partial t} - \hat{H}$. The minimization yields

$$i\hbar\frac{\partial\varphi(\mathbf{x})}{\partial t} = \left(-\frac{\hbar^2}{2m}\nabla^2 + V_{lat}(\mathbf{x}) + V(\mathbf{x}) + \frac{4\pi a_s\hbar^2}{m}|\varphi(\mathbf{x})|^2\right)\varphi(\mathbf{x}) \quad (4.4)$$

This equation is known as the Gross-Pitaevskii equation (GPE). It was derived by independently by Gross and Pitaevskii [10].

If the chemical potential is small compared to the vibrational level spacing and the lattice depth is deep enough that a tight binding picture is valid, the condensate order parameter can be expanded in a Wannier basis keeping only the lowest band orbitals:

$$\varphi(x,t) = \sum_n z_n(t)w_0(\mathbf{x}-\mathbf{x}_n). \quad (4.5)$$

Using this ansatz in Eq. (4.4), the Gross-Pitaevskii equation reduces to the discrete nonlinear Schroedinger equation (DNLSE), where the z_n amplitudes satisfy:

$$i\hbar\frac{\partial z_n}{\partial t} = -J\sum_{<n,m>} z_m + (V_n + UN|z_n|^2)z_n, \quad (4.6)$$

where $< n, m >$ restricts the sum over nearest neighbors, the parameters J and U are the ones defined in Eq. (3.5) and (3.6) and N is the total number of particles. The normalization condition for the amplitudes is given by:

$$\sum_n |z_n|^2 = 1. \quad (4.7)$$

Notice the DNLSE can also be derived by assuming the field operators present in the Bose-Hubbard Hamiltonian to be c-numbers,i.e. $\hat{a}_n = z_n(t)$. This assumption leads to a tight-binding classical Hamiltonian, which can be minimized using the variational principle.

$$H = -J\sum_{<n,m>} z_n^* z_m + \sum_n \left(V_n|z_n|^2 + \frac{U}{2}|z_n|^4\right). \quad (4.8)$$

The DNLSE is similar to its linear counterpart, the DSE or tight-binding Schrödinger equation (see 2.21), but with an extra cubic term, which takes into account mean field interaction effects. To see the modification that the nonlinear term introduces in the dispersion relation, we consider a one dimensional optical lattice with M sites and periodic boundary conditions.

In the translational invariant case with no other external potential present, $V_n = 0$, the solutions of the DNLSE that are similar to those of the noninteracting case are, $z_n = \sqrt{n_o}\exp(-inq)\exp\left(-iE_q t/\hbar\right)$, with $n_o = N/M$ the condensate density. Using this plane wave ansatz in the DNLSE we get a dispersion relation given by:

$$E_q = -2J\cos(qa) + Un_o \tag{4.9}$$

In the tight-binding approximation, mean field interactions do not modify the shape of the lowest band: it has still a cosine dependence with bandwith equal to $4J$. The only difference with respect to the single particle case is an energy shift in the dispersion relation which takes into account the average mean field energy Un_o.

It is important to mention though, that outside the range of validity of a tight-binding model, nonlinear effects does not necessarily change the dispersion relation in a simple way, especially at the edge of the Brillouin zone. It has been shown in the literature [82, 83] that if the chemical potential is bigger than the gap vibrational excitation energy to higher bands, the lowest band becomes triple valued near the Brilloiun zone edge and a loop appears at this point. This loop reflects the existence of new solutions, which only exist when the tight-binding approximation is not valid. These new solutions have a non zero velocity at the edge of the Brillouin zone, as opposed to the linear case. The nonzero velocity carried by the Bloch waves is a manifestation of the superfluidity of the system. For free particles the flow is stopped completely by Bragg scattering from the periodic potential, but if interactions are strong enough the superfluid flow can no longer be stopped.

4.2 Dragging experiment

In this section we investigate an experiment done at NIST where a Bose-Einstein condensate was prepared in a harmonic trap and adiabatically loaded into a one dimensional optical lattice moving at constant velocity Ref. [37]. We first study the dynamics in a translationally invariant lattice using a simple single particle picture, and show how the center-of-mass motion of the condensate can be used as a probe of the lattice band structure. Then we discuss the effects of the trapping potential and interaction effects on the dynamics. When mean field effects are included, they cause the effective mass of the Bloch state to depend on time, influencing the condensate dynamics in the lattice. As a consequence, characteristic nonlinear effects such as solitons, self focusing effects and dynamical stabilities might be observed.

4.2.1 Experiment

In the experiment, a condensate prepared in the ground state of a harmonic trap is loaded in an optical lattice, which is moved at constant velocity. The loading of the condensate in the optical lattice is done by turning on the lattice, linearly in time, up to some maximum height. The important part of this turning on is that it is done sufficiently slow to be adiabatic with respect to band excitations. After the maximum is reached, at $t = t_r$, the lattice depth is held constant for a fixed period of time and the system is allowed to expand in the lattice. Finally at $t = t_f$ the condensate density distribution along the lattice axis is imaged. The temporal dependence of the optical lattice depth is shown in Fig. 4.1. In the figure, experimental results obtained for the final condensate density for different lattice depths are also shown. The general observation is that the deeper the lattice, the greater the response of the condensate to the lattice motion. In this experiment, the condensate has a very narrow momentum spread compared to the lattice recoil momentum.

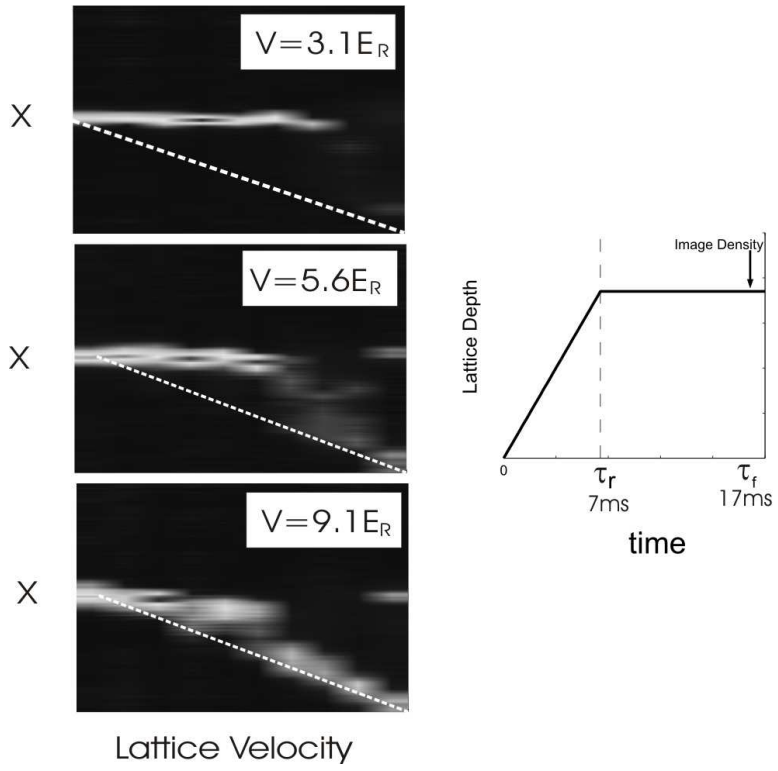

Figure 4.1: Condensate density in the x-direction at the observation time t_f. Light colors areas indicate regions of high condensate density. The dashed line indicates the final location of a co-moving point with the optical lattice.

4.2.2 Linear free particle model

In this section to a first approximation we are going to neglect interactions and apply a single particle picture to understand the dynamics.

Because the momentum spread of the condensate is very narrow compared with the lattice recoil momentum at $t = 0$, the initial wave function can be approximated by a plane wave with zero momentum. This wave function, in the lattice frame, which is moving with velocity v_{latt} with respect to the lab frame, has the form $\varphi(x') = e^{-ik_o x'}$, with $v_{latt} = \hbar k_o/m$ (we used primes to denote the coordinates and wave functions in the moving frame). As t increases, the optical potential is ramped up, the wave function evolves, but due to the fact that the Hamiltonian is invariant under translation, the quasimomentum is conserved (at least in this linear model with no other potential than the lattice) during the ramping time and the average quasimomentum at the end of the loading should remain $-k_o$. From t_r to t_f the lattice depth is held constant. During this period of time the average velocity of the atom, as seen in the lattice frame, is:

$$v = \frac{1}{\hbar}\frac{dE_q^{(n)}}{dq}\Big|_{q=-k_o}, \tag{4.10}$$

with $E_q^{(n)}$ the n^{th} band Bloch-like atomic dispersion relation evaluated at the final lattice depth. Transforming back to the lab frame, Eq. (4.10) implies that in the lab frame, during t_r to t_f, the average velocity of the atoms is given by:

$$v_{atom} = \frac{\hbar k_o}{m} + \frac{1}{\hbar}\frac{dE_q^{(n)}}{dq}\Big|_{q=-k_o}. \tag{4.11}$$

Because $x(t_f)$ is the observable of the experiment, we can calculate it as

$$\delta x = \langle x(t_f)\rangle - \langle x(t_r)\rangle \approx v_{atom}(t_f - t_r). \tag{4.12}$$

Therefore, by measuring the average position of the atoms for a fixed $t_f - t_i$ the experiment measures the atom's velocity, which is a determined by the band structure of the lattice.

In Fig. 4.2 we plot the atom's average velocity in the lab frame vs. the lattice velocity. The velocity in Eq.(4.11) is calculated using the Bloch dispersion relation for a three recoil lattice. The tight-binding results (dotted) are also shown. Even though the tight-binding velocities do not exactly match the velocities calculated using the Bloch dispersion relation, we can say that for a three recoil lattice the tight-binding approximation is fair.

We emphasize the following points:

- Because the initial quasimomentum is determined by the lattice velocity, $v_{lat} = \hbar k_o/m$, to move the lattice at different speeds corresponds to loading the condensate at a different Bloch state. How much the atoms are dragged depends on the derivative of the dispersion relation evaluated at the loaded quasimonentum.

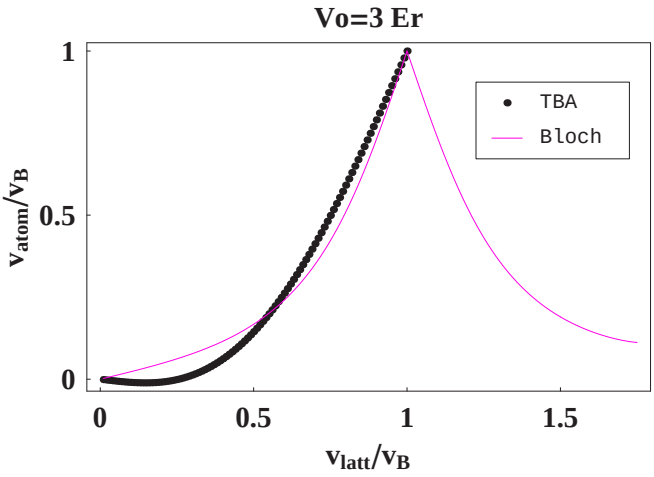

Figure 4.2: Atom's average velocity in the lab frame vs. lattice velocity. Line: results from the Bloch dispersion relation, dots: tight-binding approximation results. $v_B = \hbar\pi/am$.

- At zero lattice depth the dispersion relation is quadratic, $\frac{1}{\hbar}\frac{dE_q^{(n)}}{dq}\Big|_{q=-k_o} = \hbar k_o/m$ and therefore Eq. (4.11) predicts no dragging. As the lattice depth increases the dispersion relation desviates more from free-particle behavior and dragging ensues. This is consistent with the experimental results shown in Fig. 4.1.

- For small lattice velocities ($|k_o a| \ll 1$, a the lattice constant) the atoms are almost stationary because then the dispersion relation is more free-particle like. On the other hand, as k_o approaches the k of the Brillouin zone edge, $k_o = -q_B$, the atoms are dragged the most. At this point, as opposed to the free free system, Bloch waves carry zero velocity, i.e $dE_q^{(n)}/dq|_{q=-q_B} = 0$.

4.2.3 Effect of the magnetic confinement

In the experiment a harmonic confinement was present in addition to the lattice potential. To model the effect of the magnetic trap on the atoms dynamics we used a semiclassical model (see chapter 2). The semiclassical model is a very good approximation whenever it is unnecessary to specify the position of the atom on a scale comparable with the spread of the wave packet. The validity of the semiclassical model requires that the external potential varies slowly over the dimension of the wave packet and ignores the possibility of inter band transitions. In the experiment, the strength of the harmonic trap is less than one percent of the potential depth and we expect the semiclassical model to be valid. Following this model, in the lattice frame, the time evolution of the average position and wave vector of

the atoms are given by Eq. (2.26):

$$\dot{x} = v^{(n)}(q) = \frac{1}{\hbar}\frac{dE_q^{(n)}}{dq}, \qquad \hbar\dot{q} = -m\omega^2(x + v_{lat}t), \tag{4.13}$$

with ω the magnetic trapping frequency. The initial conditions are $k(0) = -ko$ and $x(0) = 0$. We solved these equations of motion, using the analytic dispersion relation for a sinusoidal lattice in terms of Mathieu functions. We used the parameters $V_0 = 3E_R$ and $1/2m\omega^2/E_R = 0.000025$. The results are shown in Fig. 4.3.

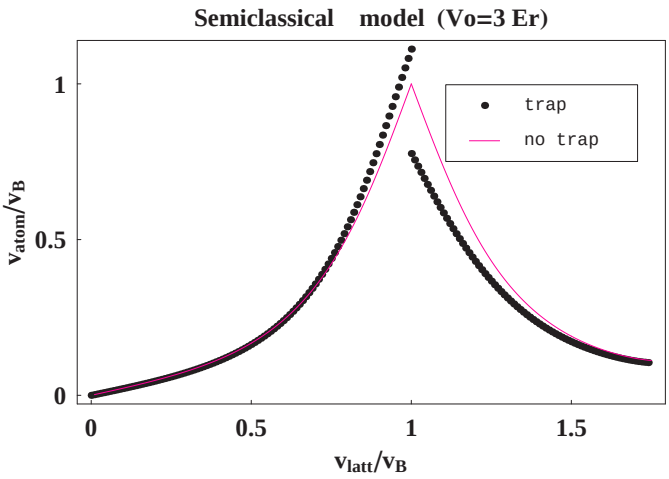

Figure 4.3: Atom's average velocity in the lab frame vs. lattice velocity in the presence of a magnetic trap. $v_B = \hbar\pi/am$.

We observe in the plot that when atoms are loaded in the first band, for a range of lattice velocities below half the Brillouin velocity ($v_{latt} \lesssim v_B/2$ with $v_B = \hbar\pi/am$), the motion of the atoms with and without trap is almost the same. For larger velocities, as long as the atoms remain in the first band, trapped atoms move faster than the un-trapped ones. However, if the lattice velocities exceeds the Brillouin velocity, v_B, the opposite behavior is observed and for an interval of velocities, $v_B < v_{latt} \lesssim 3v_B/2$, trapped atoms slow down compared with the ones in the homogeneous lattice.

This behavior can be understood as follows: Because of the trap, the atoms feel a force opposite to the direction of motion. The force not only increases with time but also with the lattice velocity (see Eq. (4.13)). The average quasimomentum of the system evolves in the presence of the force, and if at time $t = 0$ the atoms are loaded with quasimomentum $q(0) = -ko$, then at t_f the final quasimomentum is $q(t_f) = -k_o + \Delta(k_o, t_f)$. Here $\Delta(k_o, t_f)$ is a negative quantity because the force is a restoring force. Therefore, the final velocity of the atoms in the trap , is less or greater than the velocity of the atoms without the external trap depending on the

sign of the effective mass (sign of the curvature of the dispersion relation) evaluated at the final momentum. If the effective mass is positive, $\frac{d^2E_q}{dq^2} > 0$, ($0 < q < \pi/2a$, $\pi/a < q < 3\pi/2a$,...), the group velocity is an increasing function of q and the velocity of the trapped atoms is less than the untrapped atoms' velocity. On the other hand, when the effective mass is negative,($\pi/2a < q < \pi/a$,...), the group velocity is a decreasing function of q and the trapped atoms speed up with respect to the untrapped ones. The more pronounced difference between trapped and untrapped atom velocities observed in the second band with respect to the first one, is not only because Δ increases with the lattice velocity but also because of the discontinuous change of the band structure when crossing the Brillouin zone edge. Besides the sign difference in the curvature the second band has a larger band width than the first one.

4.2.4 Interaction effects

To model the effect of the interatomic interactions on the dynamics we used the tight-binding variational method proposed in Ref. ([84, 85]). In these reference the authors assume a Gaussian profile wave packet

$$z_n(t) = \sqrt[4]{\frac{2}{\gamma^2\pi}} e^{[-(n-\xi)^2/\gamma^2 + ik(n-\xi) + i\delta(n-\xi)^2/2]}, \tag{4.14}$$

and used ξ, γ, k, δ as variational parameters. The equations of motion they found are:

$$\dot{k} = -\frac{\partial V}{\partial \xi}, \tag{4.15}$$

$$\dot{\xi} = 2J\sin(k)e^{-\eta}, \tag{4.16}$$

$$\dot{\delta} = 2J\cos(k)e^{-\eta}\left(\frac{4}{\gamma^4} - \delta^2\right) + \frac{2NU}{\sqrt{\pi}\gamma^3} - \frac{4}{\gamma}\frac{\partial V}{\partial \gamma}, \tag{4.17}$$

$$\dot{\gamma} = 2J\cos(k)e^{-\eta}\gamma\delta, \tag{4.18}$$

with $\eta = \left(\frac{1}{2\gamma^2} - \frac{\delta^2\gamma^2}{8}\right)$, $V = \sqrt{2/\gamma^2\pi}\int dx V(x)\exp[-2(x-\xi)^2/\gamma^2]$ and the time scaled as $t \to tE_r/\hbar$. Notice that the variable k is just the average quasimomentum of the wave packet. We can also associate an inverse effective mass given by $m^{*-1} = 2J\cos(k)e^{-\eta}$.

We numerically integrated the equations of motion assuming no other external trapping potential besides the lattice, $V = 0$. In this case the Hamiltonian is invariant under translations and we expect conservation of the quasimomentum. This is seen in the above equations, because if $V = 0$ then $dk/dt = 0$. The parameters were chosen according to the experiment: $\gamma(0) = 10$, $\delta(0) = 0$ and $NU = 2E_R$. The bandwidth J, was found using Mathieu functions assuming a $3E_R$ lattice. We plot Fig. 4.4 v_{atom} vs v_{latt} evaluated at $t = 50$. The curve found is plotted in

When mean field effects are included, the dynamics of the system becomes very rich. Depending on the the initial quasimomentum and width of the packet,

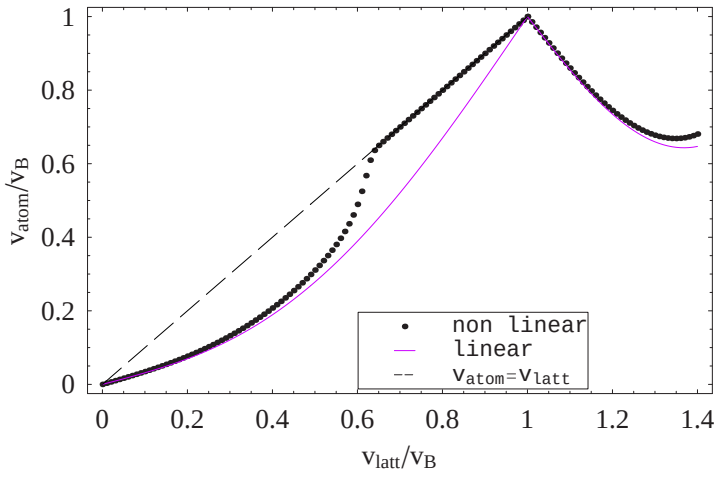

Figure 4.4: Velocity of the atoms predicted by the variational model in the case when interactions are taken into account (dotted line). The single particle case is shown in red. The parameters used were $\gamma(0) = 10, \delta(0) = 0$ and $NU = 2E_R$.

a variety of dynamical regimes can be observed. Physically, the different regimes can be understood by realizing that the nonlinear term makes the effective mass time dependent. The effective mass, $m^* = e^{\eta}/(2J\cos k)$, not only depends on the initial quasimomentum but also on the width of the wave packet, and when the nonlinearity is present η is no longer constant. The different dynamical behaviors include effects such as self-trapping, diffusion, and for special cases solitons or breathers [84].

The *self-focusing* is a genuine nonlinear effect, characterized by a diverging effective mass. In particular the self-trapped wave packet cannot translate along the array. The final value for γ_f, for a packet in the self-focusing regime predicted by the variational model is,

$$\gamma_f = \frac{UN\gamma_o}{UN - 4J\sqrt{\pi}cos(k)\gamma_o}, \tag{4.19}$$

With $\gamma_o = \gamma(0)$ the initial width of the packet, which is assumed big compared to one.

The *diffusive regime*, on the other hand, is characterized by the unbounded growth of the width of the packet. This is the behavior expected in regular linear quantum mechanics. The model predicts that the transition between the two regimes occurs, again assuming $\gamma_o \gg 1$, at

$$\begin{aligned} (UN)_c &= 4J\sqrt{\pi}cos(k)\gamma_o \quad |k| < \pi/2 \\ (UN)_c &= \frac{2J\sqrt{\pi}|cos(k)|}{\gamma_o} \quad |k| > \pi/2 \end{aligned} \tag{4.20}$$

Using a potential depth of $3E_R$ and $\gamma_o = 10$, the predicted dynamical phase diagram as a function of UN *vs* v_{lat} is shown in Fig. 4.5. It can be seen that for $UN = 2E_R$, the self-focusing regime is expected for lattice velocities greater than $v_{lat} = 0.4v_B$. At $v_{lat} = 0.5v_B$ the noninteracting effective mass becomes negative.

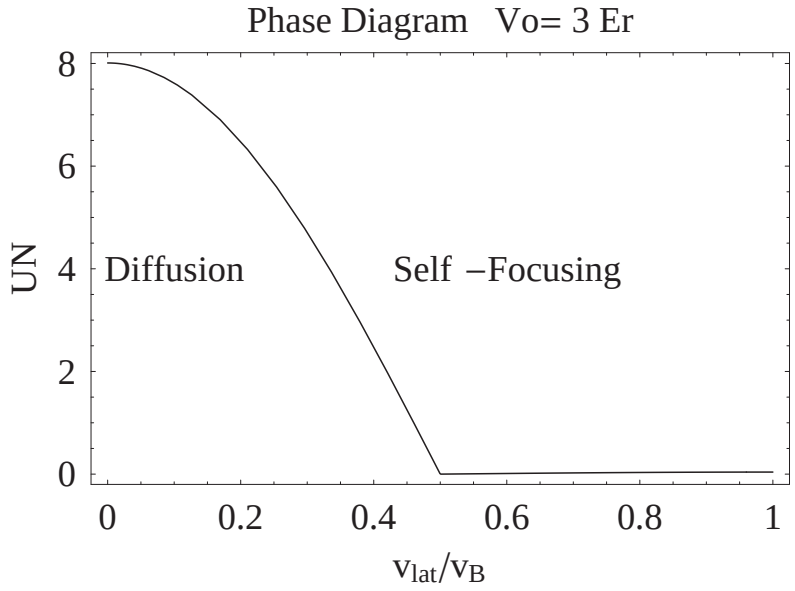

Figure 4.5: Phase diagram UN vs v_{latt} for $V_o = 3E_r$ and $\gamma_o = 10$.

Consistently, in Fig. 4.4 we see that for lattice velocities approximately greater than $v_{lat} = 0.4v_B$, the velocity of the interacting system becomes greater than the noninteracting one, and approximately at $v_{lat} = 0.7v_B$ the velocity of the atoms is just the velocity of the lattice so, the atoms stop moving in the lattice frame. This regime is a self-trapping regime and nonlinear effects tend to localize the atoms in the lattice frame. On the other hand, for $v_{latt} \lesssim 0.4v_B$ the dynamics of the system is similar to the non interacting case. To appreciate the different behaviors exhibited by the system below and above $v_B/2$ we plot in Figs. 4.6 and 4.7, the evolution of the wave packet, for two different initial velocities. For $v_{latt} = -0.7v_B$ the wave packet localizes, whereas for $v_{latt} = -0.15v_B$ the wave packet diffuses.

4.3 Dynamics of a period-three pattern-loaded Bose-Einstein condensate in an optical lattice

In this section we discuss the dynamics of a Bose-Einstein condensate initially loaded into every third site of a one dimensional optical lattice, motivated by the recent experimental realization of this system by the NIST group [33]. A condensate loaded in this way is not an eigenstate of the final period-a lattice, and the condensate will continue to evolve in the final system. Outside the strongly

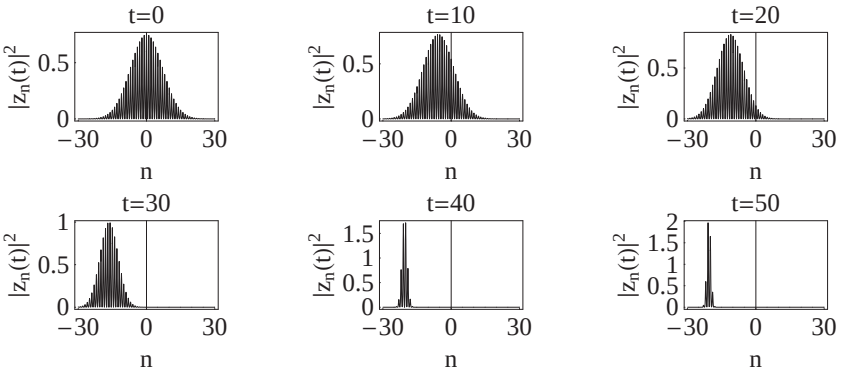

Figure 4.6: Localization of the wave packet in the self-focusing regime $v_{latt} = -0.7v_B$. Notice the change in the vertical scale in the last row

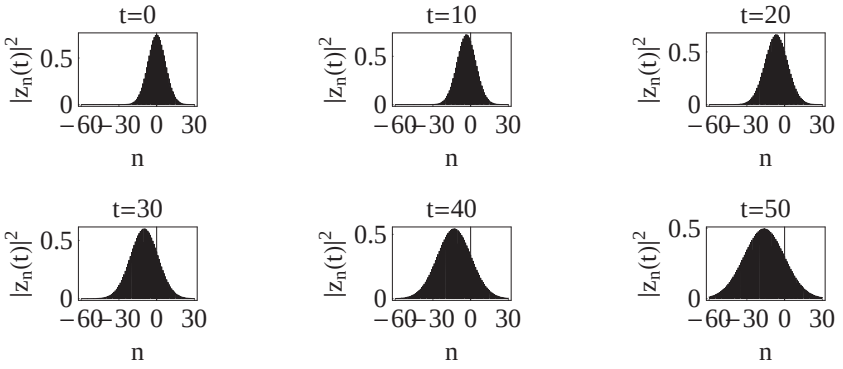

Figure 4.7: Evolution of the wave packet in the diffusive regime $v_{latt} = -0.15v_B$.

correlated regime, the GPE equation is expected to give a good description of the condensate dynamics. In our system we assume the lattice is sufficiently deep that a tight-binding description is applicable, and the DNLSE is valid. For the periodic initial condition of equal wavefunction amplitude at every third site and zero at all others, symmetry arguments can be used to reduce the wavefunction evolution to a two mode problem (analogous to a double well system with an energy offset) for which an analytic solution of the dynamics can be given. We show that for large ratios of the interatomic interaction strength to tunneling energy the condensate evolves with self-maintained population imbalance, whereby the condensate population tends to remain localized in the initially occupied lattice sites. A similar phenomenon has been studied in double-well systems [87, 88, 89, 90, 91]. We show that the momentum distribution of an interacting condensate changes in time in a manner which can be related to the spatial tunneling of condensate, and would be a suitable experimental observable.

Under the influence of an external force a Bloch state will exhibit Bloch oscillations, as described in chapter 2. To illustrate how a linear potential affects the motion of a pattern loaded condensate we find analytic solutions for the noninteracting case with periodic initial conditions and show how the dynamics for this system can be interpreted in terms of the interference of three Bloch states of the lowest band undergoing Bloch in unison. We present numerical results for more general (non-periodic) initial conditions and consider characteristic properties of the momentum distribution.

4.3.1 Experiment

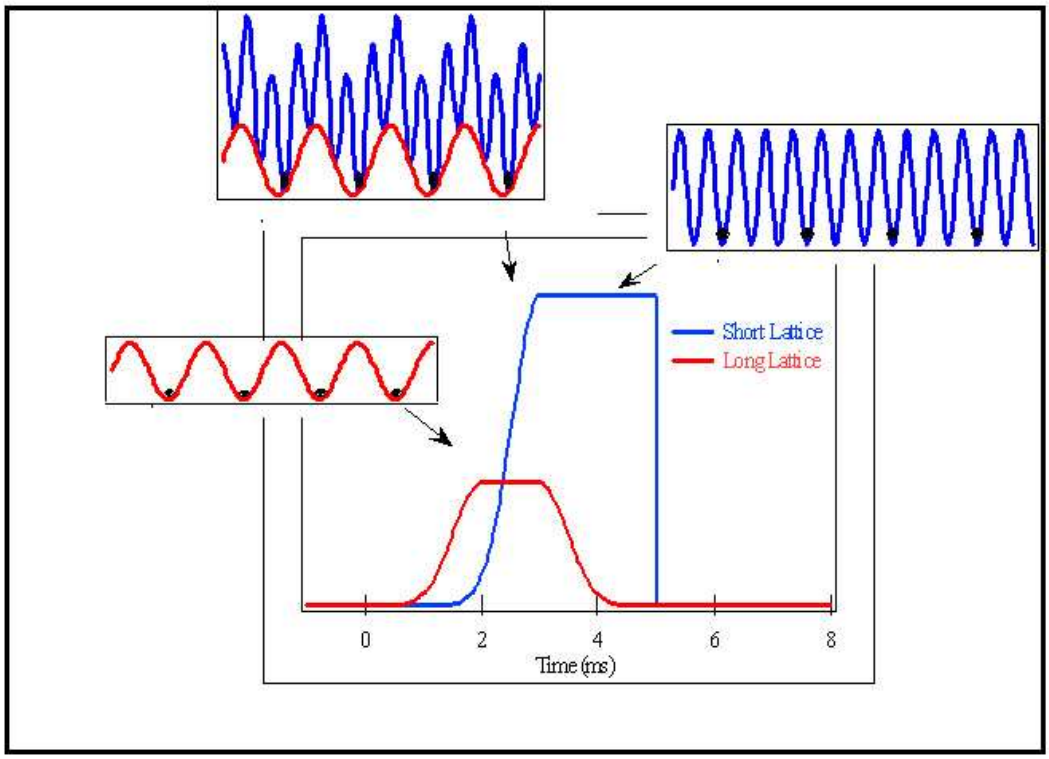

Figure 4.8: Patterned loading experiment.

In the experiment, a combination of two independently controlled lattices was used to load the condensate into every third site of a single lattice. Briefly the procedure consists, as shown in Fig. 4.8, of loading a condensate into the ground band of lattice with periodicity $3a$, so that the condensate is well localized in the potential minima of this lattice. A second lattice of periodicity a which is parallel to the first lattice, is then ramped up so that the superimposed light potentials form a *super-lattice* of period $3a$. For the ideal case both lattice potentials are inphase, and the addition of the second lattice will not shift the locations of the

potential minima from those of the first lattice alone, and the condensate will remain localized at these positions. Finally, by removing the first period-3a lattice on a time scale long compared to band excitations, but short compared to the characteristic time of transport within the lattice, the condensate will be left in every third site of the period-a lattice.

4.3.2 Case of no external potential

The major interest of this section is in the tunneling properties of the condensate in the lattice, and in the noninteracting case the time scale for tunneling is determined by the hopping matrix element J. For this reason it is convenient to define a new dimensionless scale of time $\tau = Jt/\hbar$, and dimensionless energy $E_n = V_n/J$ and coupling constant $\Lambda = NU/J$. In terms of these new variables the tight-binding evolution equation (4.6) takes the form

$$i\frac{\partial z_n}{\partial \tau} = -(z_{n-1} + z_{n+1}) + (E_n + \Lambda|z_n|^2)z_n, \tag{4.21}$$

- The case of periodic initial conditions: reduction to a two mode system

  We treat first a model case in which no external potential is present, ($E_n = 0$), and in which the initial occupancies of each third site are the same, and in which the condensate initially has a uniform phase. At $\tau = 0$, the amplitudes $z_n(\tau)$ are given by

$$z_{3n}(0) = \sqrt{\rho}, \tag{4.22}$$
$$z_{3n+1}(0) = z_{3n+2}(0) = 0, \tag{4.23}$$

  where $\rho = 3/M$ with M the total number of lattice sites. $N\rho$ represents the initial number of atoms per occupied site. This initial condition is homogeneous in the sense that each occupied site has the same amplitude and phase along the length of the lattice. For an infinite lattice, or one with periodic boundary conditions, the amplitudes for all initially occupied sites (z_{3n}) evolve identically in time, and the amplitudes for the initially unoccupied sites satisfy $z_{3n+1}(\tau) = z_{3n+2}(\tau)$ for all τ and all n. This allows us to reduce the full set of equations (4.21) to a set of two coupled equations

$$i\frac{\partial z_0}{\partial \tau} = -2z_1 + \Lambda|z_0|^2 z_0, \tag{4.24}$$
$$i\frac{\partial z_1}{\partial \tau} = -(z_1 + z_0) + \Lambda|z_1|^2 z_1, \tag{4.25}$$

  where $z_{3n} \equiv z_0$ and $z_{3n+1} = z_{3n+2} \equiv z_1$ for all n. The normalization condition is

$$|z_0|^2 + 2|z_1|^2 = \rho. \tag{4.26}$$

The Hamiltonian function, H, of this system is (from Eq. 4.8)

$$\begin{aligned} H &= \frac{J}{\rho}\Big(-2(z_0^* z_1 + z_0 z_1^*) - 2|z_1|^2 + \frac{\Lambda}{2}|z_0|^4 \\ &\quad +\Lambda|z_1|^4\Big) \\ &= \frac{J\Lambda\rho}{2}. \end{aligned} \tag{4.27}$$

By writing $z_0{=}\psi_0\sqrt{\rho}$ and $z_1{=}\psi_1\sqrt{\rho/2}$, we can transform Eqs. (4.24)-(4.25) to the form

$$i\frac{\partial}{\partial\tau}\begin{pmatrix}\psi_0\\ \psi_1\end{pmatrix} = \begin{pmatrix}\gamma|\psi_0|^2 & -\sqrt{2}\\ -\sqrt{2} & \gamma\frac{|\psi_1|^2}{\sqrt{2}} - 1\end{pmatrix}\begin{pmatrix}\psi_0\\ \psi_1\end{pmatrix}, \tag{4.28}$$

where $\gamma = \Lambda\rho$ is the ratio of on-site repulsion to tunneling energies, and the normalization condition (4.26) is now $|\psi_0|^2 + |\psi_1|^2 = 1$. The factor of $\sqrt{2}$ difference in the definition of ψ_0 and ψ_1 arises because ψ_1 represents the amplitude of the two initially unoccupied sites. With this factor incorporated, the matrix appearing in Eq. (4.28) is explicitly Hermitian. We note that this equation of motion is identical to that for a condensate in a double well trap in the two mode approximation [92, 93].

We note in passing that a similar reduction, to a system of $[m/2]+1$ equations, exists for lattice systems that are loaded such that only every m-th site is initially occupied.

- Solution of the equations of motion

  It is convenient to write the lattice site amplitudes appearing in Eqs. (4.24) and (4.25) as $z_0{=}fe^{i\theta_0}\sqrt{\rho}$ and $z_1{=}\,ge^{i\theta_1}\sqrt{\rho}$, where f, g, and θ are real. By introducing the phase difference $\phi = \theta_0 - \theta_1$, Eqs. (4.24), (4.25) and (4.27) can be recast as

$$\dot{f} = 2g\sin\phi, \tag{4.29}$$

$$\dot{g} = -f\sin\phi, \tag{4.30}$$

$$\frac{\gamma}{2} = -4fg\cos\phi + \frac{\gamma}{2}\left(f^4 + 2g^4\right) - 2g^2, \tag{4.31}$$

  The analytic solutions of Eqs. (4.29)-(4.31), found using a procedure similar to that presented by Raghavan *et al.* [87], can be expressed in terms of Weierstrassian elliptic functions $\wp(\tau; g_2, g_3)$ [69]. The analytic solutions are

$$f(\tau) = \sqrt{1 - \frac{24}{12\wp(\tau; g_2, g_3) + (9 + 2\gamma + \gamma^2)}}, \tag{4.32}$$

$$g(\tau) = \sqrt{\frac{1 - f(t)^2}{2}}, \tag{4.33}$$

where the parameters g_2 and g_3 are given by

$$g_2 = \left(81 - 14\gamma^2 + 4\gamma^3 + \gamma^4\right)/12, \tag{4.34}$$

$$g_3 = \left(729 + 243\gamma^2 - 46\gamma^3 - 15\gamma^4 + \gamma^6\right)/216. \tag{4.35}$$

The solutions $f(\tau)$ and $g(\tau)$ are oscillatory functions whose amplitudes and common period, $T(\gamma)$, are determined by the parameter γ (see Figs. 4.9 and 4.10). It is useful to qualitatively divide this behavior into two regimes, separated by $\gamma = 2$. Analysis of Eqs. (4.29) - (4.31) shows that $f(\tau_0) = g(\tau_0)$ for some value of τ_0 when $\gamma \leq 2$, and for $\gamma > 2$, $f(\tau) > g(\tau)$ for all τ.

Tunneling dominated regime

For $\gamma \lesssim 2$, we find that the oscillation period is essentially constant (see Fig. (4.9).

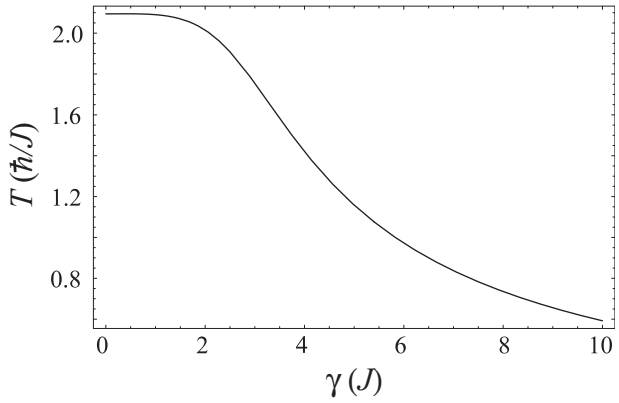

Figure 4.9: Oscillation period (in units of $\hbar/J$) as a function of the interaction strength γ.

In this case the role of interactions is relatively small, and the behavior can be approximately understood by taking $\gamma = 0$, in which case the matrix of Eq. (4.28) is constant in time. The equations of motion in this case are equivalent to those of a two-state Rabi problem [94], where the two levels are coupled by a Rabi frequency of strength $\sqrt{2}$, which is detuned from resonance by -1. This system will undergo Rabi oscillations whereby atoms periodically tunnel from the initially occupied site into the two neighboring sites. Because the coupling is detuned from resonance the transfer of populations between wells is incomplete, with $|\psi_1|^2$ attaining a maximum value of 8/9. The Rabi model predicts that the cycling frequency between the levels is equal to the difference between the eigenvalues of the matrix of matrix of Eq. (4.28), which gives the period of oscillation as $T_{\text{Rabi}} = 2\pi/3$ in units of $\hbar/J$ (see Fig. 4.9).

Interaction dominated regime

The effect of interactions on the mean-field dynamics is to cause the energies of the initially occupied sites to shift relative to those of the unoccupied sites. As γ increases and this energy shift increases relative to the strength of coupling between sites, the tunneling between sites occurs at a higher frequency, but with reduced amplitude. The population of the initially occupied sites becomes self trapped by the purely repulsive pair interaction, which in the context of a double well system has been called "macroscopic quantum self trapping" [93]. This is demonstrated quantitatively in Fig. 4.10 where we plot the minimum value of f^2 occurring during the oscillation as a function of γ. In contrast to the tunneling dominated regime, where tunneling periodically populates all sites equally, the condensate tends to be localized on the initially occupied sites in the interaction-dominated regime.

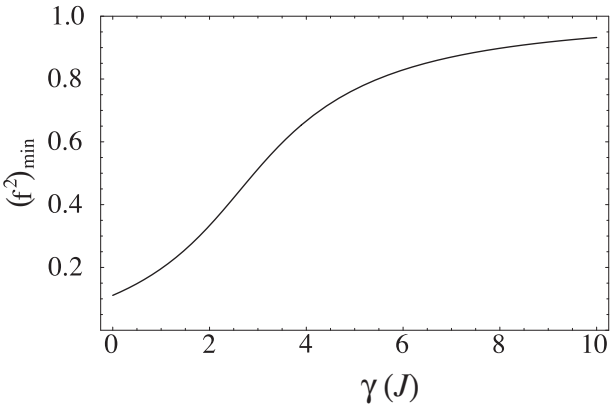

Figure 4.10: Minimum value of f^2 during an oscillation period as a function of γ. As γ increases the population imbalance between wells increases (see text).

- Momentum space dynamics

  Typically the spacing between individual wells in an optical lattice is too small to resolve the localized density distributions of atoms in neighboring sites using standard imaging techniques.

  The momentum distribution is a more convenient observable which approximately corresponds to the expanded spatial distribution of the released condensate. Here we calculate the momentum dynamics of the condensate loaded into every third site of an optical lattice, and show how this relates to the evolution of the spatial amplitudes given in Eqs. (4.32) and (4.33).

  In the tight-binding approximation the condensate order parameter $\varphi(x,\tau)$ (4.4) is expressed as a sum over the lattice sites . Because of the periodicity of the system, the momentum space wavefunction, which we denote as $\tilde{\varphi}(k,\tau)$, is expressible as the Fourier series

$$\tilde{\varphi}(k,\tau) = \sum_m z_m(\tau) e^{-ikam} \chi(k), \tag{4.36}$$

where

$$\chi(k) = \frac{1}{\sqrt{2\pi}} \int_{-\infty}^{\infty} e^{-ikx} w_0(x) dx. \tag{4.37}$$

To compute the momentum distribution, we invoke the identity $\sum_{n=0}^{M-1} e^{ikna} = M\delta_{k,2\pi m/a}$, where M is the number of lattice sites, and m an integer. Since there are only two independent amplitudes in the set $\{z_m\}$, we find that

$$\begin{aligned} \tilde{\varphi}(k,\tau) &= \sqrt{3/\rho} c_m(\tau) \chi_m \delta_{k,qm/3}, \\ \chi_m &= \chi(qm/3), \\ c_m(\tau) &= \sqrt{\frac{1}{3\rho}} \left(z_0 + z_1 e^{-iqm/3} + z_2 e^{-i2qm/3} \right), \end{aligned} \tag{4.38}$$

where q is the reciprocal lattice vector $q = 2\pi/a$. The momentum distribution of the system has very sharp peaks of relative amplitude $|c_m|^2$ at momentum $k = qm/3$, arising from the 3-lattice site spatial periodicity of the condensate wavefunction. In addition, χ_m describes a slowly varying envelope determined by the localization of the Wannier states at each lattice site.

Using the analytic solutions for f and g, and Eq. (4.31), we obtain only two independent Fourier amplitudes

$$|c_{3n}(\tau)|^2 = \frac{1}{3}\left(1 + \frac{\gamma}{4}(3f^2+1)(f^2-1)\right), \tag{4.39}$$

$$|c_{3n+1}(\tau)|^2 = \frac{1}{3}\left(1 - \frac{\gamma}{8}(3f^2+1)(f^2-1)\right) \tag{4.40}$$

$$= |c_{3n+2}(\tau)|^2. \tag{4.41}$$

In the reduced zone scheme, where we only consider momenta in the range $k \in [-q/2, q/2]$, the momentum wavefunction then consists of three peaks corresponding to Bloch states of quasimomenta $0, \pm q/3$. The identical behavior of $|c_{3n+1}|^2$ and $|c_{3n+2}|^2$ means that the $\pm q/3$ peaks always have the same intensity. If interactions between the atoms are ignored (i.e. $\gamma = 0$), the momentum components are constant in time (see Eqs. (4.39) and (4.40)), even though tunneling occurs between the lattice sites. However, when interactions are considered, the momentum intensities explicitly depend on the occupations of each site and will vary in time when tunneling occurs. The magnitude of the time variation of the $|c_n|^2$ is proportional to γ, but will reduce for sufficiently large values of γ, where the self-trapping effect causes the tunneling between lattice sites to stop (i.e. $f^2 \approx 1$ at all times). In Fig. 4.11 we show the maximum contrast between the intensity of the Fourier peaks, defined as $\Delta_{\max} \equiv (|c_1|^2 - |c_0|^2)_{\max}$, where the value is maximized by evaluating the $|c_n|^2$ at the time when f takes its minimum value (we note that $f(\tau)$ is given by Eq. (4.32)). We note that the maximum contrast occurs for $\gamma \approx 3.9$; in this case, the zero quasimomentum component $c_0(\tau)$

vanishes once during each period of oscillation $T(\gamma)$. For values of γ greater than 3.9 the contrast between the intensities starts to decrease due to the reduction in tunneling caused by the nonlinearity- induced self-trapping.

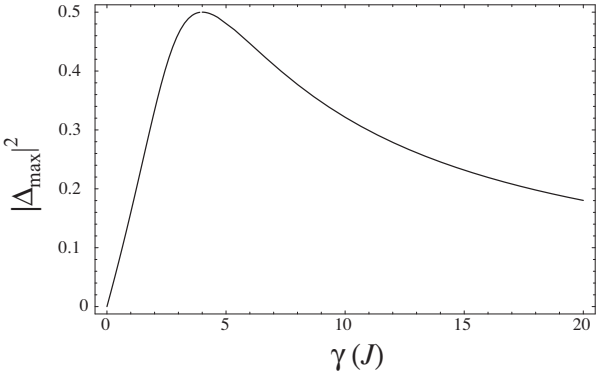

Figure 4.11: Maximum contrast of the Fourier components as a function of γ. The maximum contrast is defined as $\Delta_{\max} \equiv (|c_1|^2 - |c_0|^2)_{\max}$ with the maximum value occurring when f^2 is at its minima.

- Application to an inhomogeneous condensate

  Here we wish to consider the dynamics for an inhomogeneous condensate, applicable to a condensate initially prepared in a harmonic trap. For the pattern loaded condensate, we use inhomogeneous to refer to the overall spatial envelope of the period three initial condition. The previous homogeneous theory we have presented is expected to accurately describe inhomogeneous cases when the initial pattern of population in every third site extends over many lattice sites i.e. $M \gg 1$ so that mean-field energy associated with each triplet of sites $U(n) = \frac{\Lambda}{2}\sum_{i=1}^{3}|z_{3n+i}|^4$ varies slowly across the system. Taking a particular example we choose a Gaussian envelope to the periodic arrangement of atoms into every third site, so that the initial state is

$$z_{3n+1}(0) = z_{3n+2}(0) = 0, \tag{4.42}$$

$$z_{3n}(0) = 3\left[\frac{2}{\pi M^2}\right]^{1/4}\exp(-(9n/M)^2). \tag{4.43}$$

  For the simulations shown here, the parameters used were $N = 10^5$, $M = 76$, $U = 2.11 \times 10^{-5} E_{\rm R}$ and $J = 0.075\ E_{\rm R}$; these correspond to a condensate of 10^5 atoms of ^{87}Rb produced in a magnetic trap with axial and radial frequencies of 9 and 12 Hz respectively, and loaded into a lattice with a depth of $4.5E_{\rm R}$, with $E_{\rm R} = 2.2$kHz. These parameters are typical of the experimental regime, but also lie in a range in which the homogeneous model is expected to give a fair description. The total number of occupied wells and the strength of the on site interatomic interaction were calculated by preserving the value

of the chemical potential of the system upon reduction to one spatial dimension and by assuming that each of the localized orbitals in the tight-binding description are Gaussian. The hopping rate J was estimated by using Mathieu functions. In Fig. 4.12 we show the evolution of the population of the central wells (normalized to one) compared with the homogeneous model with γ taken to be the local mean field energy $\gamma_{\text{eff}} = \Lambda\sqrt{\frac{2}{\pi}}\,(9/M)$.

Fig. 4.12 shows the results of numerical integration of the equations of motion and the approximate analytical solution given by the quasi-homogeneous model described above. We see that the numerical and analytical results agree well at short times, but differ more as time progresses due to the different mean-field seen by different wells.

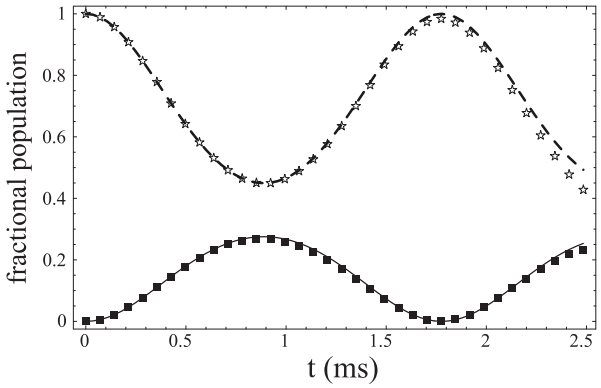

Figure 4.12: Comparison between the population evolution of the central three wells for the inhomogeneous condensate and the homogeneous model. Inhomogeneous condensate: stars for the initially populated well and boxes for the initially empty wells. Homogeneous model: dashed line represents the initially populated wells, and the solid line represented the initially unpopulated wells. We used γ_{eff} as the local mean field energy (see text). The parameters used for the simulation were $J = 0.075E_{\text{R}}$ and $\gamma_{\text{eff}} = 2.64$.

To understand the disagreement as time evolves, we show in Fig. 4.13 the numerical Fourier spectrum for the inhomogeneous case evaluated at several different times. The variation of the intensities of the peaks, which, as shown below, is related to the spatial tunneling between lattice sites in the presence of the mean field, can be seen in the plot. Initially all occupied sites are in phase and the three distinctive momentum peaks have a narrow width determined by the intrinsic momentum uncertainty of the condensate envelope. That is the reason why the homogeneous model fits very well. However, as time progresses the mean field variation across the lattice causes the tunneling rates to vary with position and leads to momentum peak broadening. This effect eventually causes the homogeneous model to become an inaccurate description of the inhomogeneous system.

We note that momentum space signature for spatially tunneling in the in-

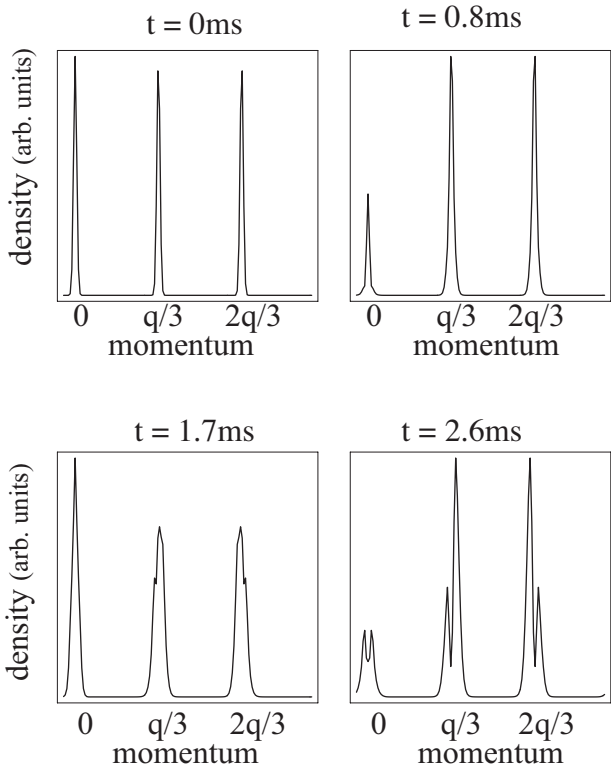

Figure 4.13: Momentum distribution of the inhomogeneous condensate evaluated at various times for the same parameters as used in Fig.4.12.

teracting system is still present in the inhomogeneous case. This is shown in Fig. 4.14, where we plot the evolution of the quantities $|c_{3n}(\tau)|^2$, $|c_{3n+1}(\tau)|^2$, $|c_{3n+2}(\tau)|^2$ (calculated from the numerical simulation by partitioning the numerical Fourier spectrum in three equal non overlapping sections, each centered around the respective peak and adding the square of the norm of the Fourier components within each section) *vs.* the ones calculated with the homogeneous model, but using an averaged value $\gamma_{\rm ave} \equiv \Lambda \sum_n |z_n|^4$ instead of $\gamma = \Lambda\rho$. It can be observed that the predictions of the simple model are in very good agreement with the numerical results when the three peaks of the spectrum are well defined. For longer times, the width of the Fourier peaks increases, until a point when they split. At this point the quantities $|c_{3n}(\tau)|^2$, $|c_{3n+1}(\tau)|^2$, $|c_{3n+2}(\tau)|^2$ are not meaningful anymore. Because the parameters used for the numerical calculations were chosen to be experimentally achievable, and as shown in the plots the model predictions are fair at least for one period of oscillation, we conclude that the Fourier distribution can be used as a signature of the mean-field quantum tunneling inhibition.

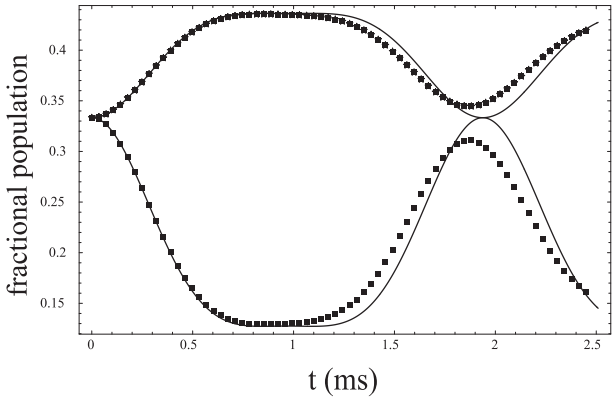

Figure 4.14: Evolution of momentum peak populations. Upper curves: population of the $q = \pm 2\pi/3$ momentum states. Lower curves: population of the $q = 0$ momentum state. Inhomogeneous condensate (dotted), homogeneous result (solid line), where the comparison is made by replacing γ by an average mean field energy $\gamma_{\rm ave} \equiv \Lambda \sum_n |z_n|^4 = 1.85$. Parameters are the same as in Fig. 4.12.

4.3.3 Dynamics with a constant external force

- Homogeneous three state model

  In this section we consider the dynamics of a periodically loaded condensate in the presence of a linear external potential, corresponding to a uniform force parallel to the lattice. In what follows we assume that the force is sufficiently weak that band excitations due to Landau-Zener tunneling are negligible, so that a tight-binding picture of the lowest band is sufficient to describe the dynamics. In this case the evolution equation differs from what we considered in the previous section by the term E_n in Eq. (4.21) taking the form $E_n = n\xi$, where ξ is the potential difference between lattice sites (in units of the hopping matrix element J). Taking the initial conditions (4.22)-(4.23), and transforming the Wannier amplitudes as $z_{3n+j}(\tau) = \tilde{\Psi}_{3n+j}(\tau)e^{-i3n\xi\tau}$ ($j = 0, 1, 2$), we obtain the evolution equations

$$\begin{aligned} i\frac{\partial\tilde{\Psi}_{3n}}{\partial\tau} &= -(\tilde{\Psi}_{3n-1}e^{i3\xi\tau} + \tilde{\Psi}_{3n+1}) \\ &\quad +\Lambda|\tilde{\Psi}_{3n}|^2\tilde{\Psi}_{3n}, \qquad (4.44) \\ i\frac{\partial\tilde{\Psi}_{3n+1}}{\partial\tau} &= -(\tilde{\Psi}_{3n+2} + \tilde{\Psi}_{3n}) + \xi\tilde{\Psi}_{3n+1} \\ &\quad +\Lambda|\tilde{\Psi}_{3n+1}|^2\tilde{\Psi}_{3n+1}, \qquad (4.45) \\ i\frac{\partial\tilde{\Psi}_{3n+2}}{\partial\tau} &= -(\tilde{\Psi}_{3n+1} + \tilde{\Psi}_{3n+3}e^{-i3\xi\tau}) + 2\xi\tilde{\Psi}_{3n+1} \\ &\quad +\Lambda|\tilde{\Psi}_{3n+1}|^2\tilde{\Psi}_{3n+1}. \qquad (4.46) \end{aligned}$$

  Assuming periodic boundary conditions, the periodicity of the initial conditions and equations of evolution allow considerable simplification from the

full set of M coupled equations. In particular, these assumptions mean that every third Wannier amplitude evolves identically (i.e. $\tilde{\Psi}_n = \tilde{\Psi}_{n+3}$) and so the evolution of the system can hence be reduced to the three independent equations

$$i\frac{\partial\tilde{\Psi}_0}{\partial\tau} = -(\tilde{\Psi}_2 e^{i3\xi\tau} + \tilde{\Psi}_1) + \Lambda|\tilde{\Psi}_0|^2\tilde{\Psi}_0, \tag{4.47}$$

$$i\frac{\partial\tilde{\Psi}_1}{\partial\tau} = -(\tilde{\Psi}_2 + \tilde{\Psi}_0) + \xi\tilde{\Psi}_1 + \Lambda|\tilde{\Psi}_1|^2\tilde{\Psi}_1, \tag{4.48}$$

$$i\frac{\partial\tilde{\Psi}_2}{\partial\tau} = -(\tilde{\Psi}_1 + \tilde{\Psi}_0 e^{-i3\xi\tau}) + 2\xi\tilde{\Psi}_2 + \Lambda|\tilde{\Psi}_2|^2\tilde{\Psi}_2, \tag{4.49}$$

where the new amplitudes map onto the original set according to $\tilde{\Psi}_0 \leftrightarrow \{\tilde{\Psi}_{3n}\}$, $\tilde{\Psi}_1 \leftrightarrow \{\tilde{\Psi}_{3n+1}\}$, and $\tilde{\Psi}_2 \leftrightarrow \{\tilde{\Psi}_{3n+2}\}$, and obey the normalization condition

$$\sum_{j=0}^{2}|\tilde{\Psi}_j|^2 = \frac{3}{M}. \tag{4.50}$$

The equations of motion (4.47)-(4.49) are more difficult to treat analytically than the case considered in the last section due to the presence of a linear potential. In this section we derive an analytic solution for a noninteracting condensate (i.e. Λ=0), which provides valuable insight into the complicated tunneling dynamics the system exhibits in the absence of nonlinearity, yet should furnish a good description for dilute condensates satisfying $\gamma \ll 1$. For the nonlinear regime we present numerical results to illustrate the typical behavior.

- Analytic solution for linear dynamics

  Defining the vector $\mathbf{x}(t) = (\tilde{\Psi}_0(\tau), \tilde{\Psi}_1(\tau), \tilde{\Psi}_2(\tau))$, and using the transformation $\mathbf{y}(\tau) = P(\tau)\mathbf{x}(\tau)$, where $P(\tau)$ is the unitary matrix

$$P(\tau) = \begin{pmatrix} 1 & 1 & 1 \\ e^{-i\xi\tau} & e^{-i(\xi\tau-\frac{2\pi}{3})} & e^{-i(\xi\tau+\frac{2\pi}{3})} \\ e^{-i2\xi\tau} & e^{-i(2\xi\tau+\frac{2\pi}{3})} & e^{-i(2\xi\tau-\frac{2\pi}{3})} \end{pmatrix}, \tag{4.51}$$

  the linear version of Eqs. (4.47)-(4.49) can be decoupled, directly yielding the solutions

$$\tilde{\Psi}_n(\tau) = \frac{e^{-in\xi\tau}}{\sqrt{3M}}\Big(e^{-i\Delta_0(\tau)} + e^{i\left(\frac{2n\pi}{3}-\Delta_1(\tau)\right)} + e^{-i\left(\frac{2n\pi}{3}+\Delta_2(\tau)\right)}\Big), \tag{4.52}$$

where we have defined the phase terms

$$\Delta_n(\tau) = -\frac{2}{\xi}\left[\sin(\xi\tau - \frac{2n\pi}{3}) + \sin(\frac{2n\pi}{3})\right], \tag{4.53}$$

for $n = 0, 1, 2$.

These solutions for the spatial amplitudes $\tilde{\Psi}_i(\tau)$ can be most easily understood by considering a Bloch state decomposition of the condensate wavefunction. The nature of our system allows us to construct an analytic form for the initial wavefunction. Because the system has a three lattice site period and is assumed to be in the lowest band, the wavefunction can be expressed as a superposition of three Bloch waves (of the lowest band) which are symmetrically spaced in quasimomentum. Assuming the condensate initially has a total crystal momentum of zero, at this time the wavefunction must be of the form

$$\varphi(x, 0) = \alpha_0\phi_0(x) + \alpha_+\phi_{q/3}(x) + \alpha_-\phi_{-q/3}(x), \tag{4.54}$$

where $\phi_k(x)$ is a Bloch state with quasimomentum k, and the α are complex constants determined by the lattice depth, with $|\alpha_+| = |\alpha_-|$.

The action of an external force on a Bloch state causes it to linearly change its quasimomentum in time according to

$$k(\tau) = -\frac{\xi}{a}\tau + k(0). \tag{4.55}$$

The periodicity of the Bloch dispersion relation in k, and hence of the group velocity of the Bloch wave, gives rise to the well-known phenomenon of Bloch oscillations (see chapter 2). For the case we are considering here, the system consists of three Bloch states whose quasimomenta will translate in unison under the action of the external force. During this evolution each state accumulates phase at a rate determined by the instantaneous Bloch energy, i.e.

$$\Delta_n(\tau) = \int_0^\tau E(k_n(s))ds, \tag{4.56}$$

where $k_n(\tau) = -\xi\tau/a + k_n(0)$ is the quasimomentum of Bloch state n at time t. In the tight-binding approximation the dispersion relation for the Bloch states has the analytic form

$$E(k) = -2\cos(ka), \tag{4.57}$$

for which $\Delta_n(\tau)$ can be evaluated, and yields the results given in Eqs. (4.53)). The wavefunction evolution in the Bloch basis is

$$\begin{aligned}\varphi(x, \tau) = {} & \alpha_0\phi_{-\frac{\xi}{a}t}(x)e^{-i\Delta_0(\tau)} + \alpha_+\phi_{-\frac{\xi}{a}t+\frac{q}{3}}(x)e^{-i\Delta_1(\tau)} \\ & +\alpha_-\phi_{-\frac{\xi}{a}t-\frac{q}{3}}(x)e^{-i\Delta_2(\tau)}.\end{aligned} \tag{4.58}$$

From this solution we can obtain solutions for the evolution of the spatial amplitudes Eqs. (4.52). To do this we expand the Bloch states in terms of Wannier functions according to, $\phi_k(x) = \sum_n e^{ikna} w_0(x - na)$ (see chapter 2) and make use of Eq. (4.5). Note: we take all $\alpha = \frac{\rho}{3}$ as determined by the initial conditions, Eqs.(4.22) and (4.23).

Bloch Oscillations

The evolution of the spatial amplitudes, and in particular the population in each well is then determined by the interference of the Bloch phases Δ_n. These functions are all periodic in time with period $\tau_B = 2\pi/\xi$ (in units of $\tau = tJ/\hbar$). This is the normal Bloch oscillation period, and gives the time scale over which the quasimomenta of the Bloch states increases by exactly one reciprocal lattice vector.

Small ξ solution - Non classical transport

To understand the dynamics, we first start by considering the case when ξ is small. For this case, the population in the wells is given by

$$|\tilde{\Psi}_0(\tau)|^2 = \frac{1}{3M}\Big(5 + 4\cos(3\tau) + \xi^2 h(\tau)\Big) \tag{4.59}$$

$$|\tilde{\Psi}_1(\tau)|^2 = \frac{1}{3M}\Big((2 + 3\xi)[1 - \cos(3\tau) - \frac{\xi^2}{2}h(\tau)]\Big) \tag{4.60}$$

$$|\tilde{\Psi}_2(\tau)|^2 = \frac{1}{3M}\Big((2 - 3\xi)[1 - \cos(3\tau) - \frac{\xi^2}{2}h(\tau)]\Big) \tag{4.61}$$

where

$$h(\tau) = \frac{\tau^3}{2}\left(6\tau + 3\tau\cos(3\tau) - 4\sin(3\tau)\right). \tag{4.62}$$

The above solution shows that when the force is applied, the degeneracy in the population of the wells represented by $\tilde{\Psi}_1$ and $\tilde{\Psi}_2$ is lifted. For $\xi > 0$, atoms in $\tilde{\Psi}_0$ start to tunnel to $\tilde{\Psi}_1$ more rapidly than to $\tilde{\Psi}_2$. This should be compared with the results in the absence of the force, where $\tilde{\Psi}_1$ and $\tilde{\Psi}_2$ behave identically. Thus, in this weak limit, the effect of a linear potential is to enhance the tunneling from the initial populated $3n$ wells to their $3n + 1$ neighbors ones, making the system closer to resonance, in the sense of Eq. (4.28), where the resonance condition results in the initially populated wells becoming empty at some later time. It is interesting to note that the system exhibits "nonclassical" dynamics whereby the atoms start to tunnel in the direction opposite the direction of the force (this statement applies even when the external field is not weak).

Resonances

In Fig. 4.15 we show the temporal evolution of the spatial amplitudes $\tilde{\Psi}_i$ for a range of values of ξ. For certain choices of ξ the initially occupied $\tilde{\Psi}_0$ amplitude periodically disappears - we refer to these as resonances.

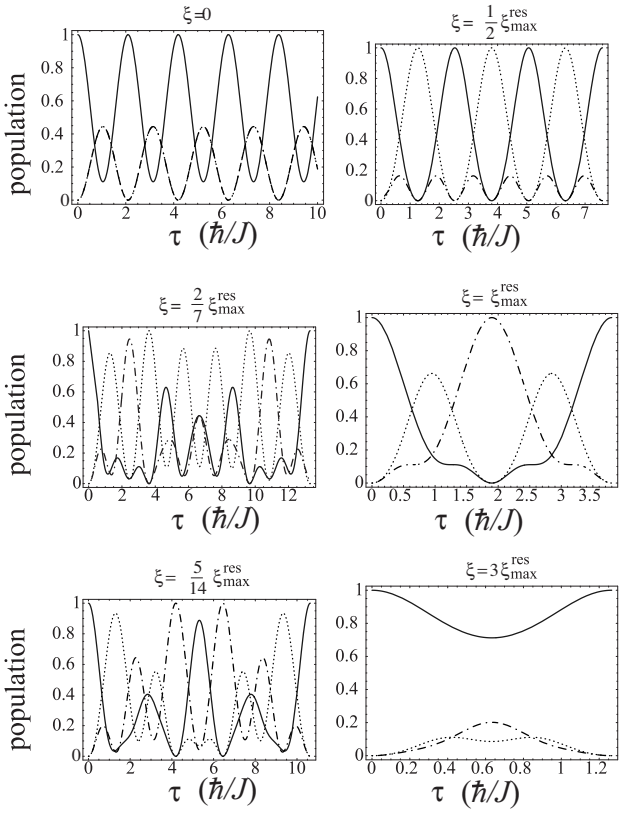

Figure 4.15: Evolution of the normalized population for different values of ξ. One Bloch period is shown in the plots except $\xi = 0$ where the period is infinite. Solid line: $|\tilde{\Psi}_{3n}|^2$, dotted line: $|\tilde{\Psi}_{3n+1}|^2$, dash-dot line: $|\tilde{\Psi}_{3n+2}|^2$. The "nonclassical" motion can be seen where the $3n$+1-well populations initially increase more rapidly that the populations of the $3n+2$-wells. It can also be seen in the plots that $\xi = \xi^{\rm res}_{\rm max}/2$ and $\xi = \xi^{\rm res}_{\rm max}$ are resonant values.

By requiring $\tilde{\Psi}_0 = 0$ in Eq. (4.52) we obtain the following conditions on the phases for these resonances

$$\Delta_1(\tau) - \Delta_0(\tau) = \pm\left(\frac{\pi}{3} + 2\pi s\right), \tag{4.63}$$

$$\Delta_2(\tau) - \Delta_1(\tau) = \pm\left(\frac{\pi}{3} + 2\pi m\right), \tag{4.64}$$

where s and m are integers and the same sign choice on the right hand side must be made for both equations. When these conditions are satisfied the population is not shared between the adjacent sites, but preferentially tunnels to one of the neighbors. In particular, the +sign choice in Eqs. (4.63) and (4.64) gives the phase condition for complete tunneling into $\tilde{\Psi}_1$. Similarly the $-$sign case gives the condition for complete tunneling into $\tilde{\Psi}_2$. Solving for the values of ξ for which Eqs. (4.63) and

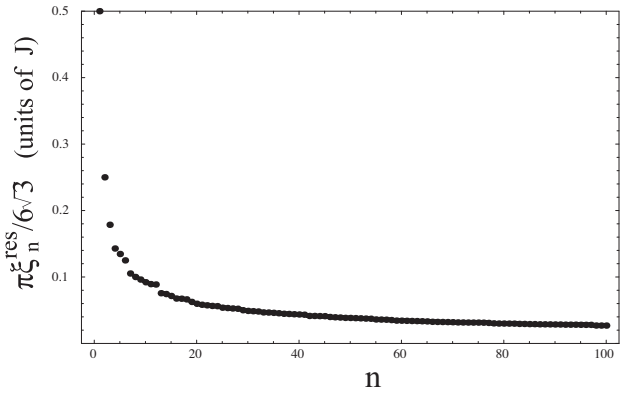

Figure 4.16: The spectrum of values of external force, ordered in decreasing magnitude, for which a population resonance occurs i.e. the values of ξ for which $\tilde{\Psi}_0$ periodically disappears.

(4.64) hold, one obtains the spectrum

$$\xi^{\rm res}_{n=(s,m)} = \pm\frac{6\sqrt{3}}{\pi}\frac{(1+3s)}{(1+3s)^2+3(s+2m+1)^2}, \tag{4.65}$$

which is shown in Fig. 4.16. For large $|s|$ or $|m|$ the resonant values of ξ are close together, and become spaced further apart as the magnitude of s decreases.

In the absence of an applied force (i.e. $\xi = 0$) the phase terms are time-independent with $\Delta_0 = -2$, $\Delta_1 = -1$ and $\Delta_2 = -1$ so that the resonance conditions can never be achieved. When the external force is applied the phases oscillate at a rate that increases with ξ and an amplitude that decreases with ξ. The largest value of ξ for which a resonance can be found is $\xi^{\rm res}_{\rm max} \equiv 6\sqrt{3}/2\pi$, since for values of ξ greater than this the amplitudes of the phase oscillations Δ_i are so small that they cannot satisfy the condition for population resonance. In the regime $\xi > \xi^{\rm res}_{\rm max}$, $|\tilde{\Psi}_0|$ exhibits only one (nonzero) minima per Bloch period and the dynamics of the system is dominated by the Bloch oscillations.

Large Force Limit

For $\xi > \xi^{\rm res}_{\rm max}$ the system exhibits a population imbalance as the Bloch oscillation suppresses the ability of the system to tunnel between sites. In the limit $\xi \gg \xi^{\rm res}_{\rm max}$ the population in the wells is described by rapid, small amplitude oscillations around its initial value,

$$|\tilde{\Psi}_0(\tau)|^2 \longrightarrow \frac{3}{M}\left(1-\frac{8}{\xi^2}\sin^2\left(\frac{\xi\tau}{2}\right)\right), \tag{4.66}$$

$$|\tilde{\Psi}_1(\tau)|^2 \longrightarrow \frac{12}{M}\frac{1}{\xi^2}\sin^2\left(\frac{\xi\tau}{2}\right), \tag{4.67}$$

$$|\tilde{\Psi}_2(\tau)|^2 \longrightarrow \frac{12}{M}\frac{1}{\xi^2}\sin^2\left(\frac{\xi\tau}{2}\right). \tag{4.68}$$

The case of $\xi = 3\xi_{\max}^{\mathrm{res}}$ depicted in Fig.4.15 shows an approach to this behavior.

- Numerical results for the non-linear case

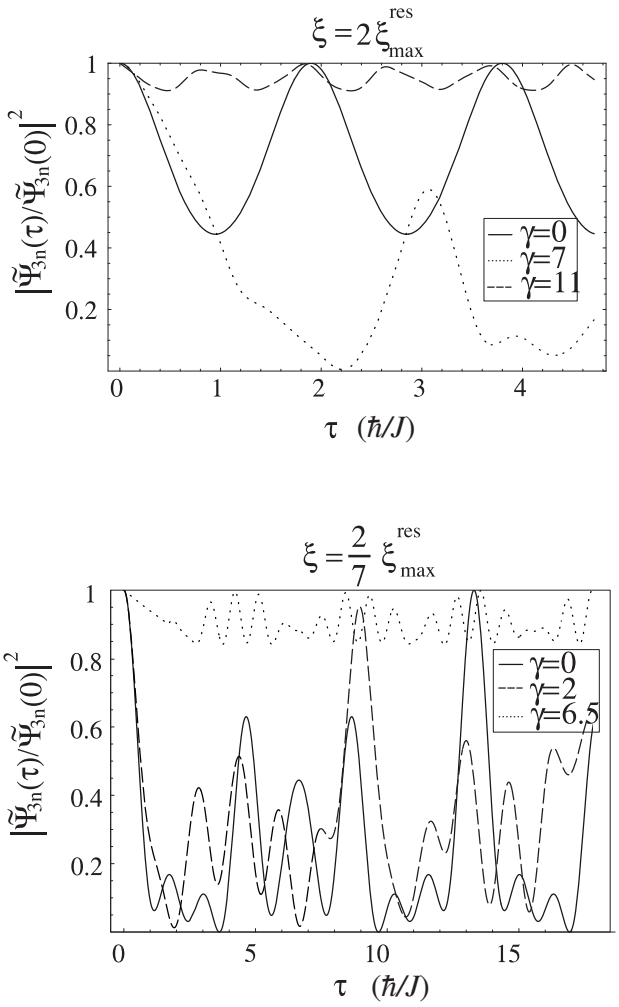

Figure 4.17: Effects of interactions on generalized Bloch oscillations for the pattern loaded system. Evolution of $|\tilde{\Psi}_n|^2$ for various interaction strengths. Upper plot: $\xi = 2\xi_{\max}^{\mathrm{res}}$. Lower plot: $\xi = 2\xi_{\max}^{\mathrm{res}}/7$.

Because of the difficulty of solving analytically the equations of motion the nonlinear equations were solved numerically. Although the dynamics in this situation is considerably more complicated than in the linear case, the resonance picture still gives us useful guidance concerning the expected behavior. In general, there exist critical values of ξ and Λ above which no resonances occur. Furthermore, nonlinearity tends to destroy the periodicity of the Bloch oscillations that is present in the noninteracting case. For example, in Fig. 4.17, we see that for $\xi = 2\xi_{\max}^{\mathrm{res}}$, the introduction of interactions brings the

system into resonance, but that for large interaction strength, nonresonant behavior is restored. For $\xi = 2\xi_{\max}^{\text{res}}/7$, on the other hand, the introduction of interactions eventually draws the system out of resonance.

Concerning the momentum distribution, similarly to the untilted case, interatomic interactions induce time variation of the momentum intensities. The contrast between momentum components vanishes at $\Lambda = 0$. As Λ increases, the contrast increases to a maximum value, then eventually decreases towards zero when macroscopic imbalance is achieved, analogous to what is seen in Fig. 4.11 for the untilted case. Because the external field together with the nonlinearity breaks down the periodicity of time evolution, the dynamics of the momentum distribution is quite complex.

To compare the predictions of the homogeneous model in the presence of a linear external potential to a more realistic case, we again solved numerically the discrete nonlinear Schrödinger equation for a condensate loaded into every third lattice site but, instead of being homogeneous, initially with a Gaussian profile. Very good agreement between the model and the numerical results was found for short times and modest mean-field energies, if, as in the untilted case, we use an effective mean field energy. In Figs. 4.18 and 4.19 we present a comparison between the evolution of the normalized population at the central wells found numerically and the prediction of the model for the parameters: $NU = 4.8E_{\text{R}}$, $M = 290$, $J = 0.075\ E_{\text{R}}$ and $\xi = 2$. For longer times, the model predictions start to disagree with numerical simulation due to the spread of the three Fourier peaks. We observe that the dynamics are much more sensitive to inhomogeneous effects in the presence of an external force, and for the more inhomogeneous initial state used in Figs. (4.12 - 4.14) (which extends over $M = 76$ sites), the inhomogeneous result much more rapidly departs from the homogeneous prediction than the example presented here.

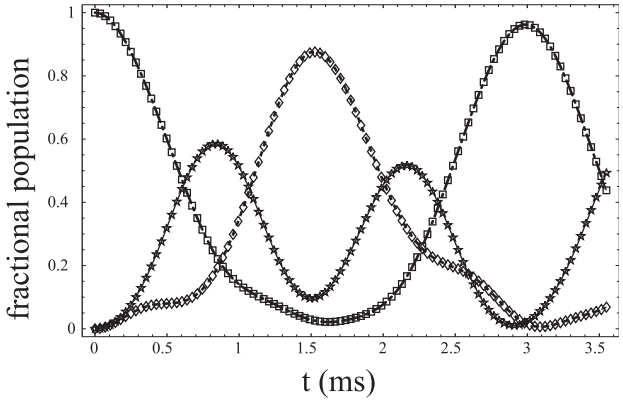

Figure 4.18: Comparison between the evolution of a inhomogeneous condensate with the homogeneous result. Inhomogeneous condensate: $|\tilde{\Psi}_0|^2$ (boxes), $|\tilde{\Psi}_1|^2$ (stars), and $|\tilde{\Psi}_2|^2$ (diamonds). Homogeneous case: $|\tilde{\Psi}_{3n}|^2$ (dash-dot line), $|\tilde{\Psi}_{3n+1}|^2$ (solid line), and $|\tilde{\Psi}_{3n+2}|^2$ (dotted line), where we have taken γ as the local mean field energy. The parameters used were $J = 0.075E_{\rm R}$, $\xi = 2$ and $\gamma_{\rm eff} = 1.59$

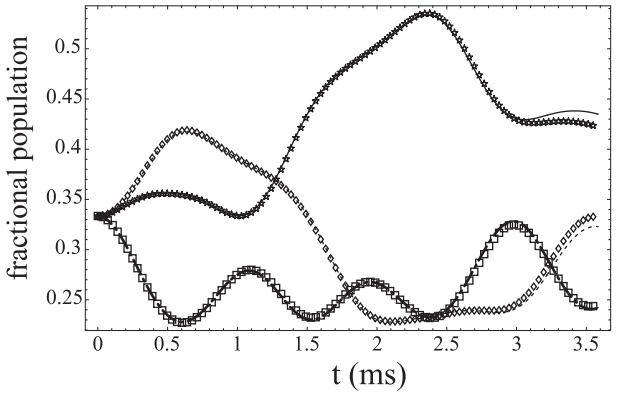

Figure 4.19: Evolution of the momentum peak populations. $q = 0$ (dashed line, squares), $q = -2\pi/3$ (dash-dot line, stars), $q = 2\pi/3$ (solid line, diamonds). Inhomogeneous condensate (dotted curves), homogeneous model (lines) using the same parameters as those in Fig. 4.18, but replacing γ by an average value $\gamma_{\rm ave} = 1.11$ for the homogeneous model.

Chapter 5

Quadratic approximations

As discussed in chapter 3, the Bose-Hubbard Hamiltonian is an appropriate model, when the loading process produces atoms in the lowest vibrational state of each well, with a chemical potential smaller than the energy gap to the first vibrationally excited state. The quartic form of the Hamiltonian makes it very difficult to deal with it in all the different regimes. The aim of this chapter is to rewrite it so that a systematic approach can be developed in the weakly interacting regime, when a condensate is present. The basic idea, which was first proposed by Bogoliubov in 1947 [11], is to treat the field operator as a c-number plus a fluctuating term. The c-number describes the condensate or the coherent part of the matter field. In the weakly interacting regime, quantum fluctuations are small, and therefore the dominant terms in the Hamiltonian are quadratic in the fluctuating field. The non-quadratic terms should be of higher order and can be treated perturbatively.

In this chapter, we apply the Bogoliubov approximation to the Bose- Hubbard Hamiltonian and derive the correspondent Bogoliubov-de Genes(BdG) equations as developed in Refs. [77, 95]. We also deal with the higher order terms by considering different approximations. Among them we discuss the Hartree-Fock-Bogoliubov (HFB) approximation, the HFB-Popov approximation and the improved Popov approximation where the bare potential is upgraded to the many-body scattering matrix. All of these approximate approaches are valid only in the weakly interacting regime when quantum fluctuations are small. They will fail to give a good description as interactions become important and the system approaches the Mott insulator transition. To test the validity of the approximations we compared them with numerical solutions obtained by diagonalizing the Bose-Hubbard Hamiltonian.

In this chapter we also derive an explicit expression for the superfluid density based on the rigidity of the system under phase variations. We show how the superfluid fraction can be thought of as a natural order parameter to describe the superfluid to Mott insulator transition.

Because we are interested in the quantum effects caused by interactions that drive the quantum phase transition instead of thermal quantum fluctuations, the analysis in the present chapter is going to be restricted to the zero temperature

case.

5.1 The characteristic Hamiltonian

In the very weakly interacting regime, to a good approximation, the creation and annihilation operators on each site can be replaced by a *c*-number(see chapter 4). To include the small quantum fluctuations in the description of the system we assume that the field operator can be written in terms of a *c*-number plus a fluctuation operator:

$$\hat{a}_n = z_n + \hat{\varphi}_n. \tag{5.1}$$

Replacing this expression for $\hat{a}_n$ in the Bose-Hubbard Hamiltonian Eq. (3.4) leads to :

$$\hat{H} = H_0 + \hat{H}_1 + \hat{H}_2 + \hat{H}_3 + \hat{H}_4, \tag{5.2}$$

with

$$H_0 = -J \sum_{<n,m>} z_n^* z_m + \sum_n \left[(V_n - \mu)|z_n|^2 + \frac{U}{2}|z_n|^4 \right], \tag{5.3}$$

$$\hat{H}_1 = -J \sum_{<n,m>} \hat{\varphi}_n z_m^* + \sum_n \left(V_n - \mu + U|z_n|^2 \right) z_n^* \hat{\varphi}_n + h.c., \tag{5.4}$$

$$\hat{H}_2 = -J \sum_{<n,m>} \hat{\varphi}_n^\dagger \hat{\varphi}_m + \sum_n (V_n - \mu)\hat{\varphi}_n^\dagger \hat{\varphi}_n + \frac{U}{2} \sum_n \left(\hat{\varphi}_n^{2\dagger} z_n^2 + \hat{\varphi}_n^2 z_n^{2*} + (\hat{\varphi}_n^\dagger \hat{\varphi}_n + \hat{\varphi}_n \hat{\varphi}_n^\dagger)|z_n|^2 \right), \tag{5.5}$$

$$\hat{H}_3 = U \sum_n \hat{\varphi}_n^\dagger \hat{\varphi}_n^\dagger \hat{\varphi}_n z_n + h.c., \tag{5.6}$$

$$\hat{H}_4 = \frac{U}{2} \sum_n \hat{\varphi}_n^\dagger \hat{\varphi}_n^\dagger \hat{\varphi}_n \hat{\varphi}_n. \tag{5.7}$$

Where $< n, m >$ restricts the sum over m to nearest neighbors and *h.c.* stands for the hermitian conjugate. The terms of the Hamiltonian have been grouped in equations according to the number of non condensate operators which they contain.

5.2 Bogoliubov-de Gennes (BdG) equations

In this section we neglect higher order terms and focus only on the quadratic Hamiltonian. The first step in the diagonalization is the minimization of the energy functional H_0 . This requires the condensate amplitudes z_n to be a stationary solution of the DNLSE (4.6), which in turn means that the linear Hamiltonian $\hat{H}_1$ vanishes. For the time independent situation the DNLSE can be written as

$$\mu z_n = -J \sum_{<m,n>} z_m + (V_n + U|z_n|^2) z_n \tag{5.8}$$

The Hamiltonian H_0 gives a description which includes only the contribution from the condensate. The quadratic Hamiltonian H_2 allows the leading order effects of the non condensate to be taken into account. By including second order terms in the Hamiltonian two classes of interactions are included besides the condensate-condensate ones: a) Interactions between one excited atom and one condensate atom leading to transitions of the form $|0j\rangle \rightarrow |0i\rangle$ (direct and exchange excitations)and b) interactions between two condensate atoms which cause the atoms to be excited to non condensate states $|00\rangle \rightarrow |ij\rangle$ (pair excitations). Schematically they are shown in fig.5.1.

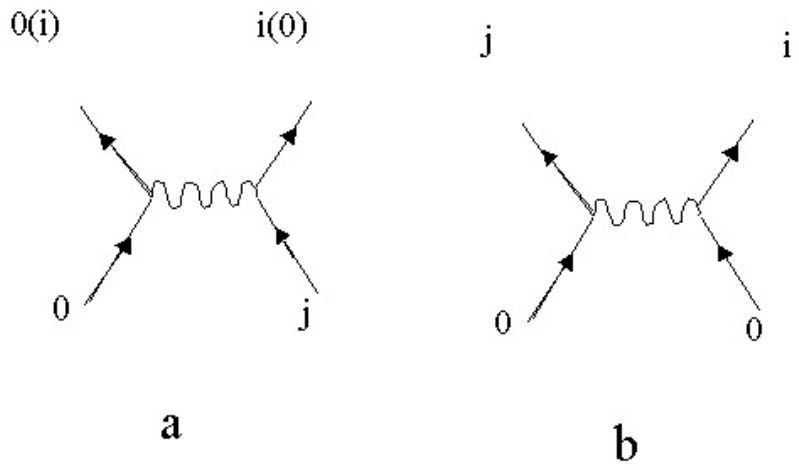

Figure 5.1: Scattering processes included in the quadratic hamiltonian: a) Direct and exchange excitations, b) Pair excitations

The quadratic Hamiltonian can be diagonalized by finding a basis of so-called quasiparticle states which do not interact which each other. Mathematically this involves a linear canonical transformation of the single-particle creation and annihilation operators $\hat{a}_n^\dagger$ and $\hat{a}_n$ into quasiparticle operators $\hat{\alpha}_s^\dagger$, $\hat{\alpha}_s$. The transformation is known as Bogoliubov transformation and is given by

$$\hat{\varphi}_n = \sum_{s\neq 0} \left(u_n^s \hat{\alpha}_s - v_n^{*s} \hat{\alpha}_s^\dagger \right). \tag{5.9}$$

In general the spectrum of fluctuations includes a zero mode. This mode is the Goldstone boson associated with the breaking of global phase invariance by the condensate. The zero mode is essentially non perturbative and it introduces an artificial infrared divergence in low dimensional models. For this reason quadratic approximations are actually improved if the contribution from this mode is neglected all together [96]. A different way to deal with the zero mode has been proposed by Castin and Dum [98], Gardiner [97] and Morgan [16]. Here the theory is written in terms of operators which exchange particles between zero and

nonzero modes, conserving the total particle number, and one further operator which changes total particle number. As shown by [16] both the latter and the former approaches lead to the same physical predictions, so for simplicity we are going to ignore zero mode fluctuations and restrict the fluctuation operators to act only on the excited states.

The Bogoliubov transformation Eq. (5.9) is required to be canonical, which means that it preserves the commutation relations and leads to bosonic quasiparticles. To satisfy this, the amplitudes $\{u_n^s, v_n^s\}$ are constrained by the conditions:

$$\sum_n \left(u_n^{*s} u_n^{s\prime} - v_n^{*s} v_n^{s\prime}\right) = \delta_{ss\prime}, \tag{5.10}$$

$$\sum_n \left(u_n^{s} v_n^{s\prime} - v_n^{*s} u_n^{*s\prime}\right) = 0. \tag{5.11}$$

The necessary and sufficient conditions that the quasiparticle amplitudes have to fulfill to diagonalize the Hamiltonian are provided by the so called Bogoliubov-de Gennes (BdG) equations

$$\begin{pmatrix} \mathcal{L} & \mathcal{M} \\ \mathcal{M}^* & \mathcal{L} \end{pmatrix} \begin{pmatrix} \mathbf{u}^s \\ \mathbf{v}^s \end{pmatrix} = \omega_s^B \begin{pmatrix} \mathbf{u}^s \\ -\mathbf{v}^s \end{pmatrix} + c_s \begin{pmatrix} \mathbf{z} \\ -\mathbf{z}^* \end{pmatrix}, \tag{5.12}$$

with $\mathbf{u}^s = (u_1^s, u_2^s, ...)$, $\mathbf{v}^s = (v_1^s, v_2^s, ...)$ and $\mathbf{z} = (z_1, z_2, ...)$. The matrices $\mathcal{L}$ and $\mathcal{M}$ are given by

$$\mathcal{L}_{nm} = -J \sum_{<n,l>} \delta_{nl}\delta_{lm} + \delta_{nm}(2U|z_n|^2 + V_n - \mu) \tag{5.13}$$

$$\mathcal{M}_{nm} = -U z_i^2 \delta_{nm}. \tag{5.14}$$

with δ_{nl} the Kronecker delta which is one if $n = l$ and zero otherwise. The parameters c_s ensure that the solutions with $\omega_s^B \neq 0$ are orthogonal to the condensate [16]. These parameters are given by

$$c_s = U \frac{\sum_n |z_n|^2 (z_n^* u_n^s - z_n v_n^s)}{\sum_n |z_n|^2} \tag{5.15}$$

The BdG equations without the c_s parameters have the same quasiparticle energies as Eq.(5.12), nevertheless the solutions are orthogonal to the condensate only in the general sense, i.e. $\sum_n (z_n^* u_n^s - z_n v_n^s) = 0$. Each of the terms, $\sum_n z_n^* u_n^s$and $\sum_n z_n v_n^s$ are not necessarily zero. To obtain the desired orthogonal modes one way to proceed is to solve the BdG equations setting the c_s to zero and then to remove from the solutions their projection onto the condensate. If the BdG equations are satisfied, the quadratic Hamiltonian takes the form

$$\hat{H}_2 = \sum_{s\neq 0} \left[\omega_s^B \hat{\alpha}_s^\dagger \hat{\alpha}_s + \frac{1}{2}\left(\omega_s^B - \mathcal{L}_{ss}\right)\right]. \tag{5.16}$$

If the Hamiltonian $\hat{H}_2$, is positive definite, which is the case when the condensate amplitudes correspond to a stable state of the system, the eigenvalues of the system are real. The solutions ω_s^B come in pairs with positive and negative energies, if $\omega_s^B$is a solution for the amplitudes $(\mathbf{u}^s, \mathbf{v}^s)$ then $-\omega_s^B$is also a solution for the amplitudes $(\mathbf{v}^{s*}, \mathbf{u}^{s*})$. There is always a solution with $\omega_s^B = 0$ and in this case the amplitudes must be proportional to the condensate $(\mathbf{v}^0, \mathbf{u}^0) \propto (\mathbf{z}, \mathbf{z})$. We explicitly exclude the zero mode solution to guarantee that the excitations are orthogonal to the condensate.

To have a complete description of the quadratic Hamiltonian, we define the one body density fluctuation matrix, ρ_{nm} and the anomalous average matrix, m_{nm} as:

$$\rho_{nm} = \langle \hat{a}_n^\dagger \hat{a}_m \rangle - \langle \hat{a}_n^\dagger \rangle \langle \hat{a}_m \rangle = \langle \hat{\varphi}_n^\dagger \hat{\varphi}_m \rangle, \tag{5.17}$$

$$m_{nm} = \langle \hat{a}_n \hat{a}_m \rangle - \langle \hat{a}_n \rangle \langle \hat{a}_m \rangle = \langle \hat{\varphi}_n \hat{\varphi}_m \rangle. \tag{5.18}$$

The averages denotes an ordinary quantum expectation value. At zero temperature, the average is over the ground quasiparticle state given by $\hat{\alpha}_s|0\rangle = 0$ and the ρ_{nm} and m_{nm} can be written in terms of quasiparticle amplitudes as:

$$\rho_{nm} = \sum_{s\neq 0} v_n^{s*} v_m^s, \tag{5.19}$$

$$m_{nm} = -\sum_{s\neq 0} u_n^s v_m^{s*}. \tag{5.20}$$

Physically, the quantity ρ_{nn} represents the non -condensate population (or depletion) at position n or depletion at position n. If the average number of atoms is N, the depletion and condensate atoms are related by the equation:

$$N = \sum_n \left\langle \hat{a}_n^\dagger \hat{a}_n \right\rangle = \sum_n \left(|z_n|^2 + \rho_{nn} \right). \tag{5.21}$$

The interpretation to the physical meaning of the anomalous term is postponed to section 5.7.2.

5.3 Higher order terms

In the preceding section we described the diagonalization of the Hamiltonian containing only terms up to quadratic order in the field operators. We now want to go beyond this approximation and consider the corrections introduced by the cubic and quartic terms. Taking into account higher order terms we are mainly introducing many-body effects on the scattering.

5.3.1 Hartree-Fock-Bogoliubov equations

Third and quartic terms in the Hamiltonian can be included by treating them in a self-consistent mean field approximation, which relies upon the factorization approximation: products of many operators are approximated by paring the operators in all possible ways and replacing these pairs by their expectation value [15]. Using the factorization approximation, one can reduce third and quartic products of fluctuation field operators to:

$$\begin{aligned} \varphi_n^\dagger \varphi_n \varphi_n &\rightarrow 2\rho_{nn}\varphi_n + 2m_{nn}\varphi_n^\dagger, & (5.22)\\ \varphi_n^\dagger \varphi_n^\dagger \varphi_n \varphi_n &\rightarrow 4\rho_{nn}\varphi_n^\dagger\varphi_n + m_{nn}\varphi_n^\dagger\varphi_n^\dagger + m_{nn}^*\varphi_n\varphi_n - (2\rho_{nn}^2 + |m_{nn}|^2) & (5.23)\end{aligned}$$

Eq.(5.23) is justified by Wick's theorem [51], which gives $\langle\varphi_n^\dagger\varphi_n^\dagger\varphi_n\varphi_n\rangle = 2\rho_{nn}^2 + |m_{nn}|^2$, while Eq.(5.22) is justified by analogy [16].
Therefore, using Eq.(5.23) and Eq.(5.22) in $\hat{H}_3$ and $\hat{H}_4$ (Eqs. (5.6) and (5.7)) one can reduce them to quadratic forms in terms of the functions ρ_{nm} and m_{nm}. The c-number term in Eq.(5.23) introduces also a energy shift in H_0 :

$$\begin{aligned} \Delta\hat{H}_0 &= \frac{U}{2}(2\rho_{nn}^2 + |m_{nn}|^2) & (5.24)\\ \hat{H}_3 &= U\sum_n (2\rho_{nn}\hat{\varphi}_n + m_{nn}\hat{\varphi}_n^\dagger)z_n + h.c., & (5.25)\\ \hat{H}_4 &= \frac{U}{2}\sum_n (2\rho_{nn}\hat{\varphi}_n^\dagger\hat{\varphi}_n + m_{nn}\hat{\varphi}_n\hat{\varphi}_n) + h.c.. & (5.26)\end{aligned}$$

The corrections from higher order terms yield a modified quadratic Hamiltonian which can be also diagonalized. The diagonalization leads to the following equations

$$\mu^{HFB} z_n = -J\sum_{<m,n>} z_m + (V_n + U|z_n|^2 + 2U\rho_{nn} + Um_{nn})z_n, \quad (5.27)$$

$$\begin{pmatrix} \mathcal{L}^{HFB} & \mathcal{M}^{HFB} \\ \mathcal{M}^{*HFB} & \mathcal{L}^{*HFB} \end{pmatrix}\begin{pmatrix} \mathbf{u}^s \\ \mathbf{v}^s \end{pmatrix} = \omega_s^{HFB}\begin{pmatrix} \mathbf{u}^s \\ -\mathbf{v}^s \end{pmatrix} + \begin{pmatrix} c_s^{HFB^-}\mathbf{z} \\ -c_s^{HFB^+}\mathbf{z}^* \end{pmatrix}, \quad (5.28)$$

$$\begin{aligned} \mathcal{L}_{nm}^{HFB} &= -J\sum_{<n,l>}\delta_{nl}\delta_{lm} + \delta_{nm}(2U|z_n|^2 + V_n - \mu^{HFB} + 2U\rho_{nn}), & (5.29)\\ \mathcal{M}_{nm}^{HFB} &= -(Uz_i^2 + Um_{nn})\delta_{nm}, & (5.30)\\ c_s^{HFB\mp} &= \frac{U\sum_n |z_n|^2(z_n^* u_n^s - z_n v_n^s) \mp U\sum_n (m_{nn}^* z_n u_n^s - m_{nn} z_n^* v_n^s)}{\sum_n |z_n|^2}. & (5.31)\end{aligned}$$

The parameters $c_s^{HFB\mp}$ are there again to enforce the orthogonality of the quasiparticle modes with the condensate [16].

The above set of equations (5.27) to (5.30) are known as Hartree-Fock-Bogoliubov (HFB) equations. Even though they take into account higher order corrections, they have the problem that violate the Hugenholtz and Pines theorem [99] which states that the energy spectrum of a Bose gas is gapless, i.e, there exists an excitation with an energy which tends to zero as the momentum tends to zero.

5.3.2 HFB-Popov approximation

One way to solve the gap problem is to set the anomalous term $\widetilde{m}_{nn}$ to zero in HFB equations. This procedure is known as HFB-Popov approximation. The HFB-Popov equations were first introduced by Popov [52], and they are considered to be a better approximation than the HFB equations because they yield a gapless spectrum.

The HFB-Popov equations have the form:

$$\mu^P z_n = -J \sum_{<m,n>} z_m + (V_n + U|z_n|^2 + 2U\rho_{nn})z_n, \tag{5.32}$$

$$\begin{pmatrix} \mathcal{L}^P & \mathcal{M}^P \\ \mathcal{M}^{*P} & \mathcal{L}^{*P} \end{pmatrix} \begin{pmatrix} \mathbf{u}^s \\ \mathbf{v}^s \end{pmatrix} = \omega_s^P \begin{pmatrix} \mathbf{u}^s \\ -\mathbf{v}^s \end{pmatrix} + c_s \begin{pmatrix} \mathbf{z} \\ -\mathbf{z}^* \end{pmatrix}, \tag{5.33}$$

$$\mathcal{L}^P_{nm} = -J \sum_{<n,l>} \delta_{nl}\delta_{lm} + \delta_{nm}(2U|z_n|^2 + V_n - \mu^P + 2U\rho_{nn}), \tag{5.34}$$

$$\mathcal{M}^P_{nm} = -(Uz_i^2)\delta_{nm}, \tag{5.35}$$

$$c_s = U\frac{\sum_n |z_n|^2(z_n^* u_n^s - z_n v_n^s)}{\sum_n |z_n|^2}. \tag{5.36}$$

5.4 The Bose-Hubbard model and superfluidity

The concept of superfluidity is closely related to the existence of a condensate in the interacting many-body system. Formally, the one-body density matrix $\rho^{(1)}(\vec{x}, \vec{x}')$ has to have exactly one macroscopic eigenvalue which defines the number of particles in the condensate; the corresponding eigenvector describes the condensate wave function $\phi_0(\vec{x}) = e^{i\Theta(\vec{x})}|\phi_0(\vec{x})|$. A spatially varying condensate phase, $\Theta(\vec{x})$, is associated with a velocity field for the condensate by

$$\vec{v}_0(\vec{x}) = \frac{\hbar}{m}\vec{\nabla}\Theta(\vec{x}). \tag{5.37}$$

This irrotational velocity field is identified with the velocity of the *superfluid flow*, $\vec{v}_s(\vec{x}) \equiv \vec{v}_0(\vec{x})$ ([100],[101]) and enables us to derive an expression for the superfluid fraction, f_s. Consider a system with a finite linear dimension, L, in the $\vec{e}_1$–direction and a ground–state energy, E_0, calculated with periodic boundary conditions. Now we impose a linear phase variation, $\Theta(\vec{x}) = \theta x_1/L$ with a total twist angle θ over

the length of the system in the $\vec{e}_1$–direction. The resulting ground–state energy, E_θ will depend on the phase twist. For very small twist angles, $\theta \ll \pi$, the energy difference, $E_\theta - E_0$, can be attributed to the kinetic energy, T_s, of the superflow generated by the phase gradient. Thus,

$$E_\theta - E_0 = T_s = \frac{1}{2} m N f_s \vec{v}_s^2, \tag{5.38}$$

where m is the mass of a single particle and N is the total number of particles so that mNf_s is the total mass of the superfluid component. Replacing the superfluid velocity, $\vec{v}_s$ with the phase gradient according to Eq. (5.37) leads to a fundamental relation for the superfluid fraction.

$$f_s = \frac{2m}{\hbar^2} \frac{L^2}{N} \frac{E_\theta - E_0}{\theta^2} = \frac{1}{N} \frac{E_\theta - E_0}{J\,(\Delta\theta)^2}. \tag{5.39}$$

where the second equality applies to a one dimensional lattice system on which a linear phase variation has been imposed. Here the distance between sites is a, the phase variation over this distance is $\Delta\theta$, and the number of sites is M. In this case, $J \equiv \hbar^2/(2ma^2)$.

Technically the phase variation can be imposed through so-called twisted boundary conditions [102]. In the context of the discrete Bose-Hubbard model it is, however, more convenient to map the phase variation by means of a unitary transformation onto the Hamiltonian [103]. For simplicity we are going to focus in a one dimensional lattice. The resulting "twisted" Hamiltonian in this case

$$\hat{H}_\theta = \sum_{n=1}^{M} \hat{n}_n V_n - J \sum_{n=1}^{M} (e^{-\mathrm{i}\Delta\theta} \hat{a}_{n+1}^\dagger \hat{a}_n + e^{\mathrm{i}\Delta\theta} \hat{a}_n^\dagger \hat{a}_{n+1}) + \frac{U}{2} \sum_{n=1}^{M} \hat{n}_n(\hat{n}_n - 1)\ . \tag{5.40}$$

exhibits additional phase factors $e^{\pm \mathrm{i}\Delta\theta}$ — the so-called Peierls phase factors — in the hopping term [104, 105]. These phase factors show that the twist is equivalent to the imposition of an acceleration on the lattice for a finite time. It is interesting to note that the present experiments enable us to make a specific connection between the formal and operational aspects of the system.

We calculate the change in energy $E_\theta - E_0$ under the assumption that the phase change $\Delta\theta$ is small so that we can write:

$$e^{-\mathrm{i}\Delta\theta} \simeq 1 - \mathrm{i}\Delta\theta - \frac{1}{2}(\Delta\theta)^2\ . \tag{5.41}$$

Using this expansion the twisted Hamiltonian (5.40) takes the following form:

$$\hat{H}_\theta \simeq \hat{H}_0 + \Delta\theta \hat{J} - \frac{1}{2}(\Delta\theta)^2 \hat{T} = \hat{H}_0 + \hat{H}_{\mathrm{pert}}\ , \tag{5.42}$$

where we retain terms up to second order in $\Delta\theta$. The current operator $\hat{J}$ (Note that the physical current is given by this expression multiplied by $\frac{1}{\hbar}$) and the hopping

operator $\hat{T}$ are given by:

$$\hat{J} = \mathrm{i}J\sum_{n=1}^{M}(\hat{a}_{n+1}^{\dagger}\hat{a}_n - \hat{a}_n^{\dagger}\hat{a}_{n+1}) \tag{5.43}$$

$$\hat{T} = -J\sum_{n=1}^{M}(\hat{a}_{n+1}^{\dagger}\hat{a}_n + \hat{a}_n^{\dagger}\hat{a}_{n+1})\ . \tag{5.44}$$

The change in the energy $E_\theta - E_0$ due to the imposed phase twist can now be evaluated in second order perturbation theory

$$E_\theta - E_0 = \Delta E^{(1)} + \Delta E^{(2)}\ . \tag{5.45}$$

The first order contribution to the energy change is proportional to the expectation value of the hopping operator

$$\Delta E^{(1)} = \langle\Psi_0|\hat{H}_{\mathrm{pert}}|\Psi_0\rangle = -\frac{1}{2}(\Delta\theta)^2\langle\Psi_0|\hat{T}|\Psi_0\rangle\ . \tag{5.46}$$

Here $|\Psi_0\rangle$ is the ground state of the original Bose-Hubbard Hamiltonian (4.27). The second order term is related to the matrix elements of the current operator involving the excited states $|\Psi_\nu\rangle$ ($\nu = 1, 2, ...$) of the original Hamiltonian

$$\Delta E^{(2)} = -\sum_{\nu\neq 0}\frac{|\langle\Psi_\nu|\hat{H}_{\mathrm{pert}}|\Psi_0\rangle|^2}{E_\nu - E_0} = -(\Delta\theta)^2\sum_{\nu\neq 0}\frac{|\langle\Psi_\nu|\hat{J}|\Psi_0\rangle|^2}{E_\nu - E_0}\ . \tag{5.47}$$

Thus we obtain for the energy change up to second order in $\Delta\theta$

$$\begin{aligned} E_\theta - E_0 &= (\Delta\theta)^2\Big(-\frac{1}{2}\langle\Psi_0|\hat{T}|\Psi_0\rangle - \sum_{\nu\neq 0}\frac{|\langle\Psi_\nu|\hat{J}|\Psi_0\rangle|^2}{E_\nu - E_0}\Big) = M(\Delta\theta)^2 D, \\ D &\equiv \frac{1}{M}\Big(-\frac{1}{2}\langle\Psi_0|\hat{T}|\Psi_0\rangle - \sum_{\nu\neq 0}\frac{|\langle\Psi_\nu|\hat{J}|\Psi_0\rangle|^2}{E_\nu - E_0}\Big). \end{aligned} \tag{5.48}$$

The quantity D, defined above, is formally equivalent to the Drude weight used to specify the DC conductivity of charged fermionic systems [106]. The superfluid fraction is then given by the contribution of both the first and second order term:

$$\begin{aligned} f_{\mathrm{s}} &= f_{\mathrm{s}}^{(1)} - f_{\mathrm{s}}^{(2)}, \\ f_{\mathrm{s}}^{(1)} &\equiv -\frac{1}{2NJ}\Big(\langle\Psi_0|\hat{T}|\Psi_0\rangle\Big), \\ f_{\mathrm{s}}^{(2)} &\equiv \frac{1}{NJ}\Big(\sum_{\nu\neq 0}\frac{|\langle\Psi_\nu|\hat{J}|\Psi_0\rangle|^2}{E_\nu - E_0}\Big). \end{aligned} \tag{5.49}$$

Here N is the number of atoms in the lattice. In general both the first and the second order term contribute. For a translationally invariant lattice the second

term vanishes (as is going to be shown latter) if one uses a quadratic approximation. However, in exact calculations the second order term plays a role.

We can further understand this approach to the superfluid density by calculating the flow that is produced by the application of the phase twist. To do this we work out the expectation value of the current operator expressed in terms of the twisted variables:

$$\hat{J}_\theta = \mathrm{i}J\sum_{n=1}^{M}(e^{-\mathrm{i}\Delta\theta}\hat{a}^\dagger_{n+1}\hat{a}_n - e^{\mathrm{i}\Delta\theta}\hat{a}^\dagger_n\hat{a}_{n+1}) \; . \tag{5.50}$$

We expand this to find the lowest order contributions, i.e.:

$$\hat{J}_\theta \simeq \hat{J} + J\Delta\theta\sum_{n=1}^{M}(\hat{a}^\dagger_{n+1}\hat{a}_n + \hat{a}^\dagger_m\hat{a}_{n+1}) = \hat{J} - \hat{T}\Delta\theta \; . \tag{5.51}$$

We use first order perturbation theory on the wave function to obtain the following expression:

$$\begin{aligned}\langle\Psi(\Delta\theta)|\hat{J}_\theta|\Psi(\Delta\theta)\rangle &= 2\Delta\theta\Big(-\frac{1}{2}\langle\Psi_0|\hat{T}|\Psi_0\rangle - \sum_{\nu\neq 0}\frac{|\langle\Psi_\nu|\hat{J}|\Psi_0\rangle|^2}{E_\nu - E_0}\Big) &(5.52)\\ &= 2NJf_{\mathrm{s}}\Delta\theta. &(5.53)\end{aligned}$$

Thus, the physical current, J_s, Eq. (5.53) multiplied by $\frac{1}{\hbar}$, can be expressed as:

$$J_s = \frac{1}{\hbar}\langle\Psi(\Delta\theta)|\hat{J}_\theta|\Psi(\Delta\theta)\rangle = Nf_{\mathrm{s}}\Delta\theta\frac{\hbar}{m^*a^2} \; . \tag{5.54}$$

This is the total flux, j_s, and we need to divide by M to get the flux density, i.e.

$$\begin{aligned}j_s = \frac{1}{\hbar M}\langle\Psi(\Delta\theta)|\,\hat{J}_\theta\,|\Psi(\Delta\theta)\rangle &= \left(\frac{\hbar\Delta\theta}{m^*a}\right)\left(\frac{Nf_{\mathrm{s}}}{aM}\right)\\ &= v_{\mathrm{s}}n_{\mathrm{s}} \; . &(5.55)\end{aligned}$$

So we see that the Drude formulation of the superfluid fraction (5.49) gives an intuitively satisfying expression for the amount of flowing superfluid.

5.5 Expectation values

Using the quadratic approximations we can evaluate expectation values of meaningful physical quantities. Useful quantities as the system approach the Mott insulator state are the number fluctuations and the quasimomentum distribution.

The number fluctuations at the site $\mathbf{x}_i$ are given in the Bogoliubov approximation by

$$\begin{aligned}\Delta n_n &= \sqrt{\langle\hat{a}^\dagger_n\hat{a}_n\hat{a}^\dagger_n\hat{a}_n\rangle - \langle\hat{a}^\dagger_n\hat{a}_n\rangle^2}\\ &= |z_n|^2\sum_s|u^s_n - v^{s*}_n|^2. &(5.56)\end{aligned}$$

The quasimomentum distribution of the atoms released from the lattice is important because it is one of the most easily accessible quantities in the experiments. The quasimomentum distribution function n_q is defined as [103]

$$\begin{aligned} n_{\mathbf{q}} &= \frac{1}{M}\sum_{n,m} e^{i\mathbf{q}\cdot(\mathbf{x}_n-\mathbf{x}_m)}\langle a_n^\dagger a_m\rangle \\ &= \frac{1}{M}\left(\left|\sum_n z_n e^{i\mathbf{q}\cdot\mathbf{x}_n}\right|^2 + \sum_{n,m}\rho_{nm}e^{i\mathbf{q}\cdot(\mathbf{x}_n-\mathbf{x}_m)}\right), \end{aligned} \tag{5.57}$$

where the quasimomentum $\mathbf{q}$ can assume discrete values which are integer multiples of $\frac{2\pi}{a_i M_i}$, where a_i and M_i are the lattice spacing and number of lattice sites in the i direction and $M = \prod_i M_i$ is the total number of lattice sites.

Neglecting interaction effects during the expansion, the quasimomentum distribution represents the Fourier transform of the original spatial distribution in the lattice. In the superfluid regime because of the phase coherence of the system, when it is released from the lattice the gas shows a nice interference pattern. As the interactions are increased phase coherence is lost, and instead of interference peaks a incoherent background is observed.

For a one dimensional optical lattice, the superfluid fraction in terms of quasiparticles amplitudes and energies can be written as:

$$f_{\mathrm{s}} = f_s^{(1)} - f_s^{(2)}, \tag{5.58}$$

$$f_s^{(1)} = \sum_{n=1}^{M} f_{sn}^{(1)} = \frac{1}{2N}\sum_{n=1}^{M}\Big[(z_{n+1}z_n^* + z_{n+1}^* z_n) + \sum_s (v_n^s v_{n+1}^{s*} + v_n^{s*} v_{n+1}^s)\Big], \tag{5.59}$$

$$\begin{aligned} f_s^{(2)} &= \frac{J}{N}\left(\sum_s \frac{\left|\sum_n \left(u_n^s + v_n^s\right)(z_{n+1} - z_{n-1})\right|^2}{\omega_s}\right) + \\ &\quad \frac{J}{N}\left(\sum_{s,s'} \frac{\left|\sum_n \left(u_{n+1}^s v_n^{s'} - u_n^s v_{n+1}^{s'}\right)\right|^2}{\omega_s + \omega_{s'}} + \delta_{ss'}\frac{\left|\sum_n (u_{n+1}^s v_n^s - u_n^s v_{n+1}^s)\right|^2}{2\omega_s}\right). \end{aligned} \tag{5.60}$$

5.6 Applications

5.6.1 Translationally invariant lattice

To understand many-body effects included in the quadratic approximations we start by studying the case where no external confinement is present, $V_n = 0$. We assume a d dimensional separable square optical lattice with equal tunneling matrix element J in all directions and periodic boundary conditions. M is the total number of wells.

Due to the translational symmetry of the system the condensate amplitudes are constant over the lattice, $z_n = \sqrt{n_o}$. Also, the quasiparticle modes have a plane wave character and therefore can be related to quasimomentum modes :

$$u_n^{\mathbf{q}} = \frac{1}{\sqrt{M}}e^{i\mathbf{q}\cdot\mathbf{x}_n}u_{\mathbf{q}}, \quad v_n^{\mathbf{q}} = \frac{1}{\sqrt{M}}e^{i\mathbf{q}\cdot\mathbf{x}_n}u_{\mathbf{q}}. \tag{5.61}$$

Here the vector $\mathbf{q}$ denotes the quasimomentum whose components assume discrete values which are integer multiples of $\frac{2\pi}{a\sqrt[d]{M}}$ with a is the lattice spacing. The amplitudes $u_{\mathbf{q}}$ and $u_{\mathbf{q}}$ must satisfy the condition $|u_{\mathbf{q}}|^2 - |v_{\mathbf{q}}|^2 = 1$ and can all be chosen to be real and to depend only on the modulus of the wave vector ($u_{\mathbf{q}} = u_{-\mathbf{q}}$, $v_{\mathbf{q}} = v_{-\mathbf{q}}$).
The translationally invariant case has the advantage that the quasi-particle modes are always orthogonal to the condensate and therefore the parameters c_s are always zero.

- Bogoliubov-de Gennes (BdG) equations and HFB- Popov approximation

  In the simplest quadratic approximation the DNLSE reduces to

  $$\mu \quad = \quad -tJ + n_o U, \tag{5.62}$$

  where t is the number of nearest neighbors $t = 2d$.

  The BdG equations in the translationally invariant case become the following 2×2 eigenvalue problem

  $$\begin{pmatrix} \mathcal{L}_{\mathbf{qq}} & -\mathcal{M}_{\mathbf{q-q}} \\ \mathcal{M}_{\mathbf{q-q}} & -\mathcal{L}_{\mathbf{qq}} \end{pmatrix} \begin{pmatrix} u_{\mathbf{q}} \\ v_{\mathbf{q}} \end{pmatrix} = \omega_{\mathbf{q}} \begin{pmatrix} u_{\mathbf{q}} \\ v_{\mathbf{q}} \end{pmatrix}, \tag{5.63}$$

  with

  $$\mathcal{L}_{\mathbf{qq}} = \epsilon_{\mathbf{q}} + n_o U, \quad \mathcal{M}_{\mathbf{q-q}} = n_o U. \tag{5.64}$$

  Here we have introduced the definition $\epsilon_{\mathbf{k}} = 4J \sum_{i=1}^{d} \sin^2(\frac{k_i a}{2})$.

  The quasiparticle energies $\omega_{\mathbf{q}}$ and modes are found by diagonalizing Eq.(5.64):

  $$\omega_{\mathbf{q}}^2 = \mathcal{L}_{\mathbf{qq}}^2 - \mathcal{M}_{\mathbf{q-q}}^2 = {\epsilon_{\mathbf{q}}}^2 + 2U n_o \epsilon_{\mathbf{q}}, \tag{5.65}$$

  $$u_{\mathbf{q}}^2 = \frac{\mathcal{L}_{\mathbf{qq}} + \omega_{\mathbf{q}}}{2\omega_{\mathbf{q}}} = \frac{\epsilon_{\mathbf{q}} + n_o U + \omega_{\mathbf{q}}}{2\omega_{\mathbf{q}}}, \tag{5.66}$$

  $$v_{\mathbf{q}}^2 = \frac{\mathcal{L}_{\mathbf{qq}} - \omega_{\mathbf{q}}}{2\omega_{\mathbf{q}}} = \frac{\epsilon_{\mathbf{q}} + n_o U - \omega_{\mathbf{q}}}{2\omega_{\mathbf{q}}}, \tag{5.67}$$

  $$u_{\mathbf{q}} v_{\mathbf{q}} = -\frac{\mathcal{M}_{\mathbf{q-q}}}{2\omega_{\mathbf{q}}} = \frac{n_o U}{2\omega_{\mathbf{q}}} \tag{5.68}$$

  and

  $$n = n_o + \frac{1}{M} \sum_{\mathbf{q} \neq \mathbf{0}} v_{\mathbf{q}}^2, \tag{5.69}$$

  with n the total density, $n = N/M$. The constrain that fixes the number of particles can be written as

$$n_o = n - \frac{1}{M}\sum_{\mathbf{q}\neq\mathbf{0}}\left(\frac{\epsilon_{\mathbf{q}} + Un_o}{2\omega_{\mathbf{q}}} - \frac{1}{2}\right). \tag{5.70}$$

In the homogeneous case, due to the cancellation of the ρ_{nn}. terms in the quasiparticle equations (5.34), the HFB-Popov approximation leads to the same quasiparticle energy spectrum and amplitudes than the BdG equations. The only difference is in the chemical potential which has an extra term $2U\rho_{nn}$

$$\mu^{(P)} = -tJ + Un_o + 2U\rho_{nn}. \tag{5.71}$$

As opposed to the free particle system, where the single particle energy dominates at high momenta (it grows as q^2), the single particle excitations in the presence of the lattice are always bounded by $4Jd$. Therefore, in the regime $Un_o/J > 1$ the interaction term dominates for all quasimomentum and so $\omega_{\mathbf{q}} \sim \sqrt{2Un_o\epsilon_{\mathbf{q}}}$. On the other hand, in the weakly interacting regime, the most important contribution to the depletion comes from the low-lying modes. For these modes is also true that $\omega_{\mathbf{q}} \sim \sqrt{2Un_o\epsilon_{\mathbf{q}}}$. Thus, to a good approximation the condensate fraction can be written as:

$$n_o \approx g - \sqrt{\frac{Un_o}{J}}\alpha, \tag{5.72}$$

with

$$\alpha = \alpha(d, M) \equiv \frac{1}{M}\sum_{\mathbf{q}\neq\mathbf{0}}\frac{\sqrt{J}}{2\sqrt{2\epsilon_{\mathbf{q}}}}, \tag{5.73}$$

$$g = \begin{cases} n + \frac{M-1}{2M} & Un/J \gtrsim 1 \\ n & Un/J \ll 1 \end{cases}. \tag{5.74}$$

In Eq.(5.74) the term $\frac{M-1}{2M}$ is a finite size effect term which is important to keep for low density systems. α is a dimensionless quantity which depends only on the dimensionality of the system. In the thermodynamics limit, $M \to \infty$ the sum can be replaced by an integral and we find

$$\alpha(1,\infty) \to \frac{1}{2\sqrt{2}\pi}\ln(\cot(q_o))\Big|_{q_o\to 0}, \tag{5.75}$$

$$\alpha(2,\infty) = 0.227293, \tag{5.76}$$

$$\alpha(3,\infty) = 0.160287. \tag{5.77}$$

$$\tag{5.78}$$

The infrared divergence in the one dimensional thermodynamic limit is a consequence of the importance of long wave length correlations in low dimensional systems. For finite one dimensional systems however $\alpha(1, M)$ has a finite value.

Because Eqs.(5.65)-(5.66) are completely determined if n_o is known, by solving Eq.(5.72) we obtain all necessary information. The solution of the algebraic equation is:

$$n_o \approx g + \frac{\alpha^2 U}{2J} - \sqrt{g\frac{\alpha^2 U}{J} + \frac{\alpha^4 U^2}{4J^2}}. \tag{5.79}$$

Eq.(5.79) tells us that for very weak interactions almost all the atoms are in the condensate. As interaction increases the condensate fraction decreases, but under the BdG (and HFB-Popov) approximation it only vanishes when $U/J \to \infty$. The BdG (and HFB-Popov) equations therefore do not predict any superfluid to Mott insulator phase transition.

The calculated quasiparticle amplitudes can be used to get analytic expressions for the number fluctuations, the momentum distribution and superfluid fraction. If we restrict our attention to the one dimensional system we have

$$\begin{aligned}
\Delta n_n &= n_o \sum_q \frac{\epsilon_q}{\omega_q} \xrightarrow[M\to\infty]{} \frac{2}{\pi} n_o \arctan(\frac{2J}{n_o U}), && (5.80)\\
n_q &= n_o \delta_{q,0} + \frac{1}{M}|v^q|^2 \delta_{q,k}, && (5.81)\\
&= n_o \delta_{q,\mathbf{0}} + \frac{1}{M}\left(\frac{\epsilon_q + U n_o}{2\omega_k} - \frac{1}{2}\right)\delta_{q,k}, && (5.82)\\
f_{\mathrm{s}} &= f_s^{(1)} - f_s^{(2)}, && (5.83)\\
f_s^{(1)} &= \frac{M}{N}\Big[n_o + \frac{1}{M}\sum_q |v^q|^2 \cos(qa)\Big], && (5.84)\\
f_s^{(2)} &= 0. && (5.85)
\end{aligned}$$

Eq. (5.80) has been studied in Ref. [95] to produce results for squeezing. There the authors show that Eq. (5.80) is consistent with those of other approaches previously reported in the literature [107, 108, 109, 110].

It is important to emphasize that due to the translational invariance of the lattice [see Eq. (5.60)], the second order term vanishes in the Bogoliubov limit.

The expression for the superfluid fraction gives a direct insight into the behavior of the system as atoms are pushed out of the condensate due to interactions. In Eq. (5.84) the sum involving the Bogoliubov amplitudes v^q characterizes the difference between the condensate fraction, which is given

by the first term, and the superfluid fraction. For weak interactions and small depletion, the depletion of the condensate has initially little effect on superfluidity. As interactions are increased the depleted population spreads into the central part of the band, (where the $\cos(qa)$ term has a negative sign) and the superfluid fraction is reduced. Finally for even larger interaction strengths, the population in the upper quarter of the band again produces a positive contribution to the superflow and the contribution from the sum decreases. In a sense the interactions are playing a role akin to Fermi exclusion "pressure" in the case of electron flow in a band. This, however can lead to perfect filling and cancellation of the flow. In the case of our Bogoliubov description we can only see reduction of the flow, not a perfect switching off of the superfluid. This happens in the Mott insulator state, which cannot be described by the Bogoliubov approximation.

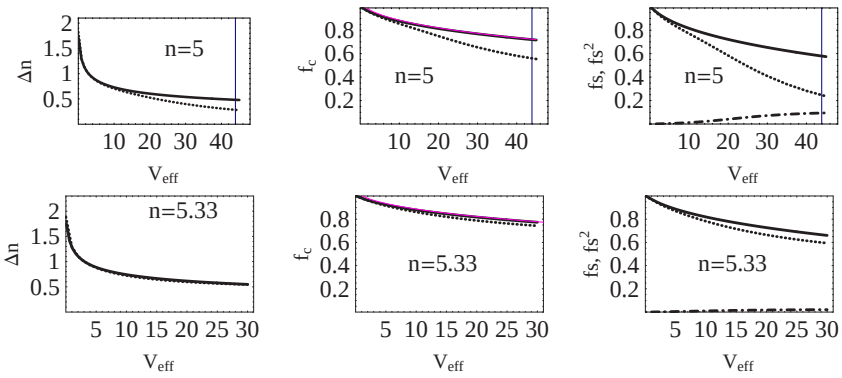

Figure 5.2: Comparisons of the exact solution and BdG (and HFB-Popov) solutions as a function of $V_{eff} = U/J$, for a system with $M = 3$ and filling factors $n = 5$ and 5.33. Left: number fluctuations (Exact: solid line, BdG(and HFB-Popov): dotted line), middle: condensate fraction (Exact: solid line, BdG(and HFB-Popov): dotted line,analytic (5.79:red line), right: superfluid fraction f_s (Exact: solid line, BdG(and HFB-Popov): dotted line). The exact second order term (dashed line) of the superfluid fraction, $f_s^{(2)}$ is also shown in these plots. The vertical line shown in the plots is an estimation of V_{eff}^{crit} when the system is commensurate

In Figs. 5.2 and 5.3 we compare the number fluctuations per lattice site, the condensate fraction and the total and second order superfluid fraction determined from the exact solution of the Bose-Hubbard Hamiltonian to the solution obtained from the BdG (and HFB-Popov) equations as a function of the ratio $V_{eff} = U/J$. The systems used for the comparisons are one dimensional lattices with three wells, $M = 3$, and commensurate filling factors $n = 5$ and 5.33 and $n = 50$ and 50.33. We were restricted to consider only three wells due to computational limitations. The size of the matrix needed in the exact solution for N atoms and M wells scales as $\frac{(N+M-1)!}{N!(M-1)!}$.

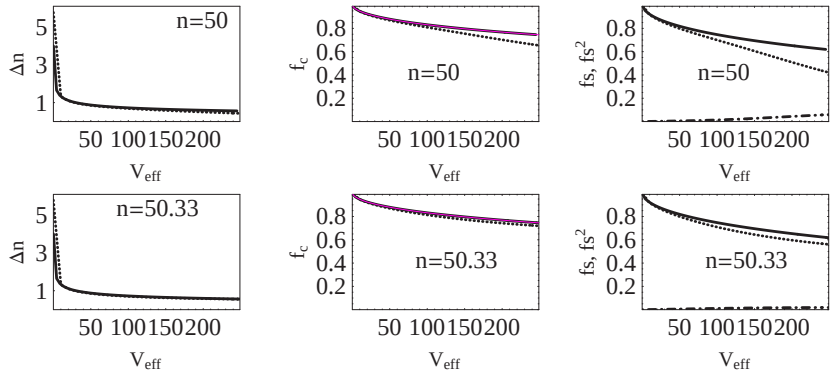

Figure 5.3: Comparisons of the exact solution and BdG(and HFB-Popov) solutions as a function of $V_{eff} = U/J$, for a system with $M = 3$ and filling factors $n = 50$ and 50.33. Left: number fluctuations (Exact: solid line, BdG(and HFB-Popov): dotted line), middle: condensate fraction (Exact: solid line, BdG(and HFB-Popov): dotted line, analytic Eq.(5.79): red line), right: superfluid fraction $f_{\rm s}$ (Exact: solid line, BdG(and HFB-Popov): dotted line). The exact second order term (dashed line) of the superfluid fraction, $f_{\rm s}^{(2)}$ is also shown in these plots. In this case the agreement is much better.

However, if the approximate approach works well for these small systems we expect it to provide a good description of the larger systems prepared in the laboratory.

Because the second order term of the superfluid fraction (second term of Eq.(5.49) vanishes in the quadratic approximations (see Eq. (5.60)), we only expect them to give a good description of the superfluid fraction in the region where the second order term is extremely small, provided it predicts accurately the first order term. This is exactly what is observed in the plots. When the second order term starts to grow, typically above $0.5V_{eff}^{\rm crit}$ (with $V_{eff}^{\rm crit} = (U/J)_c$, see Eq.(3.9)), the BdG (and HFB-Popov) equations starts to fail. An estimate of $V_{eff}^{\rm crit}$ is shown by a vertical line in some of the figures. With increasing filling factor the critical value is shifted towards larger values of the interaction strength, and the region in which the BdG (and HFB-Popov) equations are accurate gets larger. It is interesting to note that the number fluctuations predicted by the theory are accurate in a greater range than the other physical quantities shown. Its predictions of squeezing agree very well with the exact solutions right up to the point where the number fluctuations become less than unity.

In the plots for the condensate fraction we also show the analytic approximation given by Eq.(5.79). It can be observed that the analytic solution agrees well with the numerical solution of the BdG(and HFB-Popov) equations.

For the cases with non-commensurate fillings the agreement is significantly

better for all quantities. This is not surprising because when the filling is not commensurate there is always a superfluid fraction present and the Mott transition doesn't occur. As can be seen in the plots for these cases the second order term is always very small.

- HFB equantions

  In the translationally invariant case the HFB Hamiltonian leads to the following equations:

$$\begin{pmatrix} \mathcal{L}_{\mathbf{qq}} & -\mathcal{M}_{\mathbf{q-q}} \\ \mathcal{M}_{\mathbf{q-q}} & -\mathcal{L}_{\mathbf{qq}} \end{pmatrix} \begin{pmatrix} u_{\mathbf{q}} \\ v_{\mathbf{q}} \end{pmatrix} = \omega_{\mathbf{q}} \begin{pmatrix} u_{\mathbf{q}} \\ v_{\mathbf{q}} \end{pmatrix}, \tag{5.86}$$

  with

$$\mathcal{L}_{\mathbf{qq}} = \epsilon_{\mathbf{q}} + n_o U - U\widetilde{m}, \quad \mathcal{M}_{\mathbf{q-q}} = n_o U + U\widetilde{m}. \tag{5.87}$$

  The diagonalization of them yields

$$\begin{aligned} \mu &= -tJ + Un_o + 2U\widetilde{n} + U\widetilde{m}, && (5.88)\\ {v_{\mathbf{q}}}^2 &= {u_{\mathbf{q}}}^2 - 1 = \frac{\mathcal{L}_{\mathbf{qq}} - 2\omega_{\mathbf{q}}}{2\omega_{\mathbf{q}}} = \frac{\epsilon_{\mathbf{q}} + n_o U - U\widetilde{m} - \omega_{\mathbf{q}}}{2\omega_{\mathbf{q}}}, && (5.89)\\ u_{\mathbf{q}} v_{\mathbf{q}} &= \frac{\mathcal{M}_{\mathbf{q-q}}}{2\omega_{\mathbf{q}}} = \frac{n_o U + U\widetilde{m}}{2\omega_{\mathbf{q}}}, && (5.90)\\ {\omega_{\mathbf{q}}}^2 &= {\epsilon_{\mathbf{q}}}^2 + 2U(n_o + \widetilde{m})\epsilon_{\mathbf{q}} - 4U^2 n_o \widetilde{m}, && (5.91) \end{aligned}$$

  with

$$\begin{aligned} \widetilde{n} &\equiv \frac{1}{M}\sum_{\mathbf{q}\neq\mathbf{0}} v_{\mathbf{q}}^2, && (5.92)\\ \widetilde{m} &\equiv -\frac{1}{M}\sum_{\mathbf{q}\neq\mathbf{0}} v_{\mathbf{q}} u_{\mathbf{q}}. && (5.93) \end{aligned}$$

  From the above equation it can be seen that the quasiparticle energies predicted under the HFB approximation don't approach zero as $\mathbf{q}$ goes to zero. As discussed in the previous section, the most important contribution to the depletion of the condensate in the BdG equations comes from the low lying modes, because of the ${\omega_{\mathbf{q}}}^{-1}$ dependence. The finite value of $\omega_{\mathbf{q}}$ has in the HFB approximation as $\mathbf{q}$ goes to zero explains why the HFB equations are always going to predict smaller condensate depletion than the gapless approximation.

  In Fig. 5.4 we compare the condensate fraction predicted by the HFB equations with the condensate fraction obtained from the BdG equations, for a system with $M = 3$ and filling factor $n = 10$. It can be seen that the condensate fraction is always higher in the HFB solutions and remains constant at higher values of U/J which is not physically correct.

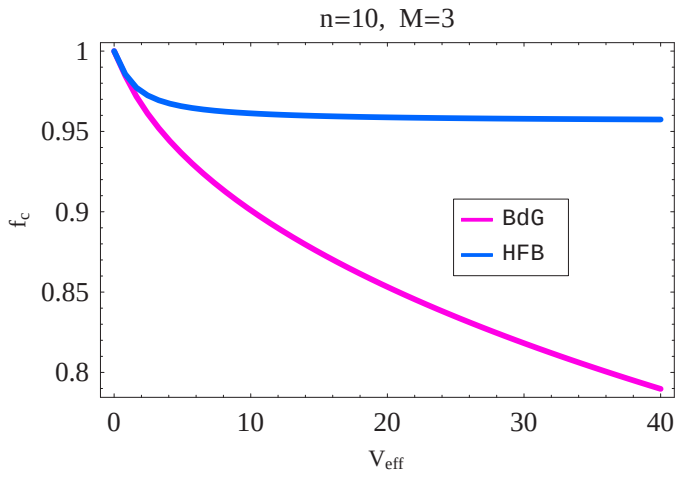

Figure 5.4: Comparisons of the condensate fraction given by the BdG solutions and the HFB equations as a function of $V_{eff} = U/J$, for a system with $M = 3$ and filling factor $n = 10$.

5.6.2 One-dimensional harmonic trap plus lattice

In this section we consider the experimentally relevant case when there is an external harmonic magnetic confinement in addition to the lattice potential. For simplicity we focus our attention on the one dimensional case. We consider the two most relevant approximations which are the BdG equations and the HFB-Popov approximation. Firstly we study the BdG equations in the weakly interacting regime and get some insight on the solutions by deriving analytic results using the so called Thomas-Fermi approximation [12]. Secondly we study the HFB-Popov approximation and use it to explore the limits of validity of the quadratic approximations as the interactions are increased.

- BdG equations

In the presence of the harmonic trap the BdG equations take the form:

$$\begin{aligned}
\omega_s^B u_n^s + c_s z_n &= -J(u_{n+1}^s + u_{n-1}^s) + (2U|z_n|^2 - \mu + \Omega n^2)u_n^s \\
&\quad -U z_n^2 v_n^s, \qquad (5.94)\\
-\omega_s^B v_n^s - c_s z_n^* &= -J(v_{n+1}^s + v_{n-1}^s) + (2U|z_n|^2 - \mu + \Omega n^2)v_n^s \\
&\quad -U z_n^{*2} u_n^s, \qquad (5.95)\\
\mu z_n &= -J(z_{n+1} + z_{n-1}) + (U|z_n|^2 + \Omega n^2)z_n, \qquad (5.96)\\
N &= \sum_n (|z_n|^2 + \tilde{n}_n), \qquad (5.97)\\
\tilde{n}_n &= \sum_s |v_n^s|^2, \qquad (5.98)\\
c_s &= U\frac{\sum_n |z_n|^2 (z_n^* u_n^s - z_n v_n^s)}{\sum_n |z_n|^2}. \qquad (5.99)
\end{aligned}$$

In the parameter regime where $U/J \ll 1$, but the number of atoms is large enough such that $NU/Ja_{ho} \gg 1$, where $a_{ho}=\sqrt{\frac{\hbar}{m^*\omega^*}}$ (See Eq. (2.39)) the Bogoliubov approximation takes a rather simple analytic form. The effect of increasing the ratio NU/Ja_{ho} is to push the atoms outwards, flattening the central density and increasing the width of the condensate wavefunction. The quantum pressure, which is proportional to the kinetic energy, takes a significant contribution only near the edges of the wavefunction, and to a good approximation it can be neglected. This is the so-called Thomas-Fermi approximation (TF). This approximation has been very useful to derive analytic expressions in magnetic confined condensates without the lattice and proved to be in agreement with experimental measurements [12, 18, 19].

Under the Thomas-Fermi approximation one gets a condensate density profile of the form of an inverted parabola which vanishes at the turning points $R_{TF} = \sqrt{\mu/\Omega}$:

$$|z_n|^2 = \begin{cases} \frac{\mu - \Omega n^2}{U} & n < R_{TF} \\ 0 & n > R_{TF} \end{cases} \qquad (5.100)$$

The chemical potential is determined by fixing the total number of particles. To first order it is possible to neglect the depletion of the condensate and assume that $\sum |z_n|^2 = N$. Changing the sum to an integral it can be solved for μ to get

$$\begin{aligned}
\mu &= \Omega R_{TF}^2, \\
R_{TF} &\approx \left(\frac{3}{4}\frac{NU}{\Omega}\right)^{1/3}. \qquad (5.101)
\end{aligned}$$

To solve for the excitation spectrum we use the Thomas-Fermi condensate amplitude, Eq.(5.100) into Eqs.(5.94)and (5.95) [18, 111] and use the parameter J as an expansion parameter in these equations. We define the variables $F_n^q = u_n^q + v_n^q$ and $G_n^s = u_n^s - v_n^s$. For simplicity we are going to set the constants c_s to zero and ignore the orthogonality constraint at the beginning. We correct this at the end by removing from the modes their projection onto the condensate. To first order in J we get the following set of equations:

$$2R_{TF}^2\Omega\left(1-\frac{n^2}{R_{TF}^2}\right)G_n^s = \omega_s^B F_n^s, \tag{5.102}$$

$$-J\left\{F_{n+1}^s + F_{n-1}^s - F_n^s\left(\frac{\sqrt{1-\frac{(n+1)^2}{R_{TF}^2}}+\sqrt{1-\frac{(n-1)^2}{R_{TF}^2}}}{\sqrt{1-\frac{n^2}{R_{TF}^2}}}\right)\right\}$$
$$= \omega_s^B G_n^s. \tag{5.103}$$

These two equations can be combined to get a simple equation of the form

$$\left\{\sqrt{1-\frac{(n+1)^2}{R_{TF}^2}}\sqrt{1-\frac{n^2}{R_{TF}^2}}\left(\widetilde{F}_{n+1}^s - \widetilde{F}_n^s\right)\right. \tag{5.104}$$
$$\left.-\sqrt{1-\frac{(n-1)^2}{R_{TF}^2}}\sqrt{1-\frac{n^2}{R_{TF}^2}}\left(\widetilde{F}_{n-1}^s - \widetilde{F}_n^s\right)\right\} = 2\left(\frac{\omega_s^B}{\omega^*}\right)^2\widetilde{F}_n^s,$$

with $\widetilde{F}_n^s = F_n^s/\sqrt{1-\frac{n^2}{R_{TF}^2}}$.

The above equation is just the discretized form of the Legendre equation, $\frac{\partial}{\partial x}\left((1-x^2)\frac{\partial}{\partial x}P_n\right) + n(n+1)P_n = 0$. Therefore the solutions of Eq. (5.104) are approximately given by :

$$\omega_s^B = \hbar\omega^*\sqrt{\frac{s(s+1)}{2}}, \tag{5.105}$$

$$F_n^s = \sqrt{\frac{\Omega R_{TF}(2s+1)}{\omega_s^B}}\sqrt{1-\frac{n^2}{R_{TF}^2}}P_s\left(\frac{n}{R_{TF}}\right), \tag{5.106}$$

$$G_n^s = \sqrt{\frac{\omega_s^B(2s+1)}{4\Omega R_{TF}^3}}\frac{1}{\sqrt{1-\frac{n^2}{R_{TF}^2}}}P_s\left(\frac{n}{R_{TF}}\right). \tag{5.107}$$

The larger the size of the condensate the closer are the approximate solutions, Eq.(5.107), to the exact solutions of Eqs. (5.104).

Finally, to make the solutions orthogonal to the condensate we have to remove their projection onto the condensate mode:

$$u_n^s \rightarrow u_n^s - c_s z_n/\omega_s^B, \tag{5.108}$$
$$v_n^s \rightarrow v_n^s - c_s z_n^*/\omega_s^B. \tag{5.109}$$

If we calculate the constants c_s using Eq. (5.99), and orthogonality properties of the Legendre polynomial we find that the only mode that needs to be corrected is the quadrupole mode, $s = 2$:

$$c_s = \sqrt{\frac{4\hbar\omega^* R^5\Omega^2}{15U}}\delta_{s,2}. \tag{5.110}$$

From Eqs. (5.110) it follows that the desired F and G amplitudes orthogonal to the condensate are thus given by

$$F_n^s \rightarrow F_n^s - 2c_s z_n/\omega_s^B, \tag{5.111}$$
$$G_n^s \rightarrow G_n^s. \tag{5.112}$$

Once solved for the quasiparticle amplitudes, it is possible to calculate the depletion of the condensate, $\widetilde{N} = \sum_{n,s} |v_n^s|^2$. It is important to point out that the term $\left(1 - \frac{n^2}{R_{TF}^2}\right)^{-1/2}$ in the G amplitudes makes the sum divergent. The divergence however is nonphysical and only indicates the failure of the TF approximation near R_{TF}. To perform the sum, we have to exclude the contribution from the boundary layer of thickness $d = \left(\frac{a_{ho}^4}{2R_{TF}}\right)^{1/3}$ where the TF approximation starts failing [111]. Finally, to fix the number of particles to N it is necessary to renormalize the condensate wave function and the chemical potential. This is done by renormalizing the Thomas Fermi radius and replacing N by $N - \widetilde{N}$ in Eq.(5.101).

In Fig. 5.5 we plot the condensate density profile found by numerically solving the BdG equations and compare it with the TF condensate solution. The TF approximation reproduces the numerical solution very accurately except at the edges where the kinetic energy can not be ignored with respect to the potential energy. In the same plot we also show the condensate depletion which is small for the chosen parameters. A small condensate depletion guarantees the validity of the quadratic approximation to describe the many-body system.

In Fig. 5.6 we show comparisons between the quasiparticle energies found numerically, the TF quasiparticle and excitation spectra of the noninteracting system (see Eq. (2.37)). It can be seen in the plot that only the lowest

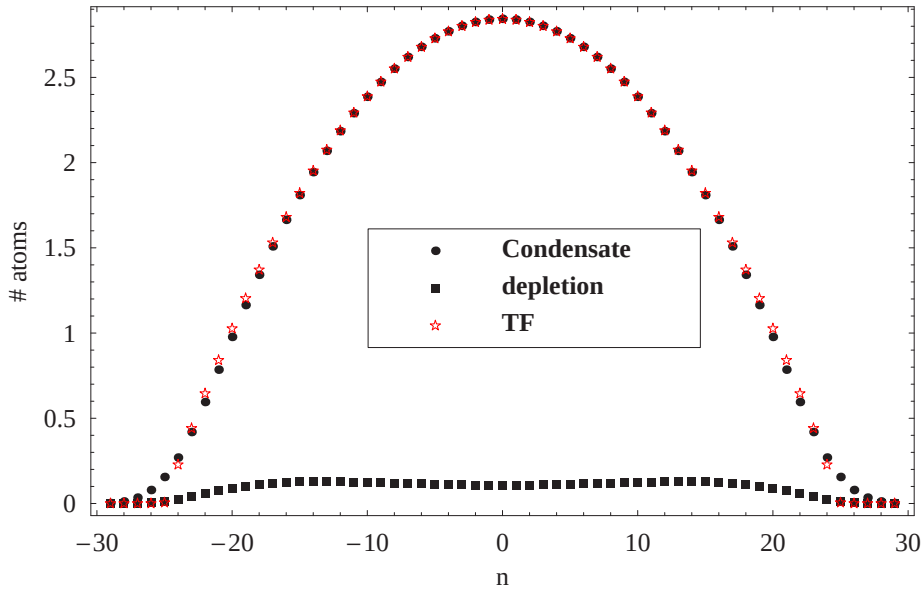

Figure 5.5: Comparisons of the condensate wave function found by numerically solving the BdG equations with the Thomas-Fermi solution. The parameters used were $U/J = 0.2$, $\Omega/J = 9.5 \times 10^{-4}$ and $N = 100$. The depletion is also shown in the plot.

lying modes are well described by the TF approximation. Higher excitation energies are closer to the noninteracting ones. In the regime where $\Omega < J$ and the system's size is large enough that discretization effects, neglected in Eqs. (5.105), are not important, the first quasiparticle excitation energy coincide with the first noninteracting excitation energy . This first excitation is known as the dipole mode and describes the oscillatory motion of the center of mass when the system is displaced. The dipole quasiparticle amplitudes $(u_n^{s=1}, v_n^{s=1})$, calculated by numerically solving the BdG equations are shown in Fig. 5.7. In the same graphic the quasiparticle amplitudes for the $s = 2, 3, 4$ excitation modes are also depicted. The $s = 2$ mode is known as the quadrupole mode and is related to the breathing of the condensate when shaken. Higher order modes describe more complicated collective excitations. In general, quasiparticle excitations other than the dipole are affected by interactions and they have different energy than the noninteracting excitations. As shown in Fig. 5.6 TF quasiparticle energies lie below their noninteracting conterparts.

To test the accuracy with which the TF approximation describes the quasiparticle amplitudes, in Fig. 5.8 we compare the product $F_n^s G_n^s$ as a function of the lattice site n using the TF approximation results (Eqs. (5.112) and (5.111)) to the product found by numerically solving the BdG equations. We observe good agreement between the two solutions except near the TF

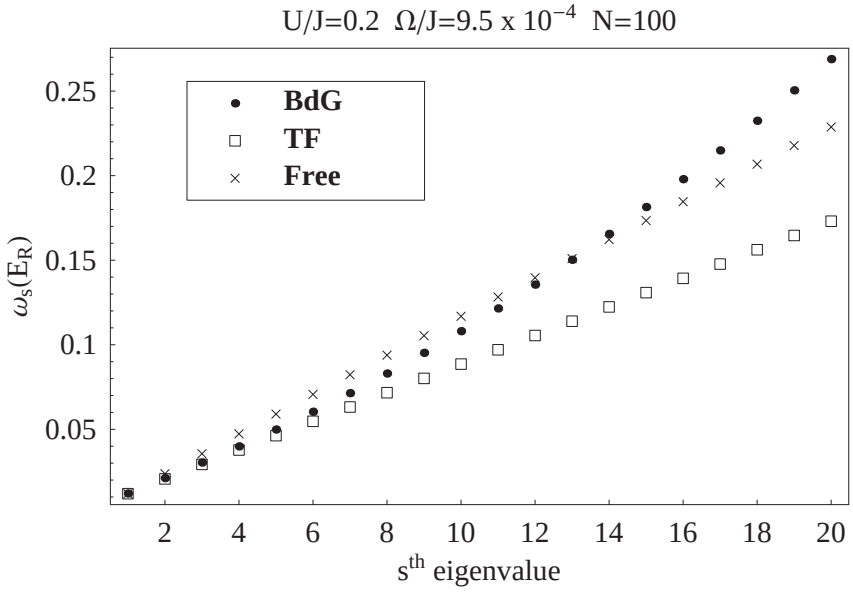

Figure 5.6: Comparisons of the quasiparticle spectrum found by numerically solving the BdG equations(BdG) with the Thomas-Fermi solution (TF) and the noninteracting energies (Free). The parameters used were $U/J = 0.2$, $\Omega/J = 9.5 \times 10^{-4}$ and $N = 100$.

radius. This behavior is consistent with the fact that near the edge of the atomic cloud, the kinetic energy becomes comparable to the potential energy and therefore the TF approximation breaks down.

- HFB-Popov approximation

  In the translationally invariant system, both the BdG and the HFB-Popov approximations give the same quasiparticle amplitudes and energies. However, when the harmonic confinement is present this is no longer the case. The HFB-Popov approximation shifts the quasiparticle energies depending on the spatial variation of the non condensate density in the region of the condensate. In this section we investigate the limits of validity of the HFB-Popov approximation as the parameter U/J is increased. We use the HFB-Popov approximation instead of the BdG approximation because of the relevant role of the noncondensate atoms into the condensate as the system is driven to the Mott insulator transition.

  In the presence of an harmonic confinement the HFB-Popov equations take

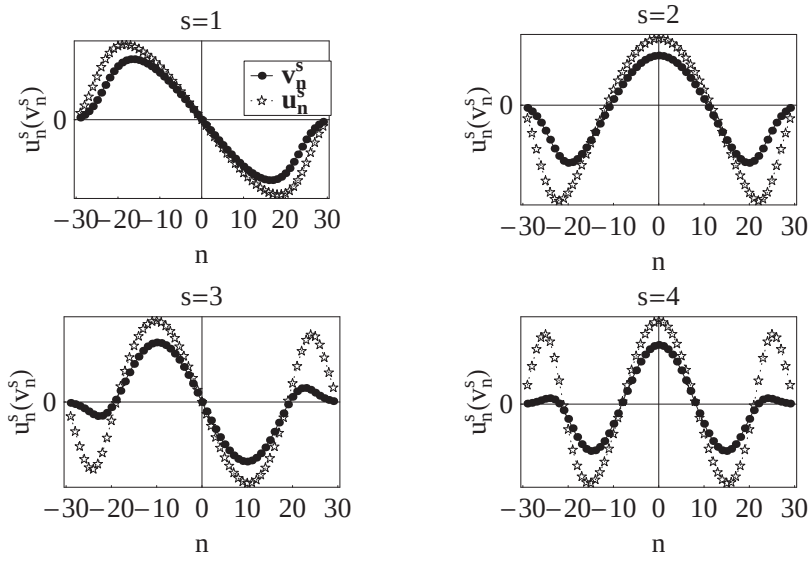

Figure 5.7: Low-lying quasiparticle amplitudes found by numerically solving the BdG equations. The parameters used were $U/J = 0.2$, $\Omega/J = 9.5 \times 10^{-4}$ and $N = 100$.

the form:

$$\begin{aligned}
\omega_s u_n^s + c_s z_n &= -J(u_{n+1}^s + u_{n-1}^s) + (2U(|z_n|^2 + \tilde{n}_n) - \mu + \Omega n^2)u_n^s \\
&\quad -U z_n^2 v_n^s, \qquad (5.113)\\
-\omega_s v_n^s - c_s z_n^* &= -J(v_{n+1}^s + v_{n-1}^s) + (2U(|z_n|^2 + \tilde{n}_n) - \mu + \Omega n^2)v_n^s \\
&\quad -U z_n^{*2} u_n^s, \qquad (5.114)\\
\mu z_n = -J(z_{n+1} &+ z_{n-1}) + \left(U(|z_n|^2 + 2\tilde{n}_n) + \Omega n^2\right) z_n, \qquad (5.115)\\
\tilde{n}_n &= \sum_s |v_n^s|^2, \qquad (5.116)\\
N &= \sum_n (|z_n|^2 + \tilde{n}_n), \qquad (5.117)\\
c_s &= U \frac{\sum_n |z_n|^2 (z_n^* u_n^s - z_n v_n^s)}{\sum_n |z_n|^2}. \qquad (5.118)
\end{aligned}$$

The HFB-Popov are nonlinear equations and therefore it is more complicated to get analytic approximations. Instead, we solved the HFB-Popov equations numerically by an iterative procedure, similar to the one followed in Ref. [19]. Each cycle of the iteration consists of two steps. In the first step we solve Eq. (5.115) subject to the constraint Eq. (5.117) by using the $\tilde{n}_n$ obtained in the previous cycle. This generates new values for the z_n. In the second step we solve for $\{u_n^s, v_n^s\}$ in Eqs. (5.113) using the $\tilde{n}_n$ from the previous cycle and the newly generated z_n. The $\{u_n^s, v_n^s\}$ are used then to update $\tilde{n}_n$.

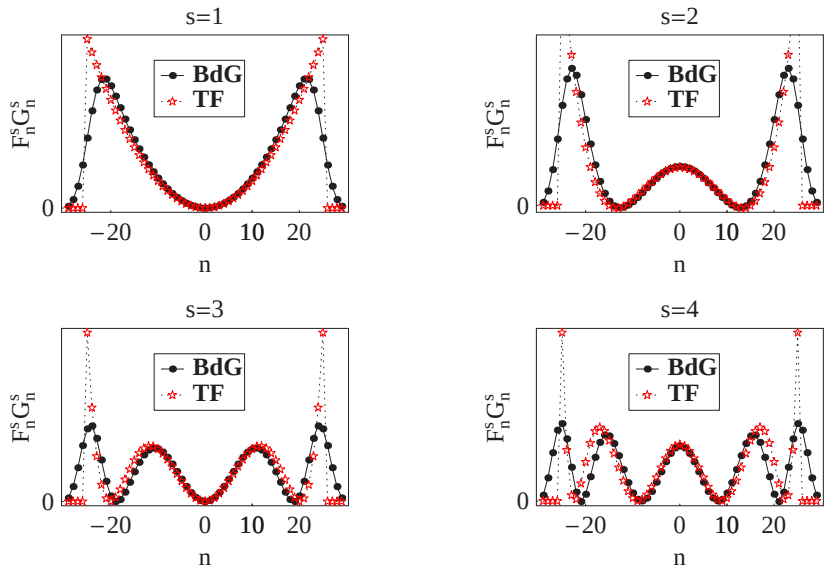

Figure 5.8: Comparisons between the product $F_n^s G_n^s$ calculated from the Thomas-Fermi approximation and the exact numerical solution of the BdG equations. The parameters used were $U/J = 0.2$, $\Omega/J = 9.5 \times 10^{-4}$ and $N = 100$.

Because the HFB-Popov is gapless, it is possible to keep the orthogonality of the excitations to the condensate by solving Eqs. (5.113) with the c^s set to zero but removing in each cycle the projection of the calculated $\{u_n^s, v_n^s\}$ amplitudes onto the condensate. Convergence is reached when the change in $\sum_n |\tilde{n}_n|^2$ from one cycle to the next is smaller than a specified tolerance.

The parameters chosen for the numerical calculations were $\Omega = 0.0015 E_R$, with E_R the one photon recoil energy, which for the case of a rubidium condensate corresponds to a trap frequency of approximately 90 Hz. We used a total number of 1000 atoms, $N = 1000$, and set $UN = 1.0 E_R$. J was varied to achieve a range of $V_{eff} = U/J$ between 0.01 and 312. The range was chosen based on a local mean field approach [77], which for our parameters estimates the transition region between $V_{eff} \approx 640$ (at the center where the local filling factor is approximately 80) and $V_{eff} \approx 12$ (at the wings).

The results of the numerical calculations are summarized in Figs. (5.9-5.13). In Fig. 5.9 we plot the evolution of the density profile (black boxes), the condensate population (triangles) and the on-site depletion (empty diamonds) as V_{eff} is increased. In the plots we also show, for comparison purposes, the ground state density profile for $J = 0$ (empty boxes). This has the advantage that it can be calculated exactly from the Hamiltonian. In general we observe the reduction of the condensate population and thus the increment

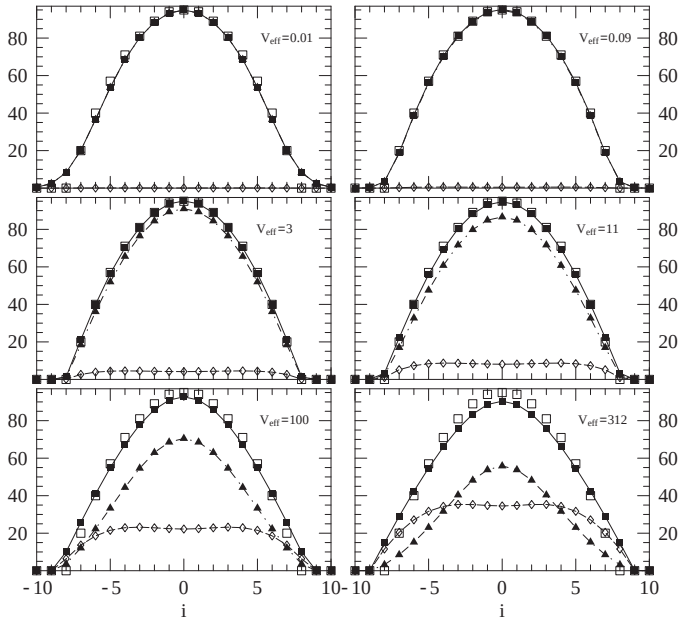

Figure 5.9: Condensate density (triangles), total density (filled boxes) and local depletion (empty diamonds) as a function of the lattice site i for different values of $V_{eff.}$.The site indices i are chosen such that $i = 0$ corresponds to the center of the trap. Although these quantities are defined only at the discrete lattice sites we join them to help visualization. The empty boxes represent the exact solution for the case J=0.

of the depletion with increasing interaction strength. When the system is in the superfluid regime, most of the atoms are in the condensate, but as J is decreased the depletion of the condensate becomes very important.

For the chosen parameters, the density profile has a parabolic shape reflecting the confining potential. By comparing the evolution of the density as J is decreased with the exact solution at $J = 0$, we can crudely estimate the validity of the HFB-Popov calculations. The density evolves from a Gaussian type (see plots for $V_{eff} = 0.01$ and 0.09) with smooth edges towards a Thomas-Fermi profile with sharp edges adjusting its shape to the $J = 0$ profile. We can appreciate that around $V_{eff} = 3$ both profiles are almost equal. For lower values of J the HFB-Popov density starts to differ from the $J = 0$ limit, even though the system is closer to the $J = 0$ limit. We can say that beyond this point higher order correlations, neglected by the theory, begin to be important. The departure of the HFB-Popov density profile from the $J = 0$ one as J is decreased begins at the edges (see the panels corresponding to $V_{eff} = 11$ and 100). This is expected if we consider the on-site depletion. For such values of V_{eff} the local depletion in the wings

corresponds to a considerable percentage of the condensate populations, and thus the validity of the HFB-Popov assumptions starts to be dubious. The homogeneous results shown in the previous sections corroborate our present statements for the confined system. For the smallest filling factor (see Fig. 5.2) the differences between the homogeneous HFB-Popov calculations and the exact solutions become important for values of V_{eff} greater than 20. For higher values of V_{eff}, see plot for $V_{eff} = 312$, the HFB-Popov density predictions differs from the $J = 0$ solution even at the central wells. At this point the failure of the method is clear and a fully quantal method is required.

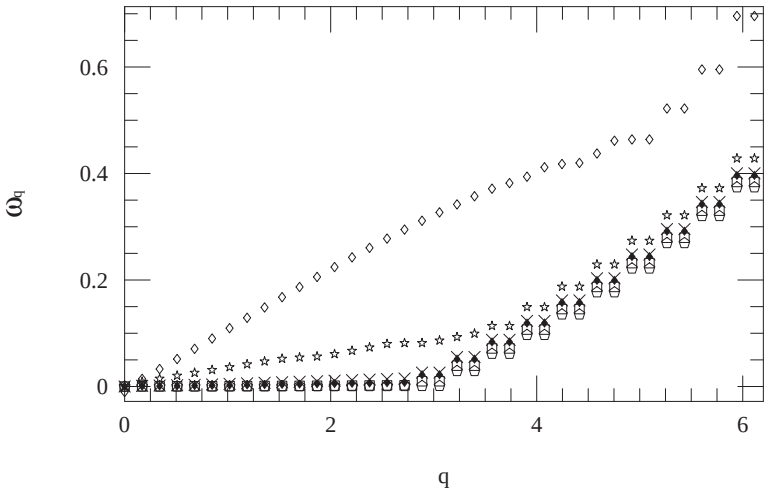

Figure 5.10: Quasiparticle spectrum predicted by the HFB-Popov theory for different values of V_{eff}: Empty diamonds ($V_{eff} = 0.01$), stars ($V_{eff} = 0.09$), crosses ($V_{eff} = 3$), filled diamonds ($V_{eff} = 11$), empty boxes ($V_{eff} = 100$) and pentagons ($V_{eff} = 312$). The letter q labels the quasiparticle energies in increasing order. The quasiparticle energies are in recoil units.

The HFB-Popov quasiparticle spectrum is shown in Fig. 5.10. It can be observed how the lower energy eigenvalues evolve from a linear non degenerated spectrum to an almost degenerated one as J is decreased. It is worth mentioning that the small energy difference between the ground and first excited states for high values of V_{eff} makes the numerical solution very unstable in the sense that it is very easy to jump to an excited state when solving for the condensate wave function. The decrement in the energy spacing predicted by the HFB-Popov theory as the system approaches the transition is very useful to keep in mind for the experimental realization of the Mott transition. As the optical lattice depth is ramped up the adiabaticity criteria is harder to

fulfill.

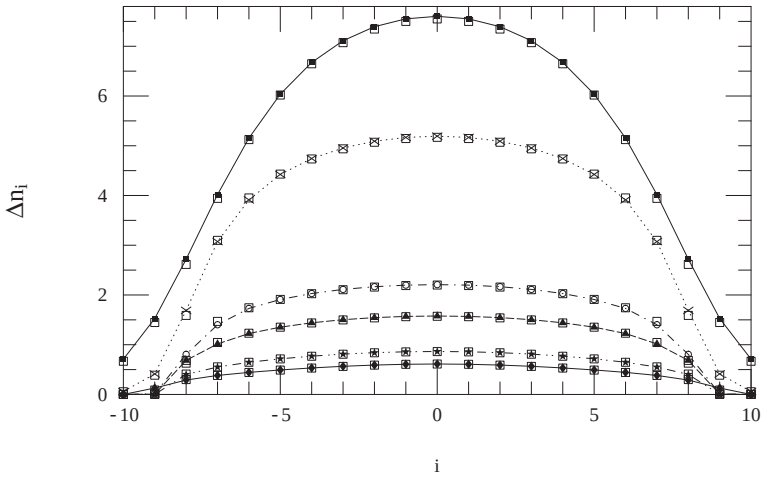

Figure 5.11: Number fluctuations in the self consistent HFB-Popov approach as a function of lattice site for $V_{eff} = 0.01$ (boxes), $V_{eff} = 0.09$ (crosses), $V_{eff} = 3$ (circles),$V_{eff} = 11$ (triangles), $V_{eff} = 100$ (stars) and $V_{eff} = 312$ (diamonds). The maximum value reached by the profile decreases as V_{eff} is increased. The empty boxes shown for each of the curves correspond to the number fluctuations predicted by the homogeneous HFB-Popov model using a local density approximation.

In Fig. 5.11 we plot the results for the number fluctuations found numerically using the inhomogeneous HFB-Popov approach. The number fluctuations profile reflects the condensate profile. We also show the number fluctuations evaluated by using a local density approximation (empty boxes). The latter was calculated by substituting in the number fluctuations expression (Eq. (5.56)) the $\{u^q, v^q\}$ amplitudes found for the homogeneous system (Eqs. (5.66) and (5.67)), but replacing the condensate density in each lattice site by the one found numerically for the trapped system (see Fig. 5.9). The complete agreement between the two approaches justifies the validity of the local density approximation for the estimations of local quantities in confined systems. Based on this agreement and the results for the homogeneous system shown in the previous section, we expect that the inhomogeneous HFB-Popov results for squeezing also agree with the exact solutions right up to the transition.

In Fig. 5.12 we present the quasimomentum distribution for the same parameters used in the previous plots. The distribution for the two lowest values of V_{eff} corresponds to the one that characterizes an uncorrelated superfluid phase with a narrow peak at small quasimomenta. As the hopping rate is decreased we observe that the sharpness of the central peak decreases and

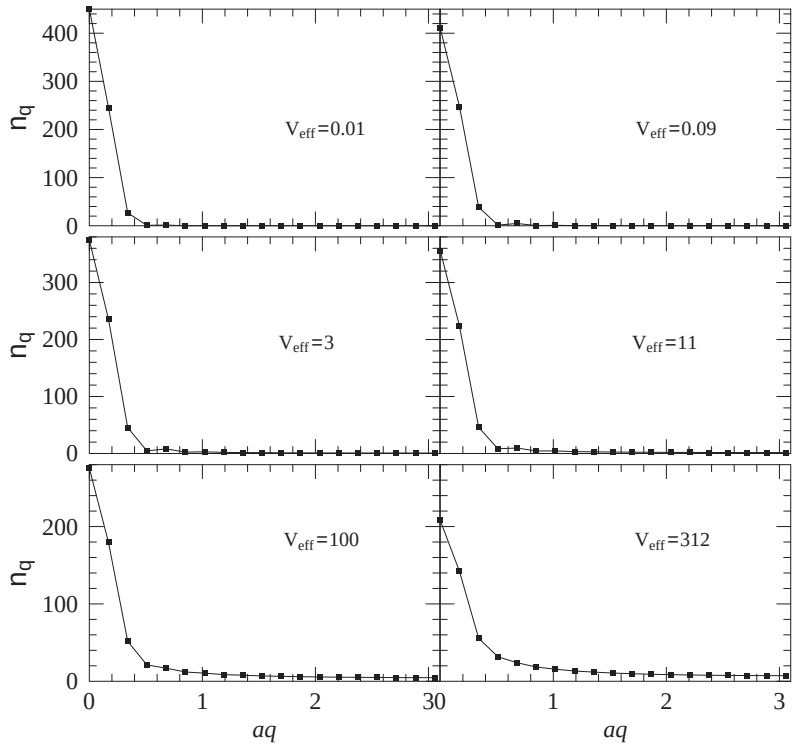

Figure 5.12: Quasimomentum distribution as a function of qa, a the lattice spacing, q the quasimomentum, for different values of V_{eff}.

the distribution extends towards large quasi-momenta. It is interesting to note the appearance of a small peak between $q = 0.5$ and 1 which is most noticeable for the $V_{eff} = 3$ case. This agrees with numerical solutions of the Bose-Hubbard Hamiltonian using Monte Carlo simulations [112]. We attribute the origin of the small peak to the depletion of the condensate at the wings. For the parameters when the small peak is present, the most important contribution to the quasimomentum distribution still comes from the condensate atoms. The step function like shape of the condensate profile causes an oscillatory $|\sin(x)/x|$ shape of the quasimomentum distribution. As the lattice depth is increased the hopping becomes energetically costly, the long-range order starts to decrease and the Fourier spectrum becomes broader.

In Fig. 5.13 we plot the first order on site superfluid fraction $f_{sn}^{(1)}$ which was defined in Eq.(5.60). The curves corresponding to $V_{eff} = 0.01 - 11$, which are in the regime where the HFB-Popov is expected to be valid, depict how as V_{eff} is increased the superfluid profile decreases faster at the wings and at the center but no major change is observed in the middle section. The evolution of the on-site superfluidity as the interaction strength is in-

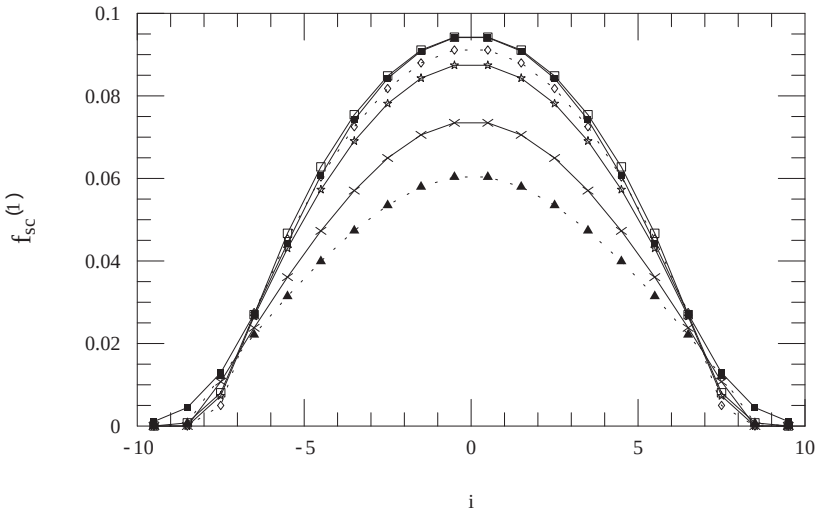

Figure 5.13: First order on-site superfluid fraction as a function of the lattice site i for different values of $V_{eff.}$.The site indices i are chosen such that $i = 0$ corresponds to the center of the trap. Filled boxes: $V_{eff.}$ =0.01, empty boxes: $V_{eff.} = 0.09$, empty diamonds: $V_{eff.} = 3$, stars: $V_{eff.} = 11$, crosses: $V_{eff.} = 100$ and triangles: $V_{eff.} = 312$.

creased, exhibiting a domain localized decrement instead of a global one, is in agreement with the development of uncompressible regions surrounded by superfluid rings predicted for trapped systems [79] as the transition is approached.

The Mott transition is a quantum phase transition and as for all critical phenomena, its behavior depends strongly on the dimensionality of the system. In the present analysis, due to computational limitations, we considered one dimensional systems. Experimentally, the Mott transition has been achieved [46] in a 3 dimensional lattice with filling factors between 1 and 3. Even though the HFB-Popov approach fails to describe the strong coupling regime for the one dimensional systems we considered, we showed how the method is incredibly powerful in describing most of its characteristic features as they are driven from the superfluid regime towards the transition. We expect the HFB-Popov method to give a better description of the transition as the dimensionality of the system is increased and therefore to be a good model in an experimental situation.

As shown in previous studies [44], [79] the Mott transition in a d-dimensional homogeneous system has two different critical behaviors: one (d+1) XY- like, for systems with fixed integer density as the interaction strength is changed, and one mean field-like exhibited when the transition is induced by changing

the density. Different from the homogeneous case where the Mott transition is characterized by the global offset of the superfluidity, for confined systems, commensuration is only well defined locally. The inhomogeneity introduced by the confining potential allows the existence of extended Mott domains (above a critical interaction strength) surrounded by superfluid ones [79], thus the total superfluid fraction doesn't vanishes in the Mott regime. This issue, together with the fact that the finite length scale introduced by the trap suppresses the long wave fluctuations which are responsible for destroying the mean field [16][1], make us believe the critical behavior in confined systems to be more mean-field like. Because the critical dimension for the latter type of transition is two [44], [79], we expect that for trapped systems in $d = 3$, the range of validity of the HFB-Popov extends closer to the transition.

5.7 Improved HFB-Popov approximation

The corrections to the quadratic Hamiltonian from higher order terms have essentially two major effects. Firstly, they include the effect of the interactions between condensate and noncondensate atoms on the behavior of the condensate. Secondly, they take into account the effect of the surrounding atoms on the nature of the interatomic collisions. We mentioned previously that although the HFB treatment should represent an advance over the BdG theory it is not useful in practice because it is not gapless. In the first part of this section we show, how, by taking into account the anomalous average $\widetilde{m}$ (Eq. (5.18)) we actually upgrade the bare interaction potential U to the many body scattering matrix which gives a better description of interparticle collisions. The problem with the HFB equations is that not all the interactions are upgraded and the diagonal elements still contain bare interaction terms. The different treatment of the off diagonal and diagonal terms is caused by the factorization approximation on which the HFB approximation is based. The factorization is appropriate for the quartic term in the Hamiltonian (as it is justified by Wick's theorem [16]) but not for the cubic terms.

To solve the problem the first approximation that one might think of is to upgrade by hand the bare interactions in the diagonal terms and replace them by the many-body scattering matrix. This procedure is known as the improved Popov approximation [53, 16]. In this section, we discuss the improved Popov approximation and apply it to a translationally invariant system. We explicitly show that the improved Popov approximation gives a better description of the many-body physics as the Mott insulator transition is approached in comparison with the regular HFB-Popov approximation.

[1] One obvious consequence of this is that BEC is possible in one and two dimensions in a trap whereas in the homogeneous, thermodynamic limit it can not occur in fewer than three dimensions

5.7.1 The two-body and many-body scattering matrices

The two-body scattering matrix, T_{2b}, describes the scattering of two particles in vacuum. It is defined as a function of a complex parameter z by the Lippmann-Schwinger equation:[51]

$$T_{2b}(z) = V + V\frac{1}{z - \hat{H}^{sp}}T_{2b}(z), \tag{5.119}$$

Here V is the interatomic potential and $\hat{H}^{sp}$ is the single particle Hamiltonian. Although T_{2b} is defined for a general complex parameter z, this is physically interpreted as the energy of the scattering process. Inserting a complete set of eigenstates in Eq. (5.119) one obtains:

$$T_{2b}(z) = V + \sum_{pq} V|\mathbf{pq}\rangle\frac{1}{z - (\varepsilon_{\mathbf{p}} + \varepsilon_{\mathbf{q}})}\langle\mathbf{pq}|T_{2b}(z), \tag{5.120}$$

where $\varepsilon_{\mathbf{p}}$ and $\varepsilon_{\mathbf{q}}$ are single particle energies (eigenvalues of $\hat{H}^{sp}$), and the kets $|\mathbf{pq}\rangle$

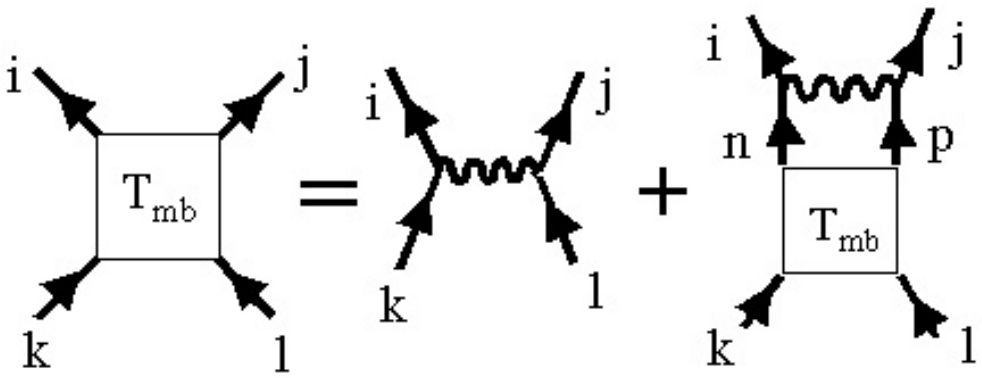

Figure 5.14: Diagrammatic representation of the two-body T_{2b} scattering matrix. In this figure $|\mathbf{kl}\rangle$ designates the initial states, $|\mathbf{ij}\rangle$ the final states and $|\mathbf{np}\rangle$ a set of intermediate states

T_{2b} describes the interaction between two particles in vacuum. In the interacting Bose system, binary collisions do not occur in vacuum but in the presence of other atoms. To describe their influence on the scattering the concept of the many-body scattering matrix is introduced. The many-body scattering matrix, T_{mb}, plays the same role as its two-body counterpart, but describes scattering occurring in many-body systems. For a bosonic gas there are two major effects

which need to be accounted for as compared to scattering in vacuum. First of all, the relevant states which enter in the matrix elements should be many-body states rather than single particle ones. Second, T_{mb} should account for Bose enhancement of a scattering process. Various forms for the T_{mb} have been been proposed in the literature [16, 53, 54, 113] depending upon the approximations made. The one that we are going to use is a simplest generalization of the two-body matrix given by [16, 113]:

$$\mathrm{T}_{mb}(z) = V + \sum_{\mathbf{pq}} V|\mathbf{pq}\rangle \frac{1 + n_{\mathbf{p}} + n_{\mathbf{q}}}{z - (\omega_{\mathbf{p}} + \omega_{\mathbf{q}})} \langle \mathbf{pq}|\mathrm{T}_{mb}(z), \tag{5.121}$$

where z is again a complex parameter, $\omega_{\mathbf{p}}$ and $\omega_{\mathbf{q}}$ are quasiparticle energies, $n_{\mathbf{q}}$ and $n_{\mathbf{p}}$ are thermal quasiparticle occupation factors which vanish at $T = 0$, and $|\mathbf{pq}\rangle$ correspond to single-particle wave functions. The full quasiparticle character of the intermediate states is not taken into account in this simple definition. A more general many-body scattering matrix which includes the full quasiparticle wave functions has been discussed by Bijlsma and Stoof [53]. However this simpler T_{mb} matrix is the one that naturally appears in the many-body theory, at least at lowest order.

At this point it is important to highlight that the zero energy of the many-body scattering matrix is not the same as the zero energy in its two-body counterpart. Because the two-body matrix is written in terms of single particle energies, in this case the z is measured relative to the energy of a stationary particle. In the many-body case T_{mb} is defined in terms of quasiparticle energies and therefore z is measured with respect to the condensate chemical potential. In the dilute gas limit, where the inter-particle distance is large compared with the s-wave scattering length, the ladder diagrams included in the T_{mb} give the largest contribution to the modification of the bare potential due to interactions.

5.7.2 The anomalous average and the many-body scattering matrix

In this section we are going to follow [16, 53] to show how by including the anomalous average the many-body scattering matrix is introduced into the theory. For interpretation purposes we are going to restrict the analysis to the translationally invariant system.

The anomalous average $\widetilde{m}$ is defined in terms of the quasiparticle amplitudes u_q and v_q according to Eq.(5.93). The product $u_q v_q$, on the other hand, is related to the off diagonal matrix elements, see Eq.(5.90). If we combine the two equations we get an expression for the off diagonal matrix element $\mathcal{M}_{\mathbf{q}-\mathbf{q}}$ given by

$$\frac{\mathcal{M}_{\mathbf{q}-\mathbf{q}}}{n_o} = U + \frac{U}{M} \sum_{p} \frac{1}{-(\omega_{\mathbf{p}} + \omega_{-\mathbf{p}})} \frac{\mathcal{M}_{\mathbf{q}-\mathbf{q}}}{n_o}. \tag{5.122}$$

To make the connection with the many-body scattering matrix, let us take the inner product of Eq. (5.121), with the states $\langle \mathbf{q} - \mathbf{q}|$ and $|\mathbf{00}\rangle$ and evaluate it at

$z = 0$. At zero temperature, the thermal occupation factors vanish, $n_q = 0$ and we get:

$$\langle \mathbf{q}-\mathbf{q}|\mathrm{T}_{mb}(0)|\mathbf{00}\rangle = \langle \mathbf{q}-\mathbf{q}|V|\mathbf{00}\rangle + \sum_{pk}\langle \mathbf{q}-\mathbf{q}|V|pk\rangle \frac{1}{-(\omega_{\mathbf{p}}+\omega_{\mathbf{k}})}\langle pk|\mathrm{T}_{mb}(0)|\mathbf{00}\rangle. \tag{5.123}$$

The quantity $\langle \mathbf{k}_1\mathbf{k}_2|\,V\,|\mathbf{k}_3\mathbf{k}_4\rangle$ is the momentum representation of the two-body interaction potential V. In the Bose-Hubbard Hamiltonian we assume a contact potential with amplitude U which yields a potential in the momentum representation given by

$$\langle \mathbf{k}_1\mathbf{k}_2|\,V\,|\mathbf{k}_3\mathbf{k}_4\rangle = \frac{U}{M}\delta_{\mathbf{k}_1+\mathbf{k}_2,\mathbf{k}_3+\mathbf{k}_4}. \tag{5.124}$$

Using Eq. (5.124) into (Eq. 5.123) we obtain

$$\mathcal{T}_{mb} \;=\; U + \frac{1}{M}\sum_{p} U \frac{1}{-(\omega_{\mathbf{p}}+\omega_{-\mathbf{p}})}\mathcal{T}_{mb}, \tag{5.125}$$

with

$$\langle \mathbf{p}-\mathbf{p}|\mathrm{T}_{mb}(0)|\mathbf{00}\rangle \;\equiv\; \frac{1}{M}\mathcal{T}_{mb}. \tag{5.126}$$

Eqs. (5.125) and (5.122) imply that $\mathcal{M}_{\mathbf{q}-\mathbf{q}} = n_o\mathcal{T}_{mb}$, and therefore that by including the anomalous average in the equations, the off diagonal matrix element given by Un_o in the BdG equations is upgraded to $\mathcal{T}_{mb}n_o$ in the HFB equations.

The many-body scattering matrix also appears in the DNLSE since Eq. (5.89) contains $\widetilde{m}$:

$$\mu = -tJ + Un_o + 2U\widetilde{n} + U\widetilde{m} = -tJ + \mathcal{T}_{mb}n_o + 2U\widetilde{n}. \tag{5.127}$$

Finally, to conclude this section we just rewrite the HFB equations in terms of $\mathcal{T}_{mb}$ obtaining:

$$\begin{pmatrix} \epsilon_{\mathbf{q}} + n_o(2U - \mathcal{T}_{mb}) & -n_o\mathcal{T}_{mb} \\ n_o\mathcal{T}_{mb} & -\epsilon_{\mathbf{q}} - n_o(2U-\mathcal{T}_{mb}) \end{pmatrix} \begin{pmatrix} u_{\mathbf{q}} \\ v_{\mathbf{q}} \end{pmatrix} = \omega_{\mathbf{q}} \begin{pmatrix} u_{\mathbf{q}} \\ v_{\mathbf{q}} \end{pmatrix}. \tag{5.128}$$

This allow us to explicitly see the different treatment that the theory gives to the diagonal and off diagonal terms: The bare potential is completely upgraded to $\mathcal{T}_{mb}$ in the off diagonal terms but is not in the diagonal ones, and in the chemical potential.

5.7.3 Improved Popov approximation

The appearance of a gap in the HFB equations is because of the different treatment of the off diagonal and diagonal terms. We will show in chapter 8 that as we go beyond the quadratic approximation of the Hamiltonian and include higher order corrections we start to incorporate the many-body scattering in the diagonal terms. However, a naive way to correct for the gap problem in the HFB equations is simple to upgrade by hand the interactions in the diagonal terms and replace them by the many-body scattering matrix. This way to proceed is known as the improved Popov approximation [16, 53]. The matrix we have to diagonalize under the improved Popov approximation is:

$$\begin{pmatrix} \epsilon_{\mathbf{q}} + n_o\mathcal{T}_{mb} & -n_o\mathcal{T}_{mb} \\ n_o\mathcal{T}_{mb} & -(\epsilon_{\mathbf{q}} + n_o\mathcal{T}_{mb}) \end{pmatrix} \begin{pmatrix} u_{\mathbf{q}} \\ v_{\mathbf{q}} \end{pmatrix} = \omega_{\mathbf{q}} \begin{pmatrix} u_{\mathbf{q}} \\ v_{\mathbf{q}} \end{pmatrix} \tag{5.129}$$

$$\mu = -tJ + \mathcal{T}_{mb}n_o + 2\widetilde{\mathcal{T}}_{mb}\widetilde{n} \tag{5.130}$$

Eqs. (5.129) and (5.130) together with Eq. (5.125) and Eq. (5.69) form a closed set of equations. They are exactly the same than the HFB-Popov equations if U is replaced by $\mathcal{T}_{mb}$. The reason why there are two different coupling constant in the equation for the chemical potential $\mathcal{T}_{mb}$ and $\widetilde{\mathcal{T}}_{mb}$, is because they describe two different scattering processes. The second term in the right hand side of Eq. (5.130) describes the scattering between two atoms in the condensate colliding at zero momentum, $\langle \mathbf{q}-\mathbf{q}|\mathrm{T}_{mb}(0)|\mathbf{00}\rangle$, and that is why the coupling constant is $\mathcal{T}_{mb}$ (see Eq. 5.126). On the other hand, the third term describes the collision between one condensate atom and one atom out of the condensate and the coupling constant in this case should be evaluated at different energy $\widetilde{\mathcal{T}}_{mb} \propto \sum_{\mathbf{p}} \langle \mathbf{p0}|\mathrm{T}_{mb}(\omega_{\mathbf{p}})|\mathbf{0p}\rangle$.

The extra difficulty that the improved Popov equations have compare with the HFB-Popov equations is that $\mathcal{T}_{mb}$ depends on the quasiparticle energies and all equations must be solved in a self consistent way. To get simple analytic expressions we start by analyzing limiting regimes.

- Case $n_o\mathcal{T}_{mb} > J$

  In this regime the quasiparticle energy can be approximated by $\omega_{\mathbf{q}} \backsim \sqrt{2n_o\mathcal{T}_{mb}\epsilon_{\mathbf{q}}}$. Using this approximation in the expression for the many-body scattering matrix we obtain

  $$\mathcal{T}_{mb} = \frac{U}{1 + \sqrt{\frac{U^2\alpha^2}{n_oJ\mathcal{T}_{mb}}}}, \tag{5.131}$$

  with α defined in Eq. (5.73). Solving the algebraic equation we get two possible solutions

  $$\mathcal{T}_{mb} = U \pm \frac{U^2}{2Jn_o}\left(\alpha^2 + \sqrt{\alpha^4 + \frac{4Jn_o\alpha^2}{U}}\right). \tag{5.132}$$

Because we want the root which increases as U increases we choose the solution with positive sign.

- Case $n_o\mathcal{T}_{mb} < J$

  In general one can show that the condition $n_o\mathcal{T}_{mb} < J$ is only satisfied if the quantity $\mathcal{T}_{mb}/J$ is small. This also implies that the parameter U/J must be small. In this regime, therefore, we can perturbatively expand Eq.(5.131) in powers of U/J to get:

$$\mathcal{T}_{mb} \backsim U\left(1 + O\left(\frac{U}{J}\right)\right). \tag{5.133}$$

The fact that Eq. (5.134) has the correct asymptotic behavior in the limit $n_o\mathcal{T}_{mb} < J$ (it approaches to U as U goes to zero) even though it was derived under the assumption $n_o\mathcal{T}_{mb} > J$, allow us to extend the validity of Eq. (5.132) to all regimes. Therefore, to a good approximation, we get a general formula for $\mathcal{T}_{mb}$ given by:

$$\mathcal{T}_{mb} = U + \frac{U^2}{2Jn_o}\left(\alpha^2 + \sqrt{\alpha^4 + \frac{4Jn_o\alpha^2}{U}}\right). \tag{5.134}$$

We have checked numerically that in fact, Eq. (5.134) is a very good approximation of $\mathcal{T}_{mb}$ in all regimes.
Having an analytic expression for $\mathcal{T}_{mb}$, we can solve for the condensate density to get:

$$\begin{aligned} n_o &= n - \frac{1}{M}\sum_{\mathbf{q}\neq\mathbf{0}} \frac{\epsilon_{\mathbf{q}} + Un_o}{2\omega_{\mathbf{q}}} + \frac{1}{2}, \\ &\approx g - \alpha\sqrt{\frac{\mathcal{T}_{mb}}{J}n_o}. \end{aligned} \tag{5.135}$$

In the above equation we used the same approximations that lead to Eq.(5.72), which was explicitly showed to be good in Figs. 5.2 and 5.3 and the definition of g given in Eq. (5.74).

If we solve Eq. (5.135), we finally obtain an analytic expression for n_o

$$n_o \approx g - \alpha\sqrt{\frac{Ug}{J}}. \tag{5.136}$$

Surprisingly, the expression for the condensate density that we get after including the many-body scattering matrix is exactly the same, as the one we get if in the BdG equations for the condensate, Eq. (5.72), we replace n_o by g in the right hand side. Except for the term $\frac{M-1}{2M}$, this corresponds to the lowest order solution we can get of Eq. (5.72), where instead of solving self consistently the algebraic equation we replace n_o by n. The term $\frac{M-1}{2M}$ is very small at high densities when $n + 1/2 \approx n$, regime where in fact we only expect a mean field treatment to be valid and it might be interpreted as a finite size effect. Hereafter we are going

to refer to the non self consistent solution of the BdG equations as the test field approximation.

Finally, if we use the expression for the condensate density Eq. (5.136) in Eq. (5.134), and assume again that $n + 1/2 \approx n$, after some algebraic manipulations the final result we get is

$$n_o \mathcal{T}_{mb} = Un. \tag{5.137}$$

For us this a striking result. The net effect of including the many-body scattering matrix in the theory reduces to replacing Un_o in the BdG equations with Un. This result is hard to understand because what it implies is that the lowest order approximation beyond the simple DNLSE, is the one that reproduces the best the exact solution as the interactions in the system are increased.

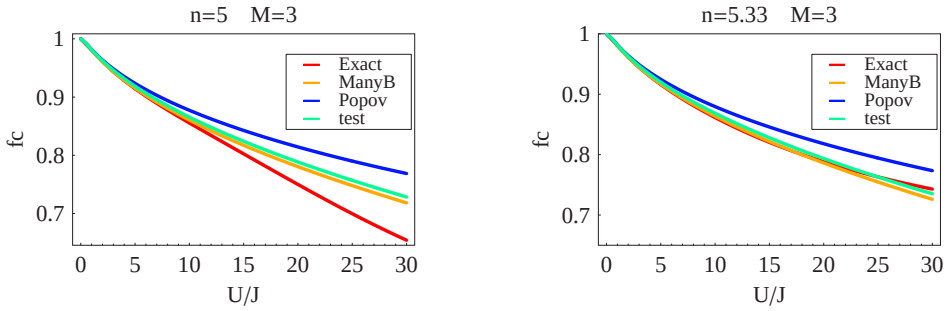

Figure 5.15: Comparisons of the condensate fraction predicted from the exact diagonalization of the BHH (red), the improved Popov approximation (yellow), the BdG (and HFB-Popov) equations (blue) and the test field approximation (green) as a function of $V_{eff} = U/J$, for a system with $M = 3$ and filling factors $n = 5$ and 5.33.

To check the improvement that we get by including the many-body scattering matrix in the theory, in Figs 5.15 and 5.16 we show comparisons of the condensate fraction, $f_c = n_o/n$, as a function of U/J calculated from the exact diagonalization of the many-body Hamiltonian (red) with the improved Popov(yellow) and the regular BdG (and HFB-Popov)(blue) approximations. We also plot the test field approximation results (green). In the plots we used a one dimensional lattice with $M = 3$ and densities $n = 5$ and $n = 5.33$ in Fig. 5.15 and $n = 50$ and $n = 50.33$ in Fig. 5.16.

It is clear in the plots that the improved Popov is a better approximation than the regular BdG (and HFB-Popov) approximation. In particular in the non commensurate, high density case the agreement between the improved Popov and the exact solution is very good. It also can be seen in the plots how the improved Popov reduces to the simple test field approximation. The small differences seen in the low density case disappear as the density is increased. To corroborate the

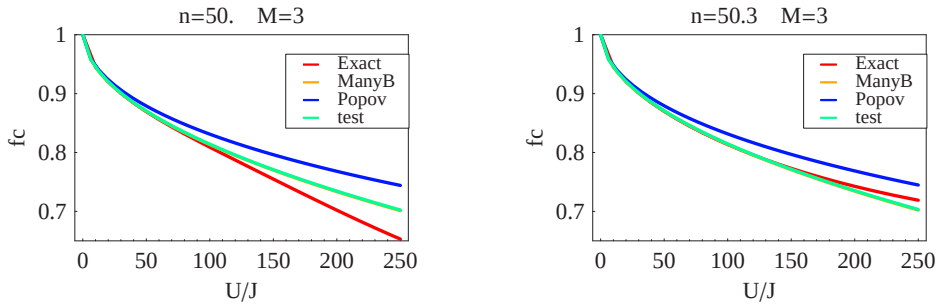

Figure 5.16: Comparisons of the condensate fraction predicted from the exact diagonalization of the BHH (red), the improved Popov approximation (yellow), the BdG (and HFB-Popov) equations (blue) and the test field approximation (green) as a function of $V_{eff} = U/J$, for a system with $M = 3$ and filling factors $n = 50$ and 50.33.

validity of Eq. (5.137), we plot in Fig. 5.17 $\mathcal{T}_{mb} f_c$, calculated from Eqs. (5.136) and (5.134), vs U. The curves just overlap in the high density regime $n = 50$ and in the low density case $n = 5$ the disagreement is very small.

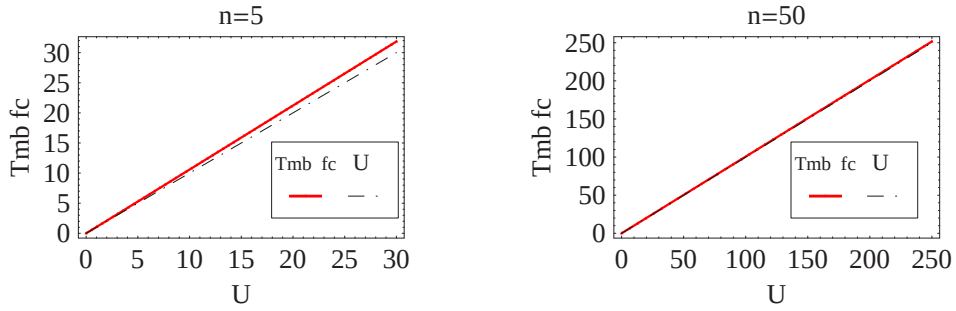

Figure 5.17: Comparisons between $n_o/n\mathcal{T}_{mb} = f_c\mathcal{T}_{mb}$ and U as a function of U for a system with $M = 3$ and filling factors $n = 5$ and 50.

Phase Transition

One of the signatures of the entrance to the Mott insulator phase is a zero condensate density. As we mentioned below, the BdG (and HFB-Popov) approximation does not predict the Mott insulator transition because the condensate density only vanishes in the limit when $U/J \to \infty$. On the other hand, the improved Popov approximation, does predict the existence of a critical value , $V^c_{eff} = (U/J)_c$, at which the condensate density vanishes:

$$V_{eff}^{c} = \frac{n + \frac{M-1}{2M}}{\alpha^2} \quad \overrightarrow{n \gg 1} \quad \frac{n}{\alpha^2}. \tag{5.138}$$

If we compare the above expression with the equation of the critical point calculated from a mean field model starting in the Mott insulator phase (see chapter 3) given by, $V_{eff}^{c} = t\left((2n+1) + \left(\sqrt{(2n+1)^2 - 1}\right)\right)$, we see that in the high density limit, the only regime where mean field theories are expected to be valid, both equations describe a critical point which scales linear with n and with a proportionality constant which depends only on the dimensionality of the system. In the improved Popov approximation the proportionality constant is $1/\alpha^2$, in the mean field theory starting from the Mott phase it is $8t$ (remember t is the number of nearest neighbors). For a one dimensional lattice in the thermodynamic limit the improved Popov approximation has the infrared divergency problem, $\alpha \to \infty$ and the critical point approaches zero. However, this is consistent with the calculations done in Ref. [44] where the authors showed using renormalization group techniques that the upper critical dimension for the transition at constant integer density is $d_c = 2$.

Nevertheless, the phase transition predicted by the improved Popov approximation does not have a clear connection to the real Mott insulator phase transition. A specific problem is the fact that the improved Popov approximation does not distinguish between commensurate and incommensurate fillings. This distinction is crucial to reproduce the characteristic superfluid to Mott insulator phase diagram. Furthermore, there is not clear signature that the system becomes incompressible in the Mott phase, and no gap in the excitation spectrum opens up as the transition is reached.

5.8 Conclusions

In summary, in this chapter we have developed quadratic approximations for describing the approach of a superfluid system towards the Mott insulator transition. We have shown that this method can be used to predict the relevant physical quantities over a useful range. However, the quadratic approximations are developed assuming small fluctuations and therefore as soon as quantum correlations become important it is clear that a fully quantal method is required.

Chapter 6

The two particle irreducible effective action (2PI) and the closed time path (CTP) formalism

In the last section we focused our attention on quadratic approximations of the many body Hamiltonian and we used them to describe equilibrium properties of ultra cold atoms loaded in optical lattices. In this chapter extend our analysis to non equilibrium systems. The description of the evolution of condensates far from equilibrium has gained considerable importance in matter-wave physics, motivated by recent experimental achievements such as the colliding and collapsing condensates [20, 21, 115, 114], collapses and revivals of the coherent matter field [47] and the NIST patterned loading experiment described in chapter 4. To date most theoretical descriptions of nonequilibrium dynamics of BEC's have been based on the time dependent Gross-Pitaevskii equation, coupled with extended kinetic theories that describe excitations in dilute weakly interacting systems close to thermal equilibrium ([15],[58]-[62],[116]). However, experiments such as those mentioned above have been able to achieve regimes where the standard mean field description is inapplicable, so new methods are required.

To treat far-from-equilibrium dynamics, in this chapter we adopt a closed time path (CTP) [56] functional-integral formalism together with a two-particle irreducible (2PI) [57] effective action approach. We retain terms of up to second-order in the interaction strength when solving these equations. This method has been generalized for and applied to the establishment of a quantum kinetic field theory [117, 118, 119] with applications to problems in gravitation and cosmology [120, 121], particles and fields [122, 123], BEC [54, 125] and condensed matter systems [124] as well as addressing the issues of thermalization and quantum phase transitions [126, 127, 128].

In this chapter we consider under the 2PI-CTP scheme different approximations: the Hartree-Fock-Bogoliubov (HFB) approximation, the next-to-leading

order $1/\mathcal{N}$ expansion of the 2PI effective action up to second-order in the interaction strength and a second-order perturbative expansion in the interaction strength. In chapter 7 we apply the 2PI-CTP approximations derived here to describe the the patterned loading experiment [33] previously discussed in chapter 4.

6.1 2PI effective action $\Gamma(z, G)$

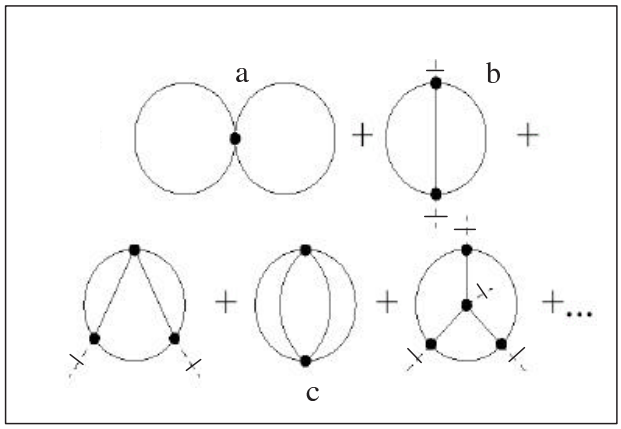

Figure 6.1: Two-loop (upper row) and three-loop diagrams (lower row) contributing to the effective action. Explicitly, the diagram a) is what we call the *double-bubble* , b) the *setting-sun* and c) the *basketball*.

The first requirement for the study of nonequilibrium processes is a general initial-value formulation depicting the dynamics of interacting quantum fields. The CTP or Schwinger-Keldysh effective action formalism [56] serves this purpose. The second requirement is to describe the evolution of the correlation functions and the mean field on an equal footing. The two particle irreducible (2PI) formalism [57] where the correlation functions appear also as independent variables, serves this purpose. By requiring the generalized (master) CTP effective action [118] to be stationary with respect to variations of the correlation functions we obtain an infinite set of coupled (Schwinger-Dyson) equations for the correlation functions which is a quantum analog of the BBGKY hierarchy. The 2PI effective action produces two such functions in this hierarchy. In this section we shall focus on the 2PI formalism, and then upgrade it to the CTP version in the next section.

Our starting point is the one dimensional Bose-Hubbard Hamiltonian (see chapter 3).

$$\hat{H} \;=\; -J\sum_i(\hat{a}_i^\dagger\,\hat{a}_{i+1}\; + \hat{a}_{i+1}^\dagger\,\hat{a}_i\,) + \frac{1}{2}U\sum_i \hat{a}_i^\dagger\,\hat{a}_i^\dagger\,\hat{a}_i\,\hat{a}_i\; + \sum_i V_i\hat{a}_i^\dagger\hat{a}_i \qquad (6.1)$$

where $\hat{a}_i$ and $\hat{a}_i^\dagger$ are the bosonic operators that annihilate and create an atom on the site i. Here, the parameter U denotes the strength of the on-site repulsion of two atoms on the site i; the parameter V_i denotes the energy offset of each lattice site due to an additional slowly- varying external potential that might be present (such as a magnetic trap), and J denotes the hopping rate between adjacent sites. Because the next-to-nearest neighbor amplitudes are typically two orders of magnitude smaller, tunneling to next-to-nearest neighbor sites can be neglected. The Bose -Hubbard Hamiltonian should be an appropriate model when the loading process produces atoms in the lowest vibrational state of each well, with a chemical potential smaller than the distance of the first vibrationally excited state.

Hereafter we consider for simplicity only a homogeneous lattice with periodic boundary conditions and no other external potential ($V_i = 0$). Once the equations of motion are derived, it is straightforward to generalize them to higher dimensions or to include additional external potentials. As usual, we denote the total number of atoms by N and the number of lattice sites by M.

The classical action associated with the Bose-Hubbard Hamiltonian (6.1), is given in terms of the complex fields a_i and a_i^* by

$$\begin{aligned} S[a_i^*, a_i] &= \int dt \sum_i i\hbar a_i^*(t)\partial_t a_i(t) \\ &+ \int dt \sum_i J\left(a_i^*(t)a_{i+1}(t) + a_i(t)a_{i+1}^*(t)\right) \\ &- \int dt \sum_i \frac{U}{2} a_i^*(t)a_i^*(t)a_i(t)a_i(t). \end{aligned} \tag{6.2}$$

To simplify our notation we introduce $a_i^a (a = 1, 2)$ defined by

$$a_i = a_i^1, \quad a_i^* = a_i^2. \tag{6.3}$$

In terms of these fields the classical action takes the form

$$\begin{aligned} S[a] &= \int dt \sum_i \frac{1}{2} h_{ab} a_i^a(t)\hbar\partial_t a_i^b(t \\ &+ \int dt \sum_i \left(J\sigma_{ab}a_{i+1}^a(t)a_i^b(t) - \frac{U}{4\mathcal{N}}(\sigma_{ab}a_i^a(t)a_i^b(t))^2\right), \end{aligned} \tag{6.4}$$

where $\mathcal{N}$ is the number of fields,which is two in this case, and summation over repeated field indices $a, b = (1, 2)$ is implied and h_{ab} and σ_{ab} are matrices defined as

$$h_{ab} = i\begin{pmatrix} 0 & -1 \\ 1 & 0 \end{pmatrix}, \qquad \sigma_{ab} = \begin{pmatrix} 0 & 1 \\ 1 & 0 \end{pmatrix}. \tag{6.5}$$

In terms of the familiar Pauli matrices, $\sigma_{ab} = \sigma_x$ and $h_{ab} = -\sigma_y$.

After second quantization the fields a_i^a are promoted to operators. We denote the expectation value of the field operator, i.e. the mean field, by $z_i^a(t)$ and the expectation value of the composite field by $G_{ij}^{ab}(t,t')$. Physically, $|z_i^a(t)|^2$ is the condensate population and the composite fields determine the fluctuations around the mean field:

$$z_i^a(t) = \langle a_i^a(t)\rangle\,, \tag{6.6}$$
$$G_{ij}^{ab}(t,t') = \left\langle T_C a_i^a(t) a_i^b(t')\right\rangle - \langle a_i^a(t)\rangle \left\langle a_i^b(t')\right\rangle. \tag{6.7}$$

The brackets denote the expectation value with respect to the density matrix and T_C denotes time ordering along a contour C in the complex plane.

All correlation functions of the quantum theory can be obtained from the effective action $\Gamma[z,G]$, the two particle irreducible generating functional for Green's functions parameterized by $z_i^a(t)$ and the composite field $G_{ij}^{ab}(t,t')$. To get an expression for the effective action we first define the functional $Z[\mathbf{J},\mathbf{K}]$ [57] as

$$Z[\mathbf{J},\mathbf{K}] = e^{iW[\mathbf{J},\mathbf{K}]/\hbar} \tag{6.8}$$
$$= \prod_a \int Da^a \exp\left\{\frac{i}{\hbar}\left(S[a] + \int dt \sum_i \mathbf{J}_{ia}(t) a_i^a(t) + \frac{1}{2}\int dtdt' \sum_{ij} a_i^a(t) a_j^b(t') \mathbf{K}_{ijab}(t,t')\right)\right\},$$

where we have introduced the following index lowering convention

$$X_a = \sigma_{ab} X^b. \tag{6.9}$$

The functional integral (6.8) is a sum over classical histories of the field a_i^a in the presence of the local source $\mathbf{J}_{ia}$ and the non local source $\mathbf{K}_{ijab}$. The coherent state measure is included in Da. The addition of the two-particle source term is what characterizes the 2PI formalism.

We define $\Gamma[z,G]$ as the double Legendre transform of $W[\mathbf{J},\mathbf{K}]$ such that

$$\frac{\delta W[\mathbf{J},\mathbf{K}]}{\delta \mathbf{J}_{ia}(t)} = z_i^a(t), \tag{6.10}$$
$$\frac{\delta W[\mathbf{J},\mathbf{K}]}{\delta \mathbf{K}_{ijab}(t,t')} = \frac{1}{2}[z_i^a(t) z_i^b(t') + G_{ij}^{ab}(t,t')]. \tag{6.11}$$

Expressing $\mathbf{J}$ and $\mathbf{K}$ in terms of z and G yields

$$\Gamma[z,G] = W[\mathbf{J},\mathbf{K}] - \int dt \sum_i \mathbf{J}_{ia}(t) z_i^a(t) - \frac{1}{2}\int dtdt' \sum_{ij} z_i^a(t) z_j^b(t') \mathbf{K}_{ijab}(t,t')$$
$$-\frac{1}{2}\int dtdt' \sum_{ij} G_{ij}^{ab}(t,t') \mathbf{K}_{ijab}(t,t'). \tag{6.12}$$

From this equation the following identity can be derived:

$$\frac{\delta\Gamma[z,G]}{\delta z_i^a(t)} = -\mathbf{J}_{ia}(t) - \int dt' \sum_j (\mathbf{K}_{ijad}(t,t'))z_j^d(t'), \tag{6.13}$$

$$\frac{\delta\Gamma[z,G]}{\delta G_{ij}^{ab}(t,t')} = -\frac{1}{2}\mathbf{K}_{ijab}(t,t'). \tag{6.14}$$

In order to get an expression for $\Gamma[z,G]$ notice that by using Eq.(6.8) for $W[\mathbf{J},\mathbf{K}]$ and placing it in Eq.(6.12) for $\Gamma[z,G]$, it can be written as

$$\begin{aligned}\exp\left(\frac{i}{\hbar}\Gamma[z,G]\right) &= \prod_a \int Da^a \exp\left\{\frac{i}{\hbar}\left(S[a] + \int dt_i\ \mathbf{J}_{ia}(t)\left[a_i^a(t) - z_i^a(t)\right]\right.\right. \\ &\quad \left.\left. + \frac{1}{2}\int dt_i dt'_j \left(a_i^a(t)\mathbf{K}_{ijab}(t,t')a_j^b(t') - z_i^a(t)\mathbf{K}_{ijab}(t,t')z_j^b(t')\right) - \frac{1}{2}TrG\mathbf{K}\right)\right\} \\ &= \prod_a \int Da^a \exp\left\{\frac{i}{\hbar}\left(S[a] - \int dt_i\ \frac{\delta\Gamma[z,G]}{\delta z_i^a(t)}\left[a_i^a(t) - z_i^a(t)\right]\right.\right. \\ &\quad \left.\left. - \int dt_i dt'_j\ \left[a_i^a(t) - z_i^a(t)\right]\frac{\delta\Gamma[z,G]}{\delta G_{ij}^{ab}(t,t')}\left[a_i^b(t') - z_i^b(t')\right] + TrG\frac{\delta\Gamma[z,G]}{\delta G}\right)\right\},\end{aligned} \tag{6.15}$$

where Tr means taking the trace. For simplicity we have denoted $\int dt \sum_i$ by $\int dt_i$. Defining the fluctuation field, $\varphi_i^a = a_i^a - z_i^a$, we have

$$\Gamma[z,G] - TrG\frac{\delta\Gamma[z,G]}{\delta G} = -i\hbar \ln \prod_a \int D\varphi^a \exp\left(\frac{i}{\hbar}S[z,G;\varphi]\right), \tag{6.16}$$

$$\begin{aligned}S[z,G;\varphi] &= S[z+\varphi] - \int dt_i\ \frac{\delta\Gamma[z,G]}{\delta z_i^a(t)}\varphi_i^a(t) - \\ &\quad \int dt_i dt'_j\ \varphi_i^a(t)\frac{\delta\Gamma[z,G]}{\delta G_{ij}^{ab}(t,t')}\varphi_i^b(t').\end{aligned} \tag{6.17}$$

By introducing the classical inverse propagator $iD^{-1}(z)$ given by

$$\begin{aligned}iD_{ijab}(t,t')^{-1} &= \frac{\delta S[z]}{\delta z_i^a(t)\delta z_j^b(t')} \\ &= (\delta_{ij}h_{ab}\partial_t + J(\delta_{i+1j} + \delta_{i-1j})\sigma_{ab})\,\delta(t-t') \\ &\quad -\frac{U}{\mathcal{N}}\left(2z_{ia}(t)z_{ib}(t) + \sigma_{ab}z_i^c(t)z_{ic}(t)\right)\delta_{ij}\delta(t-t'),\end{aligned} \tag{6.18}$$

the solution of the functional integro-differential equation (6.16) can be expressed as

$$\Gamma[z,G] = S[z] + \frac{i}{2}Tr\ln G^{-1} + \frac{i}{2}TrD^{-1}(z)G + \Gamma_2[z,G] + const. \tag{6.19}$$

The quantity $\Gamma_2[z,G]$ is conveniently described in terms of the diagrams generated by the interaction terms in $S[z+\varphi]$ which are of cubic and higher orders in φ

$$\begin{aligned} S_{int}[z+\varphi] &= -\frac{U}{4\mathcal{N}}\int dt_i(\varphi_{ib}(t)\varphi_i^b(t))^2 \\ &\quad -\frac{U}{\mathcal{N}}\int dt_i\varphi_i^a(t)z_{ia}(t)\varphi_i^b(t)\varphi_{ib}(t). \end{aligned} \tag{6.20}$$

It consists of all two-particle irreducible vacuum graphs (the diagrams representing these interactions do not become disconnected by cutting two propagator lines) in the theory with propagators set equal to G and vertices determined by the interaction terms in $S[z+\varphi]$.

Since physical processes correspond to vanishing sources $\mathbf{J}$ and $\mathbf{K}$, the dynamical equations of motion for the mean field and the propagators are found by using the expression (6.19) in equations (6.13) and (6.14) , and setting the right hand side equal to zero. This procedure leads to the following equations:

$$\begin{aligned} h_{ab}\hbar\partial_t z_i^b(t) &= -J(z_{i+1a}(t) + z_{i-1a}(t)) \\ &\quad +\frac{U}{\mathcal{N}}(z_{id}(t)z_i^d(t) + G_{ii\ c}^{\ c}(t,t))z_{ia}(t) \\ &\quad +\frac{U}{\mathcal{N}}((G_{iiad}(t,t) + G_{iida}(t,t))z_i^d(t) \\ &\quad -\frac{\delta\Gamma_2[z,G]}{\delta z_i^a(t)}, \end{aligned} \tag{6.21}$$

and

$$G^{-1}_{ijab}(t,t') = D_{ijab}(t,t')^{-1} - \Sigma_{ijab}(t,t'), \tag{6.22}$$

$$\Sigma_{ijab}(t,t') \equiv 2i\frac{\delta\Gamma_2[z,G]}{\delta G_{ij}^{ab}(t,t')}. \tag{6.23}$$

Equation (6.22) can be rewritten as a partial differential equation suitable for initial value problems by convolution with G. This differential equation reads explicitly

$$\begin{aligned} h_c^a\hbar\partial_t G_{ij}^{\ cb}(t,t') &= -J(G_{i+1j}^{ab}(t,t') + G_{i-1j}^{ab}(t,t')) + \frac{U}{\mathcal{N}}(z_{id}(t)z_i^d(t))G_{ij}^{ab}(t,t') + \\ &\quad \frac{2U}{\mathcal{N}}z_i^a(t)G_{ij}^{cb}(t,t')z_{ic}(t) + i\int dt_k''\Sigma_{ikc}^{\ a}(t,t'')G_{kj}^{cb}(t'',t') + i\delta^{ab}\delta_{ij}\delta(t-t'). \end{aligned} \tag{6.24}$$

The evolution of z^a and G^{ab} is determined by Eqs. (6.22) and (6.24) once $\Gamma_2[z,G]$ is specified.

6.2 Perturbative expansion of $\Gamma_2(z, G)$ and approximation schemes

The diagrammatic expansion of Γ_2 is illustrated in Fig. 6.1, where two and three-loop vacuum diagrams are shown. The dots where four lines meet represent interaction vertices. The expression corresponding to each vacuum diagram should be multiplied by a factor $(-i)^l(i)^{s-2}$ where l is the number of solid lines and s the number of loops the diagram contains.

The action Γ including the full diagrammatic series for Γ_2 gives the full dynamics. It is of course not feasible to obtain an exact expression for Γ_2 in a closed form. Various approximations for the full 2PI effective action can be obtained by truncating the diagrammatic expansion for Γ_2. Which approximation is most appropriate depends on the physical problem under consideration.

6.2.1 The standard approaches

1. Mean-field approximation:

   If, in Eq. (6.19), we discard all terms to the right of $S[z]$, we recover the DNLSE. This gives us the usual mean-field description, in which the system remains a pure condensate.

2. One-loop Approximation:

   The next approximation consists of discarding Γ_2 altogether. This yields the so-called one-loop approximation. The one-loop approximation has an equation for the fluctuations identical to the BdG equations (See chapter 5), however the equation of motion for the condensate does include the depletion and anomalous terms. The presence of this terms is necessary for the time dependent evolution because they guarantee the conservation of particle number and energy. The unequal treatment of the condensate and fluctuations present in this approximation introduces limitations and makes this approach not very attractive for studying the non equilibrium dynamics.

3. Time-dependent Hartree-Fock-Bogoliubov (HFB) approximation:

   A truncation of Γ_2 retaining only the first order diagram in U, i.e., keeping only the *double-bubble* diagram, Fig. 6.1, yields equations of motion for z and G which correspond to the time dependent Hartree-Fock-Bogoliubov (HFB) approximation. This approximation violates Goldstone's theorem, but conserves energy and particle number [132, 15, 133]. It is important to point out that between all the quadratic approximations discussed in chapter 5 only the HFB approximation is suitable for describing non equilibrium dynamics because it is the only one that obeys conservation laws. The HFB equations can also be obtained by using cumulant expansions up to the second-order [136] in which all cumulants containing three or four field operators are neglected. The HFB approximation neglects multiple scattering. It can be

interpreted as an expansion in terms of Ut/J, (where t is the time of evolution) and is good for the description of short time dynamics or weak interaction strengths. It will be described in more detail in section 6.4.

6.2.2 Higher order expansions

We make a few remarks on the general properties of higher order expansions and then specialize to two approximations.

- 2PI and Ladder Diagrams

  Since the work of Beliaev [63] and Popov [52] it is well known in the literature that including higher order terms in a diagrammatic expansion corresponds to renormalizing the bare interaction potential to the four-point vertex (see for example Ref. [53, 54]), thus accounting for the repeated scattering of the bosons. In particular, in chapter 5 we explicitly showed how by including the anomalous average in the equations the bare potential was upgraded in the off diagonal elements to the many body scattering matrix. In chapter 8 we will also show that by taking into account the two-loop contribution of the 2PI effective action, the bare potential in the diagonal terms is also upgraded to the many body scattering matrix up to second-order in the ladder expansion. The two-loop contribution includes diagrams topologically identical to those found by Beliaev, but with the exact propagator instead of the one-loop propagator. In the dilute gas limit, where the inter-particle distance is large compared with the s-wave scattering length, the ladder diagrams give the largest contribution to the four-point vertex. To lowest order in the diluteness parameter, the T-matrix can be approximated by a constant proportional to the scattering length (the pseudopotential approximation). However this approximation is only valid in the weak interaction limit and neglects all momentum dependencies which appears in the problem as higher order terms. In that sense the 2PI effective action approach allows us to go beyond the weakly interacting limit in a systematic way and to treat collisions more accurately.

- Nonlocal Dissipation and Non-Markovian Dynamics

  Higher order terms lead to nonlocal equations and dissipation. The presence of nonlocal terms in the equations of motion is a consequence of the fact that the 2PI effective action really corresponds to a further approximation of the master effective equation [118]. Though strict dissipation can never be observed in an energy conserving closed system, characteristic features of dissipative systems like exponential damping of correlations can be exhibited once interactions are properly taken into account.

  Non-Markovian dynamics is a generic feature of the 2PI formalism which yields integro-differential equations of motion. This makes numerical solution difficult, but is a necessary price to pay for a fuller account of the quantum dynamics. Many well acknowledged approaches to the quantum

kinetics of such systems adopt either explicitly or implicitly a Markovian approximation [62]. The Markovian approximation assumes that only the current configuration of the system, but not its history, determines its future evolution. Markovian approximations are made if one assumes instantaneous interactions, or in the kinetic theory context that the time scales between the duration of binary collisions τ_0 and the inverse collision rate τ_c are well-separated. In the low kinetic energy, weakly interacting regime the time between collisions (or mean free path) is long compared to the reaction time (or scattering length): $\tau_c >> \tau_0$. The long separation between collisions and the presence of intermediate weak fluctuations, allow for a rapid decay of the temporal and spatial correlations created between collision partners, which one can use to justify the Markovian approximation. However,non-Markovian dynamics needs to be confronted squarely in systems such as the patterned loaded lattice, in which the lattice which confines the atoms to the bottom of the wells with enhanced interaction effects, accompanied by the low dimensionality of the system and far-from-equilibrium initial conditions. That is the rationale for our adoption of the CTP 2PI scheme. Now, for the specifics:

1. Second-order expansion:

   A truncation retaining diagrams of second-order in U consists of the *double-bubble*, the *setting-sun* and the *basketball* (see Fig.6.1). By including the *setting-sun* and the *basketball* in the approximations we are taking into account two particle scattering processes [121, 119]. Second-order terms lead to integro- differential equations which depend on the time history of the system.

2. Large-$\mathcal{N}$ approximation

   The $1/\mathcal{N}$ expansion is a controlled non-perturbative approximation scheme which can be used to study non-equilibrium quantum field dynamics in the regime of strong interactions[127, 126]. In the large $\mathcal{N}$ approach the field is modelled by $\mathcal{N}$ fields and the quantum field generating functional is expanded in powers of $1/\mathcal{N}$. In this sense the method is a controlled expansion in a small parameter, but unlike perturbation theory in the coupling constant, which corresponds to an expansion around the vacuum, the large $\mathcal{N}$ expansion corresponds to an expansion of the theory about a strong quasiclassical field.

6.2.3 Zero mode fluctuactions

In chapter 5 we neglected zero mode fluctuations due to the non perturbative character of the zero mode. In the linearized theory, this approach introduces an artificial infrared divergence in low dimensional models thus the theory is actually improved if the contribution from this mode is neglected all together [96]. However, from a physical point of view the zero mode exists and is quantum in nature. There

are both fundamental and practical reasons why isolating and subtracting the zero mode is not as compelling in the dynamical evolution we want to describe in this chapter. Firstly, because the 2PI formalism goes beyond the linearized approximation, the zero mode does not have the impact it has in the linearized formalism and it is not clear that subtracting it necessarily leads to a better approximation. Secondly, the initial state that we are going to assume for our analysis is a coherent state rather than a proper state of the total particle number as will be described in chapter 7. Moreover, as the total particle number is not very high, quantum fluctuations in the total particle number are real, and non-negligible. Discarding these fluctuations would spoil the integrity of the formalism. Therefore, in this chapter we shall not attempt to isolate the contributions from the zero mode. A full non-perturbative treatment in the future is certainly desirable.

6.3 CTP formalism

In order to describe the nonequilibrium dynamics we will now specify the contour of integration in Eqs. (6.22) and (6.24) to be the Schwinger-Keldysh contour [56] along the real-time axis or *closed time path* (CTP) contour. The Schwinger-Keldysh formalism is a powerful method for deriving real and causal evolution equations for the expectation values of quantum operators for nonequilibrium fields. The basic idea of the CTP formalism relies on the fact that a diagonal matrix element of a system at a given time, $t = 0$, can be expressed as a product of transition matrix elements from $t = 0$ to t' and the time-reverse (complex conjugate) matrix element from t' to 0 by inserting a complete set of states into this matrix element at the later time t'. Since each term in the product is a transition matrix element of the usual or time reversed kind, the standard path integral representation for each one can be introduced. However, to get the generating functional we seek, we have to require that the forward time evolution takes place in the presence of a source J^+ but the reversed time evolution takes place in the presence of a different source J^-, otherwise all the dependence on the source drops out.

The doubling of sources, the fields and integration contours suggest introducing a 2 x 2 matrix notation. This notation has been discussed extensively in the literature [117, 119]. However we are going to follow Refs. [126] and [127] and introduce the CTP formalism in our equation of motion by using the composition rule for transition amplitudes along the time contour in the complex plane. This way is cleaner notationally and has the advantage that all the functional formalism of the previous section may be taken with the only difference of path ordering according to the complex time contour C_{ctp} in the time integrations.

The two-point functions are decomposed as

$$G^{ab}_{ij}(t,t') = \theta_{ctp}(t,t')G^{ab>}_{ij}(t,t') + \theta_{ctp}(t',t)G^{ab<}_{ij}(t,t'), \tag{6.25}$$

where

$$\hbar G_{ij}^{ab>}(t,t') = \left\langle \varphi_i^a(t)\varphi_j^b(t') \right\rangle, \tag{6.26}$$

$$\hbar G_{ij}^{ab<}(t,t') = \left\langle \varphi_i^b(t')\varphi_j^a(t) \right\rangle, \tag{6.27}$$

with φ_i being the fluctuation field defined prior Eq. (17) and $\theta_{ctp}(t-t')$ being the CTP complex contour ordered theta function defined by

$$\theta_{ctp}(t,t') = \begin{cases} \theta(t,t') \text{ for } t \text{ and } t' \text{ both on } C^+ \\ \theta(t',t) \text{ for } t \text{ and } t' \text{ both on } C^- \\ 1 \text{ for } t \text{ on } C^- \text{ and } t' \text{ on } C^+ \\ 0 \text{ for } t \text{ on } C^+ \text{ and } t' \text{ on } C^- \end{cases}. \tag{6.28}$$

With these definitions the matrix indices are not required. When integrating over the second half C^-, we have to multiply by a negative sign to take into account the opposite direction of integration.

To show explicitly that the prescription for the CTP integration explained above does lead to a well-posed initial value problem with causal equations, let us explicitly consider the integral in Eq. (6.24). The integrand has the CTP ordered form

$$\begin{aligned} &\Sigma(t,t'')G(t'',t') = \\ &\theta_{ctp}(t,t'')\theta_{ctp}(t'',t')\Sigma^>(t,t'')G^>(t'',t') + \theta_{ctp}(t,t'')\theta_{ctp}(t',t'')\Sigma^>(t,t'')G^<(t'',t') \\ &\theta_{ctp}(t'',t)\theta_{ctp}(t'',t')\Sigma^<(t,t'')G^>(t'',t') + \theta_{ctp}(t'',t)\theta_{ctp}(t',t'')\Sigma^<(t,t'')G^<(t'',t'), \end{aligned} \tag{6.29}$$

where we have omitted the indices because they are not relevant for the discussion. Using the rule for CTP contour integration we get

$$\begin{aligned} \int dt''\Sigma(t,t'')G(t'',t') &= \int_0^t dt'' \left[\theta(t'',t')\Sigma^>(t,t'')G^>(t'',t') + \theta(t',t'')\Sigma^>(t,t'')G^<(t'',t')\right] \\ &+ \int_t^\infty dt'' \left[\theta(t'',t')\Sigma^<(t,t'')G^>(t'',t') + \theta(t',t'')\Sigma^<(t,t'')G^<(t'',t')\right] \\ &- \int_0^\infty dt''\Sigma^<(t,t'')G^>(t'',t'). \end{aligned} \tag{6.30}$$

If $t > t'$, we have

$$\begin{aligned} \int dt''\Sigma(t,t'')G(t'',t') &= \int_0^t dt''(\Sigma^>(t,t'') - \Sigma^<(t,t''))G^>(t'',t') \\ &- \int_0^{t'} dt''\Sigma^>(t,t'')(G^>(t'',t') - G^<(t'',t')). \end{aligned} \tag{6.31}$$

On the other hand, if $t < t'$

$$\begin{aligned}\int dt''\Sigma(t,t'')G(t'',t') &= \int_0^t dt''(\Sigma^{>}(t,t'')-\Sigma^{<}(t,t''))G^{<}(t'',t') \\ &- \int_0^{t'} dt''\Sigma^{<}(t,t'')(G^{>}(t'',t')-G^{<}(t'',t')). \quad (6.32)\end{aligned}$$

The above equations are explicitly causal.
It is convenient to express the evolution equations in terms of two independent two-point functions which can be associated to the expectation values of the commutator and the anti-commutator of the fields. We define, following Ref. [127] the functions

$$G_{ij}^{(F)ab}(t,t') = \frac{1}{2}\left(G_{ij}^{ab>}(t,t')+G_{ij}^{ab<}(t,t')\right) \quad (6.33)$$

$$G_{ij}^{(\rho)ab}(t,t') = i\left(G_{ij}^{ab>}(t,t')-G_{ij}^{ab<}(t,t')\right), \quad (6.34)$$

where the (F) functions are usually called statistical propagators and the (ρ) are called spectral functions [137]. With these definitions Eq.(6.24) can be rewritten as:

$$\begin{aligned}h_c^a\hbar\partial_t G_{ij}^{(F)cb}(t,t') &= -J\left(G_{i+1j}^{(F)ab}(t,t')+G_{i-1j}^{(F)ab}(t,t')\right)+\frac{U}{\mathcal{N}}\left(z_{ic}(t)z_i^c(t))G_{ij}^{(F)ab}(t,t')\right)+ \\ &\frac{2U}{\mathcal{N}}\left(z_i^a(t)G_{ij}^{(F)cb}(t,t')z_{ic}(t)\right)+\int_0^t dt_k''\Sigma_{ik}^{(\rho)ac}(t,t'')G_{kj\ c}^{(F)\ b}(t'',t') \\ &-\int_0^{t'} dt_k''\Sigma_{ik}^{(F)ac}(t,t'')G_{kjc}^{(\rho)b}(t'',t'), \quad (6.35)\end{aligned}$$

$$\begin{aligned}h_c^a\hbar\partial_t G_{ij}^{(\rho)cb}(t,t') &= -J\left(G_{i+1j}^{(\rho)ab}(t,t')+G_{i-1j}^{(\rho)ab}(t,t')\right)+\frac{U}{\mathcal{N}}\left(z_{ic}(t)z_i^c(t))G_{ij}^{(\rho)ab}(t,t'\right)+ \\ &\frac{2U}{\mathcal{N}}\left(z_i^a(t)G_{ij}^{(\rho)cb}(t,t')z_{ic}(t)\right)+\int_{t'}^t dt_k''\Sigma_{ik}^{(\rho)ac}(t,t'')G_{kjc}^{(\rho)b}(t'',t'). \quad (6.36)\end{aligned}$$

In particular, we define the normal, ρ, and anomalous, m, spectral and statistical functions as

$$G_{ij}^{21(F)}(t,t') \equiv \rho_{ij}^{(F)}(t,t') = \frac{1}{2}\left\langle\varphi_i^\dagger(t)\varphi_j(t')+\varphi_j(t')\varphi_i^\dagger(t)\right\rangle, \quad (6.37)$$

$$G_{ij}^{21(\rho)}(t,t') \equiv \rho_{ij}^{(\rho)}(t,t') = i\left\langle\varphi_i^\dagger(t)\varphi_j(t')-\varphi_j(t')\varphi_i^\dagger(t)\right\rangle, \quad (6.38)$$

$$G_{ij}^{11(F)}(t,t') \equiv m_{ij}^{(F)}(t,t') = \frac{1}{2}\left\langle\varphi_i(t)\varphi_j(t')+\varphi_j(t')\varphi_i(t)\right\rangle, \quad (6.39)$$

$$G_{ij}^{11(\rho)}(t,t') \equiv m_{ij}^{(\rho)}(t,t') = i\left\langle\varphi_i(t)\varphi_j(t')-\varphi_j(t')\varphi_i(t)\right\rangle. \quad (6.40)$$

With these relations in place, we now proceed to derive the time evolution equations for the mean field and the two-point functions from the 2PI-CTP effective action for the Bose-Hubbard model under the three approximations described before.

6.4 HFB approximation

6.4.1 Equations of motion

The HFB equations include the leading order contribution of Γ_2. They describe the coupled dynamics of condensate and non-condensate atoms which arise from the most important scattering processes which are direct, exchange and pair excitations. The basic damping mechanisms present in the HFB approximation are Landau and Beliaev damping associated with the decay of an elementary excitation into a pair of excitations in the presence of condensate atoms[133, 134]. However, these kinds of damping [1] found in the HFB approximation (due to phase mixing, as in the Vlasov equation citeBalescu) are different in nature from the collisional dissipation (as in the Boltzmann equation) responsible for thermalization processes. Multiple scattering processes are neglected in this approximation. We expect the HFB equations to give a good description of the dynamics in the collisionless regime when interparticle collisions play a minor role.

The leading order contribution of Γ_2 is represented by the *double-bubble* diagram. Its contribution to Γ_2 is z independent and has an analytic expression of the form

$$\Gamma_2^{(1)}[G] = \\ -\frac{U}{4\mathcal{N}}\int dt_i \ \left(G^{\ a}_{iia}(t,t)G^{\ b}_{iib}(t,t) + 2G_{iiab}(t,t)G^{ab}_{ii}(t,t)\right), \tag{6.41}$$

the factor of two arises because the direct and exchange terms are identical.

Using the first order expression for Γ_2 in Eqs. (6.22) and (6.24) yields the following equations of motion.

$$h^a_b\hbar\partial_t z^b_i(t) = \zeta^z_{HFB}, \tag{6.42}$$

$$\zeta^z_{HFB} \equiv -J\left(z^a_{i+1}(t) + z^a_{i-1}(t)\right) + \frac{U}{\mathcal{N}}\left(z_{id}(t)z^d_i(t) + G^{\ d}_{ii\ d}(t,t)\right)z^a_i(t) \\ +\frac{2U}{\mathcal{N}}\left(z_{ib}(t)G^{ab}_{ii}(t,t)\right), \tag{6.43}$$

[1] we make a distinction between the meaning of the words 'damping' and 'dissipation', the former referring simply to the phenomenological decay of some function, the latter with theoretical meaning, e.g., in the Boltzmann sense.

$$
\begin{aligned}
h_c^a \hbar\partial_t G_{ij}^{cb}\ (t,t') &= \zeta_{HFB}^G, \qquad (6.44)\\
\zeta_{HFB}^G &\equiv -J(G_{i+1j}^{ab}(t,t') + G_{i-1j}^{ab}(t,t')) + \frac{U}{\mathcal{N}}(z_{id}(t)z_i^d(t) + G_{ii\ d}^{\ d}(t,t))G_{ij}^{ab}(t,t')\\
&\quad + \frac{2U}{\mathcal{N}}(z_i^a(t)z_{ic}(t)G_{ij}^{cb}\ (t,t') + G_{ii\ d}^{\ a}(t,t)G_{ij}^{db}(t,t')) + i\delta^{ab}\delta_{ij}\delta_C(t-t').
\end{aligned}
$$

In terms of the spectral and statistical functions, Eqs. (6.37) to (6.40), and setting $\mathcal{N} = 2$, the above equations take the form

$$
\begin{aligned}
i\hbar\partial_t z_i(t) &= -J(z_{i+1}(t) + z_{i-1}(t)) + U(|z_i(t)|^2 + 2\rho_{ii}^{(F)}(t,t))z_i(t)\\
&\quad + U m_{ii}^{(F)}(t,t)z_i^*(t), \qquad (6.45)
\end{aligned}
$$

$$
\begin{aligned}
-i\hbar\frac{\partial}{\partial t}\rho_{ij}^{(F)}(t,t') &= \mathcal{L}_{ik}(t)\rho_{kj}^{(F)}(t,t') + \mathcal{M}_{ik}^*(t)m_{kj}^{(F)}(t,t'), \qquad (6.46)\\
-i\hbar\frac{\partial}{\partial t}\rho_{ij}^{(\rho)}(t,t') &= \mathcal{L}_{ik}(t)\rho_{kj}^{(\rho)}(t,t') + \mathcal{M}_{ik}^*(t)m_{kj}^{(\rho)}(t,t'), \qquad (6.47)\\
i\hbar\frac{\partial}{\partial t}m_{ij}^{(F)}(t,t') &= \mathcal{L}_{ik}(t)m_{kj}^{(F)}(t,t') + \mathcal{M}_{ik}(t)\rho_{kj}^{(F)}(t,t'), \qquad (6.48)\\
i\hbar\frac{\partial}{\partial t}m_{ij}^{(\rho)}(t,t') &= \mathcal{L}_{ik}(t)m_{kj}^{(\rho)}(t,t') + \mathcal{M}_{ik}(t)\rho_{kj}^{(\rho)}(t,t'), \qquad (6.49)
\end{aligned}
$$

with

$$
\begin{aligned}
\mathcal{L}_{ij}(t) &= -J(\delta_{i+1j} + \delta_{i-1j}) + 2U\delta_{ij}\left(|z_i(t)|^2 + \rho_{ii}^{(F)}(t,t)\right), \qquad (6.50)\\
\mathcal{M}_{ij}(t) &= U\delta_{ij}\left(z_i(t)^2 + m_{ii}^{(F)}(t,t)\right). \qquad (6.51)
\end{aligned}
$$

The time dependent HFB equations are a closed set of self-consistent equations that describe the coupled dynamics of the condensate and non-condensate components of a Bose gas. It can be checked that they preserve important conservation laws such as the number of particles and energy. The conservation properties of the HFB equations can also be understood by the fact that these equations can also be derived using Gaussian variational methods [15]. These methods always yield a classical Hamiltonian dynamics which guarantees probability conservation. Because they are local in time they can be decoupled by a mode decomposition.

6.4.2 Mode expansion of the HFB equations

To decouple the HFB equations we apply the well known Bogoliubov transformation to the fluctuation field (see chapter 5)

$$
\varphi_j(t) = \sum_q \left[u_i^q(t)\hat{\alpha}_q - v_i^{*q}(t)\hat{\alpha}_q^\dagger\right], \qquad (6.52)
$$

where $(\hat{\alpha}_q, \hat{\alpha}_q^\dagger)$ are time independent creation and annihilation quasiparticle operators and all the time dependence is absorbed in the amplitudes $\{u_i^q(t), v_i^{*q}(t)\}$. To ensure that the quasiparticle transformation is canonical, the amplitudes must fulfill the relations

$$\sum_i \left[u_i^q(t)u_i^{*k}(t) - v_i^q(t)v_i^{*k}(t)\right] = \delta_{qk}, \tag{6.53}$$

$$\sum_i \left[u_i^q(t)v_i^k(t) - v_i^q(t)u_i^k(t)\right] = 0. \tag{6.54}$$

In the zero temperature limit, where the quasiparticle occupation number vanishes, $\left\langle \hat{\alpha}_q^\dagger \hat{\alpha}_k \right\rangle = 0$, the statistical and spectral functions take the form

$$\rho_{ij}^{(F)}(t,t') = \frac{1}{2}\sum_q \left(v_i^q(t)v_j^{*q}(t') + u_j^q(t')u_i^{*q}(t)\right), \tag{6.55}$$

$$\rho_{ij}^{(\rho)}(t,t') = i\sum_q \left(v_i^q(t)v_j^{*q}(t') - u_j^q(t')u_i^{*q}(t)\right), \tag{6.56}$$

$$m_{ij}^{(F)}(t,t') = -\frac{1}{2}\sum_q \left(u_i^q(t)v_j^{*q}(t') + u_j^q(t')v_i^{*q}(t)\right), \tag{6.57}$$

$$m_{ij}^{(\rho)}(t,t') = -i\sum_q \left(u_i^q(t)v_j^{*q}(t') - u_j^q(t')v_i^{*q}(t)\right). \tag{6.58}$$

Notice that at equal time and position due to Eqs.(6.53) and (6.54), $\rho_{ii}^{(F)}(t,t)$ and $m_{ii}^{(F)}(t,t)$ satisfy

$$\rho_{ii}^{(F)}(t,t) = \sum_q |v_i^q(t)|^2 + \frac{1}{2} \tag{6.59}$$

$$m_{ii}^{(F)}(t,t) = -\sum_q u_i^q(t)v_i^{*q}(t). \tag{6.60}$$

Replacing Eqs. (6.59)-(6.60) into Eqs. (6.45)-(6.49) and using the constraints (6.53) -(6.54) we recover the standard time dependent equations for the quasiparticle amplitudes

$$\begin{aligned} &i\hbar\frac{\partial}{\partial}z_i(t) \\ &= -J(z_{i+1}(t) + z_{i-1}(t)) + U(|z_i(t)|^2 + 2\rho_{ii}^{(F)}(t,t))z_i(t) + Um_{ii}^{(F)}(t,t)z_i^*(t), \end{aligned} \tag{6.61}$$

$$i\hbar\frac{\partial}{\partial t}u_i^q(t) \tag{6.62}$$
$$= -J(u_{i+1}^q(t) + u_{i-1}^q(t)) + 2U(|z_i(t)|^2 + \rho_{ii}^{(F)}(t,t))u_i^q(t) - U(m_{ii}^{(F)}(t,t) + z_i(t)^2)v_i^q(t),$$
$$-i\hbar\frac{\partial}{\partial t}v_i^q(t) = \tag{6.63}$$
$$-J(v_{i+1}^q(t) + v_{i-1}^q(t))) + 2U(|z_i(t)|^2 + \rho_{ii}^{(F)}(t,t))v_i^q(t) - U(m_{ii}^{*(F)}(t,t) + z_i(t)^{*2})u_i^q(t).$$

If we compare Eqs. (6.61)-(6.63) with their time independent version, Eqs. (5.27) to (5.87), we notice that the equations are identical as they should be if we replace $i\hbar\frac{\partial}{\partial t}u_i^q \to \omega^{HFB}u_i^q$, $\quad i\hbar\frac{\partial}{\partial t}v_i^q \to \omega^{HFB}v_i^q$ and $i\hbar\partial_t z_i \to \mu^{HFB}z_i$. The factor of 1/2 difference between $\rho_{ii}^{(F)}$ and ρ_{ii} (see Eq. (5.19)) just leads to a trivial renormalization of the chemical potential. In the time dependent equations we have included the zero mode fluctuations, which were neglected in Eqs. (5.27) to (5.87). Hence we do not need the $c_s^{HFB^{\pm}}$ variables, which simply keep the orthogonality between of the condensate and the excitations. Eqs. (6.61) -(6.63) correspond to a set of $M(2M+1)$ coupled ordinary differential equations, where M is the total number of lattice sites. They can be solved using standard time propagation algorithms. Once the time dependent quasiparticle amplitudes are calculated we can derive the dynamics of physical observables constructed from them as a function of time, such as the average number of particles in a well $n_i(t)$, etc.

6.5 Second-order expansion

6.5.1 Equations of motion

Full second-order

The second-order contribution to Γ_2 is described in terms of the *setting-sun* Fig. 6.1b and the *basketball* Fig. 6.1c diagrams. The *basketball* diagram is independent of the mean-field and is constructed with only quartic vertices. The *setting-sun* diagram depends on z and contains only three-point vertices. The second-order $\Gamma_2^{(2)}$ effective action can be written as

$$\Gamma_2^{(2)}[z,G] = \tag{6.64}$$
$$i\left(\frac{U}{\mathcal{N}}\right)^2\int dt_i dt_j z_{ib}(t)z_{jb'}(t')\times$$
$$\left(G_{ij}^{bb'}(t,t')G_{ijdd'}(t,t')G_{ij}^{dd'}(t,t') + 2G_{ij}^{bd'}(t,t')G_{ijdd'}(t,t')G_{ij}^{db'}(t,t')\right) +$$
$$i\left(\frac{U}{2\mathcal{N}}\right)^2\int dt_i dt_j' \left(G_{ijbb'}(t,t')G_{ij}^{bb'}(t,t')G_{ijdd'}(t,t')G_{ij}^{dd'}(t,t') + \right.$$
$$\left. 2G_{ijbb'}(t,t')G_{ij}^{bd'}(t,t')G_{ijdd'}(t,t')G_{ij}^{db'}(t,t')\right).$$

To simplify the notation, let us introduce the following definitions [127]:

$$\begin{aligned}
\Pi_{ij}(t,t') &= -\frac{1}{2}G_{ijab}(t,t')G^{ab}_{ij}(t,t'), && (6.65)\\
\Xi_{ijab}(t,t') &= -D(t,t')G_{ijab}(t,t'), && (6.66)\\
D(t,t') &= z_{ib}(t)z_{ja}(t')G^{ba}_{ij}\ (t,t') - \Pi_{ij}(t,t'), && (6.67)\\
\overline{\Lambda}^{\ b}_{ij\ a}(t,t') &= -G^{cb}_{ij}(t,t')G_{ijca}(t,t'), && (6.68)\\
\Lambda^{b}_{ij\ a}(t,t') &= -G^{bc}_{ij}(t,t')G_{ijac}(t,t'), && (6.69)\\
\Theta^{ac}_{ij}(t,t') &= -(z_{id}(t)z_{jb}(t') + G_{ijdb}(t,t'))G^{ab}_{ij}(t,t')G^{dc}_{ij}(t,t') + \Xi^{ac}_{ij}(t,t'). && (6.70)
\end{aligned}$$

With the above definitions we find from Eqs. (6.22) and (6.24) the following equations of motion:

$$\begin{aligned}
h^a_b\hbar\partial_t z^b_i(t) &= \zeta^z_{HFB} + && (6.71)\\
&\quad i\left(\frac{2U}{\mathcal{N}}\right)^2\int dt'_j\ z_{jb}(t')\left(\Pi_{ij}(t,t')G^{ba}_{ji}\ (t',t) + \overline{\Lambda}^{\ b}_{ij\ c}(t,t')G^{ac}_{ij}(t,t')\right),\\
h^a_c\hbar\partial_t G^{cb}_{ij}\ (t,t') &= \zeta^G_{HFB} + && (6.72)\\
&\quad i\left(\frac{2U}{\mathcal{N}}\right)^2 z^a_i(t)\int dt''_k z_{kc}(t'')\left(\Pi_{ik}(t,t'')G^{cb}_{kj}(t'',t') + \overline{\Lambda}^{\ c}_{ik\ d}(t,t'')G^{db}_{kj}(t'',t')\right)\\
&\quad +i\left(\frac{2U}{\mathcal{N}}\right)^2\int dt''\left(\Theta^{\ a}_{ik\ d}(t,t'') + \Lambda^{ca}_{ik}\ (t,t'')z_{ic}(t)z_{kd}(t'')\right)G^{db}_{kj}\ (t'',t'),
\end{aligned}$$

where ζ^z_{HFB} and ζ^G_{HFB} are defined in Eqs. (6.43) and (6.45).

To get explicit expressions of the equations of motion in terms of $\rho^{(F,\rho)}$ and $m^{(F,\rho)}$ we introduce the functions

$$\begin{aligned}
\Omega^{(F)}_{ij}\left[\mathbf{f},\mathbf{g}\right] &= \mathbf{f}^{(F)}_{ij}(t_i,t_j)\mathbf{g}^{(F)}_{ij}(t_i,t_j) - \frac{1}{4}\left(\mathbf{f}^{(\rho)}_{ij}(t_i,t_j)\mathbf{g}^{(\rho)}_{ij}(t_i,t_j)\right), && (6.73)\\
\Omega^{(\rho)}_{ij}\left[\mathbf{f},\mathbf{g}\right] &= \mathbf{f}^{(F)}_{ij}(t_i,t_j)\mathbf{g}^{(\rho)}_{ij}(t_i,t_j) + \mathbf{f}^{(\rho)}_{ij}(t,t')\mathbf{g}^{(F)}_{ij}(t_i,t_j). && (6.74)
\end{aligned}$$

Using the spectral and statistical functions and setting the number of fields $\mathcal{N}$ equal to 2, the equations of motion derived under the full second-order approximation can be written as:

$$
\begin{aligned}
i\hbar\partial_{t_i} z_i \;=\; & -J(z_{i+1}(t_i)+z_{i-1}(t_i))+U(|z_i|^2+2\rho_{ii}^{(F)})z_i+Um_{ii}^{(F)}z_i^* \qquad (6.75)\\
& -2U^2\sum_k\int_0^{t_i}dt_k\left(z_k\Omega_{ik}^{(\rho)}[\rho,\rho^*]+z_k\Omega_{ik}^{(\rho)}[m,m^*]+z_k^*\Omega_{ik}^{(\rho)}[m,\rho]\right)\rho_{ki}^{(F)}\\
& -2U^2\sum_k\int_0^{t_i}\left(z_k^*\Omega_{ik}^{(\rho)}[\rho,\rho^*]+z_k^*\Omega_{ik}^{(\rho)}[m,m^*]+z_k\Omega_{ik}^{(\rho)}[m^*,\rho^*]\right)m_{ki}^{(F)}\\
& +2U^2\sum_k\int_0^{t_i}dt_k\left(z_k\Omega_{ik}^{(F)}[\rho,\rho^*]+z_k\Omega_{ik}^{(F)}[m,m^*]+z_k^*\Omega_{ik}^{(F)}[m,\rho]\right)\rho_{ki}^{(\rho)}\\
& +2U^2\sum_k\int_0^{t_i}\left(z_k^*\Omega_{ik}^{(F)}[\rho,\rho^*]+z_k^*\Omega_{ik}^{(F)}[m,m^*]+z_k\Omega_{ik}^{(F)}[m^*,\rho^*]\right)m_{ki}^{(\rho)},
\end{aligned}
$$

$$
\begin{aligned}
& -i\hbar\partial_{t_i}\rho_{ij}^{(F)}= \qquad (6.76)\\
& -J(\rho_{i+1j}^{(F)}(t_i,t_j)+\rho_{i-1j}^{(F)}(t_i,t_j))+2U(|z_i|^2+\rho_{ii}^{(F)})\rho_{ij}^{(F)}+U(m_{ii}^{*(F)}+z_i^{*2})m_{ij}^{(F)}\\
& -2U^2\sum_k\int_0^{t_i}dt_k\left(z_iz_k^*\Omega_{ik}^{(\rho)}[\rho,\rho]+2z_iz_k\Omega_{ik}^{(\rho)}[\rho,m^*]+2z_i^*z_k^*\Omega_{ik}^{(\rho)}[m,\rho]\right)\rho_{kj}^{(F)}\\
& -2U^2\sum_k\int_0^{t_i}dt_k\left(\Omega_{ik}^{(\rho)}[\rho,\Delta]+2z_i^*z_k\left(\Omega_{ik}^{(\rho)}[\rho,\rho^*]+\Omega_{ik}^{(\rho)}[m,m^*]\right)\right)\rho_{kj}^{(F)}\\
& -2U^2\sum_k\int_0^{t_i}dt_k\left(2z_iz_k^*\Omega_{ik}^{(\rho)}[m^*,\rho]+z_iz_k\Omega_{ik}^{(\rho)}[m^*,m^*]+2z_i^*z_k\Omega_{ik}^{(\rho)}[\rho^*,m^*]\right)m_{kj}^{(F)}\\
& -2U^2\sum_k\int_0^{t_i}dt_k\left(\Omega_{ik}^{(\rho)}[m^*,\Upsilon]+z_i^*z_k^*\left(2\Omega_{ik}^{(\rho)}[\rho,\rho^*]+2\Omega_{ik}^{(\rho)}[m,m^*]\right)\right)m_{kj}^{(F)}\\
& +2U^2\sum_k\int_0^{t_j}dt_k\left(z_iz_k^*\Omega_{ik}^{(F)}[\rho,\rho]+2z_iz_k\Omega_{ik}^{(F)}[\rho,m^*]+2z_i^*z_k^*\Omega_{ik}^{(F)}[m,\rho]\right)\rho_{kj}^{(\rho)}\\
& +2U^2\sum_k\int_0^{t_j}dt_k\left(\Omega_{ik}^{(F)}[\rho,\Delta]+2z_i^*z_k\left(\Omega_{ik}^{(F)}[\rho,\rho^*]+\Omega_{ik}^{(F)}[m,m^*]\right)\right)\rho_{kj}^{(\rho)}\\
& +2U^2\sum_k\int_0^{t_j}dt_k\left(2z_iz_k^*\Omega_{ik}^{(F)}[m^*,\rho]+z_iz_k\Omega_{ik}^{(F)}[m^*,m^*]+2z_i^*z_k\Omega_{ik}^{(F)}[\rho^*,m^*]\right)m_{kj}^{(\rho)}\\
& +2U^2\sum_k\int_0^{t_j}dt_k\left(\Omega_{ik}^{(F)}[m^*,\Upsilon]+2z_i^*z_k^*\left(\Omega_{ik}^{(F)}[\rho,\rho^*]+\Omega_{ik}^{(F)}[m,m^*]\right)\right)m_{kj}^{(F)},
\end{aligned}
$$

$$
\begin{aligned}
&-i\hbar\partial_{t_i}\rho_{ij}^{(\rho)} = \qquad (6.77)\\
&-J(\rho_{i+1j}^{(\rho)}(t_i,t_j)+\rho_{i-1j}^{(\rho)}(t_i,t_j))+2U(|z_i|^2+\rho_{ii}^{(F)})\rho_{ij}^{(\rho)}+U(m_{ii}^{*(F)}+z_i^{*2})m_{ij}^{(\rho)}\\
&-2U^2\sum_k\int_{t_j}^{t_i}dt_k\left(z_iz_k^*\Omega_{ik}^{(\rho)}[\rho,\rho]+2z_iz_k\Omega_{ik}^{(\rho)}[\rho,m^*]+2z_i^*z_k^*\Omega_{ik}^{(\rho)}[m,\rho]\right)\rho_{kj}^{(\rho)}\\
&-2U^2\sum_k\int_{t_j}^{t_i}dt_k\left(\Omega_{ik}^{(\rho)}[\rho,\Delta]+2z_i^*z_k\left(\Omega_{ik}^{(\rho)}[\rho,\rho^*]+\Omega_{ik}^{(\rho)}[m,m^*]\right)\right)\rho_{kj}^{(\rho)}\\
&-2U^2\sum_k\int_{t_j}^{t_i}dt_k\left(2z_iz_k^*\Omega_{ik}^{(\rho)}[m^*,\rho]+z_iz_k\Omega_{ik}^{(\rho)}[m^*,m^*]+2z_i^*z_k\Omega_{ik}^{(\rho)}[\rho^*,m^*]\right)m_{kj}^{(\rho)}\\
&-2U^2\sum_k\int_{t_j}^{t_i}dt_k\left(\Omega_{ik}^{(\rho)}[m^*,\Upsilon]+2z_i^*z_k^*\left(\Omega_{ik}^{(\rho)}[\rho,\rho^*]+\Omega_{ik}^{(\rho)}[m,m^*]\right)\right)m_{kj}^{(\rho)},
\end{aligned}
$$

$$
\begin{aligned}
&i\hbar\partial_{t_i}m_{ij}^{(F)} = \qquad (6.78)\\
&-J(m_{i+1j}^{(F)}(t_i,t_j)+m_{i-1j}^{(F)}(t_i,t_j))+2U(|z_i|^2+\rho_{ii}^{(F)})m_{ij}^{(F)}+U(m_{ii}^{(F)}+z_i^2)\rho_{ij}^{(F)}\\
&-2U^2\sum_k\int_0^{t_i}dt_k\left(2z_i^*z_k\Omega_{ik}^{(\rho)}[m,\rho^*]+z_i^*z_k^*\Omega_{ik}^{(\rho)}[m,m]+2z_iz_k^*\Omega_{ik}^{(\rho)}[\rho,m]\right)\rho_{kj}^{(F)}\\
&-2U^2\sum_k\int_0^{t_i}dt_k\left(\Omega_{ik}^{(\rho)}[m,\Upsilon]+2z_iz_k\left(\Omega_{ik}^{(\rho)}[\rho,\rho^*]+\Omega_{ik}^{(\rho)}[m,m^*]\right)\right)\rho_{kj}^{(F)}\\
&-2U^2\sum_k\int_0^{t_i}dt_k\left(z_i^*z_k\Omega_{ik}^{(\rho)}[\rho^*,\rho^*]+2z_i^*z_k^*\Omega_{ik}^{(\rho)}[\rho^*,m]+2z_iz_k\Omega_{ik}^{(\rho)}[m^*,\rho^*]\right)m_{kj}^{(F)}\\
&-2U^2\sum_k\int_0^{t_i}dt_k\left(\Omega_{ik}^{(\rho)}[\rho^*,\Delta]+2z_iz_k^*\left(\Omega_{ik}^{(\rho)}[\rho,\rho^*]+\Omega_{ik}^{(\rho)}[m,m^*]\right)\right)m_{kj}^{(F)}\\
&+2U^2\sum_k\int_0^{t_j}dt_k\left(2z_i^*z_k\Omega_{ik}^{(F)}[m,\rho^*]+z_i^*z_k^*\Omega_{ik}^{(F)}[m,m]+2z_iz_k^*\Omega_{ik}^{(F)}[\rho,m]\right)\rho_{kj}^{(\rho)}\\
&+2U^2\sum_k\int_0^{t_j}dt_k\left(\Omega_{ik}^{(F)}[m,\Upsilon]+2z_iz_k\left(\Omega_{ik}^{(F)}[\rho,\rho^*]+\Omega_{ik}^{(F)}[m,m^*]\right)\right)\rho_{kj}^{(\rho)}\\
&+2U^2\sum_k\int_0^{t_j}dt_k\left(z_i^*z_k\Omega_{ik}^{(F)}[\rho^*,\rho^*]+2z_i^*z_k^*\Omega_{ik}^{(F)}[\rho^*,m]+2z_iz_k\Omega_{ik}^{(F)}[m^*,\rho^*]\right)m_{kj}^{(\rho)}\\
&+2U^2\sum_k\int_0^{t_j}dt_k\left(\Omega_{ik}^{(F)}[\rho^*,\Delta]+2z_iz_k^*\left(\Omega_{ik}^{(F)}[\rho,\rho^*]+\Omega_{ik}^{(F)}[m,m^*]\right)\right)m_{kj}^{(\rho)},
\end{aligned}
$$

$$
\begin{aligned}
&i\hbar\partial_{t_i} m_{ij}^{(\rho)} = \qquad (6.79)\\
&-J(m_{i+1j}^{(\rho)}(t_i,t_j) + m_{i-1j}^{(\rho)}(t_i,t_j)) + 2U(|z_i|^2 + \rho_{ii}^{(F)})m_{ij}^{(\rho)} + U(m_{ii}^{(F)} + z_i^2)\rho_{ij}^{(\rho)}\\
&+2U^2\sum_k \int_{t_j}^{t_i} dt_k \left(2z_i^* z_k \Omega_{ik}^{(\rho)}[m,\rho^*] + z_i^* z_k^* \Omega_{ik}^{(\rho)}[m,m] + 2z_i z_k^* \Omega_{ik}^{(\rho)}[\rho,m]\right)\rho_{kj}^{(\rho)}\\
&+2U^2\sum_k \int_{t_j}^{t_i} dt_k \left(\Omega_{ik}^{(\rho)}[m,\Upsilon] + z_i z_k\left(2\Omega_{ik}^{(\rho)}[\rho,\rho^*] + 2\Omega_{ik}^{(\rho)}[m,m^*]\right)\right)\rho_{kj}^{(\rho)}\\
&+2U^2\sum_k \int_{t_j}^{t_i} dt_k \left(z_i^* z_k \Omega_{ik}^{(\rho)}[\rho^*,\rho^*] + 2z_i^* z_k^* \Omega_{ik}^{(\rho)}[\rho^*,m] + 2z_i z_k \Omega_{ik}^{(\rho)}[m^*,\rho^*]\right) m_{kj}^{(\rho)}\\
&+2U^2\sum_k \int_{t_j}^{t_i} dt_k \left(\Omega_{ik}^{(\rho)}[\rho^*,\Delta] + 2z_i z_k^*\left(\Omega_{ik}^{(\rho)}[\rho,\rho^*] + \Omega_{ik}^{(\rho)}[m,m^*]\right)\right) m_{kj}^{(\rho)},
\end{aligned}
$$

with

$$
\begin{aligned}
\Delta_{ij}^{(F,\rho)} &= \Omega_{ij}^{(F,\rho)}[\rho,\rho^*] + 2\Omega_{ij}^{(F,\rho)}[m,m^*], \qquad (6.80)\\
\Upsilon_{ij}^{(F,\rho)} &= 2\Omega_{ij}^{(F,\rho)}[\rho,\rho^*] + \Omega_{ij}^{(F,\rho)}[m,m^*]. \qquad (6.81)
\end{aligned}
$$

In the above equations we adopted the notation z_k meaning $z_k(t_k)$ for the condensate and m_{kj} and ρ_{kj} meaning $m_{kj}(t_k,t_j)$ and $\rho_{kj}(t_k,t_j)$ respectively for the two point functions. These notation is also going to be used in the equations for the $1/\mathcal{N}$ expansion.

2PI-$1/\mathcal{N}$ expansion

The 2PI effective action is a singlet under O($\mathcal{N}$) rotations. It can be shown that all graphs contained in an O($\mathcal{N}$) expansion can be built from the irreducible invariants[127]: z^2, $Tr(G^n)$ and $Tr(zzG^n)$, with $n < \mathcal{N}$. The factors of $\mathcal{N}$ in a single graph contributing to the same $1/\mathcal{N}$ expansion then have two origins: a factor of $\mathcal{N}$ from each irreducible invariant and a factor of $1/\mathcal{N}$ from each vertex. The leading order large $\mathcal{N}$ approximation scales proportional to $\mathcal{N}$, the next to leading order (NLO) contributions are of order 1 and so on. At leading order only the first term of Eq. (6.42) contributes. At the next to leading order level, if we truncate up to second-order in the coupling strength, the *double-bubble* is totally included but only certain parts of the *setting-sun* and *basketball* diagrams are: the first term in both of the integrals of Eq. (6.64),

$$
\begin{aligned}
&\Gamma_2^{(2)1/\mathcal{N}}[z,G] = i\left(\frac{U}{\mathcal{N}}\right)^2 \int dt_i dt_j z_{ib}(t) z_{jb'}(t') \left(G_{ij}^{bb'}(t,t') G_{ijdd'}(t,t') G_{ij}^{dd'}(t,t')\right) +\\
&i\left(\frac{U}{2\mathcal{N}}\right)^2 \int dt_i dt'_j \left(G_{ijbb'}(t,t') G_{ij}^{bb'}(t,t') G_{ijdd'}(t,t') G_{ij}^{dd'}(t,t')\right). \qquad (6.82)
\end{aligned}
$$

The equations of motion under this approximation are the ones obtained for the full second-order expansion but with $\Lambda = \overline{\Lambda} = 0$, and $\Theta = \Xi$.

In terms of the spectral and statistical functions the equation of motion can be written as:

$$
\begin{aligned}
& i\hbar\partial_{t_i} z_i = -J(z_{i+1}(t_i) + z_{i-1}(t_i)) + U(|z_i|^2 + 2\rho_{ii}^{(F)})z_i + U m_{ii}^{(F)} z_i^* \qquad (6.83)\\
& -U^2 \sum_k \int_0^{t_i} dt_k \Pi_{ik}^{(\rho)} \left(z_k \rho_{ki}^{(F)} + z_k^* m_{ki}^{(F)} \right) + U^2 \sum_k \int_0^{t_i} dt_k \Pi_{ik}^{(F)} \left(z_k \rho_{ki}^{(\rho)} + z_k^* m_{ki}^{(\rho)} \right),
\end{aligned}
$$

$$
\begin{aligned}
& -i\hbar\partial_{t_i} \rho_{ij}^{(F)} = \qquad (6.84)\\
& -J(\rho_{i+1j}^{(F)}(t_i, t_j) + \rho_{i-1j}^{(F)}(t_i, t_j)) + 2U(|z_i|^2 + \rho_{ii}^{(F)})\rho_{ij}^{(F)} + U(m_{ii}^{*(F)} + z_i^{*2}) m_{ij}^{(F)}\\
& -U^2 \sum_k \int_0^{t_i} dt_k \left(z_i z_k^* \Omega_{ik}^{(\rho)} [\rho, \rho] + z_i z_k \Omega_{ik}^{(\rho)} [\rho, m^*] + z_i^* z_k^* \Omega_{ik}^{(\rho)} [m, \rho] \right) \rho_{kj}^{(F)}\\
& -U^2 \sum_k \int_0^{t_i} dt_k \left(\Omega_{ik}^{(\rho)} [\rho, \Pi] + z_i^* z_k \left(2\Omega_{ik}^{(\rho)} [\rho, \rho^*] + \Omega_{ik}^{(\rho)} [m, m^*] \right) \right) \rho_{kj}^{(F)}\\
& -U^2 \sum_k \int_0^{t_i} dt_k \left(z_i z_k^* \Omega_{ik}^{(\rho)} [m^*, \rho] + z_i z_k \Omega_{ik}^{(\rho)} [m^*, m^*] + z_i^* z_k \Omega_{ik}^{(\rho)} [\rho^*, m^*] \right) m_{kj}^{(F)}\\
& -U^2 \sum_k \int_0^{t_i} dt_k \left(\Omega_{ik}^{(\rho)} [m^*, \Pi] + z_i^* z_k^* \left(\Omega_{ik}^{(\rho)} [\rho, \rho^*] + 2\Omega_{ik}^{(\rho)} [m, m^*] \right) \right) m_{kj}^{(F)}\\
& +U^2 \sum_k \int_0^{t_j} dt_k \left(z_i z_k^* \Omega_{ik}^{(F)} [\rho, \rho] + z_i z_k \Omega_{ik}^{(F)} [\rho, m^*] + z_i^* z_k^* \Omega_{ik}^{(F)} [m, \rho] \right) \rho_{kj}^{(\rho)}\\
& +U^2 \sum_k \int_0^{t_j} dt_k \left(\Omega_{ik}^{(F)} [\rho, \Pi] + z_i^* z_k \left(2\Omega_{ik}^{(F)} [\rho, \rho^*] + \Omega_{ik}^{(F)} [m, m^*] \right) \right) \rho_{kj}^{(\rho)}\\
& +U^2 \sum_k \int_0^{t_j} dt_k \left(z_i z_k^* \Omega_{ik}^{(F)} [m^*, \rho] + z_i z_k \Omega_{ik}^{(F)} [m^*, m^*] + z_i^* z_k \Omega_{ik}^{(F)} [\rho^*, m^*] \right) m_{kj}^{(\rho)}\\
& +U^2 \sum_k \int_0^{t_j} dt_k \left(\Omega_{ik}^{(F)} [m^*, \Pi] + z_i^* z_k^* \left(\Omega_{ik}^{(F)} [\rho, \rho^*] + 2\Omega_{ik}^{(F)} [m, m^*] \right) \right) m_{kj}^{(F)},
\end{aligned}
$$

$$
\begin{aligned}
&-i\hbar\partial_{t_i}\rho_{ij}^{(\rho)} = \qquad (6.85)\\
&-J(\rho_{i+1j}^{(\rho)}(t_i,t_j)+\rho_{i-1j}^{(\rho)}(t_i,t_j))+2U(|z_i|^2+\rho_{ii}^{(F)})\rho_{ij}^{(\rho)}+U(m_{ii}^{*(F)}+z_i^{*2})m_{ij}^{(\rho)}\\
&-U^2\sum_k\int_{t_j}^{t_i}dt_k\left(z_iz_k^*\Omega_{ik}^{(\rho)}[\rho,\rho]+z_iz_k\Omega_{ik}^{(\rho)}[\rho,m^*]+z_i^*z_k^*\Omega_{ik}^{(\rho)}[m,\rho]\right)\rho_{kj}^{(\rho)}\\
&-U^2\sum_k\int_{t_j}^{t_i}dt_k\left(\Omega_{ik}^{(\rho)}[\rho,\Pi]+z_i^*z_k\left(2\Omega_{ik}^{(\rho)}[\rho,\rho^*]+\Omega_{ik}^{(\rho)}[m,m^*]\right)\right)\rho_{kj}^{(\rho)}\\
&-U^2\sum_k\int_{t_j}^{t_i}dt_k\left(z_iz_k^*\Omega_{ik}^{(\rho)}[m^*,\rho]+z_iz_k\Omega_{ik}^{(\rho)}[m^*,m^*]+z_i^*z_k\Omega_{ik}^{(\rho)}[\rho^*,m^*]\right)m_{kj}^{(\rho)}\\
&-U^2\sum_k\int_{t_j}^{t_i}dt_k\left(\Omega_{ik}^{(\rho)}[m^*,\Pi]+z_i^*z_k^*\left(\Omega_{ik}^{(\rho)}[\rho,\rho^*]+2\Omega_{ik}^{(\rho)}[m,m^*]\right)\right)m_{kj}^{(\rho)},
\end{aligned}
$$

$$
\begin{aligned}
&i\hbar\partial_{t_i}m_{ij}^{(F)} = \qquad (6.86)\\
&-J(m_{i+1j}^{(F)}(t_i,t_j)+m_{i-1j}^{(F)}(t_i,t_j))+2U(|z_i|^2+\rho_{ii}^{(F)})m_{ij}^{(F)}+U(m_{ii}^{(F)}+z_i^2)\rho_{ij}^{(F)}\\
&-U^2\sum_k\int_0^{t_i}dt_k\left(z_i^*z_k\Omega_{ik}^{(\rho)}[m,\rho^*]+z_i^*z_k^*\Omega_{ik}^{(\rho)}[m,m]+z_iz_k^*\Omega_{ik}^{(\rho)}[\rho,m]\right)\rho_{kj}^{(F)}\\
&-U^2\sum_k\int_0^{t_i}dt_k\left(\Omega_{ik}^{(\rho)}[m,\Pi]+z_iz_k\left(\Omega_{ik}^{(\rho)}[\rho,\rho^*]+2\Omega_{ik}^{(\rho)}[m,m^*]\right)\right)\rho_{kj}^{(F)}\\
&-U^2\sum_k\int_0^{t_i}dt_k\left(z_i^*z_k\Omega_{ik}^{(\rho)}[\rho^*,\rho^*]+z_i^*z_k^*\Omega_{ik}^{(\rho)}[\rho^*,m]+z_iz_k\Omega_{ik}^{(\rho)}[m^*,\rho^*]\right)m_{kj}^{(F)}\\
&-U^2\sum_k\int_0^{t_i}dt_k\left(\Omega_{ik}^{(\rho)}[\rho^*,\Pi]+z_iz_k^*\left(2\Omega_{ik}^{(\rho)}[\rho,\rho^*]+\Omega_{ik}^{(\rho)}[m,m^*]\right)\right)m_{kj}^{(F)}\\
&+U^2\sum_k\int_0^{t_j}dt_k\left(z_i^*z_k\Omega_{ik}^{(F)}[m,\rho^*]+z_i^*z_k^*\Omega_{ik}^{(F)}[m,m]+z_iz_k^*\Omega_{ik}^{(F)}[\rho,m]\right)\rho_{kj}^{(\rho)}\\
&+U^2\sum_k\int_0^{t_j}dt_k\left(\Omega_{ik}^{(F)}[m,\Pi]+z_iz_k\left(2\Omega_{ik}^{(F)}[\rho,\rho^*]+\Omega_{ik}^{(F)}[m,m^*]\right)\right)\rho_{kj}^{(\rho)}\\
&+U^2\sum_k\int_0^{t_j}dt_k\left(z_i^*z_k\Omega_{ik}^{(F)}[\rho^*,\rho^*]+z_i^*z_k^*\Omega_{ik}^{(F)}[\rho^*,m]+z_iz_k\Omega_{ik}^{(F)}[m^*,\rho^*]\right)m_{kj}^{(\rho)}\\
&+U^2\sum_k\int_0^{t_j}dt_k\left(\Omega_{ik}^{(F)}[\rho^*,\Pi]+z_iz_k^*\left(2\Omega_{ik}^{(F)}[\rho,\rho^*]+\Omega_{ik}^{(F)}[m,m^*]\right)\right)m_{kj}^{(\rho)},
\end{aligned}
$$

$$
\begin{aligned}
&i\hbar\partial_{t_i} m_{ij}^{(\rho)} = \qquad (6.87)\\
&-J(m_{i+1j}^{(\rho)}(t_i,t_j) + m_{i-1j}^{(\rho)}(t_i,t_j)) + 2U(|z_i|^2 + \rho_{ii}^{(F)})m_{ij}^{(\rho)} + U(m_{ii}^{(F)} + z_i^2)\rho_{ij}^{(\rho)}\\
&+U^2\sum_k \int_{t_j}^{t_i} dt_k \left(z_i^* z_k \Omega_{ik}^{(\rho)}[m,\rho^*] + z_i^* z_k^* \Omega_{ik}^{(\rho)}[m,m] + z_i z_k^* \Omega_{ik}^{(\rho)}[\rho,m]\right)\rho_{kj}^{(\rho)}\\
&+U^2\sum_k \int_{t_j}^{t_i} dt_k \left(\Omega_{ik}^{(\rho)}[m,\Pi] + z_i z_k \left(\Omega_{ik}^{(\rho)}[\rho,\rho^*] + 2\Omega_{ik}^{(\rho)}[m,m^*]\right)\right)\rho_{kj}^{(\rho)}\\
&+U^2\sum_k \int_{t_j}^{t_i} dt_k \left(z_i^* z_k \Omega_{ik}^{(\rho)}[\rho^*,\rho^*] + z_i^* z_k^* \Omega_{ik}^{(\rho)}[\rho^*,m] + z_i z_k \Omega_{ik}^{(\rho)}[m^*,\rho^*]\right) m_{kj}^{(\rho)}\\
&+U^2\sum_k \int_{t_j}^{t_i} dt_k \left(\Omega_{ik}^{(\rho)}[\rho^*,\Pi] + z_i z_k^* \left(2\Omega_{ik}^{(\rho)}[\rho,\rho^*] + \Omega_{ik}^{(\rho)}[m,m^*]\right)\right) m_{kj}^{(\rho)},
\end{aligned}
$$

with

$$
\Pi_{ij}^{(F,\rho)} = \Omega_{ij}^{(F,\rho)}[\rho,\rho^*] + \Omega_{ij}^{(F,\rho)}[m,m^*]\,. \qquad (6.88)
$$

We end this section by emphasizing that the only approximation introduced in the derivation of the equations of motion presented here is the truncation up to second-order in the interaction strength. These equations depict the nonlinear and non-Markovian quantum dynamics, which we consider as the primary distinguishing features of this work. It supersedes what the second-order kinetic theories currently presented can do, their going beyond the HFB approximation notwithstanding. For example Ref. [62] presents a kinetic theory approach that includes binary interactions to second-order in the interaction potential but uses the Markovian approximation. In Ref. [61] the authors gave a non-Markovian generalization to the quantum kinetic theory derived by Walser *et. al.*[58] by including memory effects. However in that work symmetry breaking fields, z and anomalous fluctuations, m, are neglected.

6.5.2 Conservation laws

For a closed (isolated) system the mean total number of particles N and energy are conserved quantities as they are the constants of motion for the dynamical equations.

Particle number conservation is a consequence of the invariance of the Hamiltonian under a global phase change. The mean total number of particles is given by

$$
\begin{aligned}
\left\langle \hat{N} \right\rangle &= \sum_i \left\langle \hat{a}_i^\dagger \hat{a}_i \right\rangle = \sum_i \left(|z_i|^2 + \rho_{ii}^{(F)} - \frac{1}{2}\right) \qquad (6.89)\\
&= N.
\end{aligned}
$$

The kinetic equation for N is then

$$\begin{aligned}\frac{d}{dt}\left\langle \hat{N}(t)\right\rangle &= \sum_i 2\mathrm{Re}\left(\mathrm{z_i(t)}\frac{\partial}{\partial \mathrm{t}}\mathrm{z_i^*(t)}\right) \\ &\quad + \lim_{t\to t'}\left(\frac{\partial}{\partial t}\rho_{ii}^{(F)}(t,t') + \frac{\partial}{\partial t'}\rho_{ii}^{*(F)}(t',t)\right) \\ &= 0.\end{aligned} \tag{6.90}$$

All three approximations we have considered, namely, HFB, $1/\mathcal{N}$ expansion and full second-order expansion, conserve the particle number. This can be shown by plugging in the kinetic equation of $\left\langle \hat{N}(t)\right\rangle$ (Eq. 6.90) the equation of motion for the mean field and the normal statistical propagator Eqs. (45),(46), Eqs.(6.76),(6.77) and Eqs (6.85),(6.86)), and cancelling terms. It is important to note that even though total population is always conserved there is always a transfer of population between condensate and non condensate atoms.

While number conservation can be proved explicitly, to prove total energy conservation is not obvious as the Hamiltonian cannot be represented as a linear combination of the relevant operators. It is clear that the exact solution of a closed system is unitary in time and hence disallows any dissipation. However, the introduction of approximation schemes that truncate the infinite hierarchy of correlation functions at some finite order with causal boundary conditions may introduce dissipation [118].

To discuss energy conservation we can use the phi-derivable criteria [138] which states that nonequilibrium approximations in which the self energy Σ is of the form $\delta\Phi/\delta G$, with Φ a functional of G, conserve particle number, energy and momentum. All the approximations we consider in this paper are phi derivable and thus they obey energy, particle number and momentum conservation laws. For HFB, $\Phi = \Gamma_2^{(1)}$, for the full second-order expansion, $\Phi = \Gamma_2^{(1)} + \Gamma_2^{(2)}$ and for the second-order next to leading order $1/\mathcal{N}$ expansion, $\Phi = \Gamma_2^{(1)} + \Gamma_2^{(2)1/\mathcal{N}}$. See Eqs. (6.23), (6.42), (6.64) and (6.82). For a detailed discussion of the complete next to leading order $1/\mathcal{N}$ expansion see Refs. [126, 127] and references therein.

6.6 Conclusions

In summary, we have presented a new approach for the description of the nonequilibrium dynamics of a Bose-Einstein condensate and fluctuations in a closed quantum field system. The formalism allows one to go beyond the well known HFB approximation and to incorporate the nonlinear and non-Markovian aspects of the quantum dynamics as manifest in the dissipation and fluctuations phenomena. The 2PI effective action formalism provides a useful framework, where the mean field and the correlation functions are treated on the same footing self-consistently and which respects conservations of particle number and energy. The CTP formalism ensures that the dynamical equations of motion are also causal. In their

current form the scattering terms are nonlocal in time and thus hard to estimate analytically, and their calculation is numerically demanding. However, this systematic approach can be used as a quantitative means to obtain solutions in different regimes and make comparisons with kinetic theory results where a Markovian approximation is assumed. We postpone these discussions to chapter 8.

Chapter 7

Nonequilibrium dynamics of a patterned loaded optical lattice: Beyond the mean field approximation

In this chapter the two-particle irreducible (2PI) closed-time-path (CTP) effective action formalism derived in chapter 6 is used to describe the nonequilibrium dynamics of a Bose Einstein condensate (BEC) selectively loaded into every third site of a one-dimensional optical lattice.

In chapter 4 we used a mean field approach to describe the dynamics of this system. However, we show here that even in the case when the kinetic energy is comparable to the interaction energy, interatomic collisions play a crucial role in determining the quantum dynamics of the system, and therefore a mean field approach is only accurate for short times. This result is demonstrated by comparison between the mean field solutions and the exact numerical time evolution of the initial state using the Bose Hubbard Hamiltonian for systems with small numbers of atoms ($N \sim 10$) and lattice sites ($M = 2$ or 3). The exact numerical solution is also used to test the validity of the various methods derived under the 2PI-CTP approximation.

We show that because the second-order 2PI approximations include multi-particle scattering in a systematic way, they are able to capture damping effects exhibited in the exact solution, which the mean field and the HFB approximations fail to reproduce. However, our numerical results also show that all of the approximations fail at late times, when interaction effects become significant.

7.1 Mean field dynamics

In this section we review the basic features of the mean field results obtained in chapter 4, in order to provide the context for the subsequent discussion of the

dynamics in the 2PI-CTP formalism.

7.1.1 Dynamical evolution

By making the mean field ansatz in the Bose-Hubbard Hamiltonian, we replace the field operator $\hat{a}_i$ by a c-number $z_i(t)$. The amplitudes $z_i(t)$ satisfy the DNLSE (Eq. (4.6)).

In section 4.3.2, we treated a model case in which the initial occupancies of each third site are the same, and in which the condensate initially has a uniform phase. Thus at $\tau = 0$, ($\tau \equiv \frac{tJ}{\hbar}$), the amplitudes $z_i(\tau)$ are given by $z_{3i}(0) = \sqrt{3/M}$, $z_{3i+1}(0) = z_{3i+2}(0) = 0$, where M is the total number of lattice sites. For an infinite lattice, or one with periodic boundary conditions, the amplitudes for all initially occupied sites $z_{3i}(\tau) = z_0(\tau)$ evolve identically in time, and the amplitudes for the initially unoccupied sites satisfy $z_{3i+1}(\tau) = z_{3i+2}(\tau) =$ for all τ. This allows us to reduce the full set of equations to a set of two coupled equations for $z_0(\tau)$ and $z_1(\tau)$.

The solutions $|z_0(\tau)|$ and $|z_1(\tau)|$ are oscillatory functions whose amplitudes and common period, $T(\gamma)$, are determined by the parameter $\gamma \equiv 3\frac{NU}{MJ} = 3\lambda$. The mean field dynamical behavior can be qualitatively divided into two regimes:

The tunneling dominated regime ($\gamma < 1$)**:** In this regime the oscillation period is essentially constant, the role of interactions is relatively small, and the equations of motion are equivalent to those of a two-state Rabi problem. This system will undergo Rabi oscillations whereby atoms periodically tunnel from the initially occupied site into the two neighboring sites. For $\gamma = 0$ the period of oscillation is $\frac{2\pi}{3}$.

Interaction dominated regime: The effect of interactions on the mean field dynamics is to cause the energies of the initially occupied sites to shift relative to those of the unoccupied sites. As γ increases the tunneling between sites occurs at a higher frequency, but with reduced amplitude. The population of the initially occupied sites becomes effectively self-trapped by the purely repulsive pair interaction.

7.1.2 Comparisons with the exact solution

To check the validity of the mean field approximation, we made comparisons with the exact many body solution for $N = 6$ atoms and $M = 3$ wells. We use a modest number of atoms and lattice sites for the comparisons, due to the fact that the Hilbert space needed for the calculations increases rapidly with the number of atoms and wells.

Exact solution

For the exact solution we used an initial state given by

$$|\varphi(0)\rangle = (e^{-N/2} e^{\sqrt{N}\hat{a}_o^\dagger} |0\rangle) \otimes |0\rangle \otimes |0\rangle \,. \tag{7.1}$$

The initial state represents a coherent state with an average of N atoms in the initially populated well and zero atoms in the others. We chose this state because in the experiment the loading of the atoms was done slow enough with respect to band excitations but fast with respect to many body excitations that at time $t = 0$ most of the atoms in the initially populated wells were condensed.

The fully quantal solution was found by evolving the initial state in time with the Bose-Hubbard Hamiltonian, so that $|\varphi(t)\rangle = e^{-\frac{i}{\hbar}\hat{H}t}|\varphi(0)\rangle$. To do the numerical calculations we partitioned the Hilbert space in subspaces with a fixed number of atoms and propagated independently the projections of the initial state on the respective subspaces. A subspace with N_n number of atoms and M wells is spanned by $\frac{(N_n+M-1)!}{N_n!(M-1)!}$ states. This procedure could be done because the Hamiltonian commutes with the number operator $\sum_i \hat{a_i}^\dagger \hat{a_i}$, and therefore during the dynamics the different subspaces never get mixed. The number of subspaces used for the numerical evolution were such that no change in plots of the dynamical observables was detected by adding another subspace. Generally for N atoms in the initial state, this condition was achieved by including the subspaces between $N - 4\sqrt{N}$ and $N + 4\sqrt{N}$ atoms.

Numerical comparisons

In Fig. 7.1 we plot the average population per well $\left\langle \hat{a}_i^\dagger(t)\hat{a}_i(t) \right\rangle$ and the condensate population per well $|\langle \hat{a}_i(t) \rangle|^2$ and compare them with the mean field predictions, i.e. $|z_i(t)|^2$, for three different values of γ. The salient features observed in these comparisons are:

1. Weakly interacting regime ($\gamma = 0.2$):

   In this regime the DNLSE gives a good description of the early time dynamics. We observe in Fig. 7.1 that the total population per well predicted by the mean field solution agrees with the exact solution and also that the condensate population remains large for the time under consideration. We expect the semiclassical approach to be valid for time scales less than the inverse energy level spacing. In Ref. [129] the authors show the validity of the semiclassical approach when $\tau < \tau_{cl} \sim \frac{N}{M\gamma}$ in the case of two lattice sites. This time scale is in good agreement with the numerical results shown in in Fig.7.1. After τ_{cl} quantum effects become important.

2. Intermediate regime ($\gamma = 2$):

   Quantum fluctuations lead to a non-trivial modulation of the classical oscillations. In this regime the ratio between interaction and kinetic energy is

small enough to allow the atoms to tunnel but not too small to make interaction effects negligible. Mean field results are accurate only for a short time. In this regime, the exact solution exhibits damped oscillations of the atomic population. Quantum scattering effects are crucial, even for rather early times.

To understand the dynamics in the weak and intermediate regimes, we have to focus on the coherent properties of the system. Even though interactions can be strong, the ground state is indeed superfluid. If we look at the initial coherence of the system, determined by $\left\langle \hat{a}_i^\dagger(0)\hat{a}_j(0)\right\rangle_{i\neq j}$, it can be seen to be zero due to the patterned loading. However, this is no longer the case for $t > 0$, and non-zero correlations are developed in the dynamics. The dynamical restoration of the phase coherence which tends to distribute atoms uniformly among the lattice sites and to damp the oscillations characterizes the dynamics in the superfluid regime. In Ref. [129], the authors show, not for a patterned loaded initial state but for an initial Mott state also with zero initial phase coherence, how the phase coherence is restored dynamically.

3. Strongly correlated regime ($\gamma = 12$):

   The system exhibits macroscopic quantum self-trapping of the population. Qualitatively, both the mean field and the exact solutions agree, in the sense that both predict self-trapping of atoms in the initially populated wells, due to interactions. However, the fast decrease of the condensate population and its subsequent revivals (as found in the exact solutions) give us an idea of the importance of correlation effects beyond mean field. For a uniform loaded lattice, the collapse and revivals of the condensate in this strong interacting regime and the importance of quantum effects have been experimentally observed[47].

   Even though there is minimal initial coherence between adjacent sites due to the patterned loading procedure we are still preparing the system in a superfluid state in the initially populated well. At time $t = 0$ we have a condensate fraction of order one. However, the ground state of the system is not superfluid. It is expected then that, after some time, the phase is going to randomize and this will lead to the collapse of the condensate population. After the collapse, the system will remain for a while with zero condensate population. However, it can not remain zero forever because we are dealing with a closed quantum system, with finite recurrence time. Therefore at some time t_{rev} we expect the condensate to revive again. The collapses and revivals of the condensate population in the strong interacting regime can be easily estimated by considering the energy spectrum. In this regime the energy eigenstates of the system are almost number (Fock) states and the energy spectrum is almost quadratic, $E_n \approx n(n-1)U/2$. The dynamics of the system is described by the interference of the different n-particle Fock states that span the coherent state of the initially populated well. At integer values of $t_{rev} = (U/h)^{-1}$, the phase factors add to an integer value of 2π, leading

to a revival of the initial state. This time scale agrees with the one estimated in Ref.[130] for a more general situation. That reference, also shows how the collapse time, t_{coll}, depends on the variance of the initial atomic distribution; it is given by: $t_{coll} \sim t_{rev}/(2\pi\sigma)$. If the initial state is a coherent state, the initial distribution is Poissonian and t_{coll} is given by $t_{coll} \sim \hbar/(\sqrt{N}U)$. For the parameters used in the strongly correlated regime, $\gamma = 12$ and $N = 6$, we observe that the estimated collapses and revival times are in agreement with what is shown in Fig. 7.1.

7.2 2PI-CTP approximations

It was shown in the previous section that to describe the dynamics of the patterned loaded optical lattice, approximations beyond the standard mean field theory are required. In this section we proceed to test the validity of the different 2PI-CTP approximations derived in chapter 6, explicitly, the time dependent HFB approximation, the full second-order approximation and the $1/\mathcal{N}$ expansion up to second-order in the interaction strength. Because in all these approximations we use U/J as an expansion parameter we will focus our calculations on the intermediate regime, where the ratio U/J is small enough that truncation up to second-order makes sense but not too small so that interaction effects still have to be taken into account.

We start by describing the initial conditions chosen for the numerical calculations, then we outline the numerical algorithms used, and finally we discuss the results.

7.2.1 Initial conditions and parameters

To model the patterned loading, the initial conditions assumed for the numerical solutions were $z_i(0) = N\delta_{i0}$, $\rho_{ij}^{(F)}(0,0) = \frac{1}{2}\delta_{ij}$, $\rho_{ij}^{(\rho)}(0,0) = -i\delta_{ij}$ and $m_{ij}^{(F)}(0,0)) = m_{ij}^{(\rho)}(0,0) = 0$. Here $z_i(t)$ are the condensate amplitudes and $\rho_{ij}^{(F)}(t_i,t_j)$, $\rho_{ij}^{(\rho)}(t_i,t_j)$, $m_{ij}^{(F)}(t_i,t_j)$ and $m_{ij}^{(\rho)}(t_i,t_j)$ are the statistical and spectral normal and anomalous propagators as defined in chapter 6. The initial conditions correspond to an initial coherent state with N atoms in the initially populated well.

To study the kinetic energy dominated regime we chose for the simulations three different sets of parameters:. The first set is chosen to be in the very weak interacting regime, $M = 3, N = 6, J = 1$ and $U/J = 1/30$. With this choice we wanted to show the validity of a mean field approach to describe this regime and the corrections introduced by the higher order approximations. The second set of parameters is $M = 3, N = 8, J = 1$ and $U/J = 1/3$. In this regime the kinetic energy is big enough to allow tunneling but the effect of the interactions is crucial in the dynamics.

At the mean field level (using the DNLSE) for a given number of wells, the only relevant parameter for describing the dynamics of the system is the ratio UN/J. This is not the case in the exact solution where both UN/J and N are important.

The larger the initial population N, the larger the initial population in the coherent matter field, and therefore we expect better agreement of the truncated theories with the exact solution with larger N. To study the dependence of the dynamics on the total number of atoms, the third set of parameters in our solutions is chosen to be $M = 2, J = 1/2$ and NU/J was fixed to 4, but the number of atoms was changed from 20 to 80. To increase the number of atoms in the exact calculations we had to reduce the number of wells to two due to the fact that the dimension of the Hilbert space scales exponentially with N and M.

7.2.2 Numerical algorithm for the approximate solution

The time evolution equations obtained in chapter 6 are nonlinear integro-differential equations. Though the equations are very complicated, they can be solved on a computer. The important point to note is that all equations are causal in time, and all quantities at some later time t_f can be obtained by integration over the explicitly known functions for times $t \leq t_f$.

For the numerical solution we employed a time discretization $t = na_t$, $t' = ma_t$, with n and m integers and took the advantage that, due to the presence of the lattice, the spatial dimension is discrete (indices i and j). The discretized equations for the time evolution of the matrices $\rho^{(F,\rho)}_{ijnm}$, $m^{(F,\rho)}_{ijnm}$ and z_{in} advance time stepwise in the n-direction for fixed m. Due to the symmetries of the matrices only half of the (n, m) matrices have to be computed and the values $\rho^{\rho}_{ijnn} = -i$, $m^{\rho}_{ijnn} = 0$ are fixed for all time due to the bosonic commutation relations. As initial conditions one specifies $\rho^{(F,\rho)}_{ij00}$, $m^{(F,\rho)}_{ij00}$ and $z_{i0.}$

To ensure that the discretized equations retain the conservation properties present in the continuous ones one has to be very careful in the evolution of the diagonal terms of $\rho^{(F)}_{iinn}$ and take the limit $m \to n$ in a proper way:

$$\rho^{(F,\rho)}_{ijn+1n+1} - \rho^{(F,\rho)}_{ijnn} = \tag{7.2}$$
$$\left(\rho^{(F,\rho)}_{ijn+1n} - \rho^{(F,\rho)}_{ijnn}\right) \pm \left(\rho^{*(F,\rho)}_{jin+1n} - \rho^{*(F,\rho)}_{jinn}\right),$$
$$m^{(F,\rho)}_{ijn+1n+1} - m^{(F,\rho)}_{ijnn} = \tag{7.3}$$
$$\left(m^{(F,\rho)}_{ijn+1n} - m^{(F,\rho)}_{ijnn}\right) \pm \left(m^{(F,\rho)}_{jin+1n} - m^{(F,\rho)}_{jinn}\right),$$

with the positive sign for the statistical propagators, $(F)'s$, and negative sign for the spectral functions, $(\rho)'s$. We used the fourth order Runge-Kutta algorithm to propagate the local part of the equations and a regular one step Euler method to iterate the non local parts. For the integrals we used the standard trapezoidal rule. Starting with $n = 1$, for the time step $n + 1$ one computes successively all entries with $m = 0.....n, n+1$ from known functions evaluated at previous times.

The time step a_t was chosen small enough so that convergence was observed, that is, further decreasing it did not change the results. The greater the parameter UN/J, the smaller is the time step required. The main numerical limitation of

the 2PI approximation is set by the time integrals, which make the numerical calculations time and memory consuming. However, within a typical numerical precision it was usually not necessary to keep all past values of the two point functions in the memory. A characteristic time, after which the influence of the early time in the late time behavior is negligible, is given by the inverse damping rate. This time is described by the exponential damping of the two-point correlator at time t with the initial time[127]. In our numerics we extended the length of the employed time interval until the results did not depend on it. In general, it was less than the inverse damping rate. We used for the calculations a single PII 400 MHz workstation with 260 Mb of memory. For a typical run 1-2 days of computational time were required.

7.2.3 Results and discussions

In Figs. 7.2 to 7.6 we show our numerical results. We focus our attention on the evolution of the condensate population per well, $|z_i(t)|^2$, the total atomic population per well, $|z_i|^2 + \rho_{ii}^{(F)}(t,t) - \frac{1}{2}$, the depletion per well or atoms out of the condensate, $\rho_{ii}^{(F)}(t,t) - \frac{1}{2}$, and the total condensate population,$\sum_i |z_i(t)|^2$. The total population is also explicitly shown in the figures to emphasize number conservation.

The quasi-momentum distribution of the atoms released from the lattice is important because it is one of the most easily accessible quantities from an experiment. (see sec.5.5) The quasi-momentum distribution function n_k is defined as

$$n_k(t) = \frac{1}{M} \sum_{i,j} e^{ik(i-j)} \left\langle a_i^\dagger(t) a_j(t) \right\rangle , \tag{7.4}$$

where the quasi-momentum k can assume discrete values which are integral multiples of $\frac{2\pi}{Ma}$, with M the total number of lattice sites and a the lattice spacing. The basic features of the plots can be summarized as follows:

The very weakly interacting regime: In Fig. 7.2 the dynamics of the atomic population per well resembles the Rabi oscillation phenomenon. Notice that even though there are three wells, periodic boundary conditions enforce equal evolution of the initially empty ones. In this regime damping effects remain very small for the time depicted in the plots. The numerical simulations show a general agreement between the different approaches and the exact solution. The effect of including higher order terms in the equations of motion is to introduce small corrections which improve the agreement with the exact dynamics. This shows up in the plots of the condensate population and depletion, where the small differences can be better appreciated. The second-order $1/\mathcal{N}$ expansion gives an improvement over the HFB and the complete second-order perturbative expansion almost matches the exact solution perfectly. In the duration depicted in the plots of Fig. 7.2 the total condensate constitutes an important fraction of the total population. Regarding the quasimomentum distribution, we observe that similarly to the spatial

distribution where the initial configuration and periodic boundary conditions reduce the three well system to a double well one, they enforce equal evolution of the $\pm\frac{2\pi}{3}$ quasimomentum intensities. The $k = 0$ and $\pm\frac{2\pi}{3}$ intensities oscillate with the same frequency as the atomic population per well, both are also well described by the approximations in consideration.

The intermediate regime: We can see the effect of the interactions in the dynamics. They modulate the oscillations in the population per well and scatter the atoms out of the condensate.

1. In Figs. 7.3 we plot the numerical solution for the parameters $M = 3, N = 8, J = 1$ and $U/J = 1/3$. In contrast to the case of the very weak interacting regime, it is only at early times that any of these approximations is close to the exact solution. Even though none of them are satisfactory after the first oscillation the HFB approximation is the only one that fails to capture the exponential decrease of the condensate population. This is expected, because even though this approximation goes beyond mean field theory and takes into account the most important scattering effects, it includes the effects of collisions only indirectly through energy shifts, and breaks down outside the collisionless regime where multiple-scattering effects are important. In contrast, the exponential decay of the condensate is present in the second-order approximations. Non local parts of the self-energy included in them encode scattering effects responsible for damping. It is important to point out that, even though we observe the collapse of the condensate population, the total population is always conserved: as the condensate population decreases, the noncondensate population increases.

2. Comparing the two second-order approaches we observe that the full second-order expansion gives a better description of the dynamics than the $1/\mathcal{N}$ solution only in the regime when the perturbative solutions are close to the exact dynamics. As soon as the third order terms start to be important the large $1/\mathcal{N}$ expansion gives a better qualitative description. This behavior is better appreciated in figs. 7.4 to 7.6 as the number of atoms is increased (see discussion below).

   We observe as a general issue in this regime that, regardless of the fact that the second-order solutions capture the damping effects, as soon as the condensate population decreases to a small percentage of the total population, they depart from the exact dynamics: the second-order approaches predict faster damping rates. The overdamping is more severe in the dynamics of the population per well than in the condensate dynamics. The failure can be understood under the following lines of reasoning. At zero temperature condensate atoms represent the most "classical" form of a matter wave. When they decay, the role of quantum correlations becomes more important. At this point the higher order terms neglected in the second-order approximations are the ones that lead the dynamical behavior. Thus, to have a more

accurate description of the dynamics after the coherent matter field has decayed one needs a better treatment of correlations.

Damping effects are also quite noticeable in the quantum evolution of the quasi-momentum intensities. Similarly to what happens to the spatial observables, the HFB approximation fails completely to capture the damping effects present in the evolution of the Fourier intensities whereas the second-order approaches overestimate them.

3. In Figs. 7.4 to 7.6 we explore the effect of the total number of atoms on the dynamics. In the plots we show the numerical solutions found for a double well system with fix ratio $UN/J = 4$ and three different values of $N : N = 20, 40$ and 80. We present the results obtained for the evolution of the atomic population per well in Fig. 7.4, the condensate population per well and total condensate population in Fig. 7.5 and the quasi-momentum intensities in Fig. 7.6. To make the comparisons easier we scaled the numerical results obtained for the three different values of N by dividing them by the total number of atoms. In this way for all the cases we start with an atomic population of magnitude one in the initially populated well.

   In the exact dynamics we see that as the number of atoms is increased the damping effects occur at slower rates. This feature can be noticed in the quantum dynamics of all of the observables depicted in the plots 7.4 to 7.6. The decrease of the damping rates as the number of atoms is increased is not surprising because by changing the number of atoms we affect the quantum coherence properties of the system. As discussed above the collapse time of the condensate population is approximately given by $t_{coll} \sim \frac{t_{rev}}{2\pi\sqrt{N}}$. The revival time is proportional to U^{-1} and varies with N for fixed UN/J as $t_{rev} \propto \frac{N}{J}$, thus $t_{coll} \propto \sqrt{N}$ increases with N as observed in the numerical calculations. Besides damping rates, the qualitative behavior of the exact quantum dynamics is not much affected as the number of atoms is increased for a fixed UN/J.

   The improvement of the 2PI approximations as N is increased, as a result of the increase in the initial number of coherent atoms is in fact observed in the plots. Even though the problem of underdamping in the HFB approximation and the overdamping in the second-order approaches are not cured, as the number of atoms is increased, we do observe a better matching with the full quantal solution. The $1/\mathcal{N}$ expansion shows the fastest convergence. Perhaps this issue can be more easily observed in the quasi-momentum distribution plots, Fig. 7.6. The better agreement of the $1/\mathcal{N}$ expansion relies on the fact that even though the number of fields is only two in our calculations the $1/\mathcal{N}$ expansion is an expansion about a strong quasiclassical field configuration.

7.3 Conclusions

In this work we have used the CTP functional formalism for 2PI Green's functions to describe the nonequilibrium dynamics of a condensate loaded in an optical lattice on every third lattice site. We have carried out the analysis up to second-order in the interaction strength.This approximation is introduced so as to make the numerical solution manageable, but it is sufficient to account for dissipative effects due to multiparticle scattering that are crucial even at early times. Our formulation is capable of capturing the salient features of the system dynamics in the regime under consideration, such as the decay of the condensate population and the damping of the oscillations of the quasi-momentum and population per well unaccounted for in the HFB approximation. However, at the point where an important fraction of the condensate population has been scattered out, the second-order approximations used here predict an overdamped dynamics. To improve on this a better treatment of higher correlations is required. One might try to include the full next to leading order large $\mathcal{N}$ expansion without the truncation to second-order as done in Ref. [127] but it is not obvious that this will lead to the required improvement. Alternatively, one may try to adopt a stochastic approach, but the challenge will be shifted to the derivation of a noise term (which is likely to be both colored and multiplicative) which contains the effects of these higher correlations and the solution of the stochastic equations.

Even though, as is clear that the second-order 2PI approximations fail to capture the fully correlated dynamics in the system, it has been proved to work at intermediate times when correlations are not negligible and standard mean field techniques fail poorly. Because of their success in describing moderately correlated regimes, the second-order approximations could become a useful tool for describing other experimental situations.

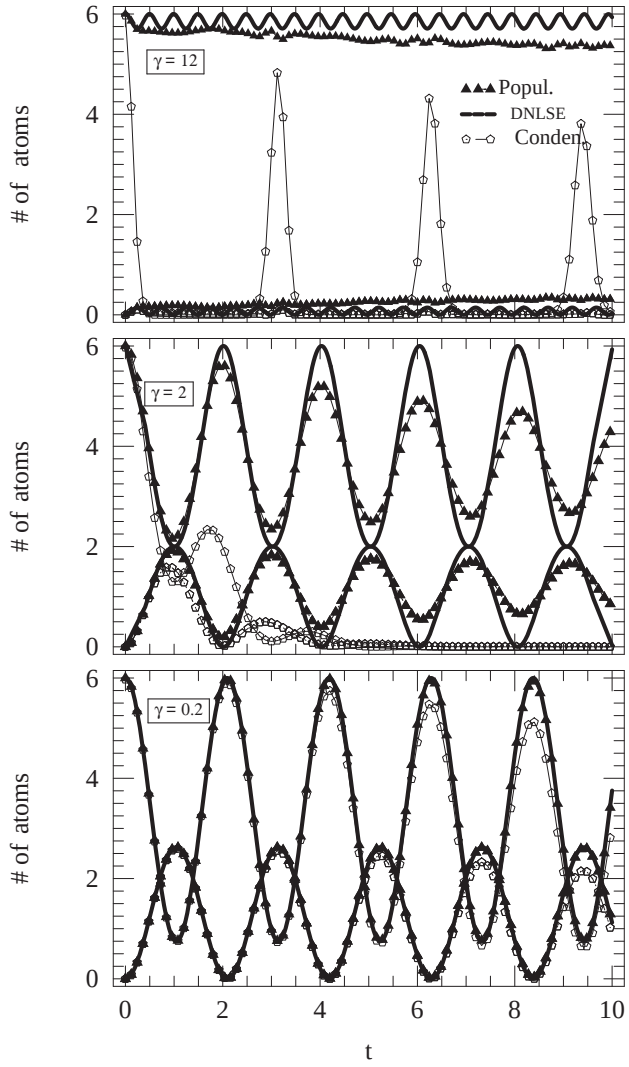

Figure 7.1: Comparisons between the exact and the DNLSE solutions for six atoms and three wells. The time is given in units of $\hbar/J$. Top panel, strongly correlated regime ($\gamma = 12$); middle panel, intermediate regime ($\gamma = 2$); bottom panel, weakly interacting regime ($\gamma = 0.2$). The solid line is the DNLSE prediction for the population per well: $|z_0(t)|^2$ and $|z_{1,2}(t)|^2$, the triangles are used to represent the exact solution for the population per well calculated using the Bose Hubbard Hamiltonian: $\langle \hat{a}_0^\dagger \hat{a}_0 \rangle$, $\langle \hat{a}_{1,2}^\dagger \hat{a}_{1,2} \rangle$. The pentagons show the condensate population per well calculated from the exact solution: $|\langle \hat{a}_0 \rangle|^2$ and $|\langle \hat{a}_{1,2} \rangle|^2$. Due to the symmetry of the initial periodic conditions the curves for the $i = 1$ and 2 wells are the same in all depicted curves .

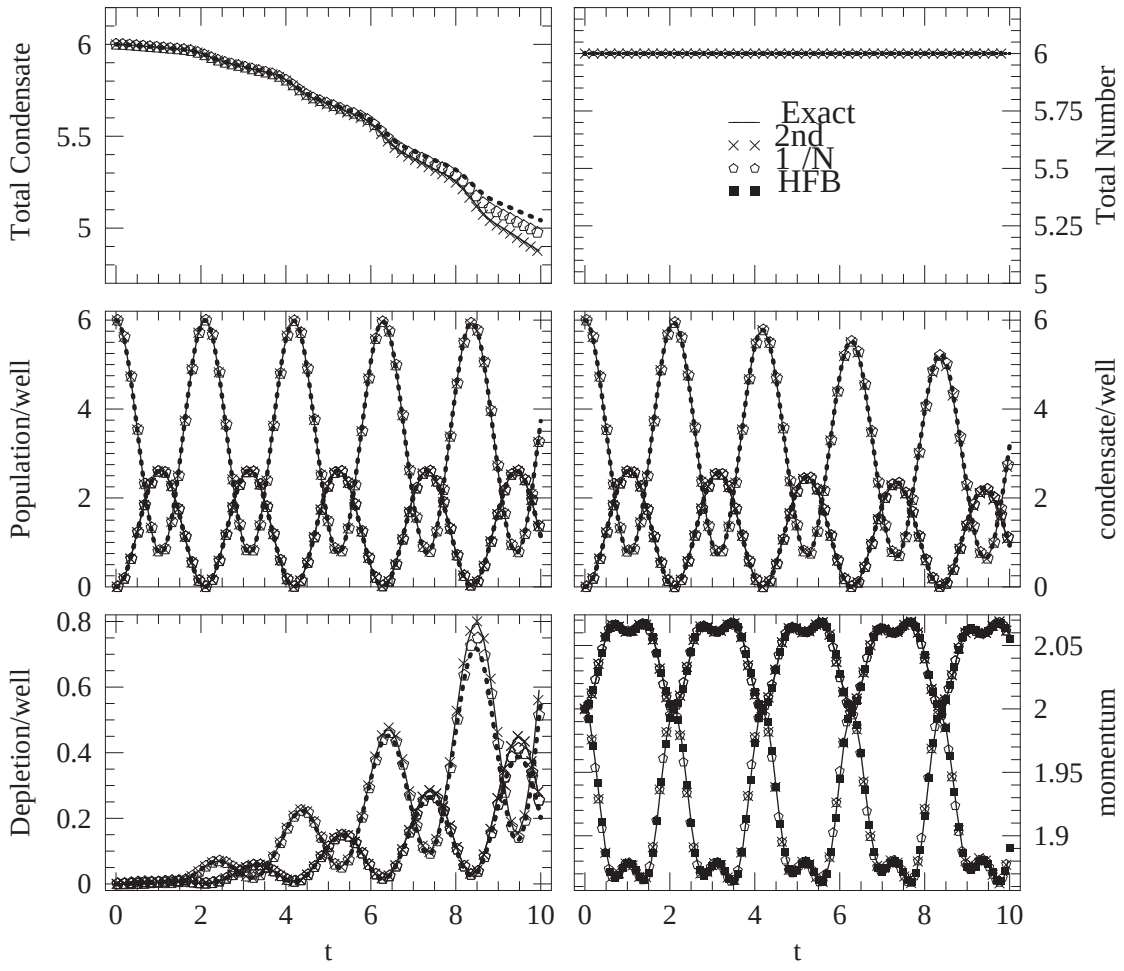

Figure 7.2: Comparisons between the exact solution(solid line), the HFB approximation (boxes), the second-order large $\mathcal{N}$ approximation (pentagons) and the full 2PI second-order approximation(crosses) for the very weak interacting regime. The parameters used were $M = 3, N = 6, J = 1$ and $U/J = 1/30$. The time is given in units of $\hbar/J$. In the plots where the population, condensate and depletion per well are depicted the top curves correspond to the initially populated well solutions and the lower to the initially empty wells. Notice the different scale used in the depletion plot. In the momentum distribution plot the upper curve corresponds to the $k = \pm 2\pi/3$ intensities and the lower one to the $k = 0$ quasi-momentum intensity.

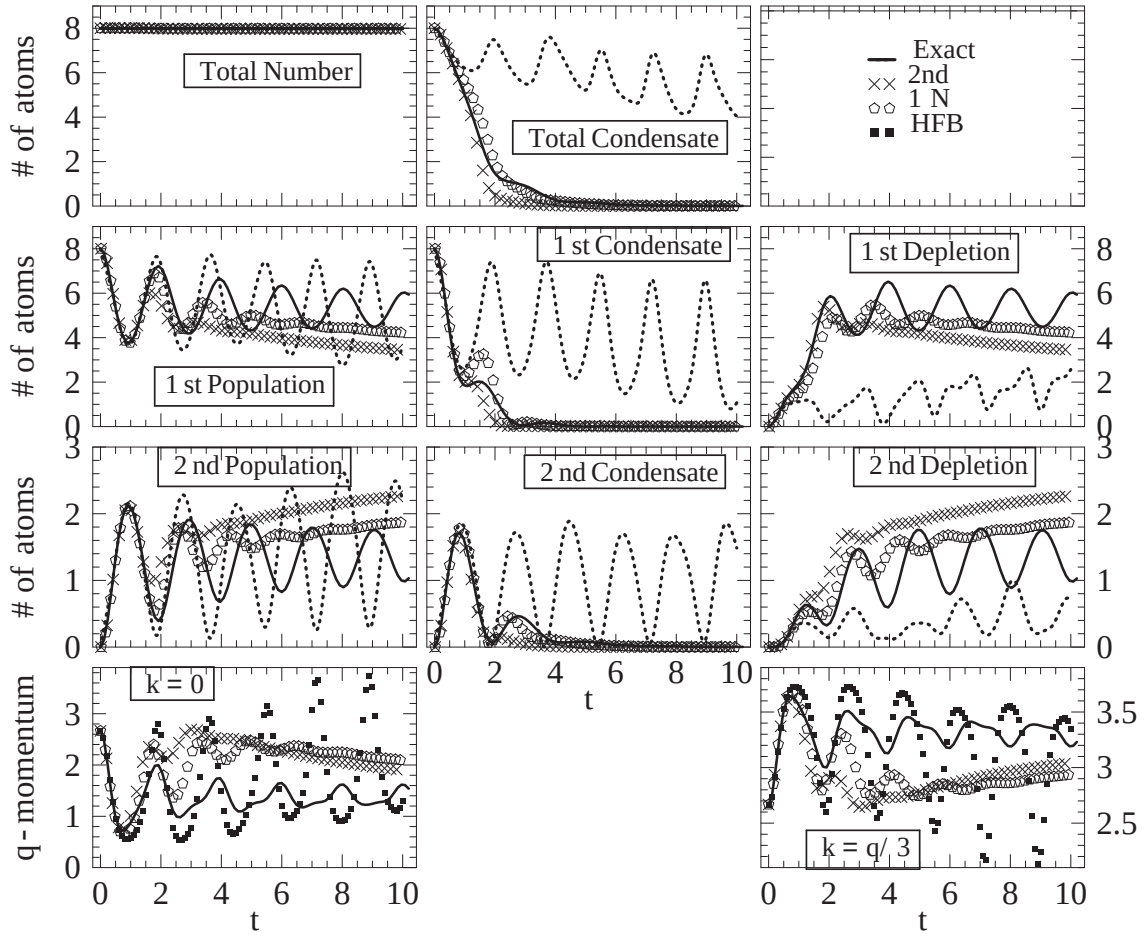

Figure 7.3: Comparisons for the case $M = 3, N = 8, J = 1$ and $U/J = 1/3$. The time is given in units of $\hbar/J$. In the plots the abbreviation 1st is used for the initially occupied well and 2nd for the initially empty wells. In the quasimomentum plots $k = 2\pi/a$ is the reciprocal lattice vector with a the lattice spacing.

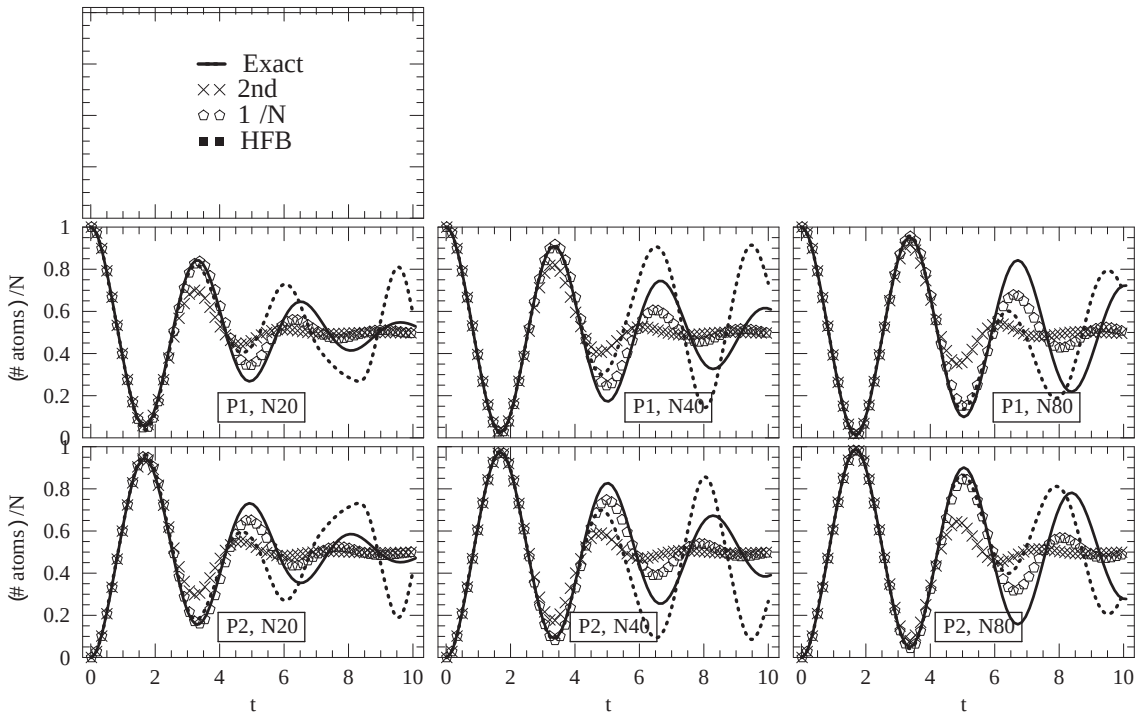

Figure 7.4: Comparison between the evolution of the atomic population per well for $M = 2, J = 1/2$, $NU/J = 4$ and $N = 20, 40$ and 80. Time is in units of $\hbar/J$. In the plots P1 stands for the fractional atomic population in the initially populated wells and P2 for the population in the initially empty wells. The number of atoms N is explicitly shown in each panel.

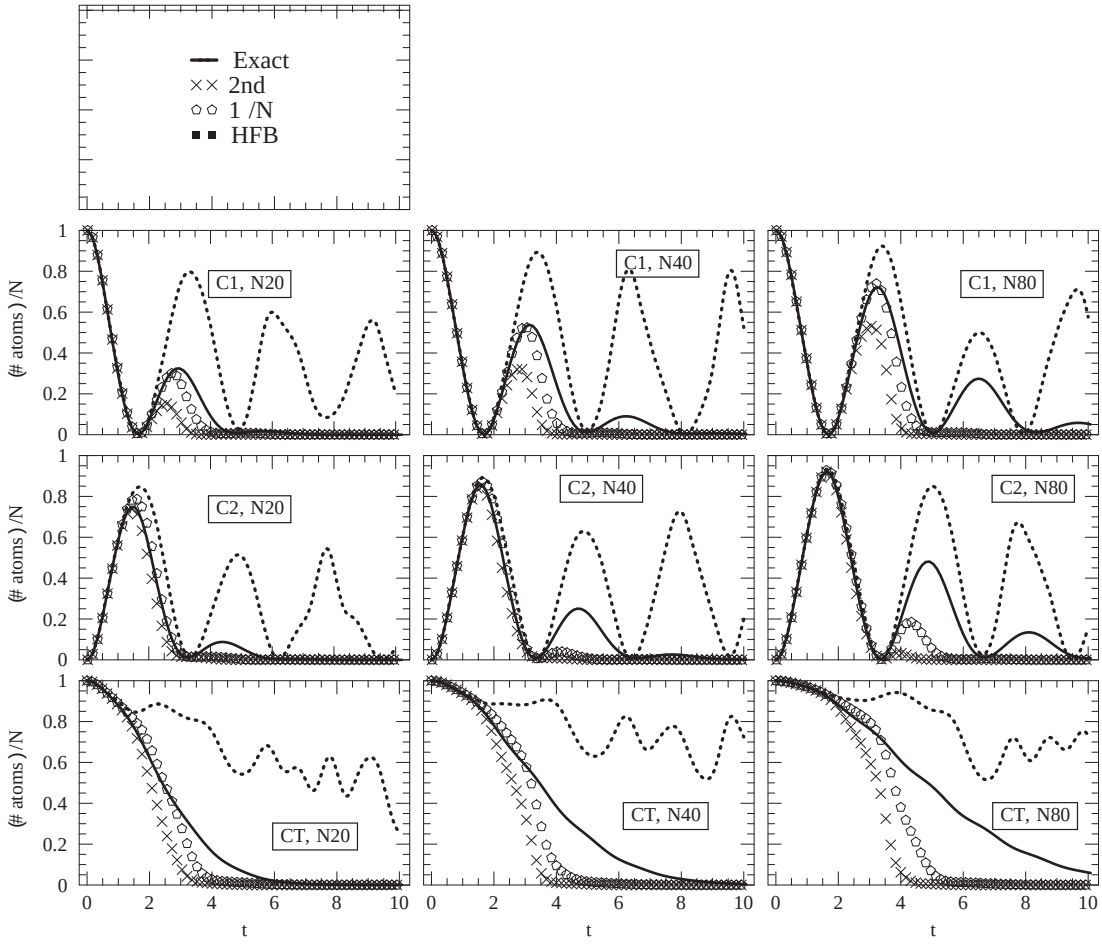

Figure 7.5: Time evolution of the condensate population per well and the total condensate population,for the same parameters as Fig. 7.4. Time is in units of $\hbar/J$. In the plots C1 stands for the fractional condensate population in the initially populated well, C2 for the fractional condensate population in the initially empty one and CT for the total condensate fraction.

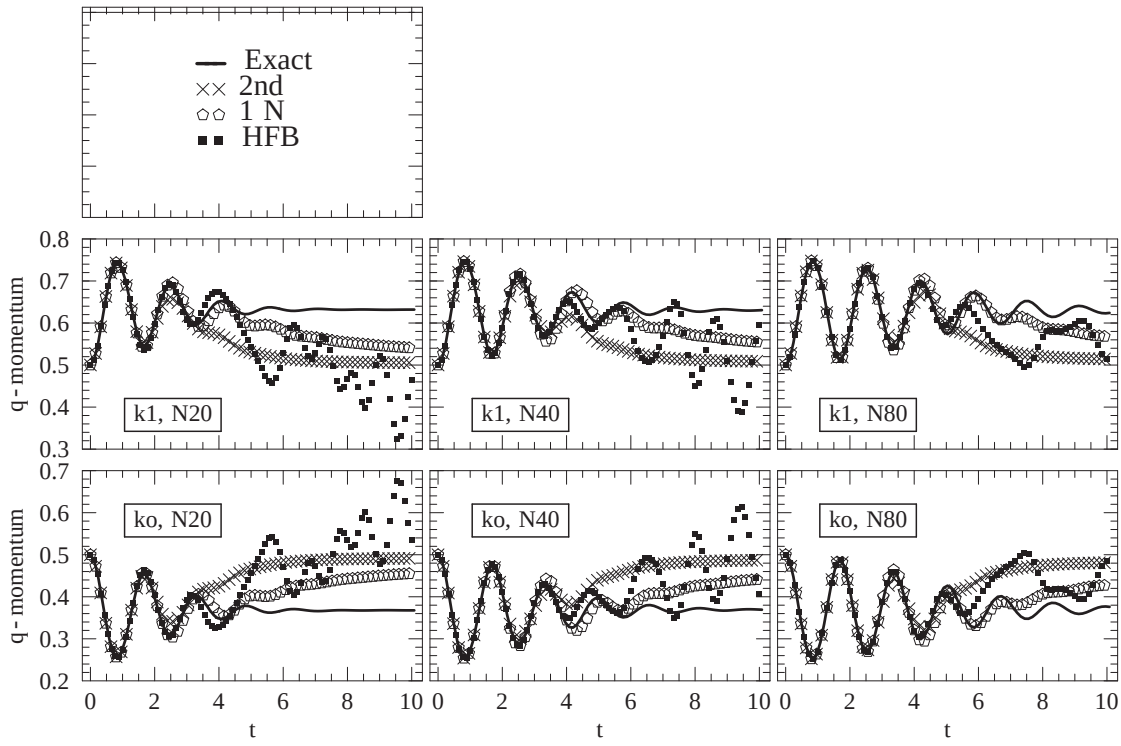

Figure 7.6: Dynamical evolution of the quasi-momentum intensities. The parameters used were $M = 2, J = 1/2$, $NU/J = 4$ and $N = 20, 40$ and 80. Time is in units of $\hbar/J$. In the plots ko denotes the $k = 0$ quasi-momentum component and k1 the $k = \pi/a$ one (a the lattice spacing). The plots are scaled to set the integrated quasi-momentum density to one for all N .

Chapter 8

From the 2PI-CTP approximations to kinetic theories and local equilibrium solutions

In chapter 6 we used the CTP functional formalism for 2PI Green's functions to derive dynamical equations of motion. We have carried out the analysis up to second-order in the interaction strength. In chapter 7 we used the formalism to investigate the nonequilibrium dynamics of a condensate loaded on every third site of an optical lattice. We showed that the formalism allowed us to go beyond the HFB approximation and to incorporate the nonlinear and non-Markovian aspects of the quantum dynamics as manifested in the dissipation and fluctuation phenomena.

However, in the present form the equations of motion are complicated nonlocal nonlinear equations from which we can hardly get any physical information regarding the system behavior except by numerical solution. Moreover, the numerical solutions are complicated enough that application to real system with many lattice sites are presently beyond the scope of standard computation capabilities. Nevertheless, when the perturbation induces disturbances in the system of wave length longer than thermal wave lengths and frequencies much smaller than characteristic particle energies then the system is in a regime where standard kinetic theories give a good description of the dynamics. The purpose of this chapter is then to simplify the complicated 2PI-CTP equations and show that they in fact reproduce, in the slowly varying regime, standard kinetic theories and equilibrium solutions for weakly interacting gases well known in the literature since the late 1950's.

8.1 Rewriting the 2PI-CTP second-order equations

In order to make the comparisons with standard approaches we will start by getting rid of the matrix indices that were useful to derive the equations of motion but which complicate the notation. We define the quantities

$$\begin{aligned}
\mathbf{z}(t_i) &\equiv z_i^a(t), && (8.1)\\
G(t_i,t'_j) &\equiv -iG_{ij}{}^a{}_b(t,t'), && (8.2)\\
H(t_i,t'_j) &\equiv -iz_i^a(t)z_{jb}(t'), && (8.3)\\
G^>(t_i,t'_j) &\equiv -iG_{ij}^{>\,a}{}_c(t,t'), && (8.4)\\
G^<(t_i,t'_j) &\equiv -iG_{ij}^{<\,a}{}_c(t,t') = -iG_{ji_c}^{>\quad a}(t',t). && (8.5)
\end{aligned}$$

Here we used the notation introduced in Eqs. (6.26) and (6.27). With these definitions we now explicitly separate the single particle, the HFB and the second-order contributions in the equations of motion for the condensate and the propagators (Eq. (6.22) and Eq. (6.24)).

$$\begin{aligned}
\sum_k \int dt'' \left(D_o^{-1}(t_i,t''_k) - S^{HFB}(t_i,t''_k)\right)\mathbf{z}\ (t''_k) &= \sum_k \int dt'' S(t_i,t''_k)\mathbf{z}(t''_k), && (8.6)\\
\sum_k \int dt'' \left(D_o^{-1}(t_i,t''_k) - \Sigma^{HFB}(t_i,t''_k)\right)G(t''_k,t'_j) &= \sum_k \int dt''\Sigma(t_i,t''_k)G(t''_k,t'_j)\\
&\quad -\delta_{ij}\delta_C(t-t'), && (8.7)
\end{aligned}$$

where $D_o^{-1}(t_i,t'_j)$ is the inverse free particle propagator given by:

$$D_o^{-1}(t_i,t'_j) \equiv (i\delta_{ij}\sigma_z\partial_t + J(\delta_{i+1j}+\delta_{i-1j}) - \delta_{ij}V_i)\,\delta(t-t'), \qquad (8.8)$$

with σ being the Pauli matrices:

$$\sigma_z = \begin{pmatrix} 1 & 0 \\ 0 & -1 \end{pmatrix}, \quad \sigma_x = \begin{pmatrix} 0 & 1 \\ 1 & 0 \end{pmatrix}. \qquad (8.9)$$

In $D_o^{-1}(t_i,t'_j)$ we have allowed the presence of an external potential V_i. The label HFB stands for the HFB contribution. Using the definition (8.1)-(8.5) in Eqs. (6.43) and (6.45) they can then be rewritten as:

$$\begin{aligned}
\Sigma^{HFB}(t_i,t'_j) &\equiv && (8.10)\\
&\quad i\frac{U}{\mathcal{N}}\left(Tr\left(H(t_i,t'_j)+G(t_i,t'_j)\right)I + 2\left(H(t_i,t'_j)+G(t_i,t'_j)\right)\right)\delta(t-t')\delta_{ij,},\\
S^{HFB}(t_i,t'_j) &\equiv i\frac{U}{\mathcal{N}}\left(Tr\left(H(t_i,t'_j)I+G(t_i,t'_j)\right)+2G(t_i,t'_j)\right)\delta(t-t')\delta_{ij}. && (8.11)
\end{aligned}$$

where I is the identity matrix. To evaluate the second-order contribution, we use Eqs. (6.31) and (6.32) but instead of setting the initial time to zero we choose it to be $-\infty$ and in this way we recover the standard Kadanoff and Baym integration contours [137]:

$$\sum_k \int_{-\infty}^{\infty} dt'' \left(D_o^{-1}(t_i,t_k'') - S^{HFB}(t_i,t_k'')\right) H(t_k'',t_j') - \int_{-\infty}^{t} dt'' \gamma(t_i,t_k'') H(t_k'',t_j') = 0, \tag{8.12}$$

$$\sum_k \int_{-\infty}^{\infty} dt'' H(t_i,t_k'') \left(D_o^{-1}(t_k'',t_j') - S^{HFB}(t_k'',t_j')\right) + \int_{-\infty}^{t} dt'' H(t_i,t_k'') \gamma(t_k'',t_j') = 0, \tag{8.13}$$

$$\sum_k \int_{-\infty}^{\infty} dt'' \left(D_o^{-1}(t_i,t_k'') - \Sigma^{HFB}(t_i,t_k'')\right) G^{(\gtrless)}(t_k'',t_j') = \tag{8.14}$$

$$\sum_k \int_{-\infty}^{t} dt'' \Gamma(t_i,t_k'') G^{(\gtrless)}(t_k'',t_j') - \sum_k \int_{-\infty}^{t'} dt'' \Sigma^{(\gtrless)}(t_i,t_k'') A(t_k'',t_j'),$$

$$\sum_k \int_{-\infty}^{\infty} dt'' G^{(\gtrless)}(t_i,t_k'') \left(D_o^{-1}(t_k'',t_j') - \Sigma^{HFB}(t_k'',t_j')\right) = \tag{8.15}$$

$$\sum_k \int_{-\infty}^{t} dt'' A(t_i,t_k'') \Sigma^{(\gtrless)}(t_k'',t_j') - \sum_k \int_{-\infty}^{t'} dt'' G^{(\gtrless)}(t_i,t_k'') \Gamma(t_k'',t_j').$$

In the above equations, Eq. (8.15) is the hermitian conjugate of Eq. (8.14), Eq. (8.13) is the hermitian conjugate of Eq. (8.12) and we have introduced the spectral functions

$$\gamma(t_i,t_j') \equiv (S^{>}(t_i,t_j') - S^{<}(t_i,t_j')), \tag{8.16}$$

$$\Gamma(t_i,t_j'') \equiv (\Sigma^{>}(t_i,t_j'') - \Sigma^{<}(t_i,t_j'')), \tag{8.17}$$

$$A(t_i,t_j'') \equiv (G^{>}(t_i,t_j'') - G^{<}(t_i,t_j'')). \tag{8.18}$$

Notice that $A(t_i,t_j'')$ is just the spectral function defined in Eq.(6.34) multiplied by a minus sign, however, we adopted the notation γ, Γ and A to be consistent with standard Kadanoff and Baym notation [137].

If we use the full second-order expansion, Eqs.(6.71 and 6.72), it can be shown that the matrices $S^{(\gtrless)}$ and $\Sigma^{(\gtrless)}$ are given by

$$S^{(\gtrless)}(t_i,t_j') \equiv -\frac{1}{2}\left(\frac{2U}{\mathcal{N}}\right)^2 \Big[G^{(\gtrless)}(t_i,t_j') Tr\left(G^{(\gtrless)}(t_i,t_j') G^{(\lessgtr)}(t_j',t_i)\right) + 2G^{(\gtrless)}(t_i,t_j') G^{(\lessgtr)}(t_j',t_i) G^{(\gtrless)}(t_i,t_j')\Big], \tag{8.19}$$

$$\Sigma^{(\gtrless)}(t_i,t'_j) \equiv -\frac{1}{2}\left(\frac{2U}{\mathcal{N}}\right)^2 \times \tag{8.20}$$
$$\Big\{H(t_i,t'_j)Tr\left(G^{(\gtrless)}(t_i,t'_j)G^{(\lessgtr)}_{ik}(t'_j,t_i)\right) + 2H(t_i,t'_j)G^{(\lessgtr)}(t'_j,t_i)G^{(\gtrless)}(t_i,t'_j)$$
$$+2G^{(\gtrless)}(t_i,t'_j)\left(H(t'_j,t_i)G^{(\gtrless)}(t_i,t'_j) + G^{(\lessgtr)}(t'_j,t_i)H(t_i,t'_j) + G^{(\lessgtr)}(t'_j,t_i)G^{(\gtrless)}(t_i,t'_j)\right)$$
$$G^{(\gtrless)}(t_i,t'_j)Tr\left(H(t'_j,t_i)G^{(\gtrless)}(t_i,t'_j) + G^{(\lessgtr)}(t'_j,t_i)H(t_i,t'_j) + G^{(\lessgtr)}(t'_j,t_i)G^{(\gtrless)}(t_i,t'_j)\right)\Big\}.$$

It is convenient to decompose the above equations in their matrix components. To do that we introduce the definitions

$$G^{>}(t_i,t'_j) = -i\begin{pmatrix} \widetilde{\rho}_{ij} & m_{ij} \\ m^*_{ji} & \rho_{ji} \end{pmatrix}, \tag{8.21}$$
$$G^{<}(t_i,t'_j) = -i\begin{pmatrix} \rho_{ij} & m_{ji} \\ m^*_{ij} & \widetilde{\rho}_{ji} \end{pmatrix}. \tag{8.22}$$

Using Eqs. (8.21) and (8.22) into the self-energy equations we get

$$\Sigma^{HFB}(t_i,t'_j) = \frac{2U}{\mathcal{N}}\begin{pmatrix} 2|z_i|^2+\rho_{ii}+\widetilde{\rho}_{ii} & z_i^2+m_{ii} \\ z_i^{*2}+m^*_{ii} & 2|z_i|^2+\rho_{ii}+\widetilde{\rho}_{ii} \end{pmatrix}\delta(t-t')\delta_{ij}, \tag{8.23}$$
$$S^{HFB}(t_i,t'_j) = \frac{2U}{\mathcal{N}}\begin{pmatrix} |z_i|^2+\rho_{ii}+\widetilde{\rho}_{ii} & m_{ii} \\ m^*_{ii} & |z_i|^2+\rho_{ii}+\widetilde{\rho}_{ii} \end{pmatrix}\delta(t-t')\delta_{ij}, \tag{8.24}$$

$$S^{>}_{11}(t_i,t'_j) = \frac{-i8U^2}{\mathcal{N}^2}\widetilde{\rho}_{ij}(2m_{ij}m^*_{ji}+\widetilde{\rho}_{ij}\rho_{ji}), \tag{8.25}$$
$$S^{>}_{12}(t_i,t'_j) = \frac{-i8U^2}{\mathcal{N}^2}m_{ij}(m_{ij}m^*_{ji}+2\widetilde{\rho}_{ij}\rho_{ji}), \tag{8.26}$$
$$S^{<}_{11}(t_i,t'_j) = \frac{-i8U^2}{\mathcal{N}^2}\rho_{ij}(2m_{ji}m^*_{ij}+\widetilde{\rho}_{ji}\rho_{ij}), \tag{8.27}$$
$$S^{<}_{12}(t_i,t'_j) = \frac{-i8U^2}{\mathcal{N}^2}m_{ji}(m_{ij}m^*_{ji}+2\widetilde{\rho}_{ji}\rho_{ij}), \tag{8.28}$$

$$\Sigma_{11}^{>}(t_i,t'_j) = \frac{-i8U^2}{\mathcal{N}^2}(\rho_{ji}\widetilde{\rho}_{ij}^2 + 2m_{ij}\widetilde{\rho}_{ij}{m_{ji}}^* + 2\widetilde{\rho}_{ij}{m_{ji}}^* z_i z_j + \widetilde{\rho}_{ij}^2 z_j {z_i}^* + 2\rho_{ji}\widetilde{\rho}_{ij} z_i {z_j}^* + 2m_{ij}{m_{ji}}^* {z_j}^* z_i + 2m_{ij}\widetilde{\rho}_{ij}{z_i}^* {z_j}^*), \tag{8.29}$$

$$\Sigma_{12}^{>}(t_i,t'_j) = \frac{-i8U^2}{\mathcal{N}^2}(2\rho_{ji}m_{ij}\widetilde{\rho}_{ij} + 2\rho_{ji}\widetilde{\rho}_{ij} z_i z_j + {m_{ij}}^2{m_{ji}}^* + 2m_{ij} z_i z_j {m_{ji}}^* + 2m_{ij}\widetilde{\rho}_{ij} z_j {z_i}^* + 2\rho_{ji}m_{ij} z_i {z_j}^* + {m_{ij}}^2 {z_i}^* {z_j}^*), \tag{8.30}$$

$$\Sigma_{11}^{<}(t_i,t'_j) = \frac{-i8U^2}{\mathcal{N}^2}(\rho_{ij}{}^2\widetilde{\rho}_{ji} + 2\rho_{ij}m_{ji}{m_{ij}}^* + 2\rho_{ij} z_i z_j {m_{ij}}^* + \rho_{ij}^2 z_j {z_i}^* + 2\rho_{ij}\widetilde{\rho}_{ji} z_i {z_j}^* + 2m_{ji} z_i {m_{ij}}^* {z_j}^* + 2\rho_{ij}m_{ji}{z_i}^* {z_j}^*), \tag{8.31}$$

$$\Sigma_{12}^{<}(t_i,t'_j) = \frac{-i8U^2}{\mathcal{N}^2}(2\rho_{ij}m_{ji}\widetilde{\rho}_{ji} + 2\rho_{ij}\widetilde{\rho}_{ji} z_i z_j + {m_{ji}}^2{m_{ij}}^* + 2m_{ji} z_i z_j {m_{ij}}^* + 2\rho_{ij}m_{ji} z_j {z_i}^* + 2m_{ji}\widetilde{\rho}_{ji} z_i {z_j}^* + {m_{ji}}^2 {z_i}^* {z_j}^*), \tag{8.32}$$

and

$$S_{22}^{(\gtrless)}(t_i,t'_j) = S_{11}^{(\gtrless)}(t_i,t'_j)\{\rho_{ij}\mapsto\widetilde{\rho}_{ij}\}, \tag{8.33}$$

$$S_{21}^{(\gtrless)}(t_i,t'_j) = S_{12}^{(\gtrless)}(t_i,t'_j)\{m_{ji}\mapsto {m_{ij}}^*\}, \tag{8.34}$$

$$\Sigma_{22}^{(\gtrless)}(t_i,t'_j) = \Sigma_{11}^{(\gtrless)}(t_i,t'_j)\{z_i\mapsto z_j, \rho_{ij}\mapsto\widetilde{\rho}_{ij}\}, \tag{8.35}$$

$$\Sigma_{21}^{(\gtrless)}(t_i,t'_j) = \Sigma_{12}^{(\gtrless)}(t_i,t'_j)\{z_i\mapsto {z_j}^*, m_{ji}\mapsto {m_{ij}}^*\}. \tag{8.36}$$

The above expressions for the self-energy exactly agree with the ones used in Refs. [59, 60, 62]. In Refs. [59, 62] the authors used these equations as their starting point before applying the Markovian approximation.

8.2 Boltzmann equations

From previous sections it can be observed that the equations of motion at second-order are quite involved: they are nonlinear and nonlocal integro differential equations, not readily solvable in closed form. To progress further we need to introduce approximations based on physical considerations. One of them is to recognize two time scales in the system, one related to quantum processes (microscopic) which determines the degree of quantum-mechanical entanglement of the system and one related to the statistical and kinetic behavior (macroscopic) determined by the range of the interactions among particles. In a classical point of view the two different scales in the system can be understood as the time (or length) scale separation between the duration of a collision event (or scattering length) and the inverse collision rate (or the mean free path). Close to equilibrium (when the external potential induces disturbances much longer than the lattice spacing and frequencies much smaller than the characteristic particle energies) and in the weakly interacting regime, we expect that a reasonable assumption would be to consider the kinetic scale larger than the quantum one, which in a classical picture corresponds to assume that be the time between collisions (or mean free path) is long compared to the reaction time (or scattering length).

Using this approximation it is possible to recast the quantum dynamics into the much simpler forms of kinetic theory. In contrast to normal systems were there is not a condensate, in condensed systems making the scale separation requires first to do a gauge transformation which makes it easier to identify (and coarse-grain away) the fast variations induced by the rapid change of the condensate phase. Following Ref. [139] we introduce the gauge transformation

$$z_i(t) = e^{i\theta_i(t)}\sqrt{n_o(t_i)}, \tag{8.37}$$

$$G^{(\gtrless)}(t_i,t'_j) = e^{i\theta_i(t)\sigma_z}\tilde{G}^{(\gtrless)}(t_i,t'_j)e^{-i\theta_j(t')\sigma_z}, \tag{8.38}$$

where $\sqrt{n_o(t_i)}$ and $\theta_i(t)$ are real. In equilibrium, $\Delta\theta_i \equiv (\theta_{i+1/2}-\theta_{i-1/2})/a$ is related to the superfluid velocity and the time derivative of the phase to the chemical potential. Extending these identifications to the nonequilibrium system we define the chemical potential and superfluid velocity as

$$\mu_i = -\hbar\partial_t\theta_i - \frac{\hbar^2}{4Ja^2}v_i^{s2} - V_i, \tag{8.39}$$

$$\hbar v_i^s = 2J\Delta\theta_i a^2. \tag{8.40}$$

After the gauge transformation the variables n_o, $\tilde{G}$, v^s and μ are expected to be slowly varying functions of

$$R=(i+j)/2, \quad T=(t+t')/2, \tag{8.41}$$

and peaked about the zeros of

$$r=(i-j), \quad \tau=(t-t'), \tag{8.42}$$

necessary conditions to derive Boltzmann-type kinetic equations.

The equations of motion are invariant under the phase transformation if we replace D_o^{-1} by $\tilde{D}_o^{-1}$:

$$\begin{aligned}\tilde{D}_o^{-1}(t_i,t'_j) = {} & (\hbar\delta_{ij}(i\sigma_z\partial_t - \partial_t\theta_i) - \delta_{ij}V_i + \\ & J(e^{i\sigma_z\Delta\theta_{i+1/2}}\delta_{i+1j} + e^{-i\sigma_z\Delta\theta_{i-1/2}}\delta_{i-1j})\Big)\,\delta(t-t').\end{aligned} \tag{8.43}$$

Since hereafter we will use the gauge-transformed functions exclusively, in the following the tildes will be dropped to simplify the notation. To obtain the kinetic equations we Fourier transform the functions G and n_o with respect to r and τ . The Fourier transform reads

$$\begin{aligned}G^{(\gtrless)}(t_i,t'_j) &= G^{(\gtrless)}\left(\left(T+\frac{\tau}{2}\right)_{R+r/2},\left(T-\frac{\tau}{2}\right)_{R-r/2}\right) \\ &\equiv -i\frac{1}{2\pi M}\sum_q\int d\omega e^{(iqr-i\omega\tau)}G^{(\gtrless)}(Rq;T,\omega),\end{aligned} \tag{8.44}$$

$$\begin{aligned}H(t_i,t'_j) &= H\left(\left(T+\frac{\tau}{2}\right)_{R+r/2},\left(T-\frac{\tau}{2}\right)_{R-r/2}\right) \\ &\equiv -i\frac{1}{2\pi M}\sum_q\int d\omega e^{(iqr-i\omega\tau)}H(Rq;T,\omega),\end{aligned} \tag{8.45}$$

Neglecting second-order variations of $n_o(Rq;T,\omega)$ we can approximate it as

$$H(Rq;T,\omega) = 2\pi M\,(I+\sigma_x)\,n_o(R,T)\delta(\omega)\delta_{q0}. \tag{8.46}$$

In Eq.(8.46), the quantity $n_o(R,T)$ is just related to the condensate density of atoms at the space time point (Ra,T). In Eq.(8.44), the two-point function $G_{11}^{(<)}(Rq;T,\omega)$ corresponds to the well known Wigner distribution function [140]. It can be interpreted as the density of noncondensed particles with quasimomentum q and energy $\hbar\omega$ at the lattice site R and time T. On the other hand, $G_{11}^{(>)}(Rq;T,\omega)$ is essentially the density of states available to a particle that is added to the system at (Ra,T) with quasimomentum q and energy $\hbar\omega$. As opposed to a normal system, the presence of the condensate gives non zero values to the off diagonal terms of the functions $G_{12}^{(\gtrless)}(Rq;T,\omega)$. We refer to them as the anomalous contributions to the respective two point functions.

The generalized Boltzmann equations can be obtained as the Fourier transform of the equations of motion for the case in which the variations in R and T are very slow. In particular when the inverse propagator D_o^{-1} and the self energies vary very little as Ra is changed by a characteristic excitation wavelength or T is changed by an inverse excitation energy. Following Ref.[139] and assuming a (q,ω,R,T) dependence of the variables, which is not explicitly written for simplicity, we get the following equations:

$$\left(D_o^{-1} - \Re S + \frac{i}{2}\gamma\right) H = -\frac{i}{2}\left[D_o^{-1},H\right] + \frac{i}{2}\left[\Re S,H\right] + \frac{1}{4}\left[\gamma,H\right], \tag{8.47}$$

$$H\left(D_o^{-1} - \Re S - \frac{i}{2}\gamma\right) = -\frac{i}{2}\left[H,D_o^{-1}\right] + \frac{i}{2}\left[H,\Re S\right] - \frac{1}{4}\left[H,\gamma\right], \tag{8.48}$$

$$\begin{aligned}\left(D_o^{-1} - \Re\Sigma + \frac{i}{2}\Gamma\right) G^{(\gtrless)} - \Sigma^{(\gtrless)}\left(\Re G + \frac{i}{2}A\right) &= -\frac{i}{2}\left[D_o^{-1},G^{(\gtrless)}\right] + \frac{i}{2}\left[\Re\Sigma,G^{(\gtrless)}\right] + \\ &\frac{i}{2}\left[\Sigma^{(\gtrless)},\Re G\right] + \frac{1}{4}\left[\Gamma,G^{(\gtrless)}\right] - \frac{1}{4}\left[\Sigma^{(\gtrless)},A\right],\end{aligned} \tag{8.49}$$

$$\begin{aligned}G^{(\gtrless)}\left(D_o^{-1} - \Re\Sigma - \frac{i}{2}\Gamma\right) - \left(\Re G - \frac{i}{2}A\right)\Sigma^{(\gtrless)} &= -\frac{i}{2}\left[G^{(\gtrless)},D_o^{-1}\right] + \frac{i}{2}\left[G^{(\gtrless)},\Re\Sigma\right] + \\ &\frac{i}{2}\left[\Re G,\Sigma^{(\gtrless)}\right] - \frac{1}{4}\left[G^{(\gtrless)},\Gamma\right] + \frac{1}{4}\left[A,\Sigma^{(\gtrless)}\right],\end{aligned} \tag{8.50}$$

with

$$D_o^{-1}(Rq;T,\omega) \equiv \left(\sigma_z\left(\hbar\omega - v_s 2J\sin(qa)\right) + \left(2J\cos(qa) + \mu_R(T)\right)I\right). \tag{8.51}$$

Because all the quantities are slowly varying functions of R and T, in Eqs (8.47-8.50) we approximated the discretized equation to continuous differential equations. The brackets denote the generalized Poisson brackets defined as:

$$[A,B] = \frac{\partial A}{\partial\omega}\frac{\partial B}{\partial T} - \frac{\partial A}{\partial T}\frac{\partial B}{\partial\omega} + \partial_R A\partial_q B - \partial_q A\partial_R B. \tag{8.52}$$

In the equations we have also introduced the following functions:

$$\begin{aligned}
\Re S(Rq;T,\omega) &= S^{HF}(Rq;T,\omega)+\Re S^{B}(Rq;T,\omega), && (8.53)\\
\Re\Sigma(Rq;T,\omega) &= \Sigma^{HF}(Rq;T,\omega)+\Re\Sigma^{B}(Rq;T,\omega), && (8.54)\\
\Re S^{B}(Rq;T,\omega) &= P\int\frac{d\omega'}{2\pi}\frac{\gamma(Rq;T,\omega)}{\omega-\omega'}, && (8.55)\\
\Re\Sigma^{B}(Rq;T,\omega) &= P\int\frac{d\omega'}{2\pi}\frac{\Gamma(qR,\omega')}{\omega-\omega'}, && (8.56)\\
\Re G &= P\int\frac{d\omega'}{2\pi}\frac{A(Rq;T,\omega)}{\omega-\omega'}. && (8.57)
\end{aligned}$$

with P denoting the Cauchy principal value and $\gamma(Rq;T,\omega)$, $\Gamma(Rq;T,\omega)$, $S^{HF}(Rq;T,\omega)$, $\Sigma^{HF}(Rq;T,\omega)$ and $A(Rq;T,\omega)$ understood as Fourier transforms of the functions $\gamma(t_i,t'_j)$, $\Gamma(t_i,t'_j)$, $S^{HF}(t_i,t'_j)$, $\Sigma^{HF}(t_i,t'_j)$ and $A(t_i,t'_j)$ respectively.

If we define the statistical variables as:

$$\begin{aligned}
F &= \frac{G^{>}+G^{<}}{2}, && (8.58)\\
\Pi &= \frac{\Sigma^{>}+\Sigma^{<}}{2}. && (8.59)
\end{aligned}$$

Eq. (8.49)and Eq. (8.50), can be rewritten in term of statistical and spectral functions as:

$$\begin{aligned}
\left(D_o^{-1}-\Re\Sigma+\frac{i}{2}\Gamma\right)F \;-\; \Pi\left(\Re G+\frac{i}{2}A\right) &= && (8.60)\\
-\frac{i}{2}\left\{\left[D_o^{-1}-\Re\Sigma+\frac{i}{2}\Gamma,F\right]-\left[\Pi,\Re G+\frac{i}{2}A\right]\right\},&&\\
F\left(D_o^{-1}-\Re\Sigma-\frac{i}{2}\Gamma\right) \;-\; \left(\Re G-\frac{i}{2}A\right)\Pi &= && (8.61)\\
-\frac{i}{2}\left\{\left[F,D_o^{-1}-\Re\Sigma-\frac{i}{2}\Gamma\right]-\left[\Re G-\frac{i}{2}A,\Pi\right]\right\},&&
\end{aligned}$$

$$\begin{aligned}
\left(D_o^{-1}-\Re\Sigma\right)A-\Gamma\Re G &= -\frac{i}{2}\left\{\left[D_o^{-1}-\Re\Sigma,A\right]-\left[\Gamma,\Re G\right]\right\}, && (8.62)\\
A\left(D_o^{-1}-\Re\Sigma\right)-\Re G\Gamma &= -\frac{i}{2}\left\{\left[A,D_o^{-1}-\Re\Sigma\right]-\left[\Re G,\Gamma\right]\right\}. && (8.63)
\end{aligned}$$

Eqs. (8.47), (8.48) and (8.60)- (8.63) are our passage to the Boltzmann equations. They describe the state of the gas at a given time. In contrast to the HFB equations, they include collisional integrals to describe binary interactions.

To progress further we can introduce even more simplifications based on physical assumptions. The ordinary Boltzmann equation emerges from the approximation in which the self energies that appear on the left side of Eqs.(8.47), (8.48) and

(8.60)- (8.63) are handled differently from those which appear on the right. These two appearances of the self-energy play a different physical role in the description of the dynamics [137]. The self energies on the right hand side describe the dynamical effects of collisions, i.e., how the collisions transfer particles from one energy-momenta configuration to another. On the other hand, the self energies on the left describe the quantum kinetic effects due to interactions, i.e. how interaction effects change the energy momentum dispersion relations from that of free particles to a more complicated spectrum. Because these two effects are physically so different, we can treat the left and the right hand sides in different ways.

In the derivation of the ordinary Boltzmann equations, one completely neglects all the kinetic effects in the second-order self energies (the dependence on T and R in the second-order self energy terms on the right hand side) and retain dynamical effects (T and R dependence on the left hand side). In this way, we get the familiar Boltzmann equations which describe the particles as free particles in between collisions. This is a reasonable assumption in dilute weakly interacting gases in which the duration of a collision is very short compared to the essentially interaction-free dynamics between isolated collisions. Neglecting kinetic effects in the second-order self energies, Eqs.(8.47), (8.48) and (8.60)-(8.63) can be approximated to

$$\left(D_o^{-1} - \Re S + \frac{i}{2}\gamma\right) H = -\frac{i}{2}\left[D_o^{-1} - S^{HF}, H\right], \quad (8.64)$$

$$H\left(D_o^{-1} - \Re S - \frac{i}{2}\gamma\right) = -\frac{i}{2}\left[H, D_o^{-1} - S^{HF}\right], \quad (8.65)$$

$$\left(D_o^{-1} - \Re\Sigma + \frac{i}{2}\Gamma\right) F - \Pi\left(\Re G + \frac{i}{2}A\right) = -\frac{i}{2}\left[D_o^{-1} - \Sigma^{HF}, F\right], \quad (8.66)$$

$$\left(D_o^{-1} - \Re\Sigma\right) A - \Gamma\Re G = -\frac{i}{2}\left[D_o^{-1} - \Sigma^{HF}, A\right], \quad (8.67)$$

$$F\left(D_o^{-1} - \Re\Sigma - \frac{i}{2}\Gamma\right) - \left(\Re G - \frac{i}{2}A\right)\Pi = -\frac{i}{2}\left[F, D_o^{-1} - \Sigma^{HF}\right], \quad (8.68)$$

$$A\left(D_o^{-1} - \Re\Sigma\right) - \Re G\Gamma = -\frac{i}{2}\left[A, D_o^{-1} - \Sigma^{HF}\right]. \quad (8.69)$$

If we take the trace of the sum and the difference of each one of the above equations with its hermitian conjugate, they can be simplified to :

$$Tr\left\{\left(D_o^{-1} - \Re S\right) H\right\} = 0, \quad (8.70)$$

$$Tr\left\{\left(D_o^{-1} - \Re\Sigma\right) F - \Pi\Re G\right\} = 0, \quad (8.71)$$

$$Tr\left\{\left(D_o^{-1} - \Re\Sigma\right) A - \Gamma\Re G\right\} = 0, \quad (8.72)$$

$$Tr\left[D_o^{-1} - S^{HF}, H\right] = -Tr(\gamma H), \quad (8.73)$$

$$Tr\left[D_o^{-1} - \Sigma^{HF}, F\right] = -Tr(\Gamma F - \Pi A). \quad (8.74)$$

$$Tr\left[D_o^{-1} - \Sigma^{HF}, A\right] = 0 \quad (8.75)$$

Moreover, if we define the operator $\urcorner rM = M_{12} + M_{21}^*$ and apply it again to the sum and the difference of each one of the equations (8.60) to (8.63) with its transpose we also get:

$$\begin{aligned}
\mathrm{Re}\left(\urcorner\mathrm{r}\left\{\left(\mathrm{D_o^{-1}} - \Re\mathrm{S}\right)\mathrm{H}\right\}\right) &= \frac{1}{2}\mathrm{Im}\left(\urcorner\mathrm{r}\left[\mathrm{D_o^{-1}} - \mathrm{S^{HF}}, \mathrm{H}\right] + \urcorner(\gamma\mathrm{H})\right), && (8.76)\\
\mathrm{Re}\left(\urcorner\mathrm{r}\left\{\left(\mathrm{D_o^{-1}} - \Re\Sigma\right)\mathrm{F} - \Pi\Re\mathrm{G}\right\}\right) &= \frac{1}{2}\mathrm{Im}\left(\urcorner\mathrm{r}\left[\mathrm{D_o^{-1}} - \Sigma^{\mathrm{HF}}, \mathrm{F}\right] + \urcorner\mathrm{r}(\Gamma\mathrm{F} - \Pi\mathrm{A})\right), && (8.77)\\
\mathrm{Re}\left(\urcorner\mathrm{r}\left\{\left(\mathrm{D_o^{-1}} - \Re\Sigma\right)\mathrm{A} - \Gamma\Re\mathrm{G}\right\}\right) &= \frac{1}{2}\mathrm{Im}\left(\urcorner\mathrm{r}\left[\mathrm{D_o^{-1}} - \Sigma^{\mathrm{HF}}, \mathrm{A}\right]\right), && (8.78)\\
\mathrm{Im}\left(\urcorner\mathrm{r}\left\{\left(\mathrm{D_o^{-1}} - \Re\mathrm{S}\right)\mathrm{H}\right\}\right) &= -\frac{1}{2}\mathrm{Re}\left(\urcorner\mathrm{r}\left[\mathrm{D_o^{-1}} - \mathrm{S^{HF}}, \mathrm{H}\right] + \urcorner(\gamma\mathrm{H})\right), && (8.79)\\
\mathrm{Im}\left(\urcorner\mathrm{r}\left\{\left(\mathrm{D_o^{-1}} - \Re\Sigma\right)\mathrm{F} - \Pi\Re\mathrm{G}\right\}\right) &= -\frac{1}{2}\mathrm{Re}\left(\urcorner\mathrm{r}\left[\mathrm{D_o^{-1}} - \Sigma^{\mathrm{HF}}, \mathrm{F}\right] + \urcorner\mathrm{r}(\Gamma\mathrm{F} - \Pi\mathrm{A})\right), && (8.80)\\
\mathrm{Im}\left(\urcorner\mathrm{r}\left\{\left(\mathrm{D_o^{-1}} - \Re\Sigma\right)\mathrm{A} - \Gamma\Re\mathrm{G}\right\}\right) &= -\frac{1}{2}\mathrm{Re}\left(\urcorner\mathrm{r}\left[\mathrm{D_o^{-1}} - \Sigma^{\mathrm{HF}}, \mathrm{A}\right]\right), && (8.81)
\end{aligned}$$

with Re and Im denoting the real and imaginary parts. To close this set of equations we need an equation of motion for the superfluid velocity which can be found from the definitions Eq.(8.39) and Eq.(8.40) to be:

$$\frac{\hbar}{2Ja^2}\frac{\partial v_s}{\partial T} = -\frac{\partial}{\partial R}\left((\mu + V) + \frac{\hbar}{4Ja^2}{v_s}^2\right). \qquad (8.82)$$

Eqs.(8.70-8.81) together with Eq.(8.82) form a closed set of equations that describe the state of the gas at a given time. Equations (8.70-8.72) and (8.76-8.78) are usually called gap equations. They describe the quantum properties of the gas which is evolving according to the Boltmaznn equations (8.73-8.75) and (8.79-8.81). Under the derived formalism the Boltzmann and gap equations form a coupled set of equations which replaces the original dynamics. The equations have to be solved self consistently for any analysis.

8.3 Equilibrium properties for a homogeneous system

In this section we will show how the nonequilibrium Boltzmann equations lead, in a special case, to the linear equilibrium solutions discussed in chapter 5 upgraded with second-order corrections in U not included in the quadratic approximations. There are two situations in which we expect an equilibrium solution to come from the Boltzmann equations. Firstly, when the system has never been disturbed it remains in its equilibrium state. Secondly, when the system has had sufficient time to relax after an applied perturbation.

At equilibrium, in the absence of any external potential, the functions $G^{\gtrless}$ and H are completely independent of R and T. In this case the generalized Poisson brakets terms are zero and Eqs.(8.72, 8.75) and (8.78, 8.75) imply that:

$$A\left(D_o^{-1} - \Re\Sigma\right) - (\Re G)\Gamma = 0. \qquad (8.83)$$

Because $\Re G(q,\omega)$ is determined by $A(q,\omega)$ as indicated in Eq. (8.57), Eq. (8.83) is satisfied when $A(q,\omega)$ is given by

$$A(q,\omega) = i\left\{\left[D_o^{-1} - \Re S + \frac{i}{2}\Gamma\right]^{-1} - \left[D_o^{-1} - \Re S - \frac{i}{2}\Gamma\right]^{-1}\right\}, \quad (8.84)$$

and the function $\Re G(q,\omega)$ given by

$$\begin{aligned}\Re G(q,\omega) &= P\int \frac{d\omega'}{2\pi}\frac{A(q,\omega')}{\omega-\omega'} \\ &= \frac{1}{2}\left\{\left[D_o^{-1} - \Re S + \frac{i}{2}\Gamma\right]^{-1} + \left[D_o^{-1} - \Re S - \frac{i}{2}\Gamma\right]^{-1}\right\}. \quad (8.85)\end{aligned}$$

From Eqs.(8.73), (8.79),(8.74) and (8.80)) we also get that at equilibrium

$$\gamma = 0, \quad (8.86)$$

$$\Gamma F - \Pi A = 0. \quad (8.87)$$

Eqs. (8.86) and (8.87) are just the mathematical statement of detailed balance. They just represent the physical condition that at equilibrium the net rate of change of the density of particles with momentum q and energy ω is zero. Since it is always possible to write [137]

$$F(q,\omega) = \left(n_q(\omega) + \frac{1}{2}\right)A(q,\omega), \quad (8.88)$$

then Eq.(8.87) can only be satisfied if

$$\Pi(q,\omega) = \left(n_q(\omega) + \frac{1}{2}\right)\Gamma(q,\omega), \quad (8.89)$$

is satisfied. Detailed study of the structure of the self energy indicates that $n_q(\omega)$ is related to the Bose-Einstein distribution, $n_q(\omega) = \frac{1}{e^{\beta\hbar\omega}-1}$ with β interpreted as the local inverse temperature in energy units [137, 139].
Since H contains delta functions in momentum and energy at equilibrium, we get from Eq. (8.70):

$$\mu = -2J + \Re S_{11}(0,0) + \Re S_{12}(0,0). \quad (8.90)$$

8.3.1 Quasiparticle formalism

In the non interacting case the diagonal terms of $A(q,\omega)$ are just delta functions with peaks at values of $\hbar\omega$ that matches the possible energy difference which results from adding a single particle with quasimomentum q to the system. In the

many body system the energy spectrum is sufficiently complex so that the diagonal elements of $A(q,\omega)$ are not delta functions but instead continuous functions of ω. However, there are always sharp peaks in A. These sharp peaks represent the coherent and long lived excitations, which behave like weakly interacting particles. These excitations are called quasiparticles. From Eq. (8.84) it is possible to see that the quasiparticle decay rate is determined by Γ. The quasiparticle approximation is obtained by considering Γ very small for small values of ω. This assumption implies that $D^{-1} \equiv D_o^{-1} - \Re\Sigma - \frac{i}{2}\Gamma$ is essentially real with only an infinitesimal imaginary part. The zeros of D^{-1} about which A is very sharply peaked are identified with the quasiparticle energies $\hbar\omega_q$.
Using the assumption of a very small Γ, and the identity $\lim_{\epsilon\to 0}\frac{1}{\omega-\omega'+i\epsilon} = P\frac{1}{\omega-\omega'} - i\pi\delta(\omega-\omega')$, it is possible to write the matrix components of D^{-1} as:

$$D^{-1}(q,\omega) = \hbar\omega \begin{pmatrix} 1 & 0 \\ 0 & -1 \end{pmatrix} - \begin{pmatrix} \mathcal{L}_{qq}(q,\omega) & \mathcal{M}_{q-q}(q,\omega) \\ \mathcal{M}^*_{q-q}(q,\omega) & \mathcal{L}^*_{qq}(-q,-\omega) \end{pmatrix}, \tag{8.91}$$

with

$$\mathcal{L}_{qq}(\omega) = -2J\cos qa - \mu + \Sigma_{11}^{HFB}(q,\omega) + \int \frac{d\omega'}{2\pi}\frac{\Gamma_{11}(q,\omega')}{\omega-\omega'+i\epsilon}, \tag{8.92}$$

$$\mathcal{M}_{q-q}(\omega) = \Sigma_{12}^{HFB}(q,\omega) + \int \frac{d\omega'}{2\pi}\frac{\Gamma_{12}(q,\omega')}{\omega-\omega'+i\epsilon}. \tag{8.93}$$

The quasiparticle amplitudes u_q and v_q are the solutions to the eigenvalue problem

$$\begin{pmatrix} \mathcal{L}_{qq}(q,\omega_q) & \mathcal{M}_{q-q}(q,\omega_q) \\ \mathcal{M}^*_{q-q}(q,\omega_q) & \mathcal{L}^*_{qq}(-q,-\omega_q) \end{pmatrix} \begin{pmatrix} u_q \\ v_q \end{pmatrix} = \hbar\omega_q \begin{pmatrix} 1 & 0 \\ 0 & -1 \end{pmatrix} \begin{pmatrix} u_q \\ v_q \end{pmatrix}, \tag{8.94}$$

and satisfy the normalization condition $|u_q|^2 - |v_q|^2 = 1$. In the absence of vortices it is always possible to find an ensemble in which the amplitudes (u_q, v_q) are purely real and $u_q = u_{-q}, \quad v_q = v_{-q}$. In terms of the quasiparticle amplitudes, the matrix elements of the spectral function A, Eq.(8.84), are given by:

$$\begin{aligned} A_{11}(q,\omega) &= -2\mathrm{Im}\left[\frac{\mathrm{u_q^2}}{\omega-\omega_\mathrm{q}+\mathrm{i}0^+} - \frac{\mathrm{v_q^2}}{\omega-\omega_\mathrm{q}+\mathrm{i}0^-}\right] \\ &= 2\pi\left[u_q^2\delta(\omega-\omega_q) - v_q^2\delta(\omega+\omega_q)\right], \qquad (8.95) \\ A_{12}(q,\omega) &= 2\mathrm{Im}\left[\frac{\mathrm{u_q v_q}}{\omega-\omega_\mathrm{q}+\mathrm{i}0^+} - \frac{\mathrm{v_q u_q}}{\omega-\omega_\mathrm{q}+\mathrm{i}0^-}\right] \\ &= -2\pi u_q v_q\left[\delta(\omega-\omega_q) - \delta(\omega+\omega_q)\right], \qquad (8.96) \\ A_{22}(q,\omega) &= -A_{11}(-q,-\omega), \qquad (8.97) \\ A_{21}(q,\omega) &= A_{12}^*(q,\omega). \qquad (8.98) \end{aligned}$$

Finally, using the definitions of F and A, we can express the matrix components: $\rho_q(\omega)$, $\widetilde{\rho}_q(\omega)$ and $m_q(\omega)$ defined as the Fourier transform of ρ_{ij}, $\widetilde{\rho}_{ij}$ and m_{ij} respectively (see Eqs. (8.21) and (8.22)) in terms of quasiparticle amplitudes:

$$\rho_q(\omega) = 2\pi \left[u_q^2 n_q(\omega)\delta(\omega-\omega_q) + v_q^2(1+n_q(\omega))\delta(\omega+\omega_q)\right], \quad (8.99)$$
$$\widetilde{\rho}_q(\omega) = 2\pi \left[u_q^2(1+n_q)(\omega)\delta(\omega-\omega_q) + v_q^2 n_q(\omega)\delta(\omega+\omega_q)\right], \quad (8.100)$$
$$m_q(\omega) = 2\pi u_q v_q \left[n_q(\omega)\delta(\omega-\omega_q) - (1+n_q(\omega))\delta(\omega+\omega_q)\right]. \quad (8.101)$$

8.3.2 HFB approximation

Under the HFB approximation the matrix $\Re\Sigma$ and $\Re S$ are just given by Σ^{HFB} and S^{HFB}. In terms of the quasiparticle amplitudes and setting $\mathcal{N}=2$, they can be written as:

$$\Sigma^{HFB} = U \begin{pmatrix} 2(n_o+\widetilde{n}) & n_o+\widetilde{m} \\ n_o+\widetilde{m} & 2(n_o+\widetilde{n}) \end{pmatrix}, \quad (8.102)$$
$$S^{HFB} = U \begin{pmatrix} n_o+2\widetilde{n} & \widetilde{m} \\ \widetilde{m} & n_o+2\widetilde{n} \end{pmatrix}. \quad (8.103)$$

with

$$\widetilde{n} = = \frac{1}{M}\sum_q (1+n_q(\omega_q))v_q^2 + u_q^2 n_q, \quad (8.104)$$
$$\widetilde{m} = \frac{1}{M}\sum_q u_q v_q \left(2n_q(\omega_q)+1\right). \quad (8.105)$$

In the HFB approximation, Eq.(8.94) and Eq. (8.90) then yield:

$$\begin{pmatrix} -2J\cos(qa)-\mu+2U(n_o+\widetilde{n}) & U(n_o+\widetilde{m}) \\ U(n_o+\widetilde{m}) & -2J\cos(qa)-\mu+2U(n_o+\widetilde{n}) \end{pmatrix} \begin{pmatrix} u_q \\ v_q \end{pmatrix} = \hbar\omega_q \begin{pmatrix} u_q \\ -v_q \end{pmatrix}, \quad (8.106)$$

$$\mu = -2J + Un_o + 2U\widetilde{n} + U\widetilde{m}. \quad (8.107)$$

As a final step, to fix the total density to n, the constraint

$$n = n_o + \widetilde{n}, \quad (8.108)$$

has to be satisfied.

For a given density and temperature Eqs. (8.106)- (8.108) form a closed set of equations. At zero temperature, they reduce to the HFB equations derived in chapter 5 using the quadratic approximation.

8.3.3 Second-order and Beliaev approximations

When second-order terms are taking into account the matrixes $\mathbf{L}_{qq}$ and $\mathbf{M}_{q-q}$ become energy dependent. For simplicity we restrict the calculations to the zero temperature case when $n_q = 0$. In terms of the quasiparticle amplitudes the contributions to the self-energy at second-order are given by

$$\begin{aligned}
\mathbf{M}_{q-q}(q,\omega) &= Un_o + U\widetilde{m} + \frac{2U^2}{M\hbar}n_o\sum_k\left(\frac{2\mathcal{A}_k\mathcal{B}_{q-k}+2\mathcal{C}_k\mathcal{A}_p+2\mathcal{C}_k\mathcal{B}_{q-k}+3\mathcal{C}_k\mathcal{C}_{q-k}}{\omega-\omega_k-\omega_{q-k}+i\epsilon}\right.\\
&\left.-\frac{2\mathcal{B}_k\mathcal{A}_{q-k}+2\mathcal{C}_k\mathcal{A}_p+2\mathcal{C}_k\mathcal{B}_{q-k}+3\mathcal{C}_k\mathcal{C}_{q-k}}{\omega+\omega_k+\omega_{q-k}-i\epsilon}\right) \qquad (8.109)\\
&+\frac{2U^2}{M^2\hbar}\sum_{k,p}\left(\frac{2\mathcal{A}_k\mathcal{B}_p\mathcal{C}_{q-k-p}+\mathcal{C}_k\mathcal{C}_p\mathcal{C}_{q-k-p}}{\omega-\omega_k-\omega_p-\omega_{q-k-p}+i\epsilon}-\frac{2\mathcal{B}_k\mathcal{A}_p\mathcal{C}_{q-k-p}+\mathcal{C}_k\mathcal{C}_p\mathcal{C}_{q-k-p}}{\omega+\omega_k+\omega_p+\omega_{q-k-p}-i\epsilon}\right),\\
\mathbf{L}_{qq}(q,\omega) &= -2J\cos qa-\mu+2Un_o+2U\widetilde{n}+\\
&\frac{2U^2n_o}{\hbar M}\sum_k\left(\frac{\mathcal{A}_k\mathcal{A}_{q-k}+2\mathcal{A}_k\mathcal{B}_{q-k}+4\mathcal{C}_k\mathcal{A}_{q-k}+2\mathcal{C}_k\mathcal{C}_{q-k}}{\omega-\omega_k-\omega_{q-k}+i\epsilon}\right.\\
&\left.-\frac{\mathcal{B}_k\mathcal{B}_{q-k}+2(\mathcal{B}_k\mathcal{A}_{q-k})+4\mathcal{C}_k\mathcal{B}_{q-k}+2\mathcal{C}_k\mathcal{C}_{q-k}}{\omega+\omega_k+\omega_{q-k}-i\epsilon}\right) \qquad (8.110)\\
&+\frac{2U^2}{\hbar M^2}\sum_{k,p}\left(\frac{\mathcal{A}_k\mathcal{A}_p\mathcal{B}_{q-k-p}+2\mathcal{A}_k\mathcal{C}_p\mathcal{C}_{q-k-p}}{\omega-\omega_k-\omega_p-\omega_{q-k-p}+i\epsilon}\right)-\left(\frac{\mathcal{B}_k\mathcal{B}_p\mathcal{A}_{q-k-p}+2\mathcal{B}_k\mathcal{C}_p\mathcal{C}_{q-k-p}}{\omega+\omega_k+\omega_p+\omega_{q-k-p}-i\epsilon}\right),
\end{aligned}$$

$$\begin{aligned}
\mu &= -2J+Un_o+2U\widetilde{n}+U\widetilde{m} \qquad (8.111)\\
&-\frac{2U^2}{\hbar M^2}\sum_{k,p}\left(\frac{2\mathcal{A}_k\mathcal{B}_p\mathcal{C}_{k+p}+2\mathcal{B}_k\mathcal{A}_p\mathcal{C}_{k+p}+2\mathcal{C}_k\mathcal{C}_p\mathcal{C}_{k+p}}{\omega_k+\omega_p+\omega_{k+p}}\right)\\
&-\frac{2U^2}{\hbar M^2}\sum_{k,p}\left(\frac{2\mathcal{A}_k\mathcal{C}_p\mathcal{C}_{k+p}+\mathcal{A}_k\mathcal{A}_p\mathcal{B}_{k+p}+2\mathcal{B}_k\mathcal{C}_p\mathcal{C}_{k+p}+\mathcal{B}_k\mathcal{B}_p\mathcal{A}_{k+p}}{\omega_k+\omega_p+\omega_{k+p}}\right),
\end{aligned}$$

where the quantities $\mathcal{A}$, $\mathcal{B}$ and $\mathcal{C}$ are defined as

$$\mathcal{A}_k = u_k^2, \quad \mathcal{B}_k = v_k^2, \quad \mathcal{C}_k = -u_kv_k. \qquad (8.112)$$

The inclusion of second-order terms modifies the structure of the HFB equations. The matrix that we need to diagonalize to find the quasiparticle energies depends now on the quasiparticle mode in consideration. This means that a separate nonlinear problem must be solved for every quasiparticle state, whereas the solution of the HFB equations yields the whole quasiparticle spectrum. The matrix which is to be diagonalized also become intrinsically non-local and to solve for a quasiparticle state with quasimomentum q we have to sum over all different

quasimomenta. Finally, the diagonal elements are no longer equal as was always the case in all the quadratic approximations considered in chapter 5.

If we omit the second-order terms containing no condensate amplitudes, the equations that we get are the tight-binding version of the ones originally derived by Beliaev [63]:

$$\begin{aligned}\mathbf{M}_{q-q}(q,\omega) = Un_o + U\widetilde{m} \quad &+ \quad \frac{2U^2}{\hbar M} n_o \sum_k \left(\frac{2\mathcal{A}_k\mathcal{B}_{q-k} + 2\mathcal{C}_k\mathcal{A}_p + 2\mathcal{C}_k\mathcal{B}_{q-k} + 3\mathcal{C}_k\mathcal{C}_{q-k}}{\omega - \omega_k - \omega_{q-k} + i\epsilon} \right. \\ &- \left. \frac{2\mathcal{B}_k\mathcal{A}_{q-k} + 2\mathcal{C}_k\mathcal{A}_p + 2\mathcal{C}_k\mathcal{B}_{q-k} + 3\mathcal{C}_k\mathcal{C}_{q-k}}{\omega + \omega_k + \omega_{q-k} - i\epsilon} \right), \end{aligned} \tag{8.113}$$

$$\begin{aligned}\mathbf{L}_{qq}(q,\omega) &= 4J\sin^2(qa/2) + Un_o - U\widetilde{m} + \qquad (8.114) \\ &\frac{2U^2 n_o}{\hbar M} \sum_k \left(\frac{\mathcal{A}_k\mathcal{A}_{q-k} + 2\mathcal{A}_k\mathcal{B}_{q-k} + 4\mathcal{C}_k\mathcal{A}_{q-k} + 2\mathcal{C}_k\mathcal{C}_{q-k}}{\omega - \omega_k - \omega_{q-k} + i\epsilon} \right. \\ &- \left. \frac{\mathcal{B}_k\mathcal{B}_{q-k} + 2(\mathcal{B}_k\mathcal{A}_{q-k}) + 4\mathcal{C}_k\mathcal{B}_{q-k} + 2\mathcal{C}_k\mathcal{C}_{q-k}}{\omega + \omega_k + \omega_{q-k} - i\epsilon} \right), \qquad (8.115) \end{aligned}$$

$$\mu = -2J + Un_o + 2U\widetilde{n} + U\widetilde{m}. \tag{8.116}$$

As discussed in chapter 5, the HFB approximation has the problem that it is not gapless. It was shown by Beliaev that when second-order Beliaev contributions are included the gap problem disappears. The reason is that as $\widetilde{m}$ introduces the many-body scattering matrix in the off-diagonal terms, second-order corrections introduce the many-body scattering matrix in the diagonal terms. This can be seen by considering the second-order Beliaev corrections in the particle approximation, $u_q \to 1, v_q \to 0$. In this case the second-order terms in Eq.(8.115) become

$$\mathbf{L}^{(2)}_{qq}(q,\omega) = -\frac{2U^2 n_o}{\hbar M} \sum_k \frac{1}{\omega - \omega_k - \omega_{q-k} - i\epsilon}. \tag{8.117}$$

Comparison with Eq. (5.121) shows that $\mathbf{L}^{(2)}_{qq}(q,\omega)$ is the second order contribution to the many body scattering matrix.

When both HFB and second-order corrections are included the quasiparticle energies not only are shifted with respect to the BdG quasiparticle energies but they also become complex. The imaginary part that the quasiparticle energies acquire comes from the poles of the second-order terms and it is associated with a damping rate. The physical meaning is that when the energy denominator in the second-order terms vanishes a real decay process is energetically allowed. The damping mechanism in which a quasiparticle decay into two of lower energy is known as Beliaev damping and was calculated by Beliaev in the case of a uniform Bose superfluid [63].

8.4 Conclusions

In summary, we showed in this chapter that the complicated non local non Markovian second-order solutions derived under the 2PI-CTP formalism, actually reduce to the standard kinetic theory solutions when the scale separation assumption is made. We also showed that at equilibrium the full second-order 2PI equations reproduce the second-order corrections to the self energy well known since Beliaev.

Chapter 9

Characterizing the Mott Insulator Phase

Besides the superfluid regime, the other regime where analytic solutions become relatively simple is the Mott insulator phase. Deep in the Mott insulator regime the kinetic energy term in the Hamiltonian, which delocalizes the atoms, can be treated as a perturbation. In this chapter we use perturbation theory to describe the basic properties of the Mott phase. We study both a translationally invariant system when no other external potential is present and the case when there is an external harmonic confinement, as is the case in real experimental situations. Specifically, the trapped system is studied assuming a parameter regime where multi-occupancy in inhibited which is the relevant regime for the lattice based quantum computation proposals.

9.1 Commensurate translationally invariant case

9.1.1 Perturbation theory

In this section we assume a commensurately filled one dimensional lattice with integer filling factor $N/M = g$, periodic boundary conditions and a parameter regime where $U/J \gg (U/J)_c$ with $(U/J)_c$ the critical point, so that we are deep in the insulating phase. In this parameter regime, it is fair to consider the kinetic term of Bose-Hubbard Hamiltonian as a perturbation:

$$\hat{H} = \hat{H}^{(0)} + \delta\hat{H}, \tag{9.1}$$

$$\hat{H}^{(0)} = \frac{1}{2}U\sum_n \hat{a}_n^\dagger \hat{a}_n^\dagger \hat{a}_n \hat{a}_n, \tag{9.2}$$

$$\delta\hat{H} = -J\sum_n (\hat{a}_n^\dagger\, \hat{a}_{n+1} + \hat{a}_{n+1}^\dagger\, \hat{a}_n\,). \tag{9.3}$$

The unperturbed Hamiltonian includes only the on-site interaction term, which is diagonal in a number Fock state basis, and to zeroth order the ground state

$|\Phi_0\rangle$ is the Fock state with g atoms in every lattice site. We refer to this state as the target state $|T\rangle$. The lowest lying excitations are described by the Fock states, $|\Psi_{nm}\rangle$, that have $g+1$ particles at site n, $g-1$ particles at site m, and exactly g particles in every other site. We call these states *one particle-hole (1-ph) excitations* . There are $M(M-1)$ 1-ph excitations and because of the translational symmetry of the system they are degenerate at zeroth order. All of them have an energy U above the ground state. This energy gap is one of the most important characteristics of the Mott insulator phase.

$$\begin{aligned} \left|\Phi_0^{(0)}\right\rangle &\equiv |T\rangle \equiv |g, g, ..., g, g\rangle\,, & (9.4)\\ \left|\Phi_i^{(0)}\right\rangle &\equiv |\Psi_{nm}\rangle_{n\neq m} \quad i = 1, \ldots, M(M-1) & (9.5)\\ &= \left| g, ..., \underbrace{g+1}_{n}, ..., \underbrace{g-1}_{m}, .., g \right\rangle. \end{aligned}$$

The unperturbed energies are

$$\begin{aligned} E_0^{(0)} &= \frac{U}{2} M g(g-1), & (9.6)\\ E_i^{(0)} &= U + E_0^{(0)} \quad i = 1, \ldots, M(M-1). & (9.7) \end{aligned}$$

At first order the kinetic energy term mixes the target state with 1-ph excitations with the particle and the hole at adjacent sites. The first order ground state wave-function is

$$\left|\Phi_0^{(1)}\right\rangle = \left(|T\rangle + \frac{J}{U}\sqrt{2Mg(g+1)}|S\rangle \right), \tag{9.8}$$

with $|S\rangle$ the normalized translationally invariant state with a particle and hole at adjacent sites:

$$|S\rangle \equiv \sum_{n=1}^{M} \frac{|\Psi_{nn+1}\rangle + |\Psi_{nn-1}\rangle}{\sqrt{2M}}. \tag{9.9}$$

Notice the factor M that appears in the first order correction. It gives a restriction on the validity of a perturbative treatment as the number of lattice sites increases. In order for perturbation theory to be valid, the parameter $\frac{Jg}{U}\sqrt{M}$ has to be small. The first order correction to the ground state energy vanishes. The second order correction is given by

$$E_0^{(2)} = -\frac{2J^2 M}{U} g(g+1). \tag{9.10}$$

Because of the degeneracy of the unperturbed states, in order to find first order corrections to the $M(M-1)$ low lying excited states we must diagonalize the kinetic

energy Hamiltonian within the 1-ph subspace. If we span the eigenstates as a linear combinations of 1-ph excitations,

$$\left|\Phi_i^{(1)}\right\rangle = \sum_{n,m=1,m\neq n}^{M} C_{nm}^i \left|\Psi_{nm}\right\rangle, \tag{9.11}$$

the necessary and sufficient conditions that the coefficients C_{nm}^i have to fulfill in order to diagonalize the kinetic energy operator are given by the following equations

$$-(g+1)(C_{n+1m}^i + C_{n-1m}^i) - g(C_{nm+1}^i + C_{nm-1}^i) = \widetilde{E}_i C_{nm}^i, \tag{9.12}$$

with $E_i^{(1)} = U - J\widetilde{E}_i$. Besides Eq. (9.12), the amplitudes have to fulfill two other equations:

$$C_{nn}^i = 0, \tag{9.13}$$

$$C_{n+Mm}^i = C_{nm+M}^i = C_{nm}^i. \tag{9.14}$$

Eq. (9.12) is analogous to the tight-binding Schrödinger equation of a two dimensional square lattice in the $x-y$ plane, with the x direction associated with the position of the extra particle and the y direction with the position of the hole. The different weights $g+1$ and g can be understood in the 2D-lattice model as different effective masses in the two directions. Eq. (9.14) imposes periodic boundary conditions, whereas the constraint $C_{nn}^i = 0$ takes into account the requirement that the extra particle and the hole at the same site annihilate each other. It can be thought of as a hard wall in the $x = y$ axis. The solutions are not straightforward due to the fact that the effective mass difference breaks the lattice symmetry around the $x = y$ axis and makes the hard wall constraint hard to fulfill.

We now describe a procedure for solving the eigenvalue equations and evaluating limiting cases where it is possible to find analytic solutions. Without any constraint, a general solution of Eq. (9.12) has the form

$$C_{nm} \propto e^{inz} e^{imt}, \tag{9.15}$$

with

$$\widetilde{E}_i = -2\left((g+1)\cos(z) + g\cos(t)\right). \tag{9.16}$$

To satisfy the constraint $C_{nn} = 0$ we use the linear character of the problem and look for a linear combination of solutions which have the same eigenvalue $\widetilde{E}_i$ but which also fulfill the hard wall constraint. We look then for a general solution of the form:

$$C_{nm} \propto \sin(r(n-m))\, e^{iml} e^{ins}, \tag{9.17}$$

and determine the free parameters, l, r, s by forcing the solution to satisfy Eq. (9.12). This procedure leads to the following equation:

$$(g+1)\cos(r+s) + g\cos(l-r) = (g+1)\cos(s-r) + g\cos(l+r). \tag{9.18}$$

Eq. (9.18) is satisfied if we choose s to be given by:

$$s = \mathrm{Arc\,sin}\left(\frac{\mathrm{g}}{\mathrm{g}+1}\sin\mathrm{l}\right). \tag{9.19}$$

The tricky part is trying to satisfy also the periodic boundary conditions, Eq.(9.14), because in general solutions of the form Eq. (9.17) are not necessarily compatible with the periodic boundary conditions in the two variables n and m. However, there are some limiting cases in which both conditions are satisfied. Such cases are discussed in the remainder of the section.

- Case $l = 0$

  If we choose $l = 0$ and use Eq. (9.19) and Eq. (9.17), we can find $M - 1$ solutions of Eq. (9.12) which satisfy all the boundary conditions and are linearly independent. These are

$$C^r_{nm} = \begin{cases} \frac{\sqrt{2}}{M}\sin\left(\frac{\pi r}{M}|n-m|\right), & r \text{ odd} \\ \frac{\sqrt{2}}{M}\sin\left(\frac{2\pi r}{M}(n-m)\right), & r \text{ even} \end{cases} \tag{9.20}$$

$$E^{(1)}_r = U - 2J(2g+1)\cos\left(\frac{\pi r}{M}\right),\ r = 1,..M-1 \tag{9.21}$$

  Inside the 1-ph subspace all the translationally invariant states are spanned by the states whose amplitudes C^r_{nm} are the $r \in$ odd solutions of Eq. (9.20). Because in the absence of an external confinement the many body Hamiltonian is translationally invariant, the ground state must also be and it is only coupled through the Hamiltonian to the subspace spanned by these translationally invariant states. The dispersion relation, Eq. (9.21), agrees to first order in J to the mean-field solution found in [77]. We want to point out that this dispersion relation only describes the spectrum of $M - 1$ of the $M(M-1)$ low tying excitations.

  When $l \neq 0$ the derivation of analytic solutions is more elaborate. However, in the limiting cases of high filling factor, $g \gg 1$, it is still easy to find an analytic solution.

- Case $g \gg 1$

  In this limiting situation $s \approx l$, (see Eq.(9.19)) and the periodic boundary conditions are satisfied if s, l and r are integer multiples of $\frac{\pi}{M}$. The eigenvalues and an orthonormal set of modes in the high filling factor regime can be chosen to be:

$$E^{(1)}_{rR} = U - 2J(2g+1)\cos\left(\frac{\pi r}{M}\right)\cos\left(\frac{\pi R}{M}\right), \tag{9.22}$$

$$C^{r,R\neq 0}_{nm} = \begin{cases} \frac{2}{M}\sin(\frac{\pi r}{M}|n-m|)\sin(\frac{\pi R'}{M}(n+m)+\alpha_{rR}), \\ \frac{2}{M}\sin(\frac{\pi r}{M}(n-m))\sin(\frac{\pi R''}{M}(n+m)+\beta_{rR}), \end{cases}$$

$$C^{r,0}_{nm} = \begin{cases} \frac{\sqrt{2}}{M}\sin\left(\frac{\pi r}{M}|n-m|\right), & r \text{ odd} \\ \frac{\sqrt{2}}{M}\sin\left(\frac{\pi r}{M}(n-m)\right), & r \text{ even} \end{cases} \tag{9.23}$$

with $r = 1, \ldots M-1$ and $R = 0, \ldots M-1$. The notation R' restricts the values of R to the ones where $R+r$ is an odd number and R'' to the values where $R+r$ is even. The constants $\alpha_{rR} = \pi(r-R+1)/4$ and $\beta_{rR} = \pi(r+R-1+M)/4$ guarantee the orthogonality of the eigenmodes. In Fig. 9.1 we show a contour plot of the two dimensional 1-ph band.

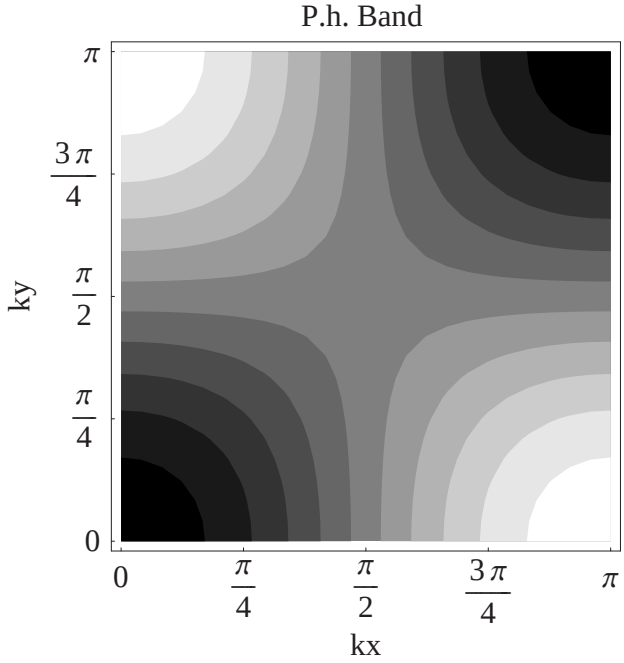

Figure 9.1: Contour plot of the two dimensional band of the 1-ph excitations to fist order in perturbation theory. In the plot the brighter the color the higher the energy. The labels are $ky = 2\pi/MR$ and $kx = 2\pi/MR$.

To check the range of validity of our analytical solutions, in Fig.9.2 we plot comparisons between the first order energy shifts calculated by the exact diagonalization of the Bose-Hubbard Hamiltonian but restricting the Hilbert space to the 1-ph subspace and Eq. (9.22). We label the eigenvalues in ascending order.

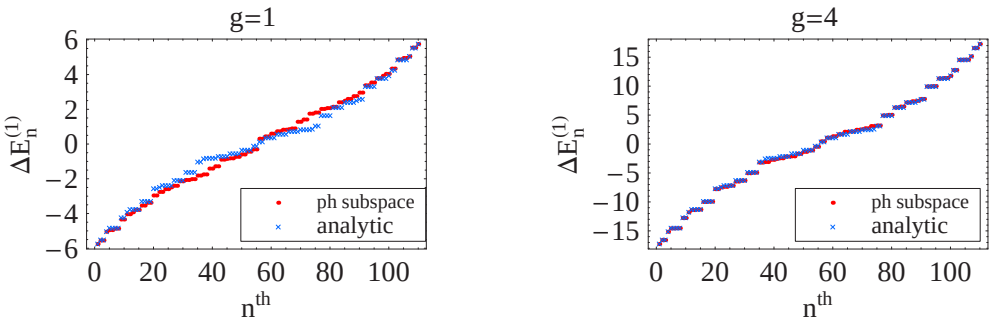

Figure 9.2: Comparisons between the first order corrections to the 1-ph excitations calculated by diagonalizing the Bose-Hubbard Hamiltonian inside the 1-ph subspace and the analytic solution Eq. (9.22). The number of sites used for the plot was $M = 11$. Energies are in units of J.

The parameters used for the comparisons were $M = 11$ and filling factors $g = 1$ and 4. We notice that even though the analytic expression was calculated under the high filling factor assumption, for values of $g = 4$, the agreement between the two solutions is very good. For the case $g = 1$ the two spectra do not agree perfectly, however, we can say that the analytic solution is fair even in this low density regime.

In Fig. 9.2 we checked for the validity of the analytic solution Eq. (9.22) when the Hilbert space is restricted to the 1-ph subspace. However, to restrict the low lying excitations to the 1-ph excitations is only good as long as first order perturbation theory is valid. This implies that the parameter $\frac{Jg}{U}\sqrt{M}$ is small. In Fig. 9.3, we explore the range of validity of perturbation theory by plotting the spectrum for different values of U/J and filling factors. The solutions presented in the plots are the eigenenergies found by the exact diagonalization of the Hamiltonian (red), by diagonalization in the restricted 1-ph subspace (green) and the analytic solution, Eq. (9.22) (blue).

We observe in the plots that for low filling factors ($g = 1$) the analytic solution is not as good as it is for high filling factors in reproducing the 1-ph subspace spectrum. Nevertheless, at low densities the validity of perturbation theory holds for a larger range of U/J values. On the other hand, when the filling is high the analytic solution gives a pretty good description of the 1-ph subspace but the parameter U/J must be approximately g times higher than the unit filled case to ensure that higher order corrections are negligible. The number of wells chosen for the plots was small because of the exponentially scaling of the Hilbert space. As the number of wells is increased, the ratio of U/J required for perturbation theory to be valid becomes larger.

Using the perturbation theory results, it is possible to calculate expectation values of physical observables that are relevant to the experiments. For example,

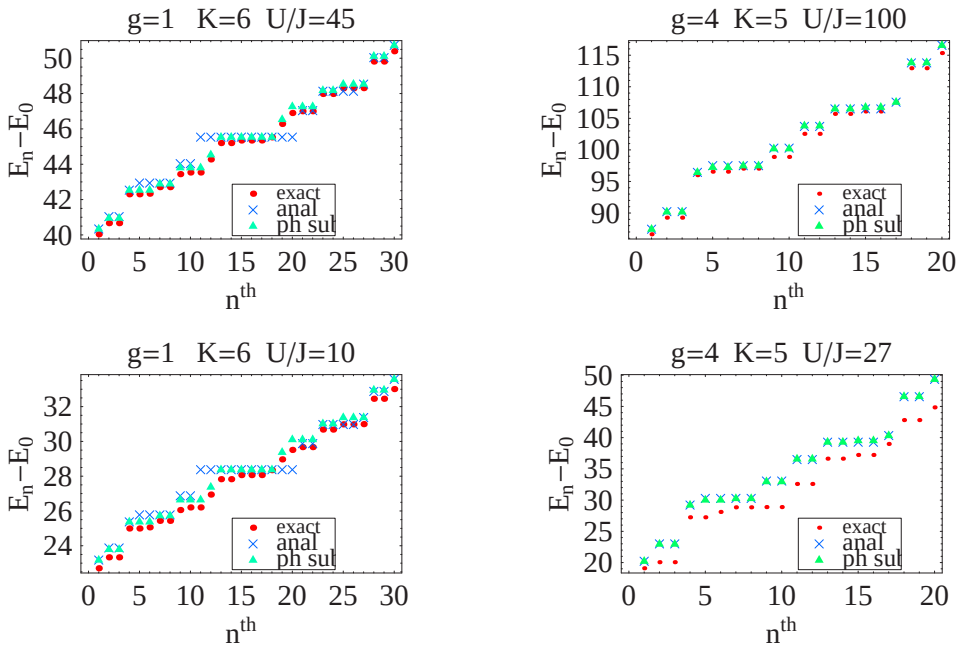

Figure 9.3: Comparisons between the energy eigenvalues calculated by the exact diagonalization of the Hamiltonian (red dots), the diagonalization of the Hamiltonian in the restricted 1-ph subspace (green triangles) and the analytic solution (blue crosses), Eq. (9.22). The index n labels the eigenvalues in increasing order of energy. The filling factor g, the number of wells M and the ratio U/J is indicated in each plot. Energies are in units of J.

the quasimomentum distribution (Eq. (5.57)) to first order in perturbation theory is given by:

$$n_q = g + \frac{4J}{U} g(g+1)\cos(qa). \tag{9.24}$$

Here q is the quasimomentum $q = \frac{2\pi j}{aM}$, $j = 0, 1, \ldots M-1$ and a the lattice spacing.

The interference pattern after ballistic expansion is closely related to the quasimomentum distribution [103]. In the superfluid regime the intensity of the principal interference peak is proportional to the occupation number of the $q = 0$ quasimomentum component, which describes the number of particles in the condensate. The washing out of the interference peaks in the Mott phase is linked to the redistribution of the population from the condensate to states with higher quasimomenta. When the system is in the Mott insulator regime, instead of a macroscopically occupied state, at zeroth order in J/U, the momentum distribution is flat and all the quasimomentum states of the lowest band are uniformly occupied. This feature is indicated in Eq. (9.24). At first order in J/U, we

take into account the nearest neighbors' remaining coherence, always present in the Mott ground state, which creates a small cosinusoidal modulation of the flat quasimomentum background.

In Fig. 9.4, we plot the quasimomentum distribution as a function of U/J for a unit filled lattice with six wells. The exact solution is depicted with solid lines and the first order perturbative results with dots. The decrease of the zero momentum population and the tendency towards a flat distribution for large U/J ratios is observed in the plot.

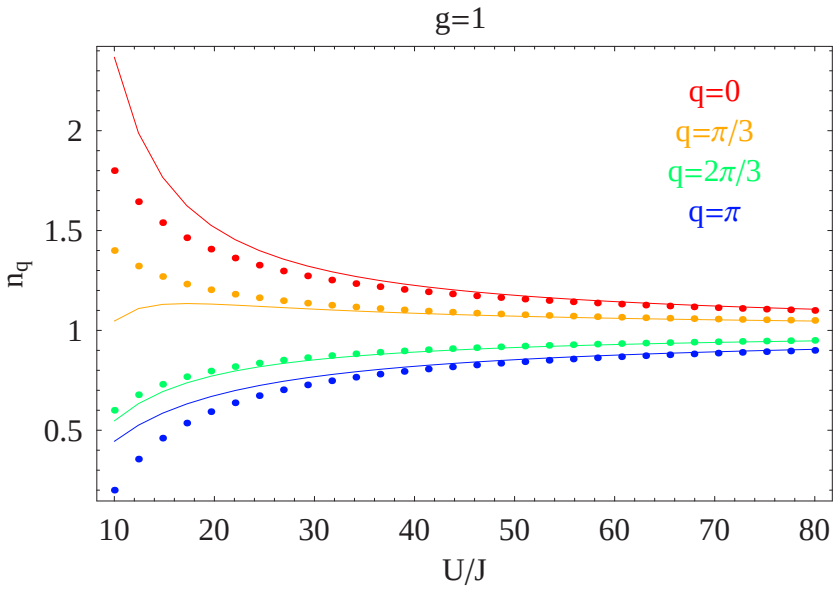

Figure 9.4: Quasimomentum distribution as a function of U/J for a unit filled lattice with six wells ($M = 6$). The exact solutions are displayed with solid lines and the first order perturbative results with dotted lines. Due to the lattice symmetry $n_{4\pi/3} = n_{2\pi/3}$ and $n_{5\pi/3} = n_{\pi/3}$.

Another characteristic feature of the Mott insulator phase is the reduction of the number fluctuations. The first non vanishing number fluctuations (see Eq. (5.56)) are quadratic in J/U and given by:

$$\Delta n \quad = \quad 4g(g+1)\frac{J^2}{U^2}. \tag{9.25}$$

We omitted the site index in Δn because of the translational symmetry. Notice that due to the fact that the true Mott ground state is not a Fock state, the number fluctuations decrease as the ratio U/J increases, but they are not exactly zero. This is a problem for the lattice based quantum computer proposals and we will try to correct for it in chapter 11.

We conclude this section by using the first order perturbation theory results, to crudely estimate the critical transition point. Quantum phase transitions such as the superfluid to Mott insulator transition can be understood based on the phenomena of level crossing: as a characteristic parameter is changed (in this case U/J), at some critical point a state that was an excited state becomes the new ground state of the system. If we use this criteria to calculate the critical point and use Eq. (9.22) we get

$$(U/J)_c \approx 2(2g+1) \sim 4g \tag{9.26}$$

This result only applies for the one dimensional case. It is a factor of two smaller than the calculated value from mean field theory (Eq. 3.9) but it is in better agreement with numerical Monte Carlo simulations and strong coupling expansions which predict a critical point for a unit filled lattice of $(U/J)_c \approx 4.65$ [78, 79].

9.2 Harmonic confinement plus lattice

In this section we consider a one dimensional optical lattice in the presence of a magnetic confinement with oscillation frequency ω_T. We assume that the magnetic trap has its minimum at the lattice site $n = 0$. The magnetic confinement introduces a characteristic energy scale $\Omega = ma^2\omega_T/2$, so that $V_n = \Omega n^2$ (see Eq.(6.1)). We first focus on the case in which the system has an odd number of atoms.

For the analysis we are also going to consider a parameter regime where

$$U > \frac{\Omega(N-1)^2}{4}, \tag{9.27}$$

$$\Omega N > J. \tag{9.28}$$

The first condition expresses the requirements that the on site interaction energy U must be bigger than the trapping energy of the most externally trapped atom, so multiple atom occupation in any well is inhibited. The second states the requirement that the kinetic energy must be smaller than the potential energy cost for an atom at the edge of the atomic cloud to tunnel to the next unoccupied site. Thus it is energetically costly for the atoms to tunnel.

In this parameter regime the Bose-Hubbard Hamiltonian can be split into two parts: an unperturbed part which includes the interaction and potential energy and which is diagonal in a Fock state representation, and a kinetic energy part which is going to be treated as a perturbation.

$$\hat{H} = \hat{H}^{(0)} + \delta\hat{H}, \tag{9.29}$$

$$\hat{H}^{(0)} = \Omega \sum_n n^2 \hat{a}_n^\dagger \hat{a}_n + \frac{1}{2} U \sum_n \hat{a}_n^\dagger \hat{a}_n^\dagger \hat{a}_n \hat{a}_n, \tag{9.30}$$

$$\delta\hat{H} = -J \sum_n (\hat{a}_n^\dagger \hat{a}_{n+1} + \hat{a}_{n+1}^\dagger \hat{a}_n). \tag{9.31}$$

With the constraints Eq. (9.27) and Eq. (9.28) we are guaranteed that to zeroth order in perturbation theory, the ground state of the system consists of a unit filled central core comprising N wells in the central region of the trap, surrounded by external empty sites, which in solid state language can be called a sea of holes. If the number of atoms is odd, due to the the assumed trap symmetry, at zero order in perturbation theory the ground state is unique and given by:

$$\left|\Phi_0^{(0)}\right\rangle = \left|0,..,0,\underbrace{1,1,....,1,1}_{N \quad sites},0,..,0\right\rangle. \tag{9.32}$$

The unperturbed ground state energy is

$$E_0^{(0)} = \frac{\Omega}{24}N(N^2-1). \tag{9.33}$$

The zeroth order low lying excitations consist of 1-ph excitations and another kind of excitations which we refer as n-hh excitations. In the following we proceed to describe them in more detail:

- One particle hole excitation (1-ph)

  The 1-ph excitations are described by the Fock states, $\left|\Psi_{nm}^{ph}\right\rangle$, with an extra particle at site m and a hole at the site n, both inside the central core.

$$\begin{aligned}\left|\Phi_{iph}^{(0)}\right\rangle &\equiv \left|\Psi_{mn}^{ph}\right\rangle \\ &= \left|0,..,0,1,...,\underbrace{2}_{m},...,\underbrace{0}_{n},..,1,0,..,0\right\rangle.\end{aligned} \tag{9.34}$$

  As opposed to the translationally invariant system, the presence of the trap breaks the degeneracy and the 1-ph excitations are not degenerate at zero order. Their energy is given by the interaction energy cost U to create a 1-ph pair plus the potential energy cost due to the trap:

$$E_{nm}^{ph(0)} = E_0^{(0)} + U + \Omega(m^2 - n^2). \tag{9.35}$$

  with n and m integers, $n, m = -\frac{N-1}{2}, \ldots, \frac{N-1}{2}$.

- Hole hopping excitations (n-hh)

  These excitations are described by the states with a maximum of one particle per well and holes inside the inner central core. They have to be included in the trapped system because of the reservoir of holes surrounding the central

core which brings an extra degree of delocalization. Because the n-hh excitations are only due to the transfer of holes to the inner core, they don't have the interaction energy cost U for having two particles at the same site and therefore they can be lower in energy than the 1-ph excitations. We label the 1-hh, states with only one hole inside the central core, by $\left|\Psi^{hh}_{mn}\right\rangle$. Explicitly they are given by:

$$\begin{aligned}\left|\Phi^{(0)}_{ihh}\right\rangle &\equiv \left|\Psi^{hh}_{mn}\right\rangle \\ &= \left|0,..,\underbrace{1}_{n},..,0,1,...,\underbrace{0}_{m},..,1,0,..,0\right\rangle.\end{aligned} \tag{9.36}$$

The zero order energy cost to create 1-hh excitations is:

$$E^{hh(0)}_{nm} = E^{(0)}_0 + \Omega(m^2 - n^2), \tag{9.37}$$

with n and m integers such that $|n| > (N-1)/2$ and $|m| < (N-1)/2$

At first order the kinetic energy term mixes the unperturbed ground state with the 1-ph excitation which have the extra particle and the hole at adjacent sites and with the 1-hh excitations were the most external trapped atom tunnels to the first available vacant site. The ground state wave function at first order is then given by

$$\begin{aligned}\left|\Phi^{(1)}_0\right\rangle &= \left|\Phi^{(0)}_0\right\rangle + 2J\sum_{n=-(N-1)/2}^{(N-3)/2}\frac{\left|\Psi^{ph}_{nn+1}\right\rangle + \left|\Psi^{ph}_{-n-(n+1)}\right\rangle}{\sqrt{2}(U-\Omega(1+2n))} \\ &\quad + \frac{\sqrt{2}J}{\Omega N}\frac{\left|\Psi^{hh}_{nn+1}\right\rangle + \left|\Psi^{hh}_{-n-(n+1)}\right\rangle}{\sqrt{2}}.\end{aligned} \tag{9.38}$$

The first order wave functions of the excitations directly coupled to the unperturbed ground state are

$$\left|\Phi^{(1)}_{\pm nph}\right\rangle = \left|\Psi^{ph}_{nn\pm1}\right\rangle - \sqrt{2}J\frac{\left|\Phi^{(0)}_0\right\rangle}{(U-\Omega(1\pm 2n))}, \tag{9.39}$$

$$\left|\Phi^{(1)}_{\pm hh}\right\rangle = \left|\Psi^{hh}_{\pm L\pm(L+1)}\right\rangle - J\frac{\left|\Phi^{(0)}_0\right\rangle}{(\Omega N)}, \tag{9.40}$$

with $L = (N-1)/2$.

In Fig. 9.5 we plot comparisons between the analytic (blue) and exact (red) excitation spectra. The index n labels the eigenenergies in increasing energy order.

The parameters used for the plots were $U/J = 40$ and 60, $\Omega/J = 1.875$, $N = 9$ and $M = 11$. The analytical spectrum was calculated to zeroth order in perturbation theory. The convergence of perturbative results to the exact ones as the interaction parameter U/J is increased can be seen in the plots. The lines indicate the energies of the states that are coupled to the zero order ground state. The first two lines correspond to the two degenerate 1-hh excitation states $\left|\Psi^{hh}_{\pm L\pm(L+1)}\right\rangle$ with energy ΩN, the others correspond to 1-ph excitations $\left|\Psi^{ph}_{nn\pm1}\right\rangle$ with energies $(U - \Omega(1 \pm 2n))$.

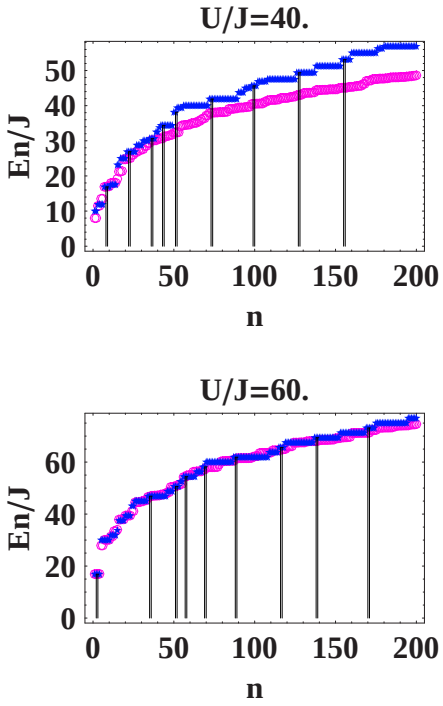

Figure 9.5: Comparisons between the exact (red) and the perturbative (blue) spectra for a trapped system with $N = 9$, $M = 11$ and $\Omega/J = 1.875$ deep in the Mott regime. The lines indicate the energies of the states that are coupled directly to the ground state.

When the number of atoms is even, the trap symmetry is broken and the ground state becomes degenerate. In this case, at zeroth order, the degenerate ground states are:

$$\begin{aligned}
\left|\Phi_{0\pm}^{(0)}\right\rangle &= \frac{1}{\sqrt{2}}\left(\left|\Phi_{L}^{(0)}\right\rangle \pm \left|\Phi_{R}^{(0)}\right\rangle\right), \qquad (9.41)\\
\left|\Phi_{L}^{(0)}\right\rangle &= \left|0,...,0,1,\underbrace{1,1,....,1,1}_{N-1 \quad sites},0,..,0\right\rangle,\\
\left|\Phi_{R}^{(0)}\right\rangle &= \left|0,..,0,\underbrace{1,1,....,1,1}_{N-1 \quad sites},1,0,..,0\right\rangle.
\end{aligned}$$

When the system has an even number of atoms, there are always going to be a nonzero number fluctuation at the trap edge. Because the states $\left|\Phi_{L}^{(0)}\right\rangle$ and $\left|\Phi_{R}^{(0)}\right\rangle$ are not coupled by the Bose-Hubbard Hamiltonian at first order, the previous analysis we did for the system with an odd number of atoms can be straightforwardly extended to the even case.

The constraint $\Omega N > J$ used for the analysis above can be an important experimental restriction if the total number of trapped atoms is large. In the regime where $\Omega N < J$, but still $U > \Omega(N/2)^2$, the energy splitting between 1-ph excitations induced by the trap is small and degenerate perturbation theory must be used at first order. An analytic treatment becomes really difficult, nevertheless, it is possible to have a qualitative analysis of the system. In this case, the system can be divided in two parts: a central unit filled core comprising $K < N$ wells at the center of the trap and a superfluid layer surrounding the central core with maximum one atom per lattice site where the mobility of the holes is high. The size K of the unit filled central core is determined by the strength of the magnetic confinement, $K \sim J/\Omega$. The properties of the unit filled core can be described to a good approximation by the commensurate homogeneous results. On the other hand, the atoms surrounding the central core are almost free to tunnel and they have superfluid like properties.

9.3 Conclusions

In summary, in this chapter we have described the basic properties of the Mott insulating phase both in translationally invariant and harmonically trapped systems. All the results derived here are going to be used as the starting point for the calculations in the following chapters.

Chapter 10

Bragg Spectroscopy

To date, the primary observable used to study ultra cold atoms in an optical lattice has been the momentum distribution of the system, observed after ballistic expansion. In particular, this type of measurement has been used to reveal the phase coherence between sites in the lattice and has been a really useful technique to characterize the superfluid phase. However, the disappearance of the interference pattern is not a conclusive diagnostic of the Mott phase. Recent analysis shows that this is more correctly related to the degree of condensate depletion. Indeed, for this reason, the diagnostic tool used in the experiments by Greiner *et al.* [46], to prove the achievement of the Mott phase, was to apply a potential gradient to the lattice and show the presence of a gap in the excitation spectrum.

Moreover, because the usual procedure for producing the Mott insulator state is to begin with a magnetically trapped Bose-Einstein condensate (with no discernible thermal component), and slowly load it into an optical lattice, finite temperature effects or non-adiabatic ramping of the lattice may lead to the production of an imperfect Mott phase. As more elaborate experiments are undertaken with optical lattices in the strongly correlated regime it will be crucially important to diagnose the properties of the states produced.

The results we present here suggest that Bragg spectroscopy can not only give information about the excitation spectrum, which is a crucial diagnostic of the Mott insulator phase as characterized by the opening of a gap, but that it can also be used in the Mott regime to estimate the temperature of the system. Specifically, we study the linear response to Bragg spectroscopy of cold atoms loaded in a one dimensional optical lattice based on a perturbative analysis. We obtain analytical expressions for the dynamical structure factor and use them to calculate the energy deposited into the system. We also test the accuracy of our approximations by comparing them with numerical solutions obtained by diagonalizing the Bose-Hubbard Hamiltonian for moderate number of atoms and wells. The calculations are done for translationally invariant lattices and in the presence of an harmonic external potential. First we start by reviewing the basic formalism that describes Bragg spectroscopy.

10.1 Formalism

The application of Bragg spectroscopy to study cold atomic systems was first pioneered by the NIST and MIT groups [65, 66]. Their scheme involved using a pair of interfering laser fields to Bragg scatter atoms into a higher momentum state. Since those experiments Bragg spectroscopy has been established as a versatile tool for probing Bose-Einstein condensates in a wide range of situations (e.g see [141, 142, 143, 144]).

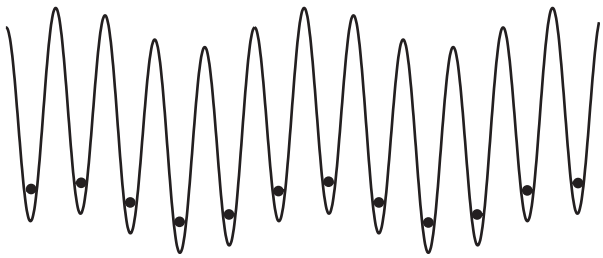

Figure 10.1: Bragg spectroscopic scheme considered in this paper. The lattice potential with atoms loaded into the ground band is perturbed by a shallow running wave perturbation (the Bragg potential).

Two-photon Bragg spectroscopy in a lattice is performed by superimposing a periodic travelling wave potential on the lattice potential. This could be arranged by modulating the lattice amplitude, as done by Stöferle *et al.* [145]. The more general situation arises when the Bragg potential is produced by an additional pair of independent laser fields, chosen to produce a shallow potential that is not necessarily commensurate with lattice potential (see Fig. 10.1). Specifically, the atomic sample is illuminated with two additional laser beams with wave vectors of magnitudes k_1 and k_2 in the direction of the lattice and frequency difference ω. The intersecting beams create a periodic potential parallel to the lattice with travelling intensity modulation given by $V_o \cos(qx - \omega t)$. The difference in wave vectors of the beams defines the Bragg momentum $q = k_1 - k_2$ and the difference in frequency the Bragg energy $\hbar\omega$. Atoms exposed to these beams can undergo stimulated light scattering by absorbing a photon from one of the beams and emitting a photon into the other.

We consider a one dimensional optical lattice with M lattice sites, sufficiently deep that the tight-binding approximation is valid, and assume that we can restrict the dynamics of the atoms to the lowest vibrational band. This is guaranteed if the loading is done slow enough to avoid band excitations,i.e. if the energy of the Bragg perturbation $\hbar\omega$ is less than the energy gap to the second band and if the momentum transfer q is contained within the first Brillioun zone. A detailed analysis of the validity of the first band approximation is found in Ref.[148]. There the authors, using a mean field approach combined with Bogoliubov analysis, extended the existing theory of Bragg spectroscopy of magnetically trapped BEC [146, 147] to lattice systems.

As shown in chapter 3, under the single-band approximation the system is described by the Bose-Hubbard Hamiltonian, which we will denote as $\hat{H}_o$. Hereafter we assume, unless otherwise specified, a harmonic magnetic confinement such that $V_n = \Omega n^2$. In the tight-binding approximation, the Hamiltonian describing the Bragg perturbation is given by

$$\hat{H}_B = \frac{1}{2} V_o (\hat{\rho}_q^\dagger e^{-i\omega t} + \hat{\rho}_q e^{i\omega t}). \tag{10.1}$$

The density fluctuation operator $\hat{\rho}_q^\dagger$ is defined as

$$\hat{\rho}_q^\dagger = \sum_{m,n=0}^{M-1} I_q^{n,m} \hat{a}_m^\dagger \hat{a}_n, \tag{10.2}$$

with

$$I_q^{n,m} = \int dx e^{iqx} w_0^*(x - am) w_0(x - an), \tag{10.3}$$

where $w_0(x)$ is the Wannier orbital centered at the origin of the lowest vibrational band. To calculate $I_q^{n,m}$ we approximate the Wannier orbitals by Gaussians localized at the bottom of the potential wells , $\phi_0(x - an) \sim \exp[-(x - an)^2/2a_{ho}^2]/(\pi^{1/4}\sqrt{a_{ho}})$, where the width a_{ho} can be estimated by minimizing the ground state energy. For a lattice potential of the form $E_R V_{lat} \sin^2(\pi x/a)$, with E_R the recoil energy of the atoms, a_{ho} scales like $a_{ho} \sim (V_{lat})^{-1/4} a/\pi$. Neglecting the overlap between Wannier orbitals located in different sites we get $I_q^{n,m} \sim I_q \delta_{n,m} \exp(ia(n + m)q/2)$, where $\delta_{n,m}$ is the Kronecker delta function. Then

$$I_q = \exp\left(-\frac{1}{\sqrt{V_{lat}}} \left(\frac{qa}{2\pi}\right)^2\right). \tag{10.4}$$

Notice that I_q approaches one for small qa and deep lattices. Using the approximate expression for $I_q^{n,m}$ we can rewrite the density operator as:

$$\hat{\rho}_q^\dagger = I_q \sum_{m=0}^{M-1} \hat{a}_m^\dagger \hat{a}_m e^{iqma}. \tag{10.5}$$

To simplify the notation and to have a better physical understanding of the excitations induced by the Bragg perturbation, it is convenient to introduce the quasimomentum field operator $\hat{b}_k$ which annihilates an atom with quasimomentum k, and is defined as the Fourier transform of the field operator $\hat{a}_n$, i.e., $\hat{b}_k = \frac{1}{\sqrt{M}} \sum_{n=1}^{M} e^{ikna} \hat{a}_n$. The quasimomentum k can assume only discrete values which are integer multiples of $\frac{2\pi}{Ma}$.

In the quasimomentum basis the operator $\hat{\rho}_q^\dagger$ can be written as

$$\hat{\rho}_q^\dagger = I_q \sum_{k=0}^{M-1} \hat{b}_{k+q}^\dagger \hat{b}_k, \tag{10.6}$$

where we have assumed that q can be also expressed as an integer multiple of $\frac{2\pi}{Ma}$. By writing the Bragg perturbation potential in the quasimomentum basis it can be seen that the two means by which momentum is imparted to the atomic sample,is either by promoting an atom from quasimomentum k to $k+q$ or by demoting a particle with momentum k to $k-q$.

10.2 Observables

Useful experimental observables in Bragg spectroscopy are related to the density-density response function. Here we focus our attention on the imparted momentum and energy, which can be measured by time-of-flight techniques. In this section we elaborate on the form of these observables.

In the tight-binding approximations the total momentum is given by

$$\hat{P} = \sum_k \hbar k \hat{b}_k^\dagger \hat{b}_k. \tag{10.7}$$

From the Heisenberg equations of motion we get

$$\begin{aligned} \frac{d\hat{P}}{dt} &= \frac{i}{\hbar}\left[\hat{H},\hat{P}\right] = \frac{i}{\hbar}\left(\left[\hat{H}_B,\hat{P}\right] + \left[\hat{H}_o,\hat{P}\right]\right) & (10.8)\\ &= -\frac{iqV_o}{2}(\hat{\rho}_q^\dagger e^{-i\omega t} - \hat{\rho}_q e^{i\omega t}) - 2\Omega\hat{X}. & (10.9) \end{aligned}$$

where $\hat{H}$ is the total Hamiltonian, $\hat{H} = \hat{H}_o + \hat{H}_B$, and $\hat{X}$ is the center of mass position given by $\hat{X} = \sum_n (na)\hat{a}_n^\dagger \hat{a}_n$. The second term in the momentum rate equation is just related to the force felt by atoms due to the presence of an harmonic external confinement. On the other hand, the first term takes into account the rate of change of the momentum due to the Bragg perturbation. If the perturbation is applied for a time short compared to the oscillator period $t_{osc}=\frac{2\pi}{\sqrt{4J\Omega a}}$ the second term in the right-hand-side is small and can be neglected in the calculations.

The energy change rate is

$$\begin{aligned} \frac{d\hat{H}_o}{dt} &= \frac{i}{\hbar}\left[\hat{H}_B,\hat{H}_o\right] = \frac{i}{\hbar}\left[\hat{H}_B,\hat{H}\right], & (10.10)\\ &= -\frac{1}{2}V_o\left(e^{-i\omega t}\frac{d\hat{\rho}_q^\dagger}{dt} + e^{i\omega t}\frac{d\hat{\rho}_q}{dt}\right). \end{aligned}$$

Because the energy of a closed system is conserved, as opposed to the momentum rate equation, the energy change rate is independent of the magnetic potential and only depends on the applied Bragg perturbation.

10.3 Linear response

The first order variation $\delta\langle\hat{O(t)}\rangle$ of the thermal average of an observable $\hat{O(t)}$ with respect to its mean value due to a weak perturbation $\hat{H}_B$ applied to a system at $t = t_o$, is given by the Kubo formula [51]

$$\delta\left\langle\hat{O}(t)\right\rangle = \frac{i}{\hbar}\int_{t_o}^{t} d\tau\left\langle\left[\hat{H}_B(\tau),\hat{O}(t)\right]\right\rangle, \tag{10.11}$$

where the operators $\hat{O}(t)$ and $\hat{H}_B(\tau)$ are in the Heisenberg representation with respect to the time independent hamiltonian $\hat{H}_o$, and the expectation value is taken using the equilibrium state of the system.

For the particular case where the observables are the momentum and energy rates, we get after some algebra :

$$\begin{aligned}
&\delta\left\langle\frac{d\hat{P}}{dt}\right\rangle = \hbar q\left(\frac{V_o}{2\hbar}\right)^2 \times \qquad (10.12)\\
&\int_{t_o}^{t} d\tau\left(e^{-i\omega(\tau-t)}\left\langle\left[\hat{\rho}_q^\dagger(\tau),\hat{\rho}_q(t)\right]\right\rangle - e^{i\omega(\tau-t)}\left\langle\left[\hat{\rho}_q(\tau),\hat{\rho}_q^\dagger(t)\right]\right\rangle\right.\\
&\left.+e^{-i\omega(\tau+t)}\left\langle\left[\hat{\rho}_q^\dagger(\tau),\hat{\rho}_q^\dagger(t)\right]\right\rangle - e^{i\omega(\tau+t)}\left\langle[\hat{\rho}_q(\tau),\hat{\rho}_q(t)]\right\rangle\right) - 2\Omega\delta\left\langle\hat{X}\right\rangle,\\
&\delta\left\langle\frac{d\hat{H}}{dt}\right\rangle = -\frac{i}{\hbar}\left(\frac{V_o}{2}\right)^2 \times \qquad (10.13)\\
&\int_{t_o}^{t} d\tau\left(e^{-i\omega(\tau-t)}\frac{d}{dt}\left\langle\left[\hat{\rho}_q^\dagger(\tau),\hat{\rho}_q(t)\right]\right\rangle - e^{i\omega(\tau-t)}\frac{d}{dt}\left\langle\left[\hat{\rho}_q(\tau),\hat{\rho}_q^\dagger(t)\right]\right\rangle\right.\\
&\left.+e^{-i\omega(\tau+t)}\frac{d}{dt}\left\langle\left[\hat{\rho}_q^\dagger(\tau),\hat{\rho}_q^\dagger(t)\right]\right\rangle - e^{i\omega(\tau+t)}\frac{d}{dt}\left\langle[\hat{\rho}_q(\tau),\hat{\rho}_q(t)]\right\rangle\right).
\end{aligned}$$

We now introduce the functions $S(q,\omega)$ and $R(q,\omega)$ given by

$$\left\langle\hat{\rho}_q^\dagger(\tau)\hat{\rho}_q(t)\right\rangle = \int e^{-i\omega(\tau-t)}S(q,\omega)d\omega, \tag{10.14}$$

$$\left\langle\hat{\rho}_q^\dagger(\tau)\hat{\rho}_q^\dagger(t)\right\rangle = \int e^{i\omega(\tau+t)}R(q,\omega)d\omega. \tag{10.15}$$

In terms of these functions it can be seen that since $\left\langle\left[\hat{\rho}_q^\dagger(\tau),\hat{\rho}_q^\dagger(t)\right]\right\rangle = \left\langle\left[\hat{\rho}_q(\tau),\hat{\rho}_q(t)\right]\right\rangle = 0$ Eq. (10.13) and Eq. (10.14) reduce to:

$$\begin{aligned}
\delta\left\langle\frac{d\hat{P}}{dt}\right\rangle &= 2\hbar q\left(\frac{V_o}{2\hbar}\right)^2\int d\omega'\left(S(q,\omega') - S(-q,-\omega')\right)\times\\
&\left(\frac{\sin\left((\omega-\omega')t\right)}{(\omega-\omega')}\right) - 2\Omega\delta\left\langle\hat{X}\right\rangle,
\end{aligned}$$

$$\delta\left\langle\frac{d\hat{H}}{dt}\right\rangle = \frac{2}{\hbar}\left(\frac{V_o}{2}\right)^2\int d\omega'\omega'\left(S(q,\omega')-S(-q,-\omega')\right)\times \left(\frac{\sin\left((\omega-\omega')t\right)}{(\omega-\omega')}\right). \tag{10.16}$$

where we have set $t_o = 0$. The quantity $S(q,\omega)$, the Fourier transform of density correlations, is the so called *dynamic structure factor* and is given by

$$S(q,\omega) = \frac{1}{Z}\sum_{ij} e^{-\beta E_i}\left|\langle i|\,\hat{\rho}_q\,|j\rangle\right|^2\delta(\omega-\omega_{ij}) \tag{10.17}$$

$$\equiv \sum_{ij} S_{ij}(q)\delta(\omega-\omega_{ij}). \tag{10.18}$$

where $|i\rangle$ and E_i are eigenstates and eigenenergies of the unperturbed Hamiltonian, $e^{-\beta E_i}$ is the usual Boltzmann factor with $\beta = 1/k_BT$ where k_B is Boltzmann's constant and T the temperature, Z is the canonical partition function, $\hbar\omega_{ij} = E_j - E_i$ and $S_{ij}(q) \equiv \frac{1}{Z}e^{-\beta E_i}\left|\langle i|\,\hat{\rho}_q\,|j\rangle\right|^2$.

Notice that because atoms could be scattered by absorbing a photon from either one of the laser beams the response of the system is determined not only by $S(q,\omega)$ but by the combination $S(q,\omega') - S(-q,-\omega')$. If the perturbation is applied for a time long with respect to the frequency of the applied field the momentum and energy rates approach the golden rule results.

Performing the frequency integration we get

$$\delta\left\langle\frac{d\hat{P}}{dt}\right\rangle = 2\hbar q\left(\frac{V_o}{2\hbar}\right)^2\sum_{ij}\left(S_{ij}(q)\left(\frac{\sin\left((\omega-\omega_{ij})t\right)}{\omega-\omega_{ij}}\right) - S_{ij}(-q)\left(\frac{\sin\left((\omega+\omega_{ij})t\right)}{\omega+\omega_{ij}}\right)\right) - 2\Omega\delta\left\langle\hat{X}(t)\right\rangle, \tag{10.19}$$

$$\delta\left\langle\frac{d\hat{H}}{dt}\right\rangle = 2\left(\frac{V_o}{2\hbar}\right)^2\sum_{ij}\hbar\omega_{ij}\left(S_{ij}(q)\left(\frac{\sin\left((\omega-\omega_{ij})t\right)}{\omega-\omega_{ij}}\right) + S_{ij}(-q)\left(\frac{\sin\left((\omega+\omega_{ij})t\right)}{\omega+\omega_{ij}}\right)\right). \tag{10.20}$$

The total momentum and energy transfer after applying the Bragg perturbation can be obtained by integrating the above equations. We get as a final result that

$$\delta\left\langle \hat{P}\right\rangle = \hbar q\left(\frac{V_o}{\hbar}\right)^2\sum_{ij}\left(S_{ij}(q)\left(\frac{\sin\left((\omega-\omega_{ij})\tau/2\right)}{\omega-\omega_{ij}}\right)^2\right. \tag{10.21}$$
$$\left. -S_{ij}(-q)\left(\frac{\sin\left((\omega+\omega_{ij})\tau/2\right)}{\omega+\omega_{ij}}\right)^2\right) - 2\Omega/a\int_0^\tau \delta\left\langle \hat{X}(t)\right\rangle dt$$

$$\delta\left\langle \hat{H}\right\rangle = \left(\frac{V_o}{\hbar}\right)^2\sum_{ij}\hbar\omega_{ij}\left(S_{ij}(q)\left(\frac{\sin\left((\omega-\omega_{ij})\tau/2\right)}{\omega-\omega_{ij}}\right)^2\right. \tag{10.22}$$
$$\left. +S_{ij}(-q)\left(\frac{\sin\left((\omega+\omega_{ij})\tau/2\right)}{\omega+\omega_{ij}}\right)^2\right),$$

where τ is the duration of the perturbation.

10.4 Zero-temperature regime

10.4.1 Bogoliubov approach

In this section we use the zero temperature Bogoliubov approximation for atoms in an optical lattice to study the dynamical structure factor in the superfluid regime. Because quadratic approximations were discussed in detail in in chapter 5, we refer the reader to this chapter for details.

Under the Bogoliubov approximation the field operator at lattice site n is written as a complex number z_n plus small fluctuations $\hat{\delta} = \sum_{s\neq\mathbf{0}}^{M}(u_n^s\widehat{\alpha}_s - v_n^{*s}\widehat{\alpha}_s^\dagger)$, with $\{u_n^s, v_n^s\}$ the quasiparticle amplitudes. Using this ansatz in Eq.(10.17) we get an expression for the dynamical structure factor given by

$$S^{T=0}(q,\omega) = S_0(q)\delta(\omega) + \sum_i S_i(q)\delta(\omega-\omega_i^B), \tag{10.23}$$

$$S_0(q) \equiv \left|\sum_{n=1}^{M}|z_n|^2 e^{iqan}\right|^2, \tag{10.24}$$

$$S_i(q) \equiv \left|\sum_n (z_n u_n^{*i} - z_n^* v_n^{*i})e^{iqan}\right|^2. \tag{10.25}$$

Translationally invariant system

To understand many-body effects included in the Bogoliubov approximation we start by studying the case of a translationally invariant lattice ($V_n = 0$) with N atoms, M wells and periodic boundary conditions. Using the results for the quasiparticle amplitudes and energies calculated using the improved Popov approximation, which was shown to be the best quadratic approximation we get:

$$S(q,\omega) = N^2\delta(\omega) + Mn_o\frac{\varepsilon_q}{\omega_q^B}\delta(\omega-\omega_q^B/\hbar) \quad (10.26)$$

$$= N^2\delta(\omega) + Mn_oS(q)\delta(\omega-\omega_q^B/\hbar), \quad (10.27)$$

with n_o given by Eq. (5.136), $\varepsilon_k = 4J\sin^2(ak/2)$ and $\omega_k^B = \sqrt{\varepsilon_k^2 + 2nU\varepsilon_k}$. Here n is the total density $n = N/M$. Notice that due to the translational invariance of the system, the quasimomentum is a good quantum number and only quasiparticle states that have the same quasimomentum as the transferred momentum q are excited.

For small q, the structure factor behaves like $\sqrt{\frac{J}{2Un}}q$ which is just the free particle expression with the bare particle mass m replaced by the effective mass, $m^* = \hbar^2/2Ja^2$ (a the lattice spacing). Suppression of $S(q)$ in the phonon regime is a direct consequence of the importance of quantum correlations in the long wave-length limit. On the other hand, away from the phonon regime, the presence of the optical lattice changes the behavior of $S(q)$ in a drastic way. As opposed to the free case where at high transferred momenta $\omega_q^B \sim q^2$ and $S(q)$ approaches one, the periodic potential modifies the single particle dispersion relation, which becomes always bounded by $4J$. The term proportional to $2nU\varepsilon_k$ dominates even at high momenta and many-body effects play a crucial role.

In Fig.10.2 we show the energy $\delta\langle\hat{H}\rangle$ imparted to the system as a function of the frequency ω of the Bragg probe, for different values of and U/J and of the momentum q. The blue curve corresponds to the solution using the Bogoliubov approximation and the red one to the solution obtained by the exact diagonalization of the Bose-Hubbard Hamiltonian. The number of lattice sites and wells used in the plots were $M = N = 9$. For $U/J = 0.001$ the Bogoliubov and exact curves perfectly overlap. The agreement is expected as the non-interacting Hamiltonian is quadratic and therefore exactly matches the Bogoliubov Hamiltonian. The almost non interacting regime may be experimentally achieved by varying the onsite interaction energy U independently of J, by means of a Feshbach resonance that changes the scattering length [20, 21]. For $U/J = 1$ the agreement is good only for the low momentum $q = 2\pi/9$. The agreement for low momenta can be understood by the fact that for low q the Bragg spectroscopy is probing the long wave-length modes. These modes have a phonon-like dispersion relation and are almost not affected by the presence of the lattice. In general Bogoliubov quasi-particle states correspond to solutions of the approximate Hamiltonian with a plane-wave character which are only valid in the weakly interacting regime. As quantum correlations become important, the exact eigenstates of the interacting system do not necessarily have the simple plane wave character,(see Ref. Lieb and Liniger [149]), especially in the commensurate filling situation where for a critical value of U/J the system exhibits the superfluid-Mott insulator transition. However the unit filled commensurate case is the worse scenario, and as discussed in chapter 5, for non commensurate fillings or commensurate systems with larger

filling factor we expect the validity of the Bogoliubov approximation to extend over a larger range of U/J values.

As a final remark, it is important to point out that the small oscillations in Fig. 10.2 are due to the square shape of the applied Bragg pulse. These oscillations would disappear if instead a pulse with Gaussian profile is applied.

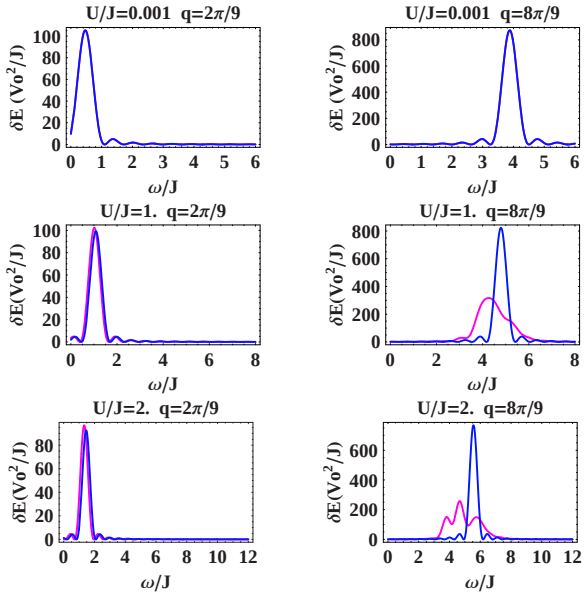

Figure 10.2: Imparted energy: Comparisons between the the exact and Bogoliubov approximation for $N = M = 9$. The horizontal axis is in units of $\hbar$. For the plot we used $J\tau/\hbar = 10$. See text Eq. (10.23).

10.4.2 Inhomogeneous system

Using the quasiparticle amplitudes derived under the T.F. approximation (see section 5.6.2), we get an expression for the dynamical structure factor given by

$$\begin{aligned} S(q,\omega) &= 9N^2 \left(\frac{\sin(x) - x\cos(x)}{x^3} \right)^2 \delta(\omega) \\ &+ \frac{\hbar\omega^*}{8U} \sum_i (i(i+1)(2i+1)) |\widetilde{P}_i(x)|^2 \delta(\omega - \omega^* \sqrt{i(i+1)/2}) \end{aligned} \quad (10.28)$$

where $x \equiv qaR_{TF}$ and $\widetilde{P}_n(x) = \int_{-1}^{1} P_n(u) e^{iux} du$.

An alternative way to calculate the dynamical structure factor is to use the so called local density approximation (LDA). This approximation is valid for large condensates, where the density profile varies in a smooth way and the system behaves locally as an uniform gas. Using a LDA the dynamical structure factor can be written as

$$S_{LDA}(q,\omega) = \left(\sum_m z(m)e^{iqam}\right)\delta(\omega) + \varepsilon_s \sum_m \frac{|z(m)|^2}{\hbar\omega_q^B(m)}\delta(\hbar\omega - \omega_q^B(m)). \quad (10.29)$$

Here $\omega_q^B(m)$ is the local homogeneous Bogoliubov dispersion relation with n replaced by the local density in the trap. The LDA ignores the Doppler effect associated with the spreading of the momentum distribution of the condensate and therefore it is not valid for large momentum transfers.

To test the validity of the HFB-Popov approximation to describe the energy imparted to the system by Bragg spectroscopy in the trapped case we use a system with 11 lattice sites and 9 atoms. Unfortunately for such a small number of atoms and wells the assumptions under which the analytic Thomas Fermi expressions were developed, i.e. large number of atoms and smooth variations of the density profile, do not apply. Therefore for the case with $M = 11, N = 9$ we restrict ourselves to comparisons between numerical solutions of the HFB-Popov equations and solutions found by the exact diagonalization of the many-body Hamiltonian. We solve numerically Eqs.(5.113) -(5.117) to obtain the quasi-particle energy and amplitudes. We then use them to calculate the imparted energy. In the presence of the trap, the number of occupied wells for a fixed number of atoms depends on the trap frequency, particles are not necessarily uniformly distributed throughout the lattice, and therefore commensurability is only meaningful locally. This explains why in contrast to the commensurate homogeneous system, the agreement between the two solutions is good up to $U/J = 5$ for the chosen parameters, as shown in Fig. 10.3. The failure of the HFB-Popov approximation for $U/J \sim 10$ can also be observed in the density plots, as shown in Fig. 10.4.

The multiple peaks depicted in the plots are due to the external trapping potential, which not only discretizes the spectrum but also changes the plane wave character of the quasiparticle amplitudes. Therefore, for a given transfer momentum q different quasiparticle modes can be excited. In Fig.10.3, we explicitly show with a line the position of the quasiparticle energies.Similar to the homogeneous case, the lower the transfer momentum q, the better is the agreement between the HFB-Popov results and the exact solution.

For small systems such as the one in consideration discretization effects can not be ignored. On the other hand, if the inverse of the transfer momentum is bigger than the size of the condensate wave function, then to first approximation the discretization in the excitation spectrum can be safely ignored and the system can be treated as locally uniform. Instead of distinguishable peaks the response curve becomes smooth.

To explore the validity of Eq.(10.28) derived under the Thomas-Fermi approximation we plot in Fig. 10.5 $S(q,\omega)$ vs. ω for different transfer momenta. The parameters used for the plot were $U/J = 0.2$, $\Omega/J = 9.5 \times 10^{-4}$ and $N = 100$. For these parameters we believe the HFB-Popov should give a good description of the system. In chapter 5 we showed that in the regime when the TF approximation is valid, it gives a very good description of the low lying excitations. However it fails

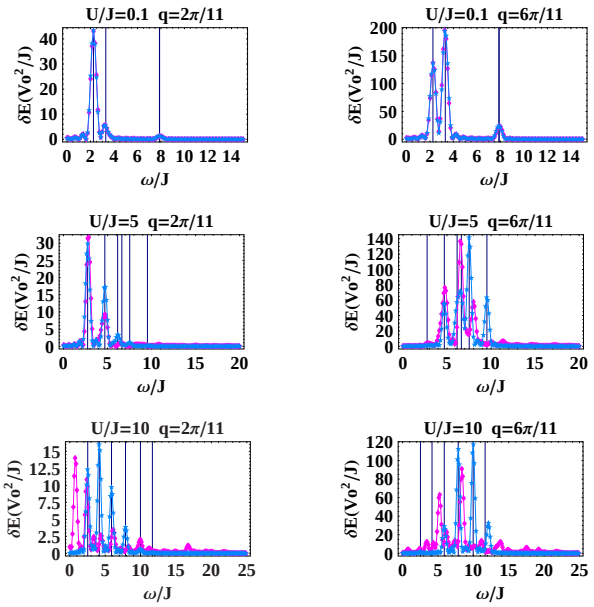

Figure 10.3: Comparisons of the imparted energy vs. Bragg frequency curves calculated from the exact diagonalization of the manybody Hamiltonian (red) and the from the HFB-Popov approximation(blue) for a trapped system with $N = 9$, $M = 11$ and $\Omega/J = 1.875$. The horizontal axis is in units of $\hbar$. The lines depicted in the plot are located at the different quasiparticle energies excited by the Bragg perturbation.

to describe high energy modes. To illustrate this issue we compare in Fig. 10.6 the TF excitation spectrum with the one found by solving the HFB-Popov Equations. The quasiparticle energies are labelled in increasing energy order. When the Thomas-Fermi approximation is used in $S(q, \omega)$, we expect then to obtain a fair description of it only if low-lying modes are probed. Low-lying modes are probed if the inverse of the transfer momentum q^{-1} is big compared to the size of the condensate wave function. This is explicitly shown in Fig. 10.5, where only for small values of q the two solutions agree. For higher Bragg momenta, $qR_{TF} > 1$, higher modes contribute to $S(q/\omega)$ and the TF approximation gives a poor description of $S(q, \omega)$.

10.5 Mott insulator regime

In this section we derive expressions for the zero temperature dynamical structure factor in the Mott regime for both the homogeneous and trapped systems and compare them with the solutions obtained by exact diagonalization of the Bose-Hubbard Hamiltonian.

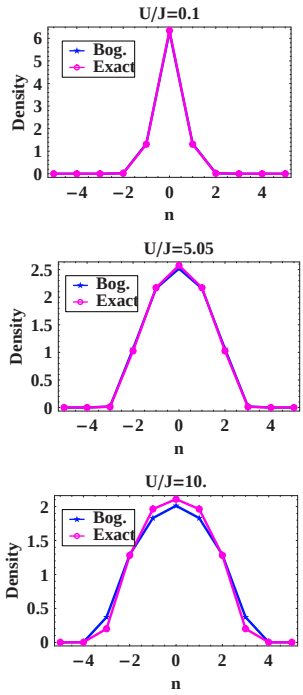

Figure 10.4: Density profile calculated from the exact diagonalization of the many-body Hamiltonian (red) and from the HFB-Popov approximation (blue) for a trapped system with $N = 9$, $M = 11$ and $\Omega/J = 1.875$. n labels the lattice site.

10.5.1 Commensurate homogeneous system

In this section we assume a commensurately filled lattice with filling factor $N/M = g$, periodic boundary conditions and a parameter regime where $U \gg J$. Using the eigenvalues and eigenstates calculated in section 9.1 with first order perturbation theory in the high filling factor limit, we get an expression for the dynamical structure factor given by

$$S^{(T=0)}(q,\omega) = N^2\delta(\omega)\delta_{q0} + \frac{J^2 g(g+1)}{\hbar U^2} \times \tag{10.30}$$

$$\sum_{r,R} \delta(\hbar\omega - E^{(1)}_{rR}) \left| \sum_{m=1}^{M} e^{iqam} \left(C^{rR}_{mm+1} + C^{rR}_{mm-1} - C^{rR}_{m+1m} - C^{rR}_{m-1m} \right) \right|^2$$

$$= N^2\delta(\omega)\delta_{q0} + \frac{32J^2 g(g+1)}{\hbar U^2} \sin^2\left(\frac{qa}{2}\right) \sum_{r}{}' \sin\left(\frac{\pi r}{M}\right)^2 \delta(\hbar\omega - E^{(1)}_{r\widetilde{q}}) \tag{10.31}$$

with $qa = 2\pi\widetilde{q}/M$, and the prime in the sum meaning that it is constrained over the r's with $\widetilde{q}+r$ even. Is important to emphasize that only the states with $R = 0$

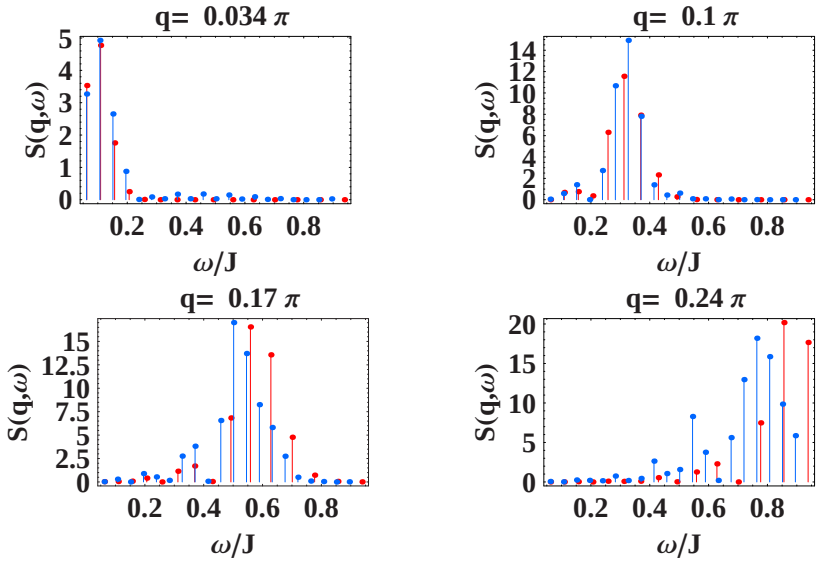

Figure 10.5: Dynamical structure factor vs. $\hbar\omega/J$ in the Thomas-Fermi (blue) and HFB-Popov (red) approximations. The horizontal axis is in units of $\hbar$. The system parameters are $U/J = 0.2$, $\Omega/J = 9.5 \times 10^{-4}$ and $N = 100$.

have a dispersion relation which agrees to first order in J to the mean-field solution found in Ref. [151]. However, these states give zero contribution to the sum of Eq. (10.31).

In Fig. 10.7 we compare the imparted energy as a function of the Bragg frequency calculated using the expression of the dynamical structure factor Eq. (10.31) to results obtained by the exact diagonalization of the Bose-Hubbard Hamiltonian with parameters $N = M = 9$ and $U/J = 45$. We show the response for two different Bragg momenta $q = 2\pi/9$ and $8\pi/9$. In contrast to the superfluid regime, where Bragg spectroscopy excites only the quasiparticle state with quasimomentum q, in the Mott regime we observe $M - 1$ peaks centered around U. The different peaks are due to the two dimensional character of the 1-ph dispersion relation. The Bragg momentum q fixes one quantum number R but the other can take $M - 1$ different values. In the analytic solution due to the constraint in Eq. (10.31), $\widetilde{q} + r$ even, only $(M - 1)/2$ of the possible $M - 1$ peaks are present. The constraint is a consequence of the extra symmetry introduced in the high filling factor solution where similar "effective masses" are assumed. Nevertheless, Fig. 10.7 shows that even in the situation with $g = 1$, the peaks captured by the analytic solution are the most relevant ones. As g is increased, as long as the perturbation analysis is valid, we expect even better agreement. The interval of frequencies over which the system responds has an approximate width of $4J(2g+1)\cos(qa/2)$. The $\cos(qa/2)$ dependence indicates that as q approaches π the response width is minimized. This behavior can be observed in Fig. 10.7, when we plot the response

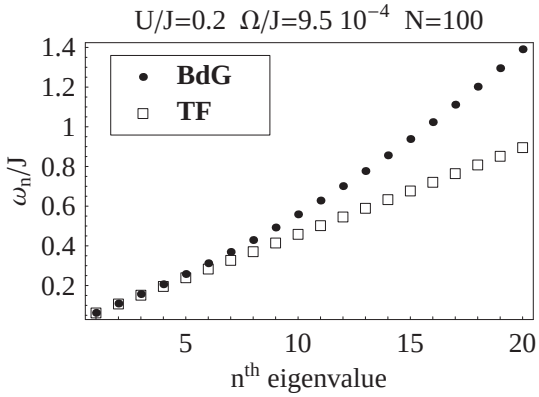

Figure 10.6: Eigenvalues of the quasiparticle spectrum plotted in increasing energy order. The vertical scale is in units of $\hbar$

for $q = 8\pi/9$. It is important to point out that the presence of distinguishable peaks in Fig. 10.7 is a result of the finite system size. As the number of lattice sites is increased, more peaks are contained in the interval $4J(2g+1)\cos(qa/2)$. The separation between one peak and the next decreases and instead of individual peaks a continuous envelope is approached.

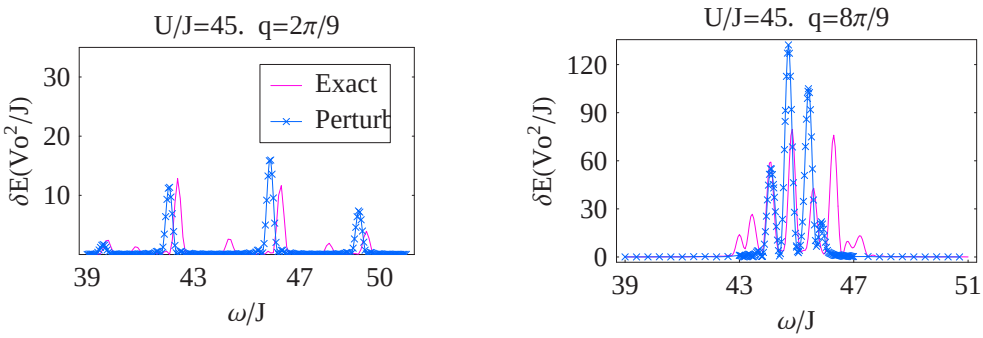

Figure 10.7: Transfer energy vs. Bragg frequency for a zero temperature homogeneous system with $M = N = 9$ and different transfer momenta q. The horizontal axis is in units of $\hbar$. The perturbation time was set to $J\tau/\hbar = 10$. Note the change of the vertical scale between the two panels.

10.5.2 Inhomogeneous system

In this section we consider a one dimensional optical lattice in the presence of a magnetic confinement. We assume that the magnetic trap has its minimum at the lattice site $n = 0$. In the regime where $U > \frac{\Omega(N-1)^2}{4}$ and $\Omega N > J$ assuming an odd number of atoms, we can use the eigenvalues and eigenmodes derived to first order

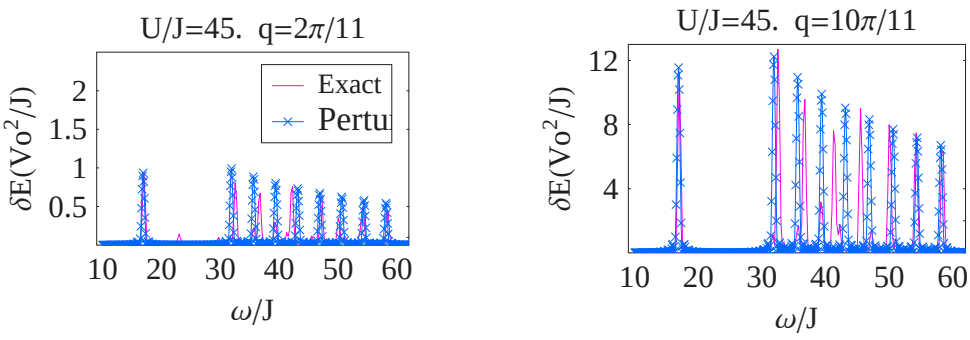

Figure 10.8: Transfer energy vs. Bragg frequency for a zero temperature trapped system with parameters U/J=45, $\Omega/J = 1.857$, $M = 11$ and $N = 9$ and different transfer momenta q. The horizontal axis is in units of $\hbar$. The perturbation time was set to $J\tau/\hbar = 10$. Note the change of the vertical scale between the two panels.

in perturbation theory in section 9.2 in the expression for the dynamical structure factor to get:

$$S^{(T=0)}(q,\omega) = N^2\delta(\omega)\delta_{q0} + \frac{8J^2\sin^2(qa/2)}{\hbar(N\Omega)^2}\delta(\hbar\omega - N\Omega)$$
$$+ \sum_{m=-L}^{L-1} \frac{16J^2\sin^2(qa/2)}{\hbar(U-\Omega(1+2m))^2}\delta(\hbar\omega - U + \Omega(1+2m)), \qquad (10.32)$$

where $L = (N-1)/2$. In Fig. 10.8 we plot the imparted energy as a function of the Bragg frequency $\hbar\omega$ and Bragg momenta $q = 2\pi/11$, $10\pi/11$. The system parameters are $\Omega = 1.8J$, $U/J = 45$, $M = 11$ and $N = 9$. We observe nine peaks both in the perturbative and exact solutions. The peak at lower frequency, $N\Omega \approx 18J$, is described by the first term in Eq. (10.32) and corresponds to the two degenerated 1-hh excitations created when a hole tunnels into one of the most externally occupied sites. The other $N-1$ peaks, separated by Ω, are described by the second term in Eq. (10.32) and correspond to the 1-ph excitations with the particle and hole at adjacent lattice sites. To explicitly show the $\sin(qa/2)$ dependence of the response of the system, we plot the imparted energy for two different transfer momenta q, one close to zero the other close to π. Even in the presence of the trap $S(q,\omega)$ tends to 0 as $q$approaches an integer value of 2π.

If the number of atoms is even, the trap symmetry is broken and the ground state becomes degenerated. To first order in perturbation theory the dynamical structure factor in this case is given by

$$S^{(T=0)}(q,\omega) = 2N^2\delta(\omega)\delta_{q0} + 8J^2\sin^2(q/2)\left(\frac{\delta(\hbar\omega-(N+1)\Omega)}{\hbar((N+1)\Omega)^2}\right.$$
$$\left.+\frac{\delta(\hbar\omega-(N-1)\Omega)}{\hbar((N-1)\Omega)^2} + 4\sum_{m=N/2}^{N/2-1}\frac{\delta(\hbar\omega-(U-\Omega(1+2m))}{\hbar(U-\Omega(1+2m))^2}\right). \quad (10.33)$$

In this case instead of a single excitation peak at $\hbar\omega = N\Omega$ we have two almost degenerate peaks at $\hbar\omega = (N \pm 1)\Omega$. Apart from this, the response of the system is analogous to the odd number case.

All the previous analysis was done for the case $\Omega N > J$. This can be a significant constraint if the total number of atoms is large. In the opposite case when $\Omega N < J$ but still $U > \Omega(N/2)^2$, the energy splitting between one particle hole excitations is small and degenerate perturbation theory must be used at first order. In this case the system can be divided in a central unit filled core, which to a good approximation has a response which can be described by the commensurate homogeneous results, surrounded by a superfluid region whose excitations are mainly due hole hopping excitations. We expect that the response to Bragg spectroscopy of the system in this parameter regime has peaks localized around U, which probes the one particle hole excitation band analogous to the commensurate translationally invariant case. We also expect lower frequency peaks around ΩN associated with hole hopping excitations inside the superfluid region that surrounds the unit filled central core.

Be aware that the parameter regime chosen for all the plots in the Mott phase lies in the regime where first order perturbation theory is valid and therefore peaks at $2U$ due to higher order excitations are suppressed even in the exact numerical results.

10.6 Finite temperature

In most of the experiments the way to load ultra-cold atoms in an optical lattice is by first forming a Bose-Einstein condensate in a weak magnetic trap and then adiabatically turning on the lattice by slowly ramping up the intensity of the laser beams. Ideally this kind of process should end up with the atoms in the many-body ground state.However, that the Bose-Einstein condensate used as a starting point is not produced exactly at $T = 0$, and the final temperature is not trivially related to the initial one. It has been shown [150] that even for an ideal non interacting gas there are different regimes where the atomic sample can be significantly heated or cooled by adiabatically changing the lattice depth. The role of interactions is and how many-body effects affect the final temperature of the sample are not yet well understood.

Besides this issue, there remains the point of how long one must wait to be truly adiabatic with respect to many-body excitations. Interactions are essential for establishing equilibrium in the system, and understanding them in detail will

be really important to determine the time scales for adiabatic loading. For a deep lattice the tunneling rate seems to be the most restrictive time scale for maintaining adiabaticity. If adiabaticity were determined by the tunneling time $\hbar/J$, it would be very hard to be satisfied experimentally because J decreases exponentially with the lattice depth.

Because of these issues, it would be very interesting from an experimental point of view to have a mechanism for determining the temperature of the system. What we show in this section is that Bragg spectroscopy could give information about the temperature, at least deep in the Mott regime. As we did for the zero temperature case, we start by describing the superfluid case, then the deep Mott insulator case, and finally showing numerical calculations in the regime where the Mott transition takes place.

- Superfluid Regime

  At finite temperature both quantum and thermal fluctuations contribute to the depletion of the condensate. We expect the Bogoliubov approach to be a good description of the many-body system for moderate lattice depths and small thermal depletion. At finite temperature the occupation number of a quasiparticle state is determined by Bose statistics, $n_s = \left\langle \hat{\alpha}_s^\dagger \hat{\alpha}_s \right\rangle$ with n_s the Bose distribution function $n_s = \frac{1}{e^{\beta\omega_s^B}-1}$. Taking into account thermal depletion, the expression for the dynamical structure factor is

$$\begin{aligned} S(q,\omega) &= S_0(q)\delta(\omega) + \sum_i (n_i+1) S_i(q)\delta(\omega-\omega_i^B) \\ &\quad + \sum_i n_i S_i(-q)\delta(\omega+\omega_i^B) \end{aligned} \tag{10.34}$$

  with $S_0(q)$ and $S_i(q)$ defined in Eqs. (10.24) and (10.25).

  Even though the finite temperature dynamic structure factor is in fact different from the zero temperature one, observables such as the imparted momentum and imparted energy do not depend on $S(q,\omega)$ but on $S(q,\omega) - S(-q,-\omega)$. This difference is independent of the temperature, at least at the order of approximation at which Eq.(10.34) was calculated [15, 147, 148].

  Therefore, Bogoliubov analysis shows that, provided the temperature is sufficient low and the interactions are weak enough that Eq.(10.34) is valid, Bragg spectroscopy is not a good method for determining the temperature of the gas.

- Mott Regime

  In the homogeneous Mott phase all the 1-ph excitations have an energy separation of order U from the ground state but splitting between them of order J. If the temperature of the system is $k_B T \gtrsim U/5$, 1-ph excitations begin to

contribute to the dynamical structure factor (Eq. (10.17)) and it starts to develop frequency peaks at frequencies resonant with the energy difference between two 1-ph excitations. These peaks survive even when the difference, $S(q,\omega) - S(-q,-\omega)$, is taken and therefore when Bragg spectroscopy is performed a small frequency response is observed. In the presence of the trap the analysis is more complicated because also n-hh excitations have to be taken into account. The relevant temperature scale in this case is $k_B T \gtrsim \Omega N/5$ and the small frequency peaks probe the energy difference between two n-hh, two 1-ph or one n-hh and one 1-ph excitations.

In Figs. 10.9 and 10.10 we plot the imparted energy as a function of the Bragg frequency calculated from the exact diagonalization of the Bose-Hubbard Hamiltonian for different temperatures and different ratios of U/J. In Fig. 10.9 we use a homogeneous system with $N = M = 9$ and in Fig. 10.10 a trapped system with $N = 9$, $M = 11$ at different temperatures. The response is consistent with the previous analysis: a response almost independent of the temperature in the superfluid regime and the appearance of low energy Bragg peaks in the Mott regime. We observe some dependence on the temperature in the intermediate region but it is not as pronounced as the one observed deep in the Mott regime.

10.7 Conclusions

In recent experiments [145], Bragg spectroscopy was performed using a setup where the laser beams for the Bragg perturbation were the same as those used to create the lattice potential, and the response was observed. Previous linear response analysis done for translationally invariant systems [148, 151]) found no scattering when the Bragg momentum equals the lattice momentum. In ref. [151], the authors attributed the signal observed in the experiments to nonlinear response or to effects of inhomogeneity or finite system size. Our linear response calculations considering small trapped systems still show no scattering at $q = 2\pi/a$ and therefore indicate nonlinear response as the most plausible explanation for the experimental results. The validity of a linear response treatment can be checked by verifying the linear dependence of the Bragg signal upon the intensity of the Bragg beams.

In summary, we have studied the linear response of cold atoms loaded in a one dimensional optical lattice to Bragg spectroscopy and showed that it can be used to probe the excitation spectrum of the system, with and without harmonic confinement. In the superfluid regime we showed the validity of the Bogoliubov approximation to describe the very weakly interacting regime and its breakdown as quantum correlations become important. A new theory beyond the simple Bogoliubov approximation is required to describe regimes beyond the very weakly interacting one. In the Mott insulator phase we showed how Bragg spectroscopy can be used to get information about the excitation spectrum: Bragg peaks are centered around the characteristic Mott excitation gap, contained in an interval whose width is proportional to the 1-ph excitation band width and have an average height which is maximized when the Bragg momentum approaches π/a. In

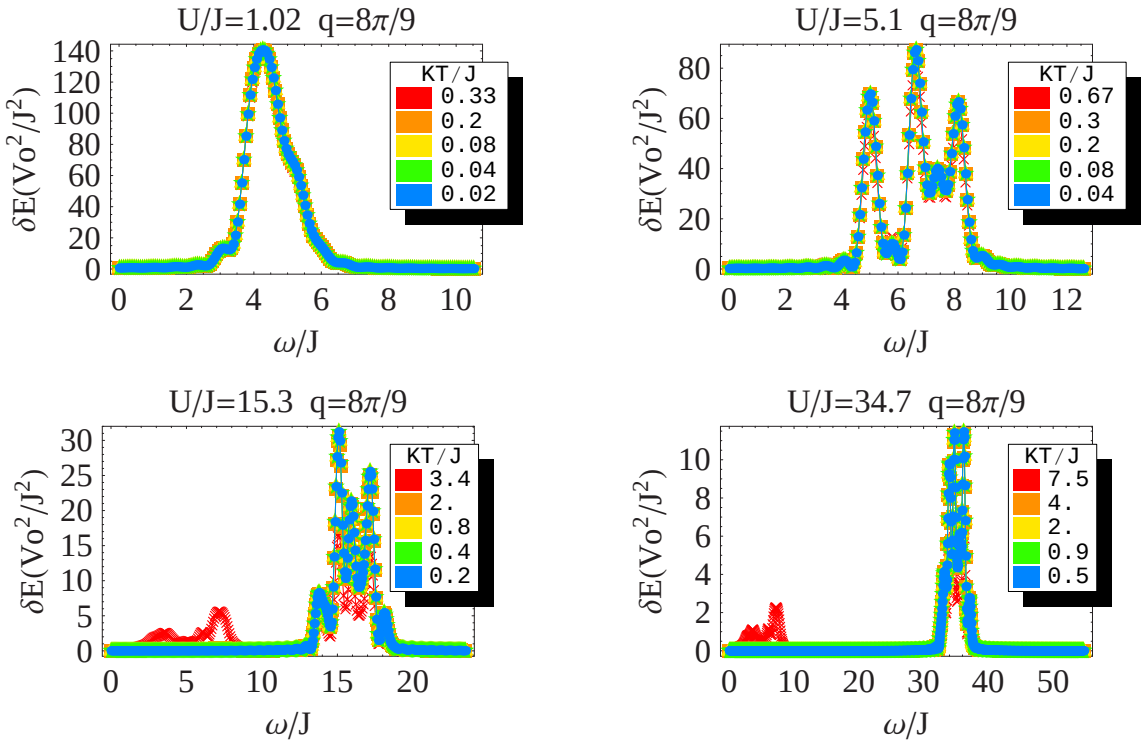

Figure 10.9: Transfer energy as a function of the temperature for different U/J parameters. The plots are for a homogeneous system with $N = M = 9$. The horizontal axis in in units of $\hbar$.

the trapped case, Bragg peaks at lower energy reveal information about 1-hh excitations. Finally, we also discussed how Bragg spectroscopy can be an important experimental tool to determine the temperature of the system in the Mott insulator phase.

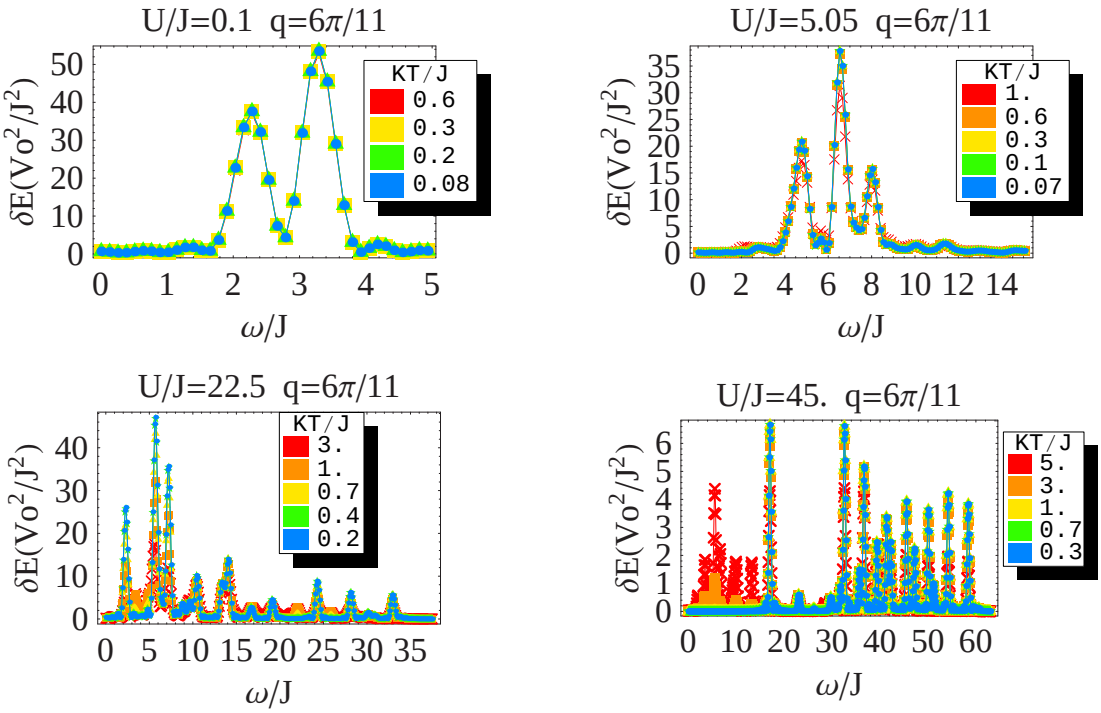

Figure 10.10: Transfer energy as a function of the temperature for different U/J parameters. The plots are for an trapped system with $M = 11$, $N = 9$ and $\Omega/J = 1.875$. The horizontal axis in in units of $\hbar$.

Chapter 11

Scalable register initialization for quantum computing in an optical lattice

The goal of building a quantum computer has spurred tremendous progress in coherent control and measurement of small quantum systems. Neutral atoms in optical lattices have been proposed as a suitable candidate for quantum computing implementation. The appeal of this system stems from the defect-free nature of the lattice potential, and the long coherence times of the constituent atoms. In order to fully realize the promised computational speedup of a quantum device, the underlying system should be scalable to a large number of information carriers or qubits. Indeed, the first two criteria delineated by DiVincenzo [152] for scalable quantum computation are:

- A scalable physical system with well characterized qubits
- The ability to initialize the state of the qubits to a simple fiducial state.

In many systems, the first criterion can be met by increasing the number of storage components for the qubits, e.g. in solid state systems the number of dopant qubits in the bulk material could be increased, in optical lattices the number of trapped atoms could be increases and in ion systems large scale micro-trap arrays have been proposed [153]. There are two main approaches to satisfy the second criterion [152]. One is to allow the system to interact with the environment and "naturally" cool to its ground state and thereafter use this state as the initial state. The other is to actively cool each qubit by projective measurement to a fiducial state $|0\rangle$. A problem arises with these approaches when the ground state of the many body Hamiltonian is not a suitable initial state. This is the case for bosonic qubits embedded in systems with periodic confinement, for example in Josephson junction arrays [154], neutral atoms trapped in electromagnetic micro-traps [155] or optical lattices [46]. For these systems, the underlying dynamics is Bose-Hubbard-like and the ground state contains residual coherences described by

non-zero number fluctuations in each mode. As shown in Eq.(9.8), these fluctuations scale as $gJ/U\sqrt{M}$, so if not corrected, the dynamics will impart a constraint to scalability. In this chapter we show how this can be corrected in two steps, first by introducing an inhomogeneity to the lattice using a quadratic trapping potential and second by projecting out components of the many-body wavefunction with multiply occupied lattice sites by selective measurements on a molecular photo-associative transition. Provided the measurement strength is sufficiently large, the system does not evolve out of the restricted basis and the measurement can maintain a unit filled register for the duration of quantum computation. This strategy allows the Mott insulator transition to become a robust mechanism for register initialization.

11.1 Homogeneous dynamics

It was recognized early on that the Mott insulator transition might be an efficient way to initialize a register of atomic qubits in an optical lattice for use in quantum information processing. A key advantage of loading from a BEC is the availability of an initially high phase space density which can be frozen to the Mott insulator state with atoms occupying most lattice sites. For the homogeneous system ($V_i = 0$), only commensurate fillings give rise to a Mott insulator transition. For the purposes of quantum computation, one particle per well is desirable. In practice, this is difficult to achieve directly because the precise number of atoms is unknown and the lattice strength is not perfectly uniform on the boundaries. There are proposals to prepare unit filled lattices using dissipative techniques involving filling the lattice atom by atom [156] or using Raman side-band cooling [157]. Additionally, it has been shown that one can repair imperfect filling from a BEC via an adiabatic transfer mechanism between two sublevels of each atom [48]. While these techniques can initialize the lattice, any mechanism used to prepare a register of qubits in the unit filled state will suffer a degradation in fidelity, defined as the population in the unit filled state. The degradation comes from the coupling between the desired unit filled state and undesired states that pertain to the exact Mott ground state.

In this section we derive the time dependent fidelity in a homogeneous commensurately filled system prepared at time $t = 0$ in the unit filled Fock state $|T\rangle$ (See Eq.(9.4)). While our results can be generalized to higher dimensions, we consider only a one dimension system. We assume an idealized homogeneous lattice with periodic boundaries and unit filling, $g = N/M = 1$, where N is the number of atoms and M is the number of wells. The regime of interest is the strong coupling limit, where first order perturbation theory is valid. This regime is experimentally achievable in an optical lattice because the tunneling decreases exponentially with the trap depth.

To study the time dependent fidelity at first order in perturbation theory, in principle we have to consider all the $M(M-1)$ eigenmodes that span the one particle hole subspace. However, by translational symmetry only the translationally

invariant states are coupled to $|T\rangle$, and only they have to be considered for the time evolution. As shown in chapter 9, the translationally invariant states inside the one particle hole subspace are the $\lfloor M/2 \rfloor$ states in the subspace, given by:

$$\begin{aligned}
\left|\Phi_r^{(1)}\right\rangle &= \sum_{n,m\neq n}^{M} C_{nm}^r \left|\Psi_{nm}\right\rangle, \\
C_{nm}^r &= \frac{\sqrt{2}}{M} \sin\left(\frac{\pi(2r-1)|n-m|}{M}\right), \qquad (11.1) \\
E_r^{(1)} &= U - 6J\cos\left(\frac{(2r-1)\pi}{M}\right), \quad r = 1, \ldots \lfloor (M)/2 \rfloor. \qquad (11.2)
\end{aligned}$$

The state vector at any time can be written as:

$$|\Psi(t)\rangle = c_0(t)\,|T\rangle + \sum_{r=1}^{\lfloor M/2 \rfloor} c_r(t)\left|\Phi_r^{(1)}\right\rangle \quad \text{with} \quad c_0(0) = 1. \qquad (11.3)$$

By solving the Schrödinger equation to first order in perturbation theory, the time dependent fidelity to be in the unit filled state $F(t) = |c_0(t)|^2$ can be estimated to be:

$$\begin{aligned}
F(t) &= 1 - \sum_{r=0}^{\lfloor M/2 \rfloor} |c_r(t)|^2, \qquad (11.4) \\
|c_r(t)|^2 &\approx 64\left(\frac{J}{E_r^{(1)}}\right)^2 \sin^2\left(\frac{\pi(2r-1)}{M}\right)\sin^2\left(\frac{E_r^{(1)}t/\hbar}{2}\right). \qquad (11.5)
\end{aligned}$$

If the number of wells $M \gg 1$, the sum in Eq. (11.4) can be approximated by an integral. In this case we get an expression for the fidelity of the form:

$$\begin{aligned}
F(t) &\simeq 1 - 64\frac{J^2 M}{U^2\pi}\int_0^{\pi} dx \sin^2(x)\sin^2\left(\frac{(U - 6J\cos(x))t}{2\hbar}\right) \\
&= 1 - 8\left(\frac{J}{U}\right)^2 M\left(1 - \frac{\cos(Ut/\hbar)J_1(6tJ/\hbar)}{3Jt/\hbar}\right), \qquad (11.6)
\end{aligned}$$

where J_n is the n^{th} Bessel function of the first kind.

To test the validity of the approximations, we first compare in Fig.11.1 the percentage fidelity given by the Eq. (11.4) (red) and the numerical solution calculated by the exact diagonalization of the Bose-Hubbard Hamiltonian (dots). Due to the exponential scalability of the Hilbert space we restrict the calculations to only 5 wells. We also show comparisons with the analytic solution, Eq. (11.6) (blue). The on site interaction strength used was $U/J = 100$.

We observe a very nice agreement between the perturbative and the exact solutions. The agreement confirms the validity of restricting the evolution to the

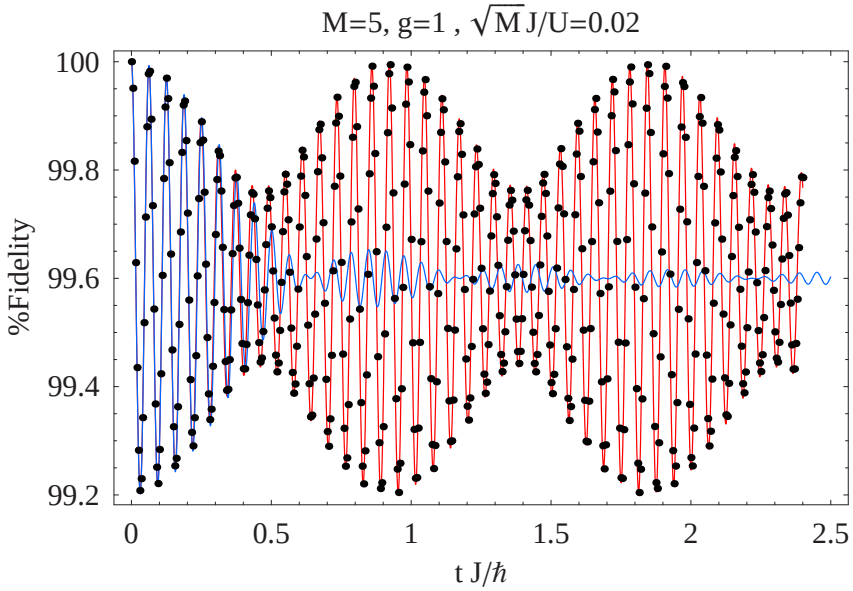

Figure 11.1: Comparisons between the time evolution of the percentage fidelity calculated by diagonalizing the Bose-Hubbard Hamiltonian (dots), the perturbative solution inside the one particle hole subspace (red) and the analytic solution Eq. 11.6 (blue).

one particle hole subspace. On the other hand, because of the small number of wells used for the simulations, we do not expect Eq. (11.6) to be a very good approximation. Nevertheless, we observe that for short times the analytic solution is a fair description of the dynamics.

In Fig.11.2 we compare the analytic solution, Eq. (11.6) (blue) with the perturbative solution given by Eq. (11.4) (red) for a larger system with $M = 31$. Even though for this large number of wells an exact solution is not available, we ensure the validity of perturbation theory by choosing the same $\sqrt{M}J/U$ than the one in Fig.11.1. In this $M = 31$ case, which lies in a regime where we expect Eq. (11.6) to be valid, the agreement between the blue and red curves is very good.

In general the behavior of $F(t)$ consists of fast oscillations with frequency equal to $U/\hbar$, modulated by longer oscillations with frequency determined by the zeros of J_1. For short times, $Jt/\hbar \ll 1$, the fidelity is

$$F(t) \approx 1 - 16\left(\frac{J}{U}\right)^2 M \sin^2\left(\frac{Ut/\hbar}{2}\right), \tag{11.7}$$

which corresponds to the Rabi oscillations of an effective two level system spanned by $|T\rangle$ and $|S\rangle$, with $|S\rangle$ the translationally invariant state directly coupled to the first order ground state (see Eq. (9.9)). For later times the coupling to other states becomes important. Notice that the time average of the fidelity over many oscillation periods is $\langle F(t)\rangle = 1 - 8(J/U)^2 M$. Consequently, the deviation from a

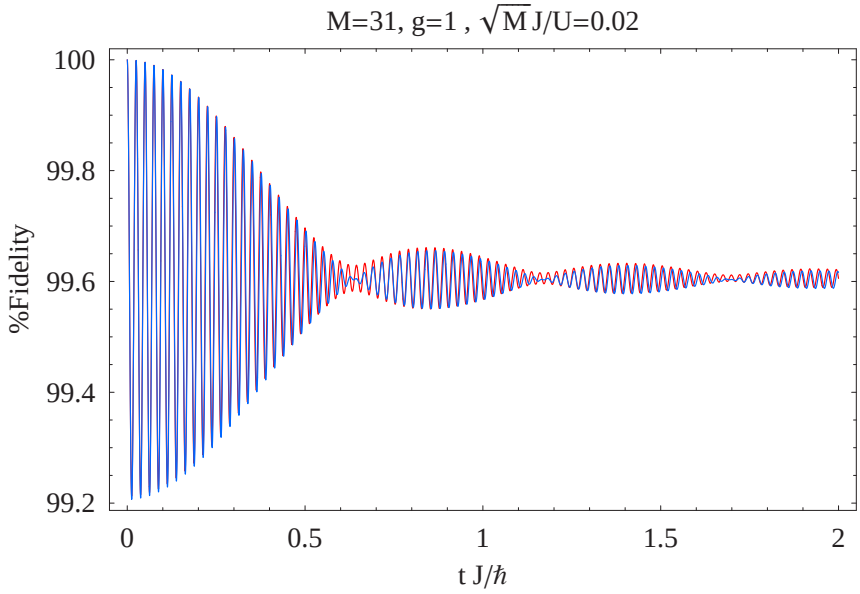

Figure 11.2: Percentage fidelity as a function of time calculated using the perturbative solution 11.4 (red) and the analytic solution Eq. 11.6 (blue).The number of sites used for the plot is $M = 31$

perfectly prepared register, described by $1-\langle F(t)\rangle$, is twice as bad as if the system were prepared in the stationary ground state of the Bose-Hubbard Hamiltonian (Eq. (9.8)). This indicates that a lattice filled with a commensurate number of atoms in the Mott insulator state may create a more robust quantum computer register than one prepared dissipatively.

11.2 Dynamics in presence of the external trap

As mentioned before, in practice it is difficult to prepare an optical lattice with exactly one atom per well. To arrange the desired configuration, we propose to use an inhomogeneous lattice with open boundaries created by a weak quadratic magnetic trap. We require fewer number of atoms than available sites, $N < M$. The addition of the trap acts to collect atoms near the potential minimum and leaves empty wells (holes) at the edges. In experiments where the optical lattice is loaded from a BEC, the external trap is already present to confine the condensate. For simplicity we assume a one dimensional trap with oscillation frequency given by ω_T. The magnetic confinement introduces a characteristic energy scale $\Omega = m/2a^2\omega_T$, so that $V_n = \Omega n^2$ (see Eq. (6.1)). To inhibit multiple atom occupation in any well in the ground state configuration, we require the on site interaction energy U to be larger than the trapping energy of the most externally trapped atoms, $U > \frac{\Omega(N-1)^2}{4}$.

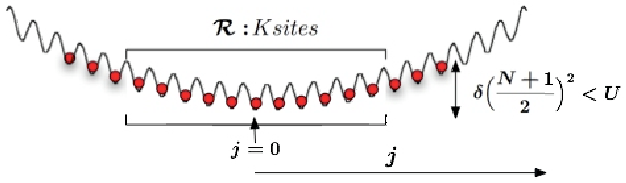

Figure 11.3: Schematic of an inhomogeneous lattice filled with N qubits with an onsite interaction energy U. An externally applied trapping potential of strength $V_j = \Omega j^2$, e.g. due to a magnetic field, acts to fill gaps in the central region of the trap. The center subspace $\mathcal{R}$ of the lattice defines the quantum computer register containing $K < N$ qubits.

We define our register as the subspace $\mathcal{R}$ comprising $K < N$ wells in the center region of the the trap (see Fig. 11.3). The barrier space flanking $\mathcal{R}$ will act to suppress percolation of holes from the edges to the center. The estimated probability for holes in $\mathcal{R}$ due to tunneling through the barrier is $p_h \approx \prod_{j=(K-1)/2}^{(N+1)/2}(J/\Omega(2j+1))^2 = (J/2\Omega)^{N-K+4}(\Gamma[K/2]/\Gamma[N/2+1])^2$, which is negligible provided the barrier region is sufficiently large and $J/K\Omega < 1$.

Hereafter, we restrict our attention to the dynamics of the reduced state of the register obtained by the tracing over spatial modes outside the register subspace of the entire many body wavefunction. The degree of inhomogeneity is quantified by the ratio Ω/J. For $0 < \Omega/J \ll 1$, the energy splitting between Fock states describing particle-hole pairs is small and the model of homogeneous dynamics is valid.

For $\Omega/J \gtrsim 1$, to first order in perturbation theory, the state space is spanned by the unit filled state in the register subspace, $|T\rangle_{\mathcal{R}}$, and the $2K$ nearest neighbor particle-hole pairs $|S_j^{\pm}\rangle$:

$$|T\rangle_{\mathcal{R}} = \underbrace{|1,1,1,\quad \ldots,\quad ,1,1,1\rangle}_{K\quad sites}, \tag{11.8}$$

$$|S_j^{+}\rangle_{\mathcal{R}} = |1,\ldots,\underbrace{2}_{j},\underbrace{0}_{j+1},\ldots,1\rangle. \quad |j| < (K-1)/2, \tag{11.9}$$

$$|S_j^{-}\rangle_{\mathcal{R}} = |1,\ldots,\underbrace{2}_{j-1},\underbrace{0}_{j},\ldots,1\rangle. \tag{11.10}$$

Here we have introduced coordinates with the site $j = 0$ coincident with the trap minimum. For each j the states $|S_j^{\pm}\rangle_{\mathcal{R}}$ are distinguished by the two energetically distinct orientations of a doubly occupied site and its neighboring hole with energies, $E(S_j^{\pm}) = U(1 \mp \frac{\Omega}{U}(2j-1))$. We define the zero of energy coincident with the state $|T\rangle_{\mathcal{R}}$.

With an eye to the projective measurement, it is important to understand the free dynamics when the trap is present and the register is initialized in the pure state $|T\rangle_{\mathcal{R}}$ inside the register, ${}_{\mathcal{R}}\langle T|\Psi(0)\rangle_{\mathcal{R}} = 1$. Here $|\Psi(0)\rangle_{\mathcal{R}}$ is the projection of the initial many body state $|\Psi(0)\rangle$ in the register subspace, i.e. $|\Psi(0)\rangle_{\mathcal{R}} = |\mathcal{P}\rangle\langle\mathcal{P}|\Psi(0)\rangle$ with $|\mathcal{P}\rangle\langle\mathcal{P}|$ the projection operator that traces over spatial modes outside the register. We proceed to estimate the fidelity to be in the unit filled state in the register: $F_{\mathcal{R}}(t) = |_{\mathcal{R}}\langle T|\mathcal{P}\rangle\langle|\mathcal{P}|\Psi(t)\rangle|^2 \equiv |_{\mathcal{R}}\langle T|\Psi(t)\rangle_{\mathcal{R}}|$.

The quantity $F_{\mathcal{R}}(t)$ is generally difficult to compute because atoms couple into and out of the register. Instead, we will first solve the simpler problem of the fidelity to be in the target state of a commensurately filled inhomogeneous lattice with K sites. We will use this fidelity to estimate $F_{\mathcal{R}}(t)$. In the commensurately filled inhomogeneous system, to first order in J/U, the dynamics can be restricted to the Hilbert space spanned by the state vectors $\{|T\rangle_{\mathcal{R}}, |S_j^{\pm}\rangle_{\mathcal{R}}\}$, and therefore the time dependent state can be written as :

$$|\Psi(t)\rangle_{com} = c_T(t)|T\rangle_{\mathcal{R}} + \sum_{j,\pm} e^{-iE(S_j^{\pm})t/\hbar} c_{S_j^{\pm}}(t)|S_j^{\pm}\rangle_{\mathcal{R}}. \tag{11.11}$$

The evolution of the amplitudes $\{c_T(t), c_{S_j^{\pm}}(t)\}$ is dictated by the following equations of motion:

$$i\hbar\frac{\partial}{\partial t}c_T(t) = -J\sqrt{2}\sum_{j,\pm} e^{-iE(S_j^{\pm})t/\hbar} c_{S_j^{\pm}}(t), \tag{11.12}$$

$$i\hbar\frac{\partial}{\partial t}c_{S_j^{\pm}}(t) = -J\sqrt{2}e^{-iE(S_j^{\pm})t/\hbar} c_T(t). \tag{11.13}$$

Using the fact that $J/U \ll 1$, for times $Jt \lesssim \hbar$ we can set the value of $c_T(t)$ in Eq. (11.13) to 1. Integrating the equation we obtain

$$|c_{S_j^{\pm}}(t)|^2 = 8\left(\frac{J}{U}\right)^2 \sin^2\left(\frac{E(S_j^{\pm})t}{2\hbar}\right), \tag{11.14}$$

$$|c_T(t)|^2 = 1 - 8\left(\frac{J}{U}\right)^2 \sum_{j,\pm}\left|c_{S_j^{\pm}}(t)\right|^2. \tag{11.15}$$

After performing the sum, the fidelity $F_{com}(K,t) \equiv |c_T(t)|^2$ is :

$$F_{com}(K,t) \approx 1 - 8\frac{J^2}{U^2}\left(K - \cos(Ut/\hbar)\left(1 + \frac{\sin(\Omega(K-1)t/\hbar)}{\sin(\Omega t/\hbar)}\right)\right). \tag{11.16}$$

Notice that for $\Omega t \to 0$, we recover the short time fidelity in the homogeneous case, Eq. (11.7).

Once $F_{com}(K,t)$ is calculated, we can bound the fidelity $F_{\mathcal{R}}(t)$ inside the register. Provided $N > K$ the following inequalities on the time averaged fidelities hold:

$$\langle F_{com}(N,t)\rangle \leq \langle F_{\mathcal{R}}(t)\rangle \leq \langle F_{com}(K,t)\rangle. \tag{11.17}$$

The lower bound arises because the probability to be in the unit filled state of a large commensurately filled lattice, given an initial state which is unit filled, is always less than or equal to the probability to be unit filled over a smaller subspace of $K < N$ of a non commensurately filled lattice whose register is prepared in the unit filled state. This inequality holds provided the probability for holes to tunnel into the register $\mathcal{R}$ is small over relevant time scales. The upper bound is a consequence of the fact that unit filling in the register state is degraded because particles can tunnel in and out of the register. Therefore its fidelity is less than that of a commensurately filled lattice of the same size K prepared in the unit filled state.

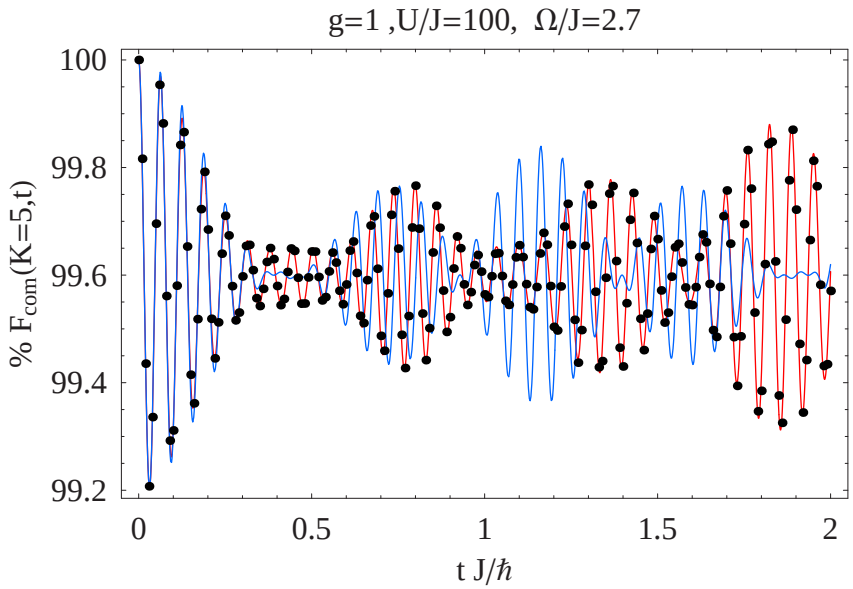

Figure 11.4: Comparisons between the time evolution of the percentage fidelity $F_{com}(K = 5, t)$ calculated by evolving the initial target state using the Bose-Hubbard Hamiltonian (dots), the restricted one particle hole basis (red) and the analytic solution Eq. 11.16 (blue). In the plot we assumed a commensurate unit filled lattice with five sites and infinitely high boundaries.

In Fig. 11.4 we compare this analytic solution, Eq. 11.16 (blue), with the solutions found by propagating the initial state using the exact Bose-Hubbard Hamiltonian (dots) and by using a restricted basis set of dimension $K(K-1)+1$ consisting of the target state and all particle-hole pairs (red). Infinitely high boundaries were assumed for the numerical solutions. The parameters used for the plot were $U/J = 100$,$\Omega/J = 2.7$ and $K = 5$. We observe complete agreement between the exact points and the red curve, which justifies the restriction of the dynamics to the one-particle hole subspace. On the other hand, the analytic approximation accurately reproduces the exact dynamics only for times $t \lesssim 0.5\hbar/J$. This is not unexpected because the analytic solution only takes into account the states with

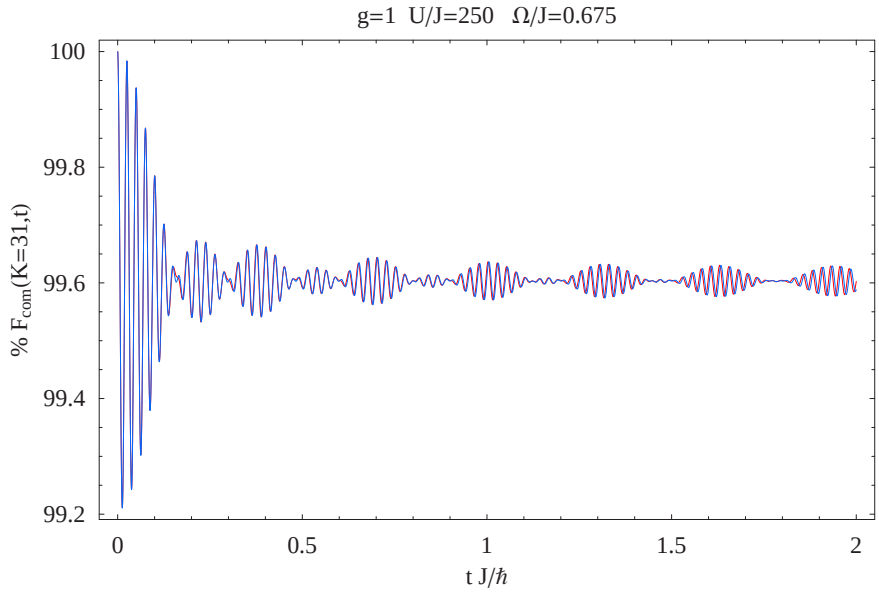

Figure 11.5: Percentage fidelity as a function time calculated using the approximated solution 11.16 (blue) and the fidelity found numerically by restricting the dynamics to the one particle hole subspace. We assumed infinity high boundaries and $K = 31$.

no separation between the atomic pair and the hole which are the ones coupled to first order in J to the ground state and sets $c_T(t)$ in Eq. (11.13) to one. In Fig. 11.5 we plot the fidelity for a lattice with more sites, $K = 31$. Because the Hilbert space is too large to have an exact solution, we decrease J to get the same $J\sqrt{K}/U$ ratio as the one used in Fig. 11.4. In this way we can be sure of the validity of the solution constrained to the one-particle hole subspace which is plotted in red. We observe for this parameter regime that the analytic solution (blue) gives a very good description of the quantum dynamics. This is consistent with the fact that as the ratio J/U is decreased, the role in the dynamics of other modes different from the $|S_j^{\pm}\rangle_{\mathcal{R}}$ modes becomes less important.

11.3 Measurement

In Sec. 11.2 we showed that the system dynamics can be restricted to a set of two level couplings $\{|T\rangle_{\mathcal{R}} \rightarrow |S_j^{\pm}\rangle\}$. We now sketch how to perform a continuous measurement to drive the register into the unit filled "target" state $|T\rangle_{\mathcal{R}}$. The full details are contained in [158]. The idea is to apply an external control field that is resonant with a coupling between the "faulty" states $\{|S_j^{\pm}\rangle\}$ and a set of excited states $\{|M_j^{\pm}\rangle_{\mathcal{R}}\}$. These states are described by $K-2$ atoms trapped in the lattice and a dipole-dipole molecular $S+P$ state at site $j+(1\mp1)/2$. The bound molecular

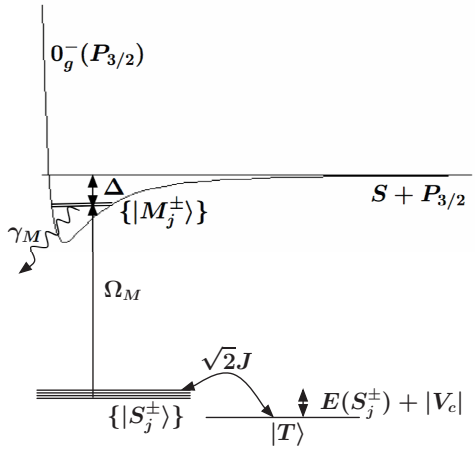

Figure 11.6: Schematic of the relevant couplings in the problem. The unit filled state $|T\rangle$ describing a target quantum register and the states $|S_j^\pm\rangle$ having one doubly occupied lattice site and a neighboring hole are coupled to first order in J. A catalysis laser resonantly couples the ground states $|S_j^\pm\rangle$ to the excited states $|M_j^\pm\rangle$ describing a bound molecule at the doubly occupied site. The bound states quickly decay and give the possibility of monitoring population in the "faulty" register states $|S_j^\pm\rangle$.

state is chosen such that the catalysis laser is far off resonance from other bound states and repulsive potentials, see Fig. 11.6. If the population in the excited states is easily measurable, for instance by the emission of photons during decay, then the presence of population in the particle-hole states can be monitored. It is vital that the coupling field be able to spectroscopically resolve the measurement transition without exciting the target state. This is possible if the atoms in multiply occupied wells see a shifted excited state, $E(M_j^\pm) = E(S_j^\pm) + E - U$, where for example E is the energy of a dipole-dipole molecular state. The "bare" energy Hamiltonian of the system is:

$$\begin{aligned} H_0 + H_{BH} &= \textstyle\sum_{j,\pm} E(S_j^\pm)|S_j^\pm\rangle_{\mathcal{R}\mathcal{R}}\langle S_j^\pm| + E(M_j^\pm)|M_j^\pm\rangle_{\mathcal{R}\mathcal{R}}\langle M_j^\pm| \\ &\quad -\sqrt{2}J\textstyle\sum_{j,\pm}(|S_j^\pm\rangle_{\mathcal{R}\mathcal{R}}\langle T| + |T\rangle_{\mathcal{R}\mathcal{R}}\langle S_j^\pm|). \end{aligned} \tag{11.18}$$

When the catalysis laser is turned on, for the bound states of interest, such as the long range bound states of the $0_g^-(P_{3/2})$ potential [159], the detuning from *atomic* resonances is several thousands of linewidths, meaning the atomic saturation is low. In this case, the excited atomic states can be adiabatically eliminated and each atom in a singly occupied well experiences a light shift equal to V_c. Because there are K singly occupied wells in the $|T\rangle$ state its total single atom light shift is equal to KV_c. The $|S_j^\pm\rangle$ states have $K-2$ singly occupied wells giving a corresponding light shift of $(K-2)V_c$. The differential *single atom* light shift between these states is then $2|V_c|$. Therefore, when the control Hamiltonian with

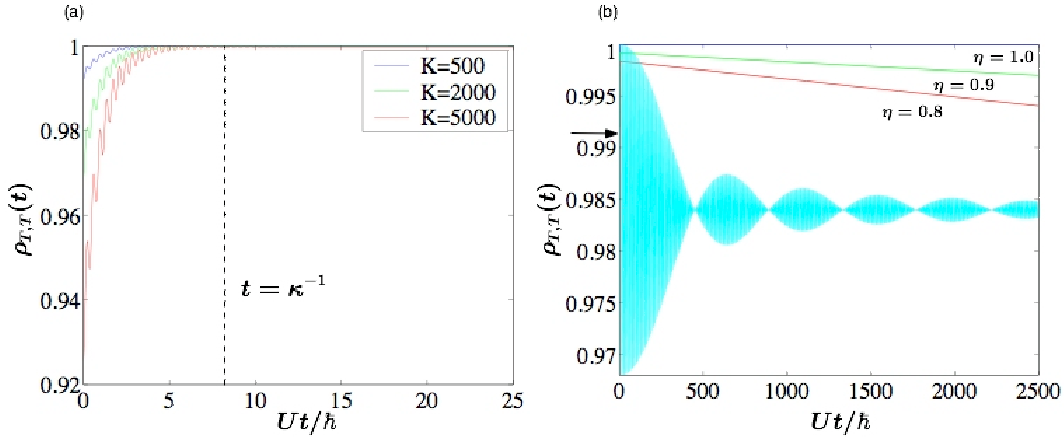

Figure 11.7: Population in the unit filled register state $|T\rangle_{\mathcal{R}}$ during continuous measurement of the register beginning in the Bose-Hubbard ground state $|\Psi_g\rangle$. The plots show dynamics appropriate to tunneling in one dimension with $U/J = 500$. (a) Quantum trajectories corresponding to a null measurement result for three different register sizes K. The time scale to saturate the target state is independent of the number of qubits: $t_{sat} \approx \kappa^{-1}$. (b) Long time dynamics for $K = 501$, $N = 551$ and finite detector efficiencies η. The population in $|T\rangle_{\mathcal{R}}$ for $\eta = 1$ is indistinguishable from one. Also shown is the oscillatory dynamics at fundamental frequency U described by Eq. (11.16) if the measurement is turned off after the target state is reached. The arrow indicates $\rho_{T,T}(0)$.

Rabi frequency Ω_M is turned on resonant, the total Hamiltonian in the rotating frame is:

$$\begin{aligned} H_I &= \textstyle\sum_{j,\pm}(2|V_c| + E(S_j^{\pm}))|S_j^{\pm}\rangle_{\mathcal{R}\mathcal{R}}\langle S_j^{\pm}| + (|2V_c| + E(S_j^{\pm}) - U)|M_j^{\pm}\rangle_{\mathcal{R}\mathcal{R}}\langle M_j^{\pm}| \\ &\quad -\sqrt{2}J(|S_j^{\pm}\rangle_{\mathcal{R}\mathcal{R}}\langle T| + |T\rangle_{\mathcal{R}\mathcal{R}}\langle S_j^{\pm}|) + \hbar\Omega_M/2(|M_j^{\pm}\rangle_{\mathcal{R}\mathcal{R}}\langle S_j^{\pm}| + |S_j^{\pm}\rangle_{\mathcal{R}\mathcal{R}}\langle M_j^{\pm}|)), \end{aligned} \tag{11.19}$$

Any population in the bound molecular states will decay at a rate $\gamma_M \approx 2\Gamma$, where Γ is the single atom decay rate. For molecular photo-association by red detuned light, the decay products are typically ground state molecular species or "hot" atoms meaning the atoms escape the trapped ground states described by Eq. (11.10). It is possible then to model the system according to a trace non-preserving master equation:

$$\dot{\rho} = -i/\hbar[H_I, \rho] - \gamma_M/2 \sum_{j,\pm}(|M_j^{\pm}\rangle_{\mathcal{R}\mathcal{R}}\langle M_j^{\pm}|\rho + \rho|M_j^{\pm}\rangle_{\mathcal{R}\mathcal{R}}\langle M_j^{\pm}|). \tag{11.20}$$

Assuming low saturation of the excited states, the dynamics in the ground state is

$$\begin{aligned}
\dot{\rho}_{S_j^\pm,T} &= -i\rho_{S_j^\pm,T}(E(S_j^\pm)+|V_c|)/\hbar + i(\rho_{T,T}-\rho_{S_j^\pm,S_j^\pm})\sqrt{2}J/\hbar - \rho_{S_j^\pm,T}\kappa \\
\dot{\rho}_{T,T} &= i(\rho_{S_j^\pm,T}-\rho_{T,S_j^\pm})\sqrt{2}J/\hbar \\
\dot{\rho}_{S_j^\pm,S_j^\pm} &= -i(\rho_{S_j^\pm,T}-\rho_{T,S_j^\pm})\sqrt{2}J/\hbar - 2\rho_{S_j^\pm,S_j^\pm}\kappa.
\end{aligned} \tag{11.21}$$

These equations describe the Bose-Hubbard coupled states with a decay in population of each state with an atomic pair at a rate $2\kappa = {\Omega_M}^2\gamma_M/(4(U/\hbar)^2 + (\gamma_M/2)^2)$, and decay of coherences between each of these states and state $|T\rangle$ at a rate κ.

This type of evolution characterized by measurement induced phase damping was studied extensively by Gagen and Milburn [160]. We now show that our system can satisfy the conditions for this effect and in particular can be driven to the $|T\rangle$ state by monitoring the environment for a signature of decay from the molecular bound state.

For the inhomogeneous system, the state $|T\rangle$ couples to $2K$ distinguishable states $|S_j^\pm\rangle$. However, we can define an effective Rabi frequency between the state $|T\rangle$ and the subspace spanned by $|S_J^\pm\rangle$. This frequency is close to the coupling matrix element between the state $|T\rangle$ and the state $|S\rangle$ in the homogeneous system, namely $2\sqrt{K}J$. The coherences between the two subspaces decay at a rate κ, and the population in the subspace $\{|S_j^\pm\rangle\}$ decays at a rate 2κ. The "good" measurement regime as derived in [160] is then:

$$\Omega_M/\gamma_M \ll 1 < \hbar\kappa/2\sqrt{K}J. \tag{11.22}$$

The left side inequality ensures that the excited states $|M_j^\pm\rangle$ are weakly populated (equivalent to the condition for adiabatic elimination of these states). The right side inequality ensures that measurement is sufficiently strong to damp coherences on the time scale that they develop due to tunneling.

When the environment is monitored, for instance by looking for photon scattering from the bound molecular state, the evolution of ground states can be modelled using quantum trajectories. The success or failure of the preparation is conclusive with failure probability $p_{fail} = 1 - \rho_{T,T}(0)$. Real experiments will be constrained to finite detector efficiencies η. For $\eta = 0$, corresponding to nonselective measurement, the system dynamics evolve according to Eq. (11.21). In the case of finite detector efficiencies, we can express the approximate fidelity to be in the target state is $F(\eta,t) = \rho_{T,T}(t) = \eta + (1-\eta)\rho_{T,T}^{\eta=0}(t)$. Simulations of successful register preparation and maintenance by measurement with different efficiencies are shown in Fig. 11.7.

It is necessary to keep the measurement on during a computation to maintain high fidelity in the unit filled state. If instead the catalysis field is turned off after the target state is reached, the system will freely evolve as shown in Sec. 11.2. To illustrate this we show in Fig. 11.7 the evolution of the fidelity described by Eq. (11.16) if the measurement is turned off after the target state is reached.

11.4 Conclusions

In summary, we have shown that efforts to prepare a register of atomic qubits in an optical lattice suffer from errors inherent in the underlying many body dynamics. By considering the free dynamics in both homogeneous and trapped systems we have shown that there is a loss of fidelity of initialization of the unit filled register which scales with the number of qubits because it is not a stationary state. Because our analysis is based on first order perturbation theory we established the parameter regime where our analytic approach is valid by comparing it with exact numerical results for moderate numbers of atoms and wells. To make the Mott insulator transition a robust mechanism for initialization, we have suggested one approach to correct for the mentioned problems by performing a continuous measurement on the system. While our discussion has focused on one dimensional dynamics, the method is also applicable to higher dimensions, which is the relevant regime for scalability.

Chapter 12

Conlusions

This thesis gives a global understanding of the basic physics that describes bosonic cold atoms in optical lattices, starting from the superfluid regime and going into the strongly correlated Mott insulator regime. In the following I am going to summarize what I consider are the most relevant contributions of this work.

- The equilibrium properties of lattice systems in the superfluid regime were studied by using standard mean field techniques and quadratic approximations.

- An explicit expression for the superfluid density based on the rigidity of the system under phase variations was derived. This expression enabled us to explore the connection between the quantum depletion of the condensate and the quasimomentum distribution on the one hand, and the superfluid fraction on the other. Also, the superfluid fraction was shown to be a natural order parameter to describe the superfluid to Mott insulator transition.

- A functional effective action approach, the 2PI-CTP formalism, capable of dealing with nonequilibrium situations that require a treatment beyond mean field theory, was studied. Using the patterned loading system, this formalism was shown to be a powerful tool to go beyond the HFB approximation and to incorporate the nonlocal and non-Markovian aspects characteristic of the quantum dynamics.

- It was shown that the complicated nonlocal and non-Markovian solutions derived using the 2PI-CTP formalism reduce to the standard kinetic theory equations when the system dynamics admits two-time separation.

- Bragg spectroscopy was shown to be a suitable experimental tool to characterizing the Mott insulator phase and to estimate the temperature of the system deep in the Mott insulator regime.

- It was shown that the use of a lattice with a spatial inhomogeneity created by a quadratic magnetic trapping potential, together with a selective mea-

surement of atomic pairs allow for the Mott insulator transition to become a robust mechanism for quantum register initialization.

In the recent years there has been spectacular progress in experimental and theoretical studies of atoms loaded into an optical lattice. However, there are still many ideas and possible experiments that could help us to address fundamental questions in solid state physics, atomic physics, quantum optics and quantum information. I want to finish this work by mentioning some of them.

One can use for example multi-component ultracold atoms in optical lattices together with Feshbach resonances to realize Hamiltonians other than the pure Bose-Hubbard one. Also by loading fermionic atoms into an optical lattice the Hubbard Hamiltonian could be realized. This could help to answer many theoretical questions still open in fermionic systems, such as the BEC-BCS crossover and the basic physics behind high temperature superconductivity. From the perspective of atomic and molecular physics an interesting experiment could be the use of the Mott insulator state with two atoms per site as a mean to create a molecular condensate. The creation of vortices in individual lattice sites could also allow the study of the integer and fractional quantum Hall effects in ultracold gases. By introducing noise in a controlled way in optical lattice, one can also study disordered periodic systems, which are very important in condensed matter physics. And finally and perhaps one of the most challenging tasks is to develop the necessary techniques and protocols that allow neutral atoms in optical lattices as a mean to implement a quantum computer.

Bibliography

[1] A. Einstein, Sitzungsbericht der Preussischein Akademie der Wissenschaften, p. 3,(1925).

[2] S. N. Bose Z. Phys **26**, 178(1924).

[3] F. London, Nature **141**, 643 (1938); Phys. Rev **54**, 947 (1938).

[4] E. C. Svensson and V. F. Sears, Progress of low temperature physics, Vol XI, ed. D.F. Brewer, (North Holland,Amsterdam,187).

[5] I. F. Silvera and J. T. M. Walraven, Phys. Rev. Lett **44**, 164 (1980).

[6] M. H. Anderson, J. R. Ensher, M. R. Matthewes, C. E. Wieman and E. A. Cornell Science **269**, 198 (1995).

[7] K. B. Davis, M. O. Mewes, M. R. Andrews, N. J. van Druten, D. S. Durfee, D. M. Kurn and W. Ketterle, Phys. Rev. lett. **75**, 3969 (1995).

[8] C. C. Bradley, C. A. Sackett, J. J. Tollet and R. Hulet, Phys. Rev. Lett. **78**, 985 (1997).

[9] C. J. Foot, Contemp. Phys. **32**, 369 (1991).

[10] E. P. Gross, Nuovo Cimiento, **20**, 454 (1961); L. P. Pitaevskii, Sov. Phys. JETP **13**, 451 (1961).

[11] N. N. Bogoliubov, J. Phys. (USSR) **11**, 23 (1947).

[12] F. Dalfovo, S. Giorgini, L. P. Pitaevskii and S. Stringari, Theory of Bose-Einstein condensation in trapped gases, Rev. Mod. Phys. 71, 463 (1999).

[13] D. A. W. Hutchinson et al., J. Phys. B: At. Mol. Opt. Phys. **57** 3825 (2000).

[14] N.P. Proukakis, S.A. Morgan, S. Choi and K. Burnett, Phys. Rev. A **58**, 2435 (1998).

[15] H. Shi and A. Griffin, Phys. Rep. 304, 1 (1998) and A. Griffin, Phys. Rev. B, **53**, 9341 (1995).

[16] S. A. Morgan *A gapless theory of Bose-Einstein Condensation in Dilute Gases at Finite Temperature,* D. Phil. Thesis, Oxford University (1999), S. A. Morgan, J. Phys. B: At. Mol. Opt. Phys. **57**, 3847 (2000).

[17] D. S. Jin, J. R. Ensher, M. R. Matthews, C. E. Wieman and E. A. Cornell, Phys. Rev. Lett. **77**, 420 (1996).

[18] S. Stringari Phys. Rev. Lett. **77**, 2360 (1996); F. Dalfovo, S. Giorgini, M. Guilleumas, L. Pitaevskii, and S. Stringari, Phys. Rev. A **56**, 3840 (1997).

[19] M. Edwards, R. J. Dodd, C. W. Clark, P. A. Ruprecht and K. Burnett, Phys. Rev. A **53**, R1950 (1996); M. Edwards, P. A. Ruprecht, K. Burnett, R. J. Dodd and C. W. Clark, Phys. Rev. Lett. **77**, 1671 (1996); M. Rusch and K. Burnett, Phys. Rev. A **59**, 3851 (1999); D. A. W. Hutchinson, E. Zaremba and A. Griffin, Phys. Rev. Lett. **78**, 1842 (1997); L. P. Pitaevskii and S. Stringari, Phys. Lett. A **235**, 398 (1997); R. J. Dodd, M. Edwards, C. W. Clark and K. Burnett, Phys. Rev. A, **57**, R32 (1998).

[20] S. L. Cornish, N. R. Claussen, J. L. Roberts, E. A. Cornell, and C. E. Wieman Phys. Rev. Lett. **85**, 1795 (2000).

[21] Elizabeth A. Donley, Neil R. Claussen, Simon L. Cornish, Jacob L. Roberts, Eric A. Cornell, Carl E. Wieman, Nature **412**, 295 (19 Jul 2001).

[22] P. O. Fedichev, M. W. Reynolds, and G. V. Shlyapnikov, Phys. Rev. Lett. **77**, 2921 (1996).

[23] Phillip L. Gould, George A. Ruff, and David E. Pritchard, Phys. Rev. Lett. **56**, 827 (1986).

[24] P. J. Martin, Bruce G. Oldaker, Andrew H. Miklich, and David E. Pritchard, Phys. Rev. Lett. **60**, 515 (1988).

[25] C.S. Adams, M. Sigel and J. Mlynek, Phys. Rep **240**, 143 (1994).

[26] A. Hemmerich and T. W. Hänsch, Phys. Rev. Lett. **70**, 410 (1993).

[27] A. Hemmerich, M. Weidemüller, T. Esslinger, C. Zimmermann, and T. Hnsch,Phys. Rev. Lett. **75**, 37 (1995).

[28] M. Weidemller, A. Hemmerich, A. Görlitz, T. Esslinger, and T. W. Hänsch, Phys. Rev. Lett. **75**, 4583 (1995).

[29] G. Grynberg, B. Lounis, P. Verkerk, J. Y. Courtois, and C. Salomon, Phys. Rev. Lett. **70**, 2249 (1993).

[30] Vladan Vuletic, Cheng Chin, Andrew J. Kerman, and Steven Chu, Phys. Rev. Lett. **81**, 5768 (1998).

[31] Andrew J. Kerman, Vladan Vuletic, Cheng Chin, and Steven Chu, Phys. Rev. Lett. **84**, 439442 (2000).

[32] Marshall T. DePue, Colin McCormick, S. Lukman Winoto, Steven Oliver, and David S. Weiss, Phys. Rev. Lett. **82**, 2262 (1999).

[33] S. Peil, J. V. Porto, B. L. Tolra et. al, Phys. Rev. A **67**, 051603 (2003).

[34] P. Blair Blakie and Charles W. Clark, J. Phys. B: At. Mol. Opt. Phys. **37** 1391 (2004).

[35] M. Greiner, I. Bloch, O. Mandel, T. W. Hänsch, and T. Esslinger, Phys. Rev. Lett. 87, 160405 (2001).

[36] J. H. Denschlag, J. E. Simsarian, H. Häffner, C. McKenzie, A. Browaeys, D. Cho, K. Helmerson, S. L. Rolston, and W. D. Phillips, J. Phys. B **35**, 3095 (2002).

[37] F. Ferlaino, P. Maddaloni, S. Burger, F. S. Cataliotti, C. Fort, M. Modugno, and M. Inguscio Phys. Rev. A **66**, 011604 (2002).

[38] O. Morsch, J. H. Muller, M. Cristiani, D. Ciampini, and E. Arimondo, Phys. Rev. Lett. **87**, 140402 (2001).

[39] B. Anderson and M. Kasevich, Science **282**, 1686 (1998).

[40] O. Morsch, M. Cristiani, J. H. Muller, D. Ciampini, and E. Arimondo, Phys. Rev. A **66**, 021601 (2002).

[41] S. Burger, F. S. Cataliotti, C. Fort, F. Minardi, M. Inguscio, M. L. Chiofalo, and M. P. Tosi, Phys. Rev. Lett. **86**, 4447 (2001).

[42] W. K. Hensinger, H. Häffner, A. Browaeys, N. R. Heckenberg, K. Helmerson, C. McKenzie, G. J. Milburn, W. D. Phillips, S. L. Rolston, H. Rubinsztein-Dunlop, Nature **412**, 52 (2001).

[43] D. Jaksch, C. Bruder, C. W. Gardiner, J.I. Cirac and P. Zoller, Phys. Rev. Lett. **81**, 3108 (1998).

[44] M. P. A. Fisher, P. B. Weichman, G. Grinstein and D. S. Fisher, Phys. Rev. B **40**, 546 (1989).

[45] C. Orzel, A. K. Tuchman, M. L. Fenselau, M. Yasuda, and M. A. Kasevich, Science **23**, 2386 (2001).

[46] M. Greiner, O. Mandel, T. Esslinger, T. W. Hänsch, and I. Bloch, Nature **415**, 39 (2002).

[47] Markus Greiner, Olaf Mandel, Theodor W. Hänsch and Immanuel Bloch, Nature **419**, 51 (2002).

[48] P. Rabl *et al.*, Phys. Rev. Lett. **91**, 110403 (2003).

[49] I. Deutsch *et al.*, Phys. Rev. A **57**, 1972 (1998).

[50] T. Calarco *et al.*, J. Mod. Opt. **47**, 2137 (2000).

[51] A. L. Fetter and J. D. Walecka,*Quantum Theory of Many Particle Systems*, (McGraw-Hill, New York, 1971).

[52] V. N. Popov, *Functional Integrals in Quantum Field Theory and Statistical Physics* (Reidel, Dordrecht, 1983).

[53] M. Bijlsma and H. T. C. Stoof, Phys. Rev. A **55**, 498 (1997); U. Al Khawaja, J. O. Andersen, N. P. Proukakis, and H. T. C. Stoof Phys. Rev. A **66**, 013615 (2002).

[54] H. T. C. Stoof,in *Coherent Matter Waves*, proceedings of the summer Les Houches Lectures, session 72,1999, (Sprinder-Verlag, Berlin, 2001).

[55] Emil Lundl and Jorgen Rammer, Phys. Rev. A **66**, 033607 (2002).

[56] J. S. Schwinger, J. Math. Phys. **2**, 407 (1961); L. V. Keldysh, Zh. Eksp. Teor. Fiz. **47** , 1515 (1964) [Engl. trans. Sov. JETP **20** 1018 (1965)]; V. Korenman, Ann. Phys. **39**, 72 (1966); G. Zhou, Z. Su, B. Hao and L. Yu, Phys. Rep. **118**, 1 (1985).

[57] J. Luttinger and J. Ward, Phys. Rev. **118**, 1417 (1960); C. de Dominicis and P. Martin, J. Math. Phys. **5**, 14 (1964); H.D. Dahmen and G. Jona Lasino, Nuovo Cimiento, **52A**, 807 (1962); J.M. Cornwall, R. Jackiw and E. Tomboulis, Phys. Rev. D **10** 2428 (1974).

[58] R. Walser, J. Williams, M. J. Holland et al., Phys. Rev. A **59**, 3878(1999); R. Walser, J. Cooper and M. Holland, Phys. Rev. A **63**, 013607 (2000).

[59] J. Wachter, R. Walser, J. Cooper and M. Holland, Phys. Rev. A **64**, 053612(2001).

[60] M. Imamovi-Tomasovi and A. Griffin, *in Progress in Nonequilibrium Green's Functions, edited by M. Bonitz* (World Scientific, Singapore, 2000), p. 404; M. Imamovi-Tomosovi and A. Griffin, Phys. Rev. A **60**, 494 (1999).

[61] S. G. Bhongale, R. Walser and M. J. Holland Phys. Rev. A **66**, 043618 (2002).

[62] J. Wachter, R. Walser, J. Cooper, and M. Holland Phys. Rev. A **65**, 039904 (2002); J. Wachter, R. Walser, J. Cooper, M. Holland, arXiv:cond-mat/0212432.

[63] S. T. Beliaev, Zh. Eksp. Teor. Fiz. **34**, 433 (1958) [Sov. Phys. JETP **7**, 299 (1958)].

[64] B. Paredes *et al.*, Nature **429**, 277 (2004).

[65] J. Stenger *et al.*, Phys. Rev. Lett. **82**, 4569 (1999).

[66] D. Stamper-Kurn *et al.*, Phys. Rev. Lett. **83**, 2876 (1999).

[67] N. W. Ashcroft and N. D. Mermin, *Solid State Physics*, W. B. Saunders Company (1976).

[68] J. M. Ziman, *Principles of the Theory of Solids*, Cambridge University Press, (1964).

[69] I. Abramowitz and I. A. Stegun, Handbook of Mathematical Functions (National Bureau of Standards, 1964).

[70] Hidestoshi Fukuyama, Phys. Rev. B, **8**, 5579 (1973).

[71] G. Wannier, Phys. Rev. **17**, 432 (1960).

[72] Gerhard Fasol, *Spectroscopy of Semiconductor Microstructures*, (NATO ASI Series, 1989, p. 333)

[73] M. BenDahan, E. Peik, J. Reichel, Y. Castin, and C. Salomon, Phys. Rev. Lett. **76**, 4508 (1996).

[74] W. Krauth, et al. Phys. Rev. B **45**, 3137 (1992).

[75] K. Seshadri et al, Europhys. Lett. **22**, 257 (1993).

[76] L. Amico and V. Penna, Phys. Rev. B **62**, 1224 (2000).

[77] D. van Oosten, P. van der Straten, and H. T. C. Stoof, Phys. Rev. A **63**, 053601 (2001).

[78] J. K. Freericks and H. Monien, Phys. Rev. B **53**, 2691 (1996).

[79] G. G. Batrouni *et al.* Phys. Rev. Lett. **65**, 1765 (1990); R. T. Scalettar *et al.*, Phys. Rev. Lett. **66**, 3144 (1991); P. Niyaz *et al.*, Phys. Rev. B. **44**, 7143 (1991); R. T. Scalettar *et al.*, Phys. Rev. Lett. **74**, 2527 (1995); G. G. Batrouni *et al.*, Phys. Rev. Lett. **89**, 117203 (2002).

[80] P. W. Anderson, Rev. Mod. Phys. **38**, 298 (1966); A. J. Leggett, Rev. Mod. Phys. **73**, 307 (2001); A. J. Leggett and F. Sols, Found. Phys. **31**, 353 (1991).

[81] V. L. Ginzburg and L. D. Landau, Zh. Eksp. Theor. Fiz. **20**, 1064 (1950); O. Penrose and L. Onsager, Phys. Rev. **104**, 576 (1956).

[82] Jared C. Bronski, Phys. Rev. Lett. **86**, 1402 (2001).

[83] B. Wu, R. B. Diener, and Q. Niu, Phys. Rev. A **65**, 025601 (2002).

[84] A. Trombettoni and A. Smerzi, J. Phys. B **34**, 4711 (2001).

[85] A. Trombettoni and A. Smerzi, Phys. Rev. Lett. **86**, 2353 (2001).

[86] D. I. Choi and Q. Niu, Phys. Rev. Lett. **82**, 2022 (1999).

[87] S. Raghavan, A. Smerzi, S. Fantoni, and S. R. Shenoy, Phys. Rev. A **59**, 620 (1999).

[88] I. Marino, S. Raghavan, S. Fantoni, S. R. Shenoy, and A. Smerzi., Phys. Rev. A **60**, 487 (1999).

[89] S. Raghavan, A. Smerzi, and V. M. Kenkre, Phys. Rev. A **60**, 1787 (1999).

[90] A. Smerzi and S. Raghavan, Phys. Rev. A **61**, 063601(2000).

[91] S. Giovanazzi, A. Smerzi, and S. Fantoni, Phys. Rev. Lett. **84**, 4521 (2000).

[92] G. J. Milburn, J. Corney, E. M. Wright, and D. F. Walls, Phys. Rev. A **55**, 4318 (1997).

[93] A. Smerzi, S. Fantoni, S. Giovanazzi, and S. R. Shenoy, Phys. Rev. Lett. **79**, 4950 (1997).

[94] C. Cohen-Tannoudji, B. Diu, and F. Laloë, *Quantum Mechanics*, Vol. 2 (John Wiley and Sons, 1977).

[95] K. Burnett, M. Edwards, C. W. Clark and M. Shotter, J. Phys. B: At. Mol. Opt. Phys. **35**, 1671 (2002).

[96] J. Andersen, U. Al Khawaja and H. T. C. Stoof, Phys. Rev. A **66**, 013615 (2002).

[97] C. W. Gardiner, Phys. Rev. A **56**, 1414 (1997).

[98] Y. Castin and R. Dum, Phys. Rev. A **57**, 308 (1998).

[99] N. M. Hugenholtz and D. Pines, Phys. Rev. **116**, 489 (1959); J. Goldstone, Nuovo Cimento **19**, 154 (1961).

[100] A. J. Legett, Rev. Mod. Phys. **71**, S318 (1999).

[101] E. M. Lifshitz and L. Pitaevskii, *Statistical Physics part 2*, Pergamon (Oxford, 1980).

[102] M. E. Fisher, M. N. Barber, and D. Jasnow, Phys. Rev. A **8**, 1111 (1973).

[103] R. Roth and K. Burnett, Phys. Rev. A **67**, 031602 (2003).

[104] D. Poilblanc, Phys. Rev. B **44**, 9562 (1991).

[105] B. S. Shastry and B. Sutherland, Phys. Rev. Lett. **65**, 243 (1990).

[106] B. S. Shastry and B. Sutherland, Phys. Rev. B **47**, 7995 (1993).

[107] J. Javanainen and M. Yu. Ivanov, Phys. Rev. A **60**, 2351(1999).

[108] J. Javanainen, Phys. Rev. A **60**, 4902 (1999).

[109] M. Shotter, J. Phys. B: At. Mol. Opt. Phys. **35**, 3019-3028 (2002).

[110] G. Baym, J. Phys. B: At. Mol. Opt. Phys. **34**, 4541-4550 (2001).

[111] F. Dalfovo, L. Pitaevskii, and S. Stringari, Phys. Rev. A **54**, 4213 (1996); A. L. Fetter and D. L. Feder Phys. Rev. A **58**, 3185 (1998).

[112] V. A. Kashurnikov, N. V. Prokofev, and B. V. Svistunov Phys. Rev. A **66**, 031601 (2002).

[113] M. D. Lee, S. A. Morgan, M. J. Davis, and K. Burnett Phys. Rev. A 65, 043617 (2002).

[114] S. Inouye et al, Nature **392**, 151 (1998).

[115] C. Regal et al. Nature **424**, 47 (2003).

[116] C. W. Gardiner and P. Zoller, Phys. Rev. A **61**, 033601 (2000); C.W. Gardiner, J.R. Anglin, T. I. A. Fudge, arXiv:cond-mat/0112129; C.W. Gardiner and M. J. Davis, arXiv:cond-mat/0308044.

[117] E. Calzetta and B. L. Hu, Phys. Rev. D **37**, 2878(1988)

[118] E. Calzetta and B. L. Hu, in *Heat Kernel Techniques and Quantum Gravity*, Vol. 4 of *Discourses in Mathematics and Its Applications*, edited by S. A. Fulling, Texas (A&M University Press, College Station, TX, 1995) or hep-th/9501040; E. Calzetta and B. L. Hu, Phys. Rev. D **61**, 025012 (2000).

[119] E. Calzetta, B. L. Hu, S. A. Ramsey, Phys. Rev. D **61** 125013 (2000).

[120] E. Calzetta and B. L. Hu, Phys. Rev. D **35**, 495(1987).

[121] S.A. Ramsey and B. L. Hu, Phys. Rev. D **56** 661 (1997).

[122] E. Calzetta and B. L. Hu, Phys. Rev. **D40**, 656 (1989).

[123] D. Bodeker, Nucl Phys. B **559**, 502 (1999); **566**, 402 (2000); J. Blaizot and E. Iancu, Phys. Rep. (2001).

[124] J. Rammer, *Quantum Transport theory*, Perseus books (Massachusetts, 1998).

[125] D. Boyanovsky, Ann. Phys, **300**, 1 (2002).

[126] F. Cooper, S. Habib, Y. Kluger, E. Mottola, J.P. Paz and P. Anderson, Phys. Rev. D **50**, 2848 (1994); Bogdan Mihaila, John F. Dawson and F. Cooper, Phys. Rev. D **56**, 5400 (1997); Bogdan Mihaila, John F. Dawson and F. Cooper, Phys. Rev. D **63**, 096003(2001); Bogdan Mihaila et al, Phys. Rev. D **62**, 125015(2000).

[127] G. Aarts et al, arXiv:hep-ph/0201308; J. Berges, Nucl. Phys. A **699**, 847 (2002); J. Berges and J. Cox, Phys. Lett. B **517**, 369 (2001); G. Aarts and J. Berges, Phys. Rev. D **64**, 105010 (2001).

[128] F. Lombardo, F. D. Mazzitelli and R. Rivers, arXiv:hep-ph/0204190.

[129] A. Polkovnikov, S. Sachdev, and S. M. Girvin, Phys. Rev. A **66**, 053607 (2002).

[130] A. Smerzi and S. Raghavan, Phys. Rev. A **61**, 063601(2000); A. J. Leggett and F. Sols, Foundations of Physics, **21**, 353 (1991); F. Sols, Physica B **194**, 1389 (1994).

[131] E. M. Wright , T. Wong, M. J. Collett, S. M. Tan, and D. F. Walls, Phys. Rev. A **56**, 591(1997).

[132] P. Hohenberg and P. Martin, Ann. Phys. (NY) **34**, 291 (1965).

[133] S. Giorgini, Phys. Rev. A **57** 2949(1997); S. Giorgini, Phys. Rev. A **61** 063615(2000).

[134] B. L. Hu and D. Pavon, Phys. Lett. B **180**, 329 (1986); H. E. Kandrup, Phys. Rev. D **37**, 3505 (1988); Phys. Rev. D **38**, 1773 (1988); S. Habib, Y. Kluger, E. Mottola and J. P. Paz, Phys. Rev. Lett. **76**, 4660 (1996); Y. Kluger, E. Mottola and J. M. Eisenberg, Phys. Rev. D **58**, 125015 (1998).

[135] R. Balescu, *Equilibrium and Nonequilibrium Statistical Mechanics*, John Wiley (New York, 1975).

[136] N. P. Proukakis and K. Burnett, J. Res. Natl. Inst. Stand. Technol. **101** 457 (1996); N. P. Proukakis and K. Burnett, Phys. Rev. A **57** 1230 (1998); T. Köhler and K. Burnett ,Phys. Rev. A **65** 033601 (2002).

[137] L.P. Kadanoff and G. Baym, *Quantum Statistical Mechanics: Green's Function Methods in Equilibrium and Nonequilibrium Problems*, Addison Wesley (New York, 1962).

[138] G. Baym, Phys. Rev. **127**, 1391 (1962), B. Vanderheyden and G. Baym, J. Stat. Phys. **93**, 843 (1998); M. Bonitz *Progress in Nonequilibrium Green's functions*, World Scientific (Singapore, 2000).

[139] J. W. Kane and L. P. Kadanoff, J. Math. Phys. **6**, 1902 (1965).

[140] E. Wigner, Phys. Rev. **40**, 749 (1932).

[141] S. Richard, F. Gerbier , J.H. Thywissen, M. Hugbart, P. Bouyer and A. Aspect, Phys. Rev. Lett. **91**, 010405 (2003).

[142] J. Steinhauer N. Katz, R. Ozeri , N. Davidson, C. Tozzo and F. Dalfovo, Phys. Rev. Lett. **91**, 060404(2003).

[143] J.M. Vogels, K. Xu, C. Raman, J. R. Abo-Shaeer and W. Ketterle, Phys. Rev. Lett. **88**, 060402(2002).

[144] R. Geursen, N.R. Thomas, A.C. Wilson, Phys. Rev. A **68**, 043611(2003).

[145] T. Stöferle, Henning Moritz, Christian Schori, Michael Köhl and Tilman Esslinger, Phys. Rev. Lett. **92**, 130403 (2004).

[146] P. B. Blakie, R. J. Ballagh and C. W. Gardiner, Phys. Rev. A **65**, 033602 (2002).

[147] A. Brunello, F. Dalfovo, L. Pitaevskii, S. Stringari and F. Zambelli, Phys. Rev. A **64**, 063614 (2001).

[148] C. Menotti, M. Krämer, L. Pitaevskii and S. Stringari, Phys. Rev. A, **67**, 053609 (2003).

[149] Elliott H. Lieb and Werner Liniger, Phys. Rev. **130**, 1605 (1963); Elliott H. Lieb, Phys. Rev. **130**, 1616 (1963).

[150] P. B. Blakie and J. V. Porto Phys. Rev. A **69**, 013603 (2004).

[151] D. van Oosten *et al.*, cond-mat/0405492.

[152] D. P. DiVincenzo, Fortschr. Phys. **48**, 771 (2000).

[153] D. Kielpinski, C. Monroe, and D. J. Wineland, Nature **417**, 709 (2002).

[154] A. van Oudenaarden and J. E. Mooij, Phys. Rev. Lett. **76**, 4947 (1996).

[155] P. Krüger, *et al.*, Phys. Rev. Lett. **91**, 233201 (2003).

[156] D. J. Han, M. T. DePue, and D. S. Weiss, Phys. Rev. A **63**, 023405 (2001).

[157] S. E. Hamann *et al.*, Phys. Rev. Lett. **80**, 4149 (1998).

[158] G. K. Brennen, G. Pupillo, A. M. Rey, C. W. Clark, C. J. Williams, submitted to Phys. Rev. Lett., arXiv:cond-mat/0312069.

[159] A. Fioretti *et al.*, Eur. Phys. J. D **15**, 189 (2001).

[160] M.J. Gagen and G.J. Milburn, Phys. Rev. A **47**, 1467 (1993).